University of Southampton

Faculty of Physical Science and Engineering

School of Electronics and Computer Science

Simulated Performance and Characterisation of a Small Ring-Cusp Gridded Ion Engine using Alternative Propellants

by

Nazareno Fazio

ORCID ID – 0000-0003-0968-304X

Thesis for the degree of Doctor of Philosophy

November 2024

University of Southampton

Abstract

Faculty of Physical Science and Engineering

School of Electronics and Computer Science

Doctor of Philosophy

Simulated Performance and Characterisation of a Small Ring-Cusp Gridded Ion Engine using Alternative Propellants

by

Nazareno Fazio

Nowadays, xenon is the most common propellant used for space applications as a result of its favourable physical and chemical properties. However, it is particularly expensive due to its limited availability and complex extraction process. Therefore, the search for a viable alternative is gaining importance to meet the need for a growing diversification of satellites, missions, and manoeuvres. This aspect has been boosted by the "New Space" revolution, which demands cheaper and simpler systems even at the cost of lower performance.

This thesis refers to the investigation to assess the possibility of replacing xenon as the main propellant for gridded ion engines. Krypton and a mixture of xenon and krypton were identified as possible alternatives. While only limited publications, dating back a few decades, exist for krypton with gridded ion engines and the majority were focused on large size discharge chambers, the literature on mixture of xenon and krypton with this type of thrusters is non-existent.

Two experimental campaigns were carried out to investigate the performance gap between xenon and the two alternative propellants: one with a small ring-cusp gridded ion engine, operated in discharge-only mode, and one with a hollow cathode, operated in diode mode. Both the thruster and the cathode were originally designed for xenon and, therefore, the results of these experiments represent a baseline and worst-case scenario for the alternative propellants. In both setups, the investigation was supported by an array of diagnostics tools (e.g. thermocouples and Langmuir probes) to allow an internal characterisation of the discharge chamber's phenomena and the measurement of the plasma properties (i.e. electron temperature, and plasma potential and density) with the objective to identify possible areas for improvement and optimisation (e.g. ion optics, operational points, cathode orifice, etc.).

Table of Contents

Table of Tables

Table of Figures

Table of Figures

Research Thesis: Declaration of Authorship

Print name: NAZARENO FAZIO

Title of thesis: Simulated Performance and Characterisation of a Small Ring-Cusp Gridded Ion Engine using Alternative Propellants

I declare that this thesis and the work presented in it are my own and has been generated by me as the result of my own original research.

I confirm that:

1. This work was done wholly or mainly while in candidature for a research degree at this University;
2. Where any part of this thesis has previously been submitted for a degree or any other qualification at this University or any other institution, this has been clearly stated;
3. Where I have consulted the published work of others, this is always clearly attributed;
4. Where I have quoted from the work of others, the source is always given. With the exception of such quotations, this thesis is entirely my own work;
5. I have acknowledged all main sources of help;
6. Where the thesis is based on work done by myself jointly with others, I have made clear exactly what was done by others and what I have contributed myself;
7. Parts of this work have been published as:
    - Conference papers
        - N. Fazio, I.O. Golosnoy, and S.B. Gabriel, “Alternative Propellants for Gridded Ion Engines”, in *6th Space Propulsion Conference*. Seville, Spain, 2018
        - N. Fazio, I.O. Golosnoy, S.B. Gabriel, and B. Wollenhaupt, “Mission Cost for Gridded Ion Engines using Alternative Propellants”, in *36th International Electric Propulsion Conference*. Vienna, Austria, 2019
        - N. Fazio, I.O. Golosnoy, and S.B. Gabriel, “Discharge Performance Analysis of Different Types of Gridded Ion Engines using Alternative Propellants”, in *37th International Electric Propulsion Conference*. Cambridge, Massachusetts, USA, 2022
        - N. Fazio, I.O. Golosnoy, and S.B. Gabriel, “Alternative Propellants for Gridded Ion Engines: Hollow Cathode Operation using Kr and Xe/Kr mixture”, in *37th International Electric Propulsion Conference*. Cambridge, Massachusetts, USA, 2022

  - N. Fazio, I.O. Golosnoy, S.B. Gabriel, F. Bosi, and F. Guarducci, “Characterisation of a Small Ring-Cusp Gridded Ion Engine using Alternative Propellants”, in *9th Space Propulsion Conference*. Glasgow, Scotland, 2024
  - N. Fazio, I.O. Golosnoy, S.B. Gabriel, F. Bosi, and F. Guarducci, “Experimental Characterisation of a Small Ring-Cusp Gridded Ion Engine using Alternative Propellants”, in *38th International Electric Propulsion Conference*. Toulouse, France, 2024
- Journal paper
  - N. Fazio, I.O. Golosnoy, and S.B. Gabriel, “Effects of Alternative Propellants on the Performance of Gridded Ion Engines”, *Journal of Electric Propulsion* (accepted for publication)

Signature: ..... Date:..... 10/11/2024

Acknowledgements

I would like to thank my supervisors, Prof. Stephen B. Gabriel and Dr Igor O. Golosnoy, for the opportunity to investigate this topic, and for their support via numerous discussions and suggestions. This project would not have been possible without the effort, time, guidance, and patience they have provided.

I would also like to thank my “Space propulsion group” colleagues: Cristian Dobranszki and Alexander Daykin-Iliopoulos for their help throughout the experimental setup in the TDHVL and the many discussions on electric space propulsion, Duncan Bell for the tutorials on electronics and circuits, and Christopher Tacon for the discussions about coding.

I also appreciated the support offered by the Tony Davies High Voltage Laboratory’s staff, and especially Neil Palmer for the in-depth expertise of work safety and procedures, and Alan Welford for his suggestions about “the best tools for the job”, which have simplified my life countless times.

A huge support for the preparation of the experimental setup has been provided by the ECS Workshop team, in the persons of Mark Long and James Chalk, with their precious comments and suggestions which helped improve the experimental designs from a manufacturing and quality point of view.

I would like to extend my appreciation to all the staff at the University of Southampton and to the colleagues in the ECS department who have contributed to this project.

In addition, I would also like the personnel at Mars Space Ltd, Dr Franco Bosi and Dr Francesco Guarducci, for allowing me to use the small thruster and for their help and support with the testing at their facilities.

Finally, I want to thank my family and relatives who have always been there to morally support and motivate me in this very long process. And last but not for importance, thanks to my fiancée, Krisztina, for everything you have done for me: I don’t think I would be where I am and who I am without your infinite patience throughout this challenging journey.

Definitions and Abbreviations

A	Cross-sectional area [m^2]
A_g, A_{grid}	Grid area [m^2]
A_{Lp}	Langmuir probe surface area [m^2]
B	Magnetic field [G]
C_0	Primary electron utilisation factor [A eq.$^{-1}$]
d	Sheath thickness [m]
d_s	Screen grid aperture diameter [m]
D	Diameter of round grid aperture [m]
E	Electric field [N/C] or [V/m]
f_b	Beam flatness
f_B	Extracted ion fraction
f_C	Fraction of ion current produced that goes to cathode potential surfaces
f_{conf}	Confinement factor
$F(\varepsilon)$	Electron energy distribution function as function of the electron kinetic energy ε
$\boldsymbol{I}$	Total impulse [N·s]
I_{accel}	Accelerator grid current [A]
I_b	Beam current [A]
$I_{b,j}$	Beam current of the j-th species [A]
$\hat{I}_{beam\_dc}$	Ion beam current in discharge-only mode [A]
I_C	Ion current to cathode potential surfaces [A]
I_d	Discharge current [A]
I_e	Electron current [A]
I_{e0}	Electron saturation current [A]
I_{grid}	Current to the grid [A]
I_i	Ion current [A]
I_k	Keeper current [A]
I_{Lp}	Langmuir probe collected current [A]
I_P	Ion production current [A]
I_s	Ion current to the screen grid [A]
I_{screen}	Screen grid current [A]
I_{sp}	Specific impulse [s]
I_{tot}	Total ion current collected in discharge-only mode [A]
I^+	Singly ionised particle production current [A]
I^{++}	Doubly ionised particle production current [A]

I^*	Excited neutral production current [A]
j_{avg}	Average current density [A/m^2]
j_i	Ion current density [A/m^2]
j_{max}	Peak current density [A/m^2]
Kn	Knudsen number
l_c	Primary electron containment length [m]
l_e	Corrected sheath thickness [m]
l_g	Grid gap length [m]
l_{Lp}	Langmuir probe length [m]
ℓ	Diffusion length [m]
m_d	Total delivered mass (dry mass plus payload mass)[kg]
m_p	Propellant mass [kg]
$\dot{m}_{dc}$	Reduced total mass flow rate without beam extraction [g/s]
$\dot{m}_i$	Ion mass flow rate [g/s]
$\dot{m}_{i,j}$	Ion mass flow rate of a given species j with ion mass M_j [g/s]
$\dot{m}_p$	Total propellant mass flow rate [g/s]
$\dot{m}_{p,j}$	Total propellant mass flow rate of the j-th species [g/s]
M	Ion mass [kg], mass of the vehicle [kg]
M_a	Ion mass [AMU]
$M_{a,j}$	Ion mass of the j-th species [AMU]
M_j	Ion mass of the j-th species [kg]
n_0	Neutral atom density [m^{-3}]
n_e	Plasma density [m^{-3}]
n_i	Ion density [m^{-3}]
$n_{i,j}$	Ion density of the j-th species [m^{-3}]
P	Perveance [A/V$^{3/2}$], Pressure [Pa]
P_b	Beam electrical power [W]
P_c	Critical pressure [Pa]
P_d	Discharge power [W]
P_{in}	Input electrical power [W]
P_{jet}	Kinetic thrust power of the beam [W]
P_{other}	Other electrical power input to the thruster required to create the thrust bean [W]
P_{tot}	Total electrical power into the thruster [W]
Q_{out}	Unused flow leaving the discharge chamber [A]
r, R	Radius [m]
r_e	Electron gyroradius [m]

r_{Lp}	Langmuir probe radius [m]
t_s	Screen grid thickness [m]
T	(Nominal) Thrust [N]
T_j	Thrust of the j-th species [N]
T_{beam}	Ion optics beam transparency with beam extraction
T_{corr}	Corrected thrust [N]
T_{dc}	Grid transparency in discharge-only mode
T_{ideal}	Ideal thrust [N]
T_e, T_{eV}	Plasma electron temperature [K] or [eV]
T_s	Effective grid transparency
T_{eff}	Effective electron temperature [eV]
T_g	Neutral temperature [K]
T_i	Ion temperature [K]
U^+	First ionisation potential [eV]
U^{++}	Second ionisation potential [eV]
U^*	Average excitation potential over the excited species [eV]
v	Velocity of the vehicle [m/s]
v_a	Ion acoustic velocity [m/s]
v_B	Bohm velocity [m/s]
v_e	Electron velocity [m/s]
v_{ex}	Propellant exhaust velocity [m/s]
v_i	Ion velocity [m/s], ion flow velocity [m/s]
$v_{i,j}$	Ion velocity of the j-th species [m/s]
v_0	Neutral atom velocity [m/s]
V	Potential drop through the sheath [V], Applied voltage [V]
V_{accel}	Accelerator grid voltage [V]
V_b	Net beam voltage [V]
V_C	Potential (relative to cathode) from which electrons are accelerated to become primaries [V]
V_d	Discharge voltage [V]
V_f	Floating potential [V]
V_k	Keeper potential [V]
V_{Lp}	Langmuir probe bias voltage [V]
V_{neutr}	Neutraliser floating potential relative to ground [V]
V_P	Plasma potential [V], Plasma volume [m^3]
V_{screen}	Screen grid voltage [V]

V_T	Total voltage across accelerator gap [V]
X_j	Mole fraction of the j-th species
$\langle \quad \rangle$	Average over the entire electron energy distribution function, reaction rate coefficient
$\widehat{\quad}$	Value in discharge-only mode (without beam extraction)

Greek symbols

γ	Thrust correction factor (TCF)
γ_{i-n}	Ratio of ions impacting the accel grid that successively leaves the grids as neutrals
Δv	Change in velocity [m/s]
ε	Electron kinetic energy [J]
ϵ_0^*	Average plasma ion energy cost for ionisation and excitation processes only [eV]
ϵ_M	Average energy of Maxwellian electrons leaving the plasma at the anode [eV]
ϵ_P^*	Baseline plasma ion energy cost [eV]
ϵ_r	Relative error
η_d	Ionisation efficiency or discharge loss (specific discharge power)[W/A] or [eV/ion]
η_e	Electrical efficiency of the thruster
η_m	Thruster mass utilisation efficiency
$\eta_{m,j}$	Thruster mass utilisation efficiency of the j-th species
η_T	Total thruster efficiency
λ_D	Electron Debye length [m]
λ_{MPF}	Ion or electron mean free path [m]
$\ln \Lambda$	Coulomb logarithm
μ_e	Electron mobility [$m^2\ V^{-1}\ s^{-1}$]
ν_e	Electron collision frequency [$m^3\ s^{-1}$]
ν_{en}	Electron-neutral collision frequency [$m^3\ s^{-1}$]
ν_{ei}	Electron-ion collision frequency [$m^3\ s^{-1}$]
σ_0	Total inelastic collision cross section for primary electron-neutral atom collisions [m^2]
σ_{en}	Electron-neutral scattering cross section [m^2]
σ_+, σ_i^+	First ionisation collision cross section [m^2]
σ_i^{++}	Second ionisation collision cross section [m^2]
σ^*	Excitation collision cross section [m^2]
ϕ	Potential of the plasma in the discharge chamber [eV]
ϕ_0	Grid transparency to neutral atoms
τ_l	“End effects” parameter

Constants

AMU	Atomic mass unit	$1.6602176487 \times 10^{-27}$ kg
e	Electron charge	$1.602176487 \times 10^{-19}$ C
e/k	Temperature associated with one electron volt	11604.5 K
eV	Energy associated with one electron volt	$1.602176487 \times 10^{-19}$ J
g_0	Gravitation acceleration	9.80665 m/s^2
k	Boltzmann's constant	1.3807×10^{-23} J/K
m, m_e	Electron mass	$9.1093822 \times 10^{-31}$ kg
P_0	Standard pressure (760 torr = 1 atm)	101325 Pa
T_0	Standard temperature (0 °C)	273.15 K
ϵ_0	Permittivity of free space	8.8542×10^{-12} F/m
μ_0	Permeability of free space	$4\pi \times 10^{-7}$ H/m

Acronyms

0-D	Zero-Dimensional
2-D	Two-Dimensional
3-D	Three-Dimensional
ABRC	Allen-Boyd-Reynolds-Chen theory
AC	Alternate Current
AP	Alternative Propellant
ASU	Air Separation Unit
BRL	Bernstein-Rabinowitz-Laframboise theory
CEX	Charge-Exchange collisions
DC	Direct Current
DMM	Digital Multi-Meter
ECR	Electron Cyclotron Resonance
EEDF	Electron Energy Distribution Function
EP	Electric Propulsion
EPPC	Electron Part of the Probe Characteristic
FCU	Flow Control Unit
FEEP	Field-Emission Electric Propulsion
FMF	Free Molecular Flow model
FP	Faraday Probe
GIE (GIT)	Gridded Ion Engine (Gridded Ion Thruster)
HC	Hollow Cathode
HET	Hall Effect Thruster
IPPC	Ion Part of the Probe Characteristic

LP	Langmuir Probe
MC	Monte Carlo
MFC	Mass Flow Controller
MPDT	Magnetoplasmadynamic Thruster
MSL	Mars Space Ltd
NIST	National Institute of Standards and Technology
OML	Orbital Motion Limited theory
PIC	Particle-in-Cell
ppm	Parts Per Million (by Mass)
ppmv	Parts Per Million by Volume
PPT	Pulsed Plasma Thruster
PPU	Power Processing Unit
RCDC	Ring-Cusp Discharge Chamber
RF	Radio Frequency
RFG	Radio Frequency Generator
RMT	Radial Motion Theory
RPA	Retarding Potential Analyser
RTG	Radioisotope Thermoelectric Generator
SMU	Source Measurement Unit or SourceMeter
STP	Standard Temperature and Pressure (273.15 K and 101325 Pa)
TCF	Thrust Correction Factor
VC	Vacuum Chamber

Units

This report uses MKS units of the International System of Units (SI); occasionally energies may be given in terms of electron volts (eV), but this will be stated.

Chapter 1 Introduction

Any space vehicle requires a propulsion system to perform any manoeuvre in outer space, such as orbit transfer, station keeping and attitude control. An essential element of any propulsion system is the rocket engine, which operates according to the basic principle of momentum exchange. Nowadays, there are two major rocket engine technologies based on the energy source utilised to accelerate the propellant: chemical and electric propulsion. Chemical propulsion uses the specific energy stored as chemical bonds in the propellant to heat, expand through a nozzle and accelerate it, while electric propulsion (EP) uses externally stored electric energy to energise and accelerate the propellant. In EP, this acceleration mode allows for achieving a much higher propellant exhaust speed that directly translates into a lower propellant consumption for a given manoeuvre, giving increased flexibility during the mission design phase compared to chemical propulsion systems. However, EP systems present some disadvantages, such as very low thrust levels achievable mainly due to power source limitations and power available in space.

The development of EP systems started at the beginning of the 1960s, and a wide range of mature and well-established technologies are available today with a long flight heritage of hundreds of such thrusters having been operated on a variety of space vehicles (e.g. satellites, exploration probes, etc.). Despite this background, the increasing availability of electrical power onboard of spacecrafts and the recent development of large constellations of EP-powered satellites forecast an even brighter future for this sector.

Among the other EP technologies, gridded ion engines (GIEs) are considered to be one of the most developed, and there is a long list of missions where they have been employed from north-south station keeping of big telecommunication satellites, primary propulsion on interplanetary missions, to atmospheric drag compensation, etc. In a typical GIE, an inert gas, commonly xenon, is ionised in a discharge chamber and the resulting ions are extracted and accelerated using biased multi-aperture grids via electrostatic forces. In Figure 1, a schematic of a DC gridded ion thruster is shown. Applying potentials of several kV, the ions are accelerated to velocities of the order of 40000 m/s [1]. At the exit of the grids, a neutraliser cathode is present to neutralise the positive ion beam by providing an electron current. Any remaining negative charge would have unfavourable effects on the spacecraft and the grids (e.g. damage through arcing or sputtering due to the backstream of ions) and compromise the functionality of the thruster itself.

An important factor that influences the performance of a GIE and, more in general, the complexity and cost of the entire system is the choice of the propellant. Any available propellant presents advantages and drawbacks, and this selection is a result of a trade-off between different criteria, such as the mission objectives and spacecraft configuration.

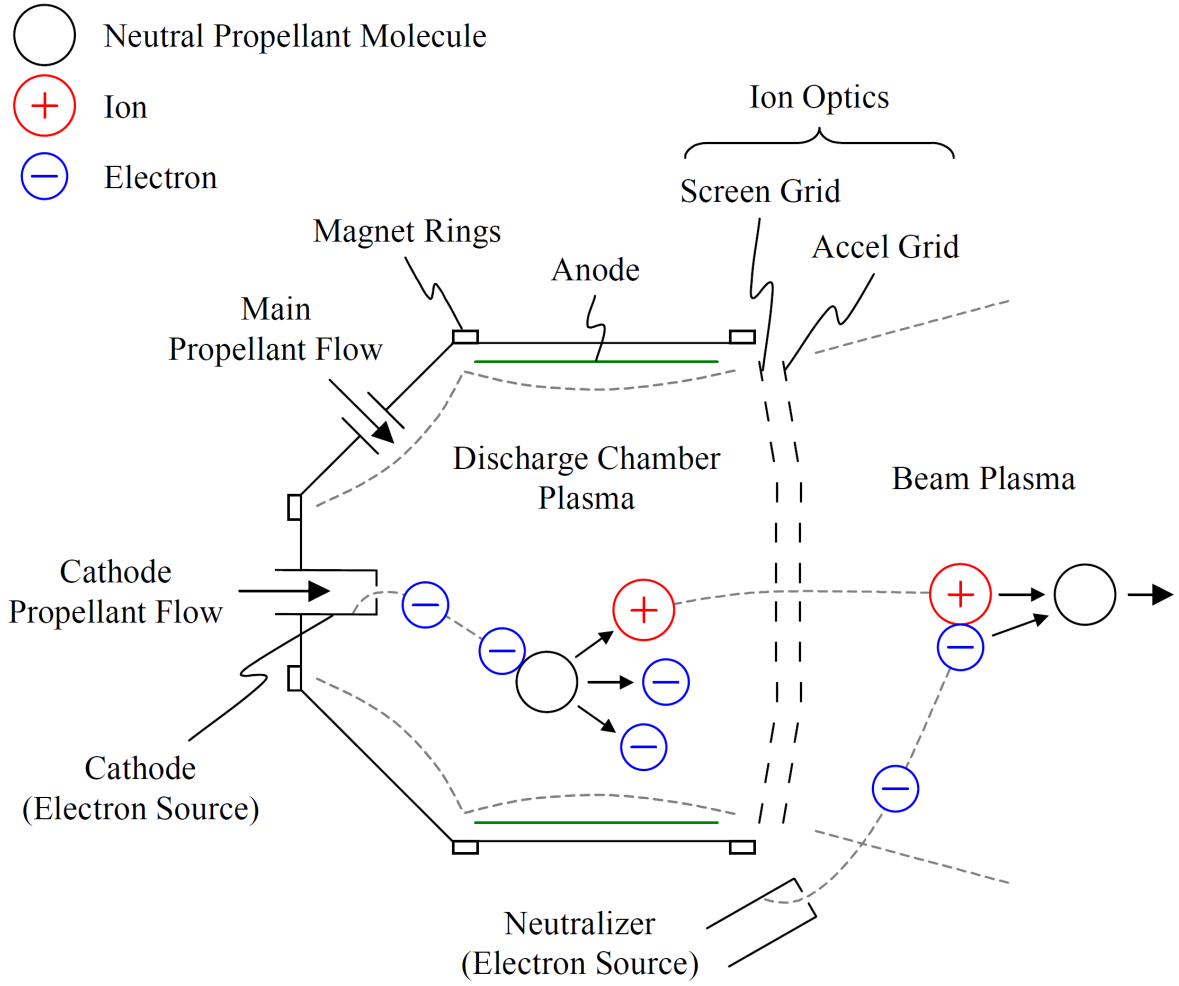

Figure 1 – Schematic of an ion thruster [1]

1.1 Research Motivation

Xenon is the most common propellant used for space applications, particularly in GIEs and HETs, thanks to its distinctive physical and chemical properties, such as low first ionisation energy, high atomic mass, and chemical inertness. Nonetheless, this gas is found naturally in the atmosphere at a concentration of 0.087 ppmv (parts per million by volume) or 0.39 ppm (parts per million by mass), which makes it the rarest of the stable elements on Earth. It is not manufactured but collected as a by-product of cryogenic air separation. As a reference, an extraction plant with the capacity to process 1000 tonne/day of liquified air would extract only 280 g/day of xenon at a typical 70% production efficiency, and an estimated worldwide annual production of around 70 tons in 2017 [2]. Consequently, its limited availability and highly complicated production process lead to it being extraordinarily expensive. These aspects can

become a severe constriction when planning space missions, such as cargo missions and orbital transfer missions, or simply for extended ground testing campaigns.

In searching for solutions to this problem, a variety of alternative propellants (APs) have been proposed and tested in the past, ranging from other noble gases (i.e. krypton, argon, etc. [3]), through liquid and solid elements (e.g. mercury, caesium, iodine, etc. [4], [5]), to heavy molecules (e.g. Buckminsterfullerene, Adamantane, etc. [6], [7]).In the last decade, a renewed effort has been made by the space community towards the search for a readily available, efficient, and cost-effective alternative to xenon as the propellant for space vehicles to meet the need of a growing diversification of satellites, missions and manoeuvres [8].

A further boost has been provided by the so-called “New Space” revolution [9]: this term encompasses a new approach to space activities, and it can be defined using three key characteristics, such as a new business model (private investors instead of institutional), new product development attitude, and customer focus. One of the main consequences of this innovation is the change of requirements that need to be addressed by the industry, like the need for simpler, smaller, cheaper propulsion devices, and the acceptance of a performance trade-off for lower cost. Hence, this new business model clashes with the high cost and the price fluctuations of xenon. In fact, it is worth highlighting that krypton has been recently used by SpaceX for their Starlink constellation coupled with Hall Effect Thrusters (HETs)[10].

In light of this, the search for alternative propellants has become of fundamental research interest in the EP area. The actual focus is on heavy molecules and solid propellants (iodine, in particular), and on other noble gases (i.e. krypton) that would have the lowest impact on the propulsion system, allowing an almost direct replacement (no propellant reactivity or phase change problems) if a small performance penalty can be tolerated [11]. Krypton, in particular, offers several desirable benefits for space missions: it is more abundant (1.14 ppmv or 3.3 ppm) than xenon and, since it is produced in the same process, its cost is typically less than 10% of the cost of xenon by volume (15% by mass) resulting in reduced mission and development costs (see Appendix A). Krypton is also lighter than xenon (83.8 AMU for Kr compared to 131.3 AMU for Xe) allowing to achieve higher specific impulse, which can be advantageous in specific missions (e.g. planetary missions). However, lower performance due to lower atomic mass and higher ionisation potential, the requirement of a larger/heavier propellant tank and a higher storage pressure due to its lower density are among the disadvantages of using krypton. Additionally, only limited data exist in the literature for gridded ion engines running with krypton, and the existing publications date a few decades back (between the early 1970s and early 1990s [3], [11]–[15]) and mainly with larger size discharge chambers.

Therefore, the motivation for this research comes from the need to investigate the performance of a small ring-cusp gridded ion engine that uses krypton as propellant with a particular focus on the performance gap between xenon and krypton. Furthermore, another option that is worth investigating and that has never been explored in conjunction with GIE's systems is the use of xenon/krypton mixtures, although few papers on the use of mixtures with HETs [16], [17] and hollow cathodes [18] have been published.

1.2 Research Objectives

Following the motivations listed in the previous section, this work aims to investigate the behaviour of gridded ion engines with two alternative propellants: krypton and the mixture of Xe/Kr in the production ratio of 1:4.

Consequently, the key objectives of the research programme are as follows:

- The characterisation of the performance gap between xenon and krypton in a small ring-cusp GIE, which was designed and developed for xenon, to establish a baseline for possible modifications that could reduce this gap.
- No previous experimental results are available in the literature on the use of a mixture of xenon/krypton with a GIE, and the performance characterisation allows for the evaluation of the feasibility of operating a thruster using this alternative propellant, and if any performance penalty compared to those of the pure gases could be mitigated by its economic advantage (e.g. could offer a 15-fold cost saving when compared to pure xenon, and 2-3 times cheaper when compared to pure krypton [19]).
- The identification of possible areas for improvement (e.g. via the optimisation of the ion optics or operational points) by performing an internal (i.e. close to the screen grid) characterisation of the discharge chamber's phenomena and plasma properties (i.e. electron temperature, and plasma potential and density) via internal diagnostic tools (e.g. single Langmuir probes) and measurement techniques.
- The determination of the nominal operation performance with alternative propellants (i.e. krypton and the 1:4 Xe/Kr mixture) compared to xenon in a hollow cathode in diode configuration to identify the operating conditions that cause the loss of discharge stability (i.e. spot-to-plume transition) and to assess any performance penalties of operating with alternative propellants.

1.3 Thesis Organisation

A summary of the work undertaken in this dissertation is provided here:

- Chapter 1 deals with the overview, the research motivation, the research aims, and the dissertation organisation.
- Chapter 2 offers an overview of electric propulsion systems and their classification, a short background on the characteristics and working principles of GIEs, and the literature review about the propellants used with GIEs with a particular focus on the propellants of interest for this work (i.e. krypton and mixtures of xenon and krypton).
- Chapter 3 describes the calculations of the main parameters used to evaluate the performance of a GIE outlining the impact of the propellant atomic mass on these parameters at a first-order approximation, the performance models (for discharge chamber, discharge-only operations, and ion optics) and the plasma diagnostics tools used for the analysis of the experimental data.
- Chapter 4 provides an overview of the two experimental configurations, including the description of the vacuum facilities, experimental arrangement, and diagnostic setups utilised for the operational characterisation of a ring-cusp discharge chamber and a hollow cathode with different propellants. Finally, the testing procedures followed during the testing phase are also outlined.
- Chapter 5 presents the results of the experimental campaign and the discussion of the measured data for the small ring-cusp ion engine and for the hollow cathode running with xenon, krypton and the 1:4 Xe/Kr mixture.
- Chapter 6 outlines the conclusions and recommendations for future research.

Chapter 2 Background and Literature Review

This chapter presents an overview of electric propulsion systems and their classification, outlines the characteristics and working principles of GIEs, and reviews previous publications on the different propellants used with GIEs with a particular focus on the propellants of interest for this work (i.e. krypton and mixtures of xenon and krypton).

2.1 Overview of Electric Propulsion Systems and their Classification

The motion of a space vehicle is based on Newton's law of action-reaction or momentum conservation principle: the expulsion of propellant mass generates acceleration. Both the two current propulsion systems (chemical and electric) work based on this same principle; however, they present important differences in the operating mode. The force acting on a spacecraft or thrust on the vehicle of mass M moving at velocity v can be expressed as [20]:

$$\text{Force} = T = M\frac{\mathrm{d}v}{\mathrm{d}t} \tag{2-1}$$

According to the law of conservation of momentum, the thrust is also equal to the time rate of change of momentum of the propellant being ejected:

$$T = -\frac{\mathrm{d}}{\mathrm{d}t}\left(m_p v_{ex}\right) = -v_{ex}\frac{\mathrm{d}m_p}{\mathrm{d}t} \tag{2-2}$$

where v_{ex} is the propellant exhaust velocity and m_p is the propellant mass.

The ideal rocket equation, or the Tsiolkovsky rocket equation, can be obtained by combining Eq. (2-1) and Eq. (2-2), integrating them over the thruster firing period and neglecting external forces such as drag and gravity:

$$\Delta v = v_{ex}\ln\frac{m_d+m_p}{m_d} = I_{sp}g_0\ln\frac{m_d+m_p}{m_d} \tag{2-3}$$

where Δv is the change in velocity, m_d is the total delivered mass (dry mass plus payload mass), I_{sp} is the specific impulse, and g_0 is the Earth's gravitational acceleration (9.80665 m/s^2).

Equation (2-3) relates the velocity increment of a spacecraft to the propellant exhaust speed, the propellant mass, and the final mass, and it shows that to achieve a large Δv is necessary either to burn a considerable mass of propellant or to generate a high v_{ex}. The second option allows for bigger and heavier delivered mass and, hence, it is preferable.

Since the necessary Δv to perform a manoeuvre or to complete a mission is a known parameter, Equation (2-3) can be expressed in terms of propellant mass:

$$m_p = m_d \left[\exp\left\{\frac{\Delta v}{v_{ex}}\right\} - 1\right] = m_d \left[\exp\left\{\frac{\Delta v}{I_{sp} g_0}\right\} - 1\right] \quad (2\text{-}4)$$

To reduce the propellant requirements, the propellant exhaust velocity v_{ex} must be comparable to or, better, larger than the required Δv.

The equation above shows the benefits of electric thrusters over chemical ones. Chemical thrusters burn propellant and eject the hot gas through a nozzle; therefore, the exhaust velocity is limited by the specific energy stored in the propellant (i.e. in the chemical bonds) and v_{ex} cannot exceed 4 km/s. However, chemical thrusters can achieve high levels of thrust even for low exhaust velocity with high mass flow rates, as shown in Eq. (2-2). In an electric thruster, the energy source (e.g. from solar panels) is separated from the propellant and these limitations can be circumvented. The propulsion system uses electrical energy converted into kinetic energy to accelerate particles and achieve higher exhaust velocities (usually one order of magnitude higher). However, the typical mass flow rate and thrust for electric thrusters are much lower than those of chemical engines. Therefore, chemical thrusters are ideal for high-thrust missions (i.e. Earth's orbit escape), while electric propulsion is the only viable option for missions with large Δv.

Several technologies and accelerating mechanisms can be used in electric propulsion to achieve the high exhaust velocities that are typical of these systems. One of the first attempts to categorise the different technologies used in electric propulsion was made by R.G. Jahn [21] in the 1960s defining EP as '*the acceleration of gases for propulsion by electrical heating and/or by electric and magnetic body forces*'. According to this definition, the EP field can be divided into three main categories:

- Electrothermal propulsion (arcjets and resistojets): the electric energy is used to heat the propellant in a chamber. This thermal energy is converted into kinetic energy by expanding the hot gas through a nozzle.
- Electrostatic propulsion (gridded ion engines, FEEPs): the electric energy is used to ionise the propellant and then, to accelerate the propellant ions through the direct application of an electric field between two electrodes.
- Electromagnetic propulsion (HETs, MPDTs, and PPTs): the combined action of electric and magnetic forces accelerates the ionised propellant.

From now on, the focus of this work will be exclusively on gridded ion engines.

2.2 Gridded Ion Engines: Background

Gridded ion engines (GIEs), or ion thrusters, are included in the electrostatic propulsion category since the thrust is generated by electrostatic forces between the ions and the grids: essentially, a beam of positive ions is accelerated by a suitable electrostatic field.

The development of this technology started in the 1960s [20]–[22], and the working principles and the science supporting them are well-known and understood, allowing reliable predictions of performance and lifetime via numerical simulation. Furthermore, their extensive flight heritage puts them at the forefront as leading EP technology on par with HETs.

In the following subsections, some of the technical details will be described, such as GIE architecture and working principles, and the thrust generation process.

2.2.1 GIE Architecture: Geometry and Working Principles

A typical electric thruster can be divided into three regions based on the involved process (Figure 2):

- The plasma source region, where the propellant is ionised to obtain plasma
- The ion extraction/acceleration region, where the ionised propellant is accelerated to produce thrust
- The ion beam neutralisation region, where the electrically charged plasma plume is neutralised to avoid charge imbalance with the spacecraft.

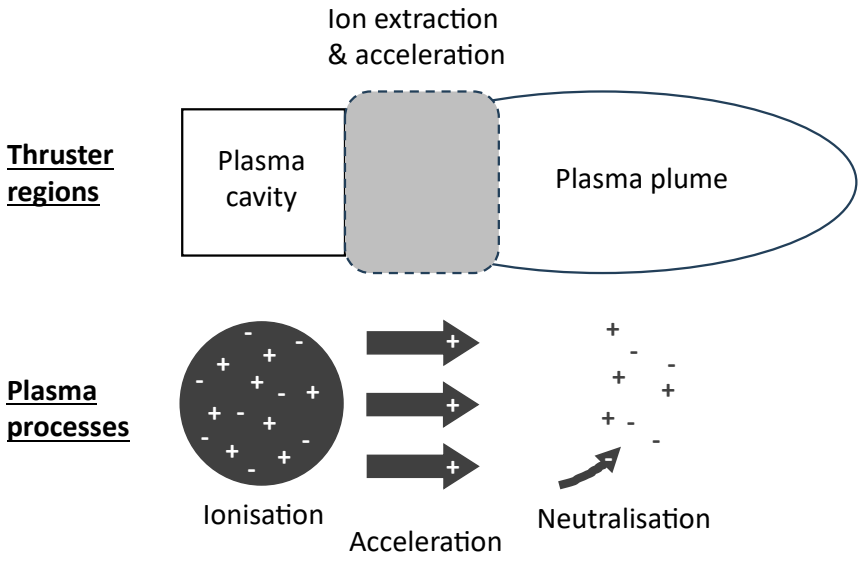

Figure 2 – Schematic of the three regions and relative processes

In an ion thruster, these three basic processes are almost physically distinct with a strong coupling at the boundaries and interfaces. This is the main feature that distinguishes this type of

thruster from other electric thrusters, and it allows greater control over thrust and exhaust velocity.

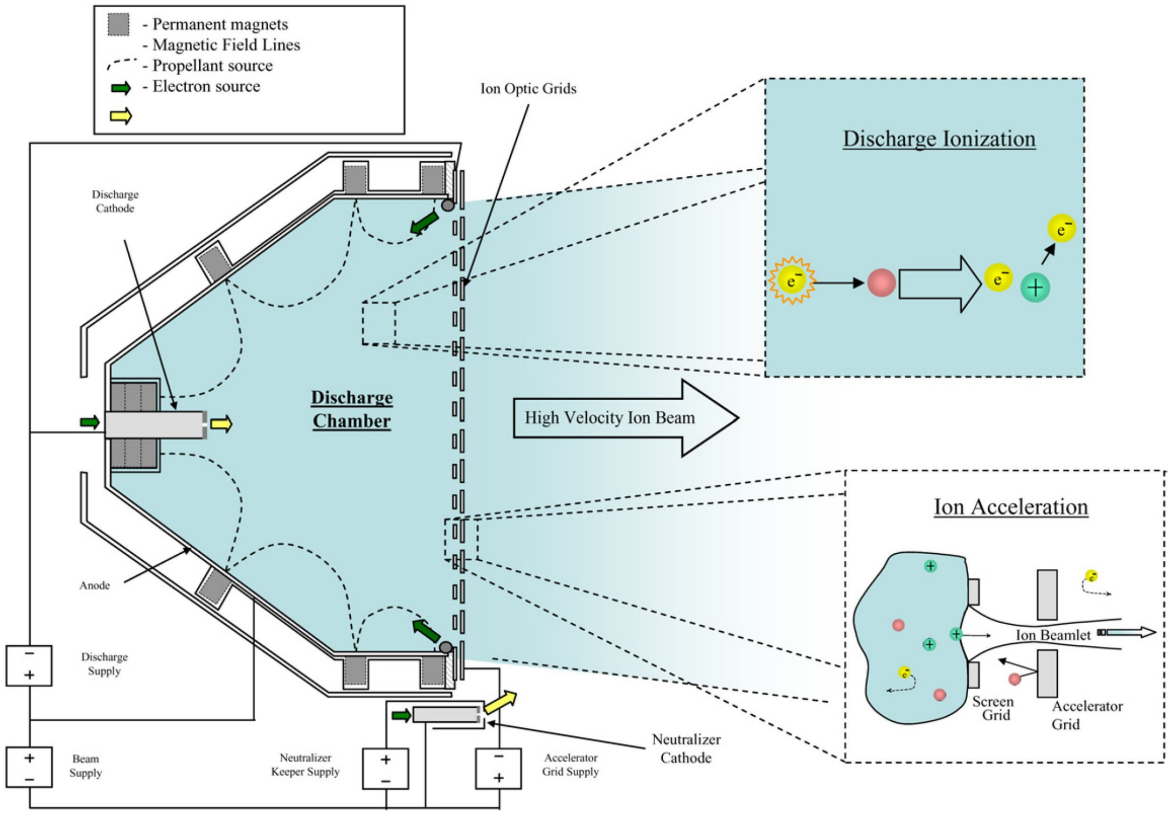

Figure 3 – Schematic diagram of a DC ring-cusp GIE and fundamental processes [23]

Figure 3 shows a schematic cross-section of an ion thruster and its three main elements: the ion source, the accelerating grids, and the neutraliser. The chamber where the propellant is ionised can be of different geometries: cylindrical, rectangular, and conical. From here, ions flow to the grids where they are accelerated to form the beam and, then, neutralised with a flow of electrons provided by the neutraliser cathode. In the following subsections, these three processes will be described in more detail.

2.2.2 Plasma Generation

In a GIE, the propellant injected in the discharge chamber (plasma generator) must be ionised transferring electrical energy to it. As seen in the previous paragraph, the plasma generation and the ion acceleration stages are distinct. As a consequence, different types of plasma production mechanisms have been tested and used but only three have survived to the application [24]:

- DC coupled discharge (electron bombardment)
- RF inductive discharge
- Microwave discharge (electron cyclotron resonance, ECR).

In an ion thruster working in DC mode, a discharge of energetic primary electrons (10-50 eV) between a cathode and an anode impacts the propellant to create ions and generate the plasma. To improve the discharge efficiency, the electrons are confined using magnetic confinement to increase the time they reside in the chamber, hence increasing the ionisation degree. Two main variants of this configuration are still used (Figure 4):

- Kaufman configuration (mostly in the UK [25] and Russia): the cylindrical anode is isolated from the thruster body and the electrons, generated by the hollow cathode, reach this anode by cross-field diffusion. A strongly divergent magnetic field is present, and it is generated by solenoids, which require a power supply and allows for very fine control of the plasma density (and thrust) and a large throttleability. Furthermore, a baffle is present at the cathode exit to flatten the plasma density profile.
- Ring cusp configuration (mostly in the USA [26]): the discharge chamber becomes the anode, and it is the cathode body that is isolated from the chamber. The magnetic field is generated by permanent magnets which give less flexibility than the Kaufman variant, but it gives a more efficient discharge (higher thrust-to-power ratio, less thermal dissipation), and a flatter plasma profile without the need for an extra power supply for the solenoids.

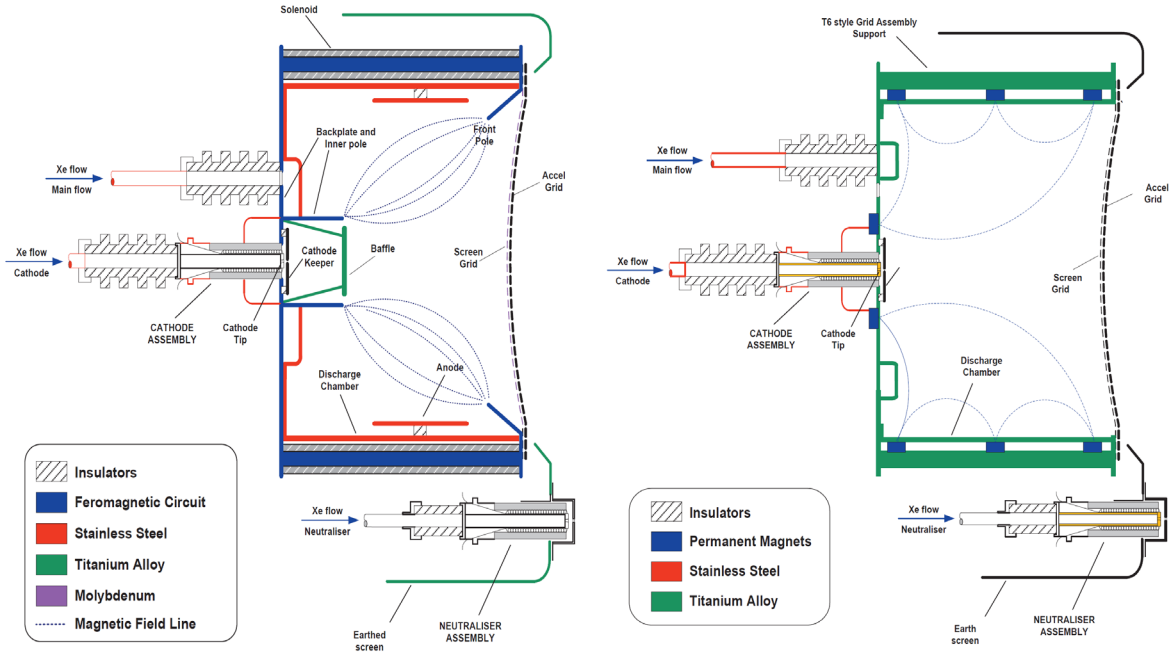

Figure 4 – Kaufman configuration (on the left) vs. ring cusp configuration (on the right)[27]

Figure 4 shows an attempt at conversion of a thruster from a Kaufman-type (i.e. QinetiQ T6) to a ring-cusp-type (i.e. QinetiQ T6RC breadboard) carried out by removing the baffle, inner pole, solenoids and discharge chamber anode, and by adding four magnetic rings, an insulator ring between the discharge hollow cathode and the discharge chamber, and insulators between the discharge chamber and the screen grid. Initial tests showed an improvement in terms of

discharge cost of up to 30% and a reduction in discharge voltage of about 5 V for the T6RC with respect to a Kaufman T6. A further advantage of the ring-cusp-type is the weight reduction compared to the Kaufman-type due to the significant thruster design simplification (e.g. the NSTAR ring-cusp thruster with a 30 cm-ion optics weights only 8.2 kg compared to the IT-200 Kaufman-type with a 20 cm-ion optics that weights 10.5 kg [28]).

An alternative plasma generator design utilises electromagnetic fields to heat the plasma electrons and ionise the injected propellant. This heating process is achieved using an inductive plasma generator, hence the name radiofrequency (RF) ion thruster (Figure 5). In this configuration, an RF current (a few MHz) is generated in a coiled antenna structure wrapped around the thruster body, and the RF energy is coupled to the electrons. This RF current induces an axial magnetic field which heats the plasma electrons and maintains the ionisation process. The RF coil needs to be insulated to avoid erosion due to electron collection from the space plasma. Since few electrons are available to start the ionisation process, a pulse start is used to increase the pressure within the chamber and ignite the discharge, or electrons are injected into the chamber from a spark generator, a small cathode, or the neutraliser cathode (with the acceleration grid voltage turned off temporarily). RF ion thrusters have a slightly lower thrust efficiency compared to DC thrusters (~5% lower) due to higher discharge loss (mainly caused by higher ion losses to walls) and to the necessity of a DC-to-RF conversion (Radio Frequency Generator, RFG)[20]. However, they offer several advantages, such as reduction of any potential life (lower erosion of the chamber and absence of the internal cathode) or power supply (DC-electron discharge) issues, removal of the requirement for an external magnetic confinement, lower sensitivity to impurities in the propellant (i.e. the possibility to use xenon of lower purity), and higher compatibility with APs (due to the absence of the internal cathode)[29]. This kind of thruster originated and is mainly developed in Germany (Airbus' RIT-series [30]), and, recently, also in the USA [31] and in the UK [32]–[34].

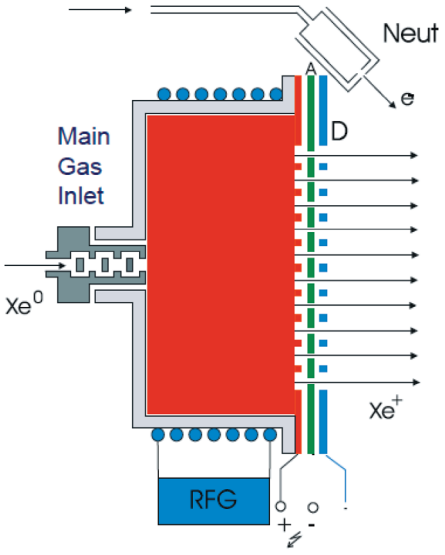

Figure 5 – Schematic of a RF ion thruster [35]

The third variant of plasma generator design, microwave ion thruster, adopts an approach similar to RF thrusters, but the frequencies are in the GHz range and the ionisation is based on the Electron Cyclotron Resonance (ECR) (Figure 6). A microwave is transferred via a waveguide to the discharge chamber, where a strong magnetic field is generated to magnetise the electrons and achieve electron resonance. Once the electrons start to resonate at the microwave frequency, they absorb enough energy to ionise the propellant. A critical aspect of microwave GIE is the design of the chamber to limit the reflection of the waveguide, which can reduce the thrust level and the requirement of fine-tuning the injected power to make sure the microwave energy is efficiently transmitted to the plasma. In addition, these thrusters present similar problems to RF thrusters during the ignition process and possible interferences with the spacecraft communication systems must also be taken into account. Microwave ion thrusters are mainly and almost exclusively developed in Japan (ECR at 2.4 GHz [36]).

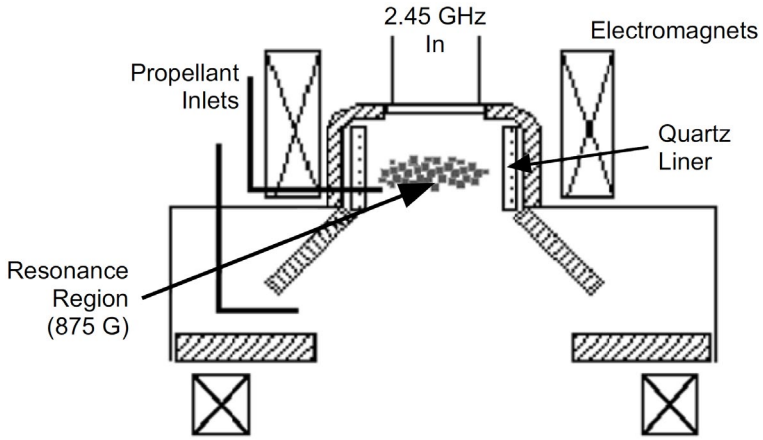

Figure 6 – Schematic of a microwave ion thruster [20]

2.2.3 Beam Extraction and Neutralisation

Once the propellant is ionised to create plasma, an ion beam can be extracted to high velocity by using an electrically-biased multi-aperture grid assembly, which is often called ion optics. Different configurations have been tested from two to four grids [20], [37], but the three-grid variant is the most commonly used and the grids are labelled screen grid, accelerator (accel) grid and decelerator (decel) grid (Figure 7). This extraction stage is a common aspect of all GIEs regardless of the plasma production mechanism.

The design of the ion optics is critical to the thruster's performance, life, and size. The ion beam extracted from the discharge chamber must be collimated through the downstream (accel and decel) grids over the entire range of ion densities provided by the plasma profile in the chamber and over different power levels. Furthermore, the grid system must minimise the ions' impact on the screen grid and neutral atom loss out of the chamber to increase the mass utilisation efficiency of the engine, and maximise the number of ions that reach the screen grid surface.

The design of the grids' holes has an impact on the beam divergence, which should be limited to reduce thrust loss and plume interaction with the space vehicle. Finally, the driving factor in the design of the ion optics is their lifetime, since, as described previously, these kinds of thrusters need to work for longer periods to compensate for the low levels of thrust available. In fact, the lifetime of a GIE is heavily related to that of the ion optics, even if an operational life in excess of 30,000 hours has been demonstrated [39]. This critical factor often imposes compromises over the other aspects (i.e. performance, size, and materials).

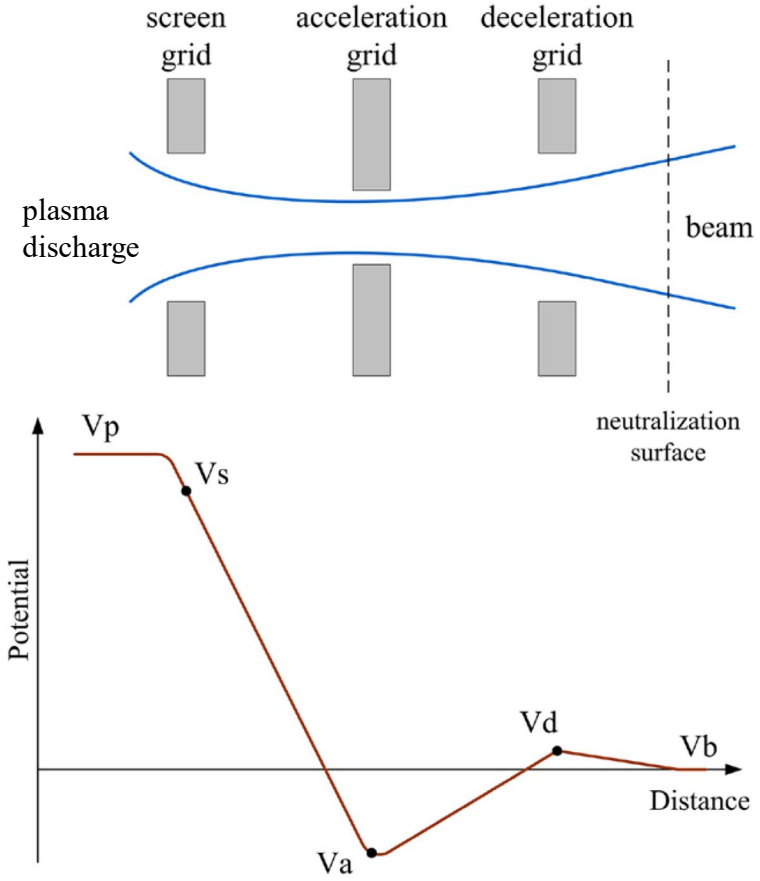

Figure 7 – Schematic of a three-grid ion optics with the corresponding potential profile [38]

The first grid, or screen grid, is in contact with the plasma and it works at high electric potential. It is mainly used to screen the electrons and to protect the accel grid from erosion by focusing the ion beam through the apertures. The second grid, or accel grid, works at low potential in order to accelerate the ion beam since the exhaust velocity of the beam is directly related to the potential difference between these two grids. This difference also characterises the shape of the sheath near each extraction hole in the screen grid, and the current density that can be extracted. When present, the third grid, or decel grid, is located downstream of the accel grid at a higher potential than the accel grid (i.e. near ground potential) and it allows a decoupling between ion extraction and acceleration with an increment of the ion beam density (bigger potential difference between screen and accel grids) while maintaining the same exhaust velocity. The added complexity and mass increment in the ion optics due to this third grid are

justified by the improved beamlet focusing (only over limited ranges of geometric and operating conditions) by the reduction of the erosion of the accel grid caused by cold charge-exchange ions (CEX) returning towards the discharge chamber [15].

Finally, the ion beam downstream of the ion optics needs to be neutralised to avoid space-charge unbalance that could affect the entire spacecraft. This neutralisation is realised using electrons (supplied by an external cathode called neutraliser) that mix with the extracted ions to produce a neutral beam. The reliability of the neutraliser is of fundamental importance for the functionality of a GIE since its misbehaviour can lead to partial neutralisation and a resulting residue space charge that can severely affect the performance of the thruster.

2.2.4 The Hollow Cathode

Hollow cathodes (or electron sources) are one of the most important components in electric propulsion systems, such as GIEs and HETs, and they serve the main purpose of providing electrons for the neutralisation of the ion beam space charge as an external neutraliser, and as a source of primary electrons in the case of electron bombardment thrusters. Furthermore, they affect the stability of the plasma discharge produced and, hence, the overall thruster performance. Their lifetime is critical (as in the case of the ion optics) having an impact on the lifetime of the whole system, even if operational lifetime in excess of 20,000 hours have been obtained [40].

Hollow cathodes for electric thrusters have two distinct modes of operation: spot mode and plume mode. The observation of these two modes is more evident when the hollow cathode is tested in diode configuration, and they are defined as follows:

- Spot mode is characterised by a small and convergent plume, and it is desirable due to more stable plasma, low amplitude oscillations, low voltage discharge characteristics, and reduced erosion of the orifice. It occurs at high mass flow rates and discharge currents and, visually, it is associated with the observation of an intense luminous spot at the cathode orifice.
- Plume mode is associated with a bright divergent plume downstream of the cathode tip, and it is characterised by relatively large oscillations of high discharge voltages. It occurs at low discharge currents and low mass flow rates.
- The transition between spot and plume mode can usually be triggered by lowering the flow rate at a given current but also by changing the discharge current, and it can be visually detected and associated with ample oscillations of the cathode potential. The transition can also exhibit a hysteresis effect dependent on whether the discharge current or flow rate is being increased or decreased (Figure 8). In the literature [42], there

is extensive documentation that the cathode tends to operate in spot mode at less favourable operating conditions in full thruster geometry compared to the diode mode case with the almost complete suppression of the dual mode (i.e. spot/plume) behaviour. This is probably due to the higher pressure within the discharge chamber and to the presence of the magnetic field [41], [43], [44].

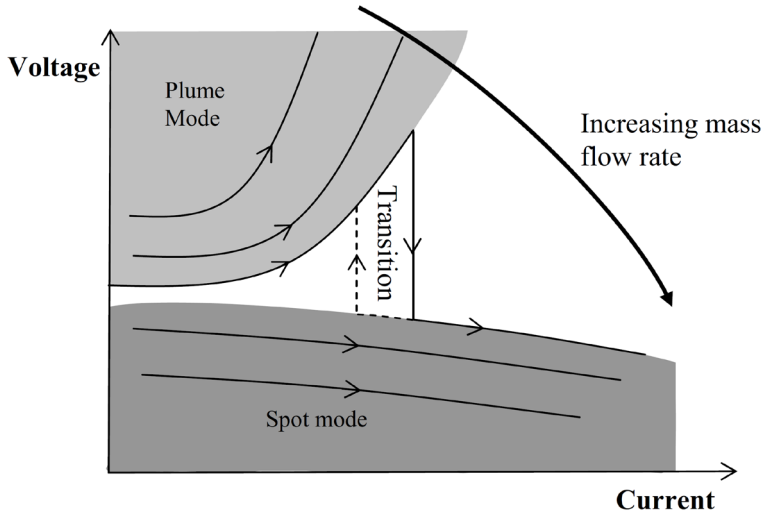

Figure 8 – Voltage-current characteristics of a hollow cathode discharge showing plume-to-spot transitions at different values of current and flow rate [41]

2.3 Propellants in Electric Propulsion (EP) Systems

In an electric propulsion (EP) system, the selection of the propellant is of fundamental importance. In fact, its choice influences the performance of the thruster (e.g. specific impulse, thrust efficiency, power-to-thrust ratio) and, more in general, the complexity and cost of the entire system. Ideally, a propellant for ion engines should combine [7]:

- *Low ionisation threshold* with a *high ionisation cross-section* to minimise the energy required to create a high-density plasma.
- *High molecular weight* to reduce the required power-to-thrust ratio.
- *Good handling* and *storage qualities*: liquid or solid propellants offer higher density and, consequently, lower storage volume.
- *High system* and *material compatibility*.
- *Low spacecraft contamination potential* to limit the damage caused to sensitive spacecraft surfaces (e.g. solar arrays).

Keeping in mind that any propellant presents some drawbacks, the final choice is a trade-off between different criteria, and it also depends on the mission objectives and spacecraft configuration. The typical criteria that influence the propellant choice are listed in Table 1 together with the dependent propellant properties.

Table 1 – Criteria driving propellant choice and dependent propellant properties

Criterion	*Propellant properties*
Total thrust efficiency	Atomic/molecular mass Ionisation potential Gas temperature Ionisation cross-section
Specific impulse	Atomic/molecular mass
Storage	Phase (solid, liquid or gas) Density
Complexity of feed system	Phase (solid, liquid or gas) Vapour pressure
Ground test conditions	Toxicity Vapour pressure Chemical reactivity
Compatibility with spacecraft materials	Vapour pressure Chemical reactivity
Availability	–

Xenon is traditionally selected as the preferred choice since it offers the best combinations of the above-mentioned properties, and it has been the favoured propellant for EP (in particular for GIEs, HETs, and MPDTs) since the 1980s. However, several propellants have been used in the past before settling on xenon: in the 1960s, mercury and caesium were used in early tests, but they were abandoned in the 1980s in favour of inert gases. Moreover, since the 1990s, several other options have been evaluated spanning from atomic to molecular propellants and the following subsections provide a historical review of the propellants used with GIEs with a particular focus on those that are relevant to this work. The physical properties of those alternative propellants are compared to xenon's properties in Appendix A.

2.3.1 Overview on Alternative Propellants in GIEs

In the early 1960s, at the beginning of the development of GIEs for space applications, liquid metals (i.e. mercury and caesium) were selected [4] because of their attractive properties, such as large atomic mass, high density, ease of flow control by vaporisation, and low ionisation energy (i.e. high power efficiency). In fact, it is plausible that this choice was based mainly on thruster subsystem considerations rather than spacecraft integration problems, such as contamination and coating of the spacecraft surfaces due to backflow caused by charge exchange ions. These issues led the researchers to consider the use of noble gases (argon, krypton, and xenon) as possible alternatives to liquid metals. In the 1970s, different experiments [12], [13] were conducted to verify the functionality of GIEs (10-cm and 15-cm Kaufman-type SERT II, in particular) with these gases, given their many advantages over mercury and caesium at system level: inertness, lack of spacecraft and environmental contamination,

no thermal conditioning required, fewer components in the propellant storage system, faster thrust response, and non-toxicity. The main disadvantages linked with the use of noble gases were the lack of development background and the need to modify existing systems in order to work with the gaseous propellants. Also, from a performance point of view, the discharge performance with inert gases was similar to that obtained with mercury [12], establishing their suitability for future uses with ion bombardment sources. In the following years and up to the mid-1980s, parallel works on mercury and noble gases were carried out [3], [14] allowing a comparison of the same thrusters with different propellants and identifying the modifications required to provide operability at high power with inert gases. The details and the outcomes of these experiments involving noble gases and krypton, which are of particular interest to this work, are comprehensively discussed in the following subsection.

Concurrently, the introduction of a new type of plasma containment (i.e. ring-cusp) GIEs [14] specifically developed and operated with inert gases demonstrated significant improvements in the discharge chamber performance (e.g. lower ion beam production cost, higher propellant efficiency, and more collimated ion beam) over the previous Kaufman-type (i.e. SERT II and J-series) thrusters. From there on, xenon was almost the exclusive choice as the propellant for EP because of its superiority over the other noble gases even if availability problems started to be considered [45], [46].

Since the 1990s, the search for a viable alternative to xenon focused on molecular propellants, since their masses easily exceed those of atomic propellants. However, their molecular nature introduces a major problem that worsens with the size of the molecule: part of the available input power is lost into dissociation in smaller fragments and into excitation of internal vibration and rotation modes. The first attempt in using molecular propellants was made with Buckminsterfullerene (C_{60}) both theoretically [6] and experimentally [47], [48]. This heavy molecule is the most stable of all fullerenes (a carbon-based nanomaterial in the form of hollow spheres, tubes, etc.) and it has a molecular weight of 720.11 AMU. At room temperature, it is solid and decomposes above 800 °C, but re-sublimates at around 400 °C. After a decade of research, this propellant was abandoned because of insurmountable problems related to its use [7] such as severe fragmentation during plasma processes (e.g. after excitation via electron-impact ionisation), the large cross-section for negative ion formation, a plasma can only be sustained with another support gas, and formation of a residual coating inside the plasma chamber which has negative effects on the thruster lifetime.

In the 2000s, a second attempt with molecules was made with iodine (I_2)[5], [49], which is a fairly simple molecule and, therefore, it should show just partially the above-described problems related to molecules. The main advantages of this propellant are: lower ionisation

potential and larger cross-section compared to xenon, high abundance in the Earth's crust (25000 times higher than that of xenon) which makes it relatively inexpensive even at high purity grade, and, finally, its high density (roughly three times higher than xenon) due to its natural appearance as solid. However, iodine presents some noteworthy drawbacks: it is chemically reactive with many materials (i.e. strongly corrosive for the majority of metals and alloys used in space propulsion), it can introduce contamination problems for thruster and spacecraft elements due to its condensability (similar to the problems experienced in the past with liquid metals, as described above), its high electron affinity can lead to the formation of negatively charged species in the plasma, and lost energy into dissociation and excitation results in an average mass that is close to the I atom mass. Nevertheless, iodine is one of the main candidates as alternative to xenon and its use is actively investigated, mainly combined with RITs and HETs [29], [50]–[52] including a recent in-orbit demonstration [53].

Recently [7], preliminary theoretical and experimental studies have been carried out on a molecule called Adamantane ($C_{10}H_{16}$). It is part of the diamondoids, a group of materials with a carbon cluster in a cubic diamond lattice saturated with hydrogens. Amongst the positive aspects introduced by this molecule are: slightly higher atomic mass (136 AMU) and lower ionisation potential than xenon (9.23 eV vs 12.13 eV), easily brought to the gas phase with low heating power due to low sublimation temperature, possibility to modify the molecular structure to optimise certain desired properties (e.g. the electronic structure to reduce ionisation threshold or increase stability by decreasing fragmentation), and high abundance as a by-product of the petroleum industry that makes it relatively cheap. On the other hand, the negative points of using this propellant are fragmentation in plasma environments caused by the interaction with electrons, negative electron affinity that can reduce propellant efficiency, and possible condensation problems. Nonetheless, further experiments [54] have been performed with RITs to investigate the possibility of using this molecule as an alternative propellant.

2.3.2 Krypton and Gridded Ion Engines

As mentioned in the previous subsection, in the 1970s, inert gases started to be of increasing interest for space propulsion systems: xenon was the main alternative because its physical characteristics are well suited to thruster operations, and krypton and argon were considered as possible, more economical options if a large amount of propellant was required.

Following an initial effort to assess the feasibility of a noble gas ion propulsion system as a possible alternative to mercury or caesium [12], [13] with Kaufman-type ion engines (i.e. 10-cm and 15-cm SERT II), various researches were published during the following decades about GIEs

of different sizes and configurations focusing on the performance of cathodes, discharge chamber, and ion optics with inert gases.

At the beginning of the 1980s, a relevant and comprehensive investigation was carried out with the Kaufman-type J-Series 30-cm diameter thruster [3], which was initially designed and optimised for operation with mercury up to 3 kW, comparing the original results with the liquid metal propellant with those obtained with xenon, krypton, and argon. The analysis covered various aspects of the thruster performance and lifetime, and the main results of the experimental campaign were as follows (flow rates given in A eq.):

- Discharge chamber
    - The minimum values of discharge loss were nearly the same for all the propellants.
    - The performance parameters (i.e. propellant efficiency and discharge voltage) for mercury and xenon were nearly identical, while for krypton a penalty in the propellant efficiency of 4% was measured at comparable values of discharge loss.
    - The maximum values of propellant efficiency obtained with Kr were about 8% lower than those with Xe despite higher values (about 10-20 V) of discharge voltage, probably due to the combined effect of the smaller ionisation cross-sections, of the lighter mass of krypton, and of the relatively short length of the discharge chamber which yields shorter neutral atom residence times.
    - An increase in the discharge chamber length [55] would lead to higher values of the propellant efficiency for lighter gases with the consequence of a possible increase in discharge loss.
- Cathode and neutraliser
    - The ratio of cathode to main flow rate was higher (0.10-0.20) for krypton compared to mercury and xenon (0.03-0.12). This issue could be addressed with cathode modifications, which would allow lower cathode flow rates.
    - The minimum cathode flow rate for stable discharge was similar for mercury and xenon, but an increase in the discharge voltage was required for operation with krypton and argon in order to maintain the same flow rate.
    - Overall, decreasing the gas atomic mass requires an increase of the minimum cathode flow rate as a consequence (valid for both cathode and neutraliser).
- Overall thruster performance
    - As expected, the power required for a given thrust increased as the propellant's atomic mass decreased.
- Thruster/grid lifetime (estimated via analytical modelling)

- The increased discharge voltage needed to operate the thruster with inert gases compared to mercury could reduce the lifetime because of the higher erosion of the discharge chamber due to the greater energy of the ions incident on such surfaces.
- The estimated screen grid erosion rates (due to sputtering by discharge plasma ions) were several times greater for the three gases compared to those for mercury.
- The expected increased erosion could be mainly justified by the higher minimum values of discharge voltage and refractory metal sputtering yields due to the decreasing atomic mass and, possibly, poor optimisation of the ion optics.
- Two secondary effects that should balance each other's contribution to the grid erosion rates are the decrease in doubly-charged ion content with decreasing ion mass and the need for increased ion beam current to maintain constant thrust at constant beam voltage.
- A possible mitigation to the expected reduced lifetime is to use discharge chamber configurations (e.g. ring-cusp) that produce flatter beam current profiles at the screen grid than those possible with a Kaufman-type discharge chamber.

Similar results were obtained in a parallel experiment carried out with a much smaller 5-cm Kaufman-type thruster [56], designed for mercury, but operated with inert gases: using a small open ratio ion optics of 0.41, an upper limit of utilisation efficiency of about 70% was observed for both xenon and krypton, but the discharge voltages and flow rates for Kr were notably higher (flow rates given in A eq.). A further test was carried out with the same setup but with a bigger open ratio ion optics of 0.69, showing an increase in the beam current of about 10% for the same discharge power although the discharge voltage was higher for each case; therefore, the performance curves shifted to higher efficiency and lower discharge loss compared to the case with smaller grid holes: the maximum efficiencies were about 75% and 80%, respectively, for krypton and xenon, and similar discharge losses at the knee of the curve for both propellants, but with a lower propellant utilisation efficiency for krypton (65% compared to 74% for xenon). The results with both grid sets showed that the nominal flow rate (in A eq.) was proportional to $\frac{1}{\sigma_+\sqrt{M_a}}$, where σ_+ is the ionisation cross section and M_a is the ion mass.

In those same years (early 1980s), the development of a new discharge chamber configuration using permanent magnets to obtain strong boundary ring-cusp magnetic fields [14] allowed significant improvements in the discharge chamber performance over conventional Kaufman-

type discharge chambers. The results of the operation of a 30-cm ring-cusp ion thruster [14] with argon, krypton, and xenon were as follows (flow rates given in A eq.):

- The baseline discharge loss values were nearly independent of the propellant type, but the performance with xenon was higher compared to krypton as obtained in previous experiments using Kaufman-type thrusters.
- Propellant efficiencies over 0.90 were achieved for the three inert gases probably due to the longer aspect ratio of the discharge chamber yielding longer neutral atom residence times, as predicted by Rawlin [3].
- As a result of the magnetic field characteristics of this configuration, lower concentrations of doubly charged ions and flatter current density at the grids were measured compared to divergent-field thrusters with a beneficial effect on the centreline screen grid erosion.

As a consequence of these and other investigations, xenon was selected as the propellant for electric propulsion due to numerous technological, economic, and environmental reasons, such as similar performance, but without the related problems linked to liquid metal propellants, and superiority over the other inert gases.

In the following decades, very few attempts were made to use krypton as an alternative to xenon for very specific reasons, such as to establish a performance database on krypton propellant due to initial concerns about the cost and availability of xenon [11], [15] and to take advantage of krypton's specific properties (e.g. lighter mass) for very precise cases (e.g. high specific impulse and/or high-power missions)[57]–[59].

Based on the reviewed literature, no publications are available on either the use of krypton or the difference in performance between xenon and krypton in a small ring-cusp gridded ion engine. Therefore, the experimental campaign was motivated by these limits in the published literature and the above results were used as a reference and comparison of the data obtained during the testing campaign.

2.3.3 Mixtures of Xenon/Krypton and Gridded Ion Engines

A possible mitigation to the issues introduced by using krypton instead of xenon (e.g. increased power requirement for a given thrust, lower discharge efficiency and discharge stability) could be to operate the thruster with mixtures of inert gases and, in particular, a mixture of xenon and krypton in different ratios. This mixture occurs naturally in a proportion of 11:1 in volume (natural mixture ratio), but the production ratio of 1:4 Xe/Kr is of particular interest. In fact, these two gases are conventionally obtained as a by-product of liquid oxygen and nitrogen production

from the atmosphere by cryogenic distillation [60], since krypton and xenon are present in Earth's atmosphere at concentrations of 1.14 and 0.087 ppmv, respectively, and the penultimate by-product stream from air separation consists of 80% krypton and 20% xenon [61]. This mixture is then sent to a separate Xe–Kr separation plant to undergo another cryogenic distillation to obtain pure xenon and pure krypton. The use of the penultimate by-product (1:4 Xe/Kr) and, therefore, the avoidance of the last separation stage allows consistent savings on the price of the propellant, even compared to pure krypton (2-3 times cheaper [62]). However, it should be noted that the purity levels and the exact composition of the mixture are not completely clear (e.g. possible traces of oxygen, methane, and carbon dioxide), since they are dependent on the specific distillation process.

This mixture in any ratio has never been tested with gridded ion engines and only a few explorative attempts have been performed in conjunction with HETs: in Russia in the early 2000s [16], [63], [64] and, more recently, in Italy [17], [65] with different variants of HETs, and in the UK [18] to test the behaviour within a hollow cathode.

The main advantages of using this mixture are that it is much cheaper than the pure gases, the possibility to obtain higher specific impulse, and minimal modifications required to existing systems. On the other hand, the main disadvantages compared to xenon are a possible increase in the mass of storage tanks, a reduction of the thruster efficiency, and an increase in power consumption. Finally, due to the lack of publications about the use of this mixture with GIEs, there are several unknowns in the behaviour of the various components of these thrusters, such as the plasma sheath at the grids, impact on thruster and the ion optics lifetime. The latter one is very relevant since the grids are usually optimised for a specific propellant, and, in this case, the difference in atomic mass between the two gases would require some compromises when designing the grids, and a reduced lifetime is expected.

An important part of the experimental campaign focused on the analysis of the performance of this mixture compared to xenon and krypton, and the behaviour of the mixture inside the discharge chamber in proximity of the ion optics using a Langmuir probe as a diagnostics tool.

2.3.4 Hollow Cathodes with Krypton and Mixtures of Xenon/Krypton

In the previous subsections, the small number of studies that are available in the literature about the discharge characteristics and the operations of alternative inert gas propellants in full thruster geometry has been described and reported. However, as mentioned in Section 2.2.4, the behaviour of a hollow cathode in full thruster configuration is very different from the diode configuration, since there is almost complete suppression of the dual-mode operation with the absence of the plume mode, and no plume-to-spot transition is observed. Therefore, if only the

studies comparing the various inert gases in diode configuration are considered, the number of publications is even smaller [42], [66]–[69]: the studies highlight the need for a much higher flow rate and a general increase in discharge voltages to operate the cathode in spot mode with krypton.

Only a couple of studies are available about the use of a Xe/Kr mixture (or any mixture of inert gases) as propellant, but none of them has utilised the mixture production ratio of 1:4: in Ref. [18], the natural ratio of 1:11 was considered, and the ratios 1:3 and 1:10 were tested in Ref. [69].

2.3.5 Testing with Alternative Propellants

Ground testing of any ion thrusters is an essential activity to evaluate the performance and life data, and the testing facilities are required to maintain sufficiently low background pressure to obtain accurate results. As described in the previous subsections, xenon has been the choice for EP thrusters for the last few decades and, consequently, the existing testing facilities are mainly designed to pump down this gas. Cryopumps are the typical choice to guarantee clean and high vacuum levels during the testing process of the thruster and similar systems can be used for krypton, but some modifications need to be considered depending on the propellant being used.

Commercially available cryopumps operate on the principle that the working gas condensates on cryocooled surfaces and, therefore, the saturation vapour pressure as function of the temperature determines the surface temperature of the cryopanels required to maintain a suitable low pressure in the vacuum chamber (Figure 9 for common vacuum system gases). However, the condensation temperature is usually chosen to obtain a saturation vapour pressure of one order of magnitude lower than the required final chamber pressure to account for any increase of temperature after condensation that might lead to an increase of pressure. Since the typical ultimate pressure for vacuum chambers is in the order of $1x10^{-7}$ mbar, it means that the cryopanels temperature needs to be set in the range of 45-50 K for xenon and 30-35 K for krypton to obtain a vapour pressure better than $1x10^{-8}$ mbar, as shown in Figure 9. Usually, reducing the size of the cryopanels is an effective way to achieve the lower temperature needed to pump krypton, but this reduction has an impact on the overall pumping speed and on the dynamic vacuum performance of the chamber. Finally, it is evident from Figure 9 that lighter gases are more difficult (i.e. argon) or practically impossible (i.e. neon, helium, etc.) to pump using cryocooled systems.

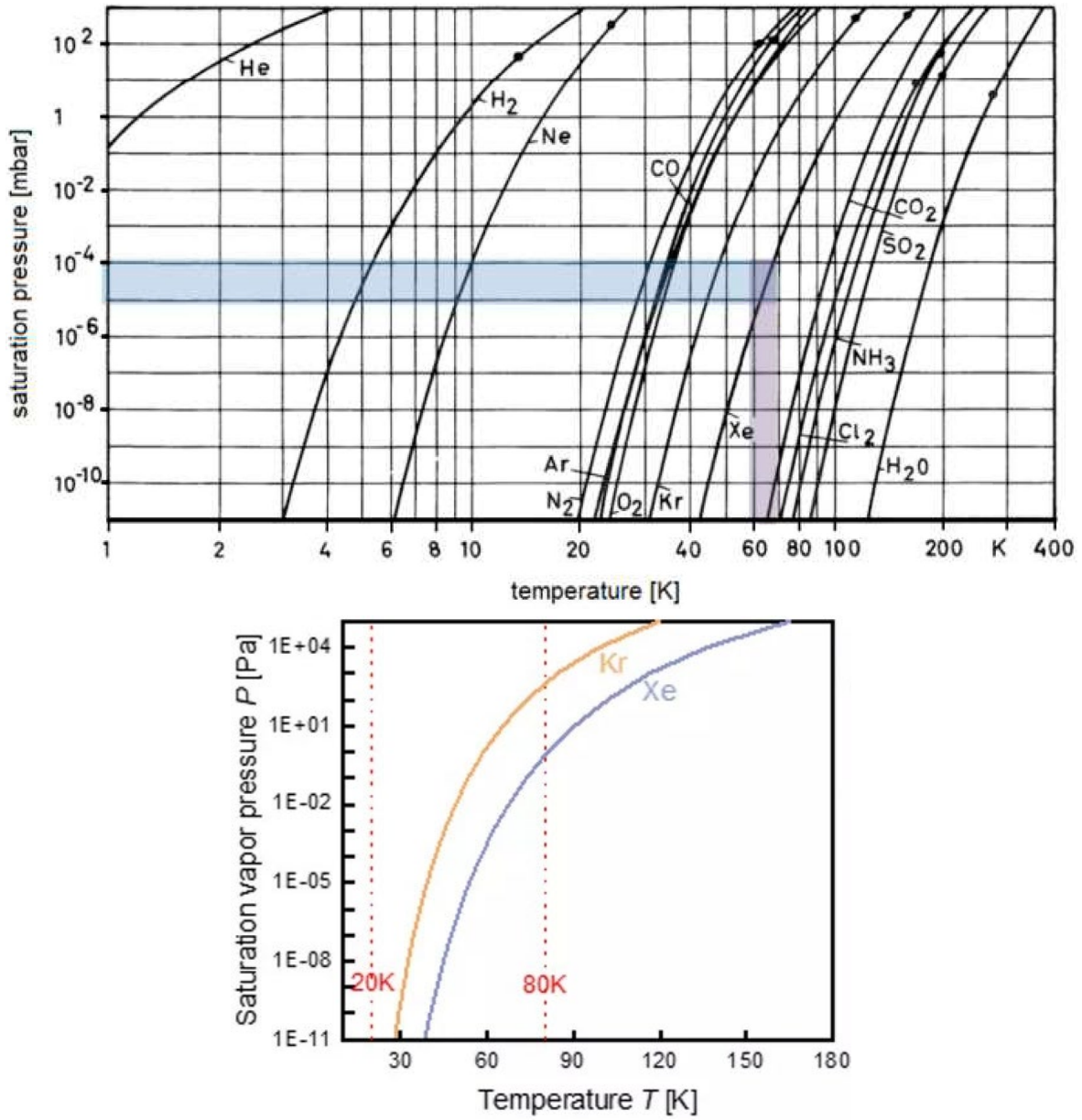

Figure 9 – Saturation vapour pressure as function of the temperature for common vacuum system gases (top [70]) and for xenon and krypton (in particular, bottom [71])

2.4 Summary

The above discussion offers a quick overview of electric propulsion systems, the characteristics and working principles of GIEs, and the propellant selection criteria for an EP system, giving a clear picture of the advantages and disadvantages of using xenon.

In fact, while xenon represents the state-of-the-art, its limited availability and high cost could have repercussions on the rapid growth of the EP market and, therefore, the search for alternative propellants is gaining importance to meet this new demand (e.g. mega constellations). A review of some of the past publications on the different propellants used with GIEs has been carried out with a particular focus on krypton and on mixtures of xenon and

krypton, which has never been tested with gridded ion engines and only a couple of studies are available about its use with hollow cathodes. Finally, some of the modifications required to the ground testing facilities when using different propellants were also reported in this section.

The next chapter will describe the calculations of the main parameters used to evaluate the performance of a GIE outlining the impact of the propellant atomic mass on these parameters at a first-order approximation, the performance models (for discharge chamber, discharge-only operations, and ion optics) and the plasma diagnostics tools used for the analysis of the experimental data.

Chapter 3 Gridded Ion Engines: Theoretical Background

This chapter covers the calculations of the main parameters used to evaluate the performance of a GIE outlining the impact of the propellant atomic mass on these parameters at a first-order approximation, and provides a brief description of the performance models (for discharge chamber, discharge-only operations, and ion optics) and the plasma diagnostics tools used for the analysis of the experimental data.

3.1 Gridded Ion Engines: Performance Parameters

As mentioned in Section 2.1, both chemical and electric propulsion systems work using the same basic principle: the expulsion of the accelerated propellant mass generates propulsion. However, the acceleration mechanisms are different for the different thrusters' technologies.

In the following subsections, the parameters that measure the performance and efficiency of a gridded ion engine (such as thrust, specific impulse, thruster efficiency, and thrust-to-power ratio) are described with a particular focus on the impact of changing propellant on each parameter.

3.1.1 Thrust

In Section 2.1, the equation for the thrust was derived from the law of conservation of the momentum (Eq. (2-2)). In a gridded ion engine, the acceleration of ions to high exhaust velocity is achieved using an electrical power source and, considering that ion velocity is much higher than any unionised propellant escaping the thruster, the ideal thrust can be described as [20]:

$$T_{ideal} = \dot{m}_i v_i \tag{3-1}$$

where $\dot{m}_i$ is the ion mass flow rate and v_i is the ion velocity. Using the conservation of energy, the ion velocity is given by:

$$v_i = \sqrt{\frac{2eV_b}{M}} \tag{3-2}$$

where V_b, beam voltage, is the net voltage through which the ions are accelerated, e is the electron charge, and M is the ion mass (kg). The beam voltage V_b is determined by:

$$V_b = V_{screen} + V_d - V_{neutr} \tag{3-3}$$

with V_d discharge voltage and V_{neutr} neutraliser floating potential relative to ground. The ion mass flow rate is correlated to the ion beam current I_b by:

$$\dot{m}_i = \frac{I_b M}{e} \tag{3-4}$$

Eq. (3-4) is valid for an ideal case of a unidirectional, singly ionised, monoenergetic beam of ions. In order to take into account the presence of multiply charged species and the beam divergence, a thrust correction factor (TCF) γ is introduced and it is defined as follows [72]:

$$\gamma = \alpha F_t \tag{3-5}$$

where α is the correction factor due to multiply charged species and in the case of doubly ionised atoms is given by:

$$\alpha = \frac{I^+ + \frac{1}{\sqrt{2}} I^{++}}{I^+ + I^{++}} \tag{3-6}$$

and F_t is the factor due to the beam divergence and it is defined as the ratio of the axially aligned beam current (where θ is the average half-angle divergence of the beam) to the total beam current:

$$F_t = \frac{\int_A j_b \cos\theta \, \mathrm{d}A}{I_b} \tag{3-7}$$

Therefore, the total corrected thrust is given by [20]:

$$T_{corr} = \gamma \dot{m}_i v_i = \gamma \sqrt{\frac{2M}{e}} I_b \sqrt{V_b} \tag{3-8}$$

3.1.2 Specific Impulse

In Equation (2-3), the specific impulse I_{sp} was introduced since it is an important parameter in space propulsion as it gives a measure of the efficiency of a thruster in terms of fuel consumption. To define I_{sp}, we start by defining the total impulse $\boldsymbol{I}$, which measures the change in momentum that a thruster can transmit to a space vehicle, as follows:

$$\boldsymbol{I} = \int \dot{m}_p \boldsymbol{v_{ex}} \, dt = m_p \boldsymbol{v_{ex}} \tag{3-9}$$

where $\dot{m}_p$ is the propellant flow rate. Eq. (3-9) shows the two ways to obtain the same impulse: either a strong force over a short time (chemical propulsion approach) or a lower force over a longer period (electric propulsion approach).

Consequently, the specific impulse I_{sp} can be defined as the impulse delivered per unit of propellant consumed (or thrust produced per unit of propellant flow rate) and is conventionally described in terms of weight at the surface of the Earth:

$$I_{sp} = \frac{I}{g_0 m_p} = \frac{T}{\dot{m}_p g_0} = \frac{v_{ex}}{g_0} \approx \frac{v_{ex}}{10} \tag{3-10}$$

It is clear that a higher specific impulse means less propellant required to produce the same impulse and this is the main reason that makes electric thrusters an attractive option as long as the mission duration is not a crucial aspect.

For a GIE, the specific impulse I_{sp} can be calculated as follows [20]:

$$I_{sp} = \frac{T}{\dot{m}_p g_0} = \frac{\gamma \eta_m}{g_0} \sqrt{\frac{2eV_b}{M}} = 1.417x10^3 \gamma \eta_m \sqrt{\frac{V_b}{M_a}} \tag{3-11}$$

where M_a is the ion mass (in AMU) and $\eta_m = \frac{\dot{m}_\iota}{\dot{m}_p}$ is the thruster mass utilisation efficiency, which accounts for the ionised versus unionised propellant.

3.1.3 Beam Current

As seen in Section 2.2.3, in a gridded ion engine, the propellant that is ionised in the discharge chamber is then accelerated electrostatically by the field applied between two (or more) grids. In particular, the current density j_i that can be extracted is limited by space-charge saturation, since only ions fill the gap between the grids. This interstice constitutes a high-voltage sheath, or Child-Langmuir's sheath, that complies with the Child-Langmuir's law [73]:

$$j_i = \frac{4}{9} \epsilon_0 \sqrt{\frac{2e}{M}} \frac{V^{\frac{3}{2}}}{d^2} \tag{3-12}$$

where e is the electron charge, M is the ion mass, V is the potential drop, and d is the sheath thickness. The total current I_b that can be extracted and focused into a beam for a given applied voltage V is defined by the perveance P:

$$P \equiv \frac{I_b}{V^{\frac{3}{2}}} = \frac{4}{9} \epsilon_0 \sqrt{\frac{2e}{M}} \tag{3-13}$$

The maximum perveance for round grid apertures of diameter D is then:

$$P_{max} \equiv \frac{\pi \epsilon_0}{9} \sqrt{\frac{2e}{M}} \left(\frac{D^2}{d^2}\right) \tag{3-14}$$

It is clear from this equation that operating conditions close to the maximum perveance are optimal.

Using Eq. (3-1) and Eq. (3-12), an important characteristic of gridded ion engines can be demonstrated [20]:

$$\frac{T}{A} = \frac{8}{9} \epsilon_0 \left(\frac{V}{d}\right)^2 \tag{3-15}$$

that the thrust per unit of area A, or thrust density, is independent of the nature of the propellant. However, it is worth noting that the atomic/molecular mass of the propellant impacts the total thruster efficiency and the specific impulse among other performance parameters, as mentioned in Section 2.3 and Table 1. Equation (3-15) stands true for a mixture of gases.

Child-Langmuir's equation (Eq. (3-12)) assumes that the plasma sheath is essentially planar. However, at the screen grid in a gridded ion engine, the sheath shape is not planar and the above equation should be modified as follows to account for the modified sheath thickness [20]:

$$j_i = j_{max} = \frac{4}{9}\epsilon_0\sqrt{\frac{2e}{M}}\frac{V_T^{\frac{3}{2}}}{l_e^2} \tag{3-16}$$

where $V_T = V_{screen} + |V_{accel}|$ is the total voltage across the sheath between the screen grid and the accel grid, and $l_e = \sqrt{\left(l_g + t_s\right)^2 + \frac{d_s^2}{4}}$ is the sheath thickness with l_g grid gap, t_s screen thickness, and d_s screen grid aperture diameter (Figure 10).

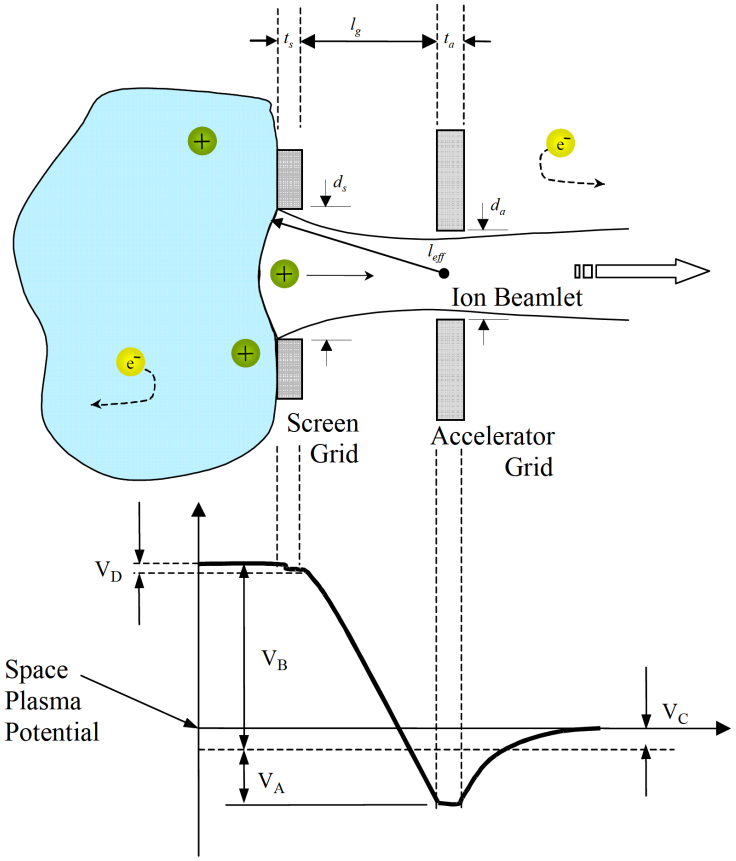

Figure 10 – Detail of a grid beamlet [72]

Using the values of the ion current density of a single beamlet j_i, it is possible to calculate the beam current I_b, which can be written as:

$$I_b = j_i A_g T_s \tag{3-17}$$

where A_g is the grid area and T_s is the effective transparency of the screen grid.

3.1.4 Total Power and Thruster Efficiency

As described in Section 3.1.2, the mass utilisation efficiency η_m can be defined as the fraction of ionised over the unionised propellant and can be also defined as the portion of the input propellant mass that is converted into ions in the discharge chamber and accelerated outside the engine through the ion optics:

$$\eta_m = \frac{\dot{m}_i}{\dot{m}_p} = \frac{I_b}{e}\frac{M}{\dot{m}_p} \tag{3-18}$$

An important parameter is the electrical efficiency of the thruster, η_e, which can be expressed as follows [20]:

$$\eta_e = \frac{P_b}{P_{tot}} = \frac{I_b V_b}{I_b V_b + I_d V_d + P_{other}} \tag{3-19}$$

where $P_b = I_b V_b$ is the beam power, $P_d = I_d V_d$ is the discharge power (i.e. the electrical cost of producing the ions) and P_{other} represents the other power input to the thruster required to create the thrust beam (e.g. cathode heater and keeper power, neutraliser power, etc.).

In order to describe the cost of producing ions in the discharge chamber, the discharge loss η_d is introduced: this value is usually measured in terms of the power (in watts) necessary to produce, but not accelerate an ion beam current of 1 A at a given propellant utilisation efficiency and it has units of watts per ampere (W/A) or electron volts per ion (eV/ion):

$$\eta_d = \frac{I_d V_d + I_k V_k}{I_b} \simeq \frac{I_d V_d}{I_b} = \frac{P_d}{I_b} \tag{3-20}$$

The keeper power is normally small compared with the discharge power and it can be neglected. Since this term represents a power loss, it is desirable to minimise it while maintaining high propellant utilisation. The plot of discharge loss as a function of the propellant utilisation efficiency, known as the performance curve, usually characterises the discharge chamber performance of an ion thruster. It is worth noting that performance curves are normally taken at constant beam current and discharge voltage so that the efficiency of producing and delivering ions to the beam is not masked by changes in the discharge voltage or average plasma density at the grids.

Furthermore, another important parameter when comparing different thruster technologies is the total thruster efficiency η_T defined as follows [20]:

$$\eta_T = \frac{P_{jet}}{P_{in}} = \frac{\dot{m}_p v_{ex}^2}{2P_{in}} = \frac{T^2}{2\dot{m}_p P_{in}} \tag{3-21}$$

where P_{jet} is the kinetic thrust power of the beam and P_{in} is the input electrical power. This equation can be rewritten using the efficiencies just introduced as:

$$\eta_T = \gamma^2 \eta_e \eta_m \tag{3-22}$$

Finally, related to the thruster efficiency is the thrust-to-power ratio or thrust per unit input power:

$$\frac{T}{P_{in}} = \frac{2\eta_T}{g_0 I_{sp}} \tag{3-23}$$

This equation shows that, for a given input power and thruster efficiency, an increase in the specific impulse implies a reduction in the thrust, so there is a compromise between T and I_{sp}. As said in the previous section, electric thrusters can deliver a high specific impulse with low thrust levels, while the opposite is valid for chemical thrusters.

3.1.5 The Effects of Propellant Mass and Mixture on Thruster Performance Parameters

As seen in the previous subsections, the performance parameters of a gridded ion engine depend on the propellant properties (i.e. propellant atomic mass) either directly or indirectly. In this subsection, the impact that the change of propellant has on the performance of a gridded ion engine is evaluated at a first-order estimation. In fact, while it is unrealistic to change the mass of the propellant without considering the other properties (e.g. ionisation potential, ionisation cross-section, etc.), this assessment can be considered a useful design tool to understand the effect that the change may have on performance.

In Section 3.1.1, the thrust was calculated using Eq. (3-8) and, if the beam current is held constant and the thruster is run at a given beam voltage, the power consumption will be constant and the thrust will vary proportionally to the square root of the propellant atomic mass as follows:

$$T = \gamma \dot{m}_i v_i = \gamma \sqrt{\frac{2M}{e}} I_b \sqrt{V_b} \propto \sqrt{M} \tag{3-24}$$

Consequently, krypton generates a thrust that amounts to 0.8 times that of xenon. In this equation, the thrust correction factor γ is indirectly dependent on the propellant mass, e.g. for identical ion optics, lighter propellant will have a bigger divergence.

In the case when a mixture is used, the exhaust plume will contain ions with different exhaust velocities resulting in a lower average exhaust velocity compared to the case when only the heavier propellant is used. Similarly to the presence of doubly charged ions (Equation (3-6)), the magnitude of this loss can be approximated for the Xe/Kr mixture as follows:

$$\frac{T_{Xe/Kr}}{T_{Xe}} = \frac{I_{b,Xe} + \sqrt{\frac{M_{Kr}}{M_{Xe}}} I_{b,Kr}}{I_{b,Xe} + I_{b,Kr}} \tag{3-25}$$

In addition, Eq. (3-8) can be remodelled and generalised to calculate the thrust produced by a mixture of gases as follows:

$$T = \gamma \sum_j \dot{m}_{i,j} v_{i,j} = \gamma \sqrt{\frac{2V_b}{e}} \sum_j I_{b,j} \sqrt{M_j} \tag{3-26}$$

where

$$\dot{m}_{i,j} = \frac{I_{b,j} M_j}{e} \tag{3-27}$$

is the mass flow rate of a given ion species with ion mass M_j (in kg) and

$$v_{i,j} = \sqrt{\frac{2eV_b}{M_j}} \tag{3-28}$$

is the exhaust velocity for a given ion species in a gridded ion engine. In Eq. (3-26), the factor γ is assumed to be constant at a first-order approximation.

Similarly, the Eq. (3-11) for the specific impulse can be simplified to show that I_{sp} is inversely proportional to propellant mass as follows:

$$I_{sp} = \frac{T}{\dot{m}_p g_0} = \frac{\gamma \eta_m}{g_0} \sqrt{\frac{2eV_b}{M}} \propto \sqrt{\frac{1}{M}} \tag{3-29}$$

So, assuming that the other parameters are held constant, a propellant with a lighter mass will yield a higher I_{sp} at a given power, hence I_{sp} for krypton is 1.25 times greater than the value of xenon. Rearranging Eq. (3-11), it is also possible to calculate the specific impulse for a mixture of gases as follows:

$$I_{sp} = \sum_j \frac{T_j}{\dot{m}_{p,j} g_0} = 1.417 x 10^3 \gamma \sqrt{V_b} \sum_j \eta_{m,j} \frac{1}{\sqrt{M_{a,j}}} \tag{3-30}$$

where

$$\eta_{m,j} = \frac{\dot{m}_{i,j}}{\dot{m}_{p,j}} = \frac{I_{b,j}}{e} \frac{M_j}{\dot{m}_{p,j}} \tag{3-31}$$

is the mass utilisation efficiency of a given ion species with ion mass $M_{a,j}$ (in AMU).

Likewise, it can be demonstrated from Eq. (3-13) that the perveance is inversely proportional to the propellant mass as follows:

$$P = \frac{4}{9} \epsilon_0 \sqrt{\frac{2e}{M}} \propto \sqrt{\frac{1}{M}} \tag{3-32}$$

and the perveance can be re-derived for multiple-species plasmas as follows [74]:

$$P = \frac{4\sqrt{2}}{9}\epsilon_0\sqrt{\left[\frac{q}{M}\right]_{eff}} \tag{3-33}$$

where the effective mass-to-charge ratio is defined as:

$$\left[\frac{q}{M}\right]_{eff} \equiv \left(\left[\frac{M}{q}\right]_{eff}\right)^{-1} = \left(\sum_{i=1}^{n} c_i\sqrt{\frac{M_i}{q_i}}\right)^{-2} \tag{3-34}$$

with $c_i \equiv \frac{J_i}{J}$ represents the current weight of the i-th species.

Finally, using Eq. (3-16) it is possible to show that the sheath thickness l_e is proportional to the propellant mass as follows:

$$l_e \propto M^{-\frac{1}{4}} j_i^{-\frac{1}{2}} V_T^{\frac{3}{4}} \tag{3-35}$$

Therefore, changing the propellant and keeping j_i and V_T constant, the geometric values (e.g. grid thicknesses, extraction hole diameters and interspaces) should be changed consequently and, for krypton, they should be enlarged by a factor of 1.12 compared to xenon.

3.2 Gridded Ion Engines: Performance Models

The complexity associated with on-ground testing is often mitigated by using models and simulations to evaluate the performance of a novel concept (e.g. new thruster, modified configuration, alternative propellant, etc.), or at least part of it. A detailed description of performance models is beyond the scope of this work and the models presented in the following subsections (for discharge chamber, and ion optics) will be kept to a minimum level of detail (additional information is available in Appendix A), as the purpose is to offer an understanding of the impact of using alternative propellants on GIE's performance.

3.2.1 Discharge Chamber Models: Impact of the Propellant Selection on a 0-D Model for Ring-Cusp Ion Thrusters

The main purpose of the discharge chamber's performance models for GIE is to understand in detail the processes occurring during the thruster's operation. In fact, the development of these models, ranging from a simple 0-D approach based on power and particle balance to more complicated 2-D and 3-D multiphysics models, contributes to a better knowledge of the modelling object and of the impact of the thruster characteristics on its performance. Furthermore, experimental work can be reduced with a consequent cost reduction and, more importantly, computational models allow the design of more optimised high-performance devices in a shorter amount of time.

In Appendix B.1, a brief background is reported on 0-D models for ring-cusp thrusters. Brophy's model [75] was used for the modelling of the discharge chamber's performance in this work because such a model has proven to be in good agreement with experimental results for a different range of thrusters and it has also shown some flexibility when used to predict the performance of thrusters run with alternative propellants (such as xenon, krypton, and argon in [75], and Buckminsterfullerene in [76]).

This model [75] was developed for ring-cusp magnetic confinement electron bombardment thrusters and the following assumptions apply:

- The plasma inside the discharge chamber is uniform and its boundaries are the inside walls of the chamber. It follows that temperatures, densities, and other physical parameters are constant and equal to a value averaged over the volume of the chamber.
- Inside the discharge chamber, the electrons can be divided into two groups, primary and secondary, with two different energy distributions. The coexistence of these two groups of electrons is possible because of their small collision frequencies.
    - The primary electrons are defined as those electrons emitted by the cathode that have not undergone any inelastic collisions with neutrals and, consequently, they can be considered to have a mono-energetic energy distribution.
    - The secondary electrons comprise the primary electrons involved in one or more inelastic collisions, and the electrons made available during the ionisation process of neutral atoms. Their energy distribution can be approximated by a Maxwellian distribution and, because of this, they are called Maxwellian electrons (see Appendix A.5.2).

According to this model, the discharge loss can be written as:

$$\eta_d = \frac{\epsilon_P^*}{f_B\{1-\exp[-C_0\dot{m}_p(1-\eta_m)]\}} + \frac{f_C}{f_B}V_d \tag{3-36}$$

where

$$C_0 = \frac{4\sigma_0 l_c}{e v_0 A_g \phi_0} \tag{3-37}$$

and

$$\epsilon_P^* = \frac{\epsilon_0+\epsilon_M}{1-\left[\frac{V_C+\epsilon_M}{V_d}\right]} \tag{3-38}$$

The quantity C_0, called the primary electron utilisation factor, describes the interaction between primary electrons and neutral atoms, and it depends on the primary electron containment length (l_c), the propellant gas (through σ_0, the total inelastic collision cross section for primary

electron-neutral atom collisions, and v_0, the neutral atom velocity), and the quality of the containment of neutrals (through the grid area A_g, the grid transparency to neutral atoms ϕ_0, and v_0). The factor C_0 gives a qualitative measurement of the utilisation of the primary electrons inside the discharge chamber and, therefore, it should be as high as possible to have a lower plasma ion energy cost. The impact of the parameters in Eq. (3-37) on the value of C_0 is analysed in Appendix B.2. For example, a propellant with a larger total inelastic collision cross section (σ_0) will have a larger C_0 as well as heavier gas particles which have lower neutral velocities (v_0), and C_0 can also be increased by decreasing the grid transparency to neutral atoms, ϕ_0.

The quantity ϵ_P^*, called the baseline ion energy cost, is related to different energy loss mechanisms such as the energy cost expended in excitation compared to ionisation of neutral atoms through ϵ_0^*, the average energy of Maxwellian electrons leaving the plasma at the anode ϵ_M, and the cathode efficiency V_C that represents an additional potential drop from the hollow cathode insert to where the electrons enter the discharge chamber.

The other parameters present in Eq. (3-36) are:

- the extracted-ion fraction $f_B = \frac{I_b}{I_P}$, and
- the fraction of ion current produced that goes to cathode potential surfaces $f_C = \frac{I_C}{I_P}$

where $I_P = en_0 n_e \langle \sigma_+ \, v_e \rangle V_P$ is the ion production current, with n_0 and n_e neutral density and plasma density, respectively, $\langle \sigma_+ v_e \rangle$ representing the product of the ionisation collision cross-section and the electron velocity averaged over the electron speed distribution, and V_P is the plasma volume. A complete listing of the inelastic collision cross sections and the reaction rate coefficients for ionisation and excitation averaged over a Maxwellian electron distribution for xenon and krypton are given in Appendix A. The value of the volume of the ion production region, V_P, can be determined using a computer-drawn magnetic field map of the discharge chamber and, as Brophy [75] suggests, the volume to be considered is where the magnetic flux density is 0.005 T or less. In a ring-cusp ion thruster, the ion production volume can be assumed to be half of the discharge chamber volume. However, since the propellant utilisation efficiency only depends linearly on the plasma volume, the precise measurement of this volume is not needed.

According to Eq. (3-36), to predict the performance of a thruster, it is necessary to calculate ϵ_P^* which depends on the type of propellant and the operating conditions, f_B and f_C which depend on the design of the thruster, and C_0 which depends on both. Since the values for l_c, f_B and f_C cannot be predicted using this model, this reliance on experimental measurements represents the main weakness of this model, as seen in Section B.1. Therefore, it is not self-consistent, and it cannot be used to predict the performance of a completely new thruster design. However,

such parameters can be assumed to be constant for a given thruster because they depend mainly on the geometry and the magnetic field configuration and, hence, it is possible to predict the performance of the thruster for different types of propellants or operating conditions.

In particular, the primary electron confinement length l_c, which is defined [75] as the length of the helical path that a primary electron would traverse in the discharge chamber before being collected by the anode, assuming that it had no inelastic collisions through its travel, depends primarily on the thruster geometry, magnetic field configuration, and cathode position, and it does not depend on the propellant type, mass flow rate, propellant utilisation efficiency, etc. In cusped magnetic field thrusters, primary electrons are lost to the anode through the cusps, and it follows that this length can be increased by decreasing the number of cusps at anode potential or increasing the flux density at the cusp. However, the effective anode cusp area cannot be reduced below a certain limit, where the discharge becomes unstable [77].

In addition, the Equations (3-36)-(3-38) can be rederived for Xe/Kr mixtures as follows:

$$\eta_d = \frac{\epsilon_P^{*mix}}{f_B\{1-\exp[-C_0^{mix}\dot{m}_p(1-\eta_m^{mix})]\}} + \frac{f_C}{f_B}V_d \tag{3-39}$$

where

$$C_0^{mix} = \frac{4\sigma_0^{mix} l_c}{e v_0^{mix} A_g \phi_0} \tag{3-40}$$

and

$$\epsilon_P^{*mix} = \frac{\epsilon_0^{mix} + \epsilon_M}{1-\left[\frac{V_C+\epsilon_M}{V_d}\right]} \tag{3-41}$$

The terms with the superscript mix are the quantities that were modified to account for the presence of the second species and they can be written as (X_j is the mole fraction of the j-th species):

- the average plasma ion energy cost for ionisation and excitation processes only, ϵ_0^{mix}

$$\epsilon_0^{mix} = \frac{X_{Xe}\langle\sigma_+^{Xe}v_e\rangle U_{Xe}^+ + X_{Kr}\langle\sigma_+^{Kr}v_e\rangle U_{Kr}^+}{X_{Xe}\langle\sigma_+^{Xe}v_e\rangle + X_{Kr}\langle\sigma_+^{Kr}v_e\rangle} + \frac{X_{Xe}\langle\sigma_{Xe}^{*}v_e\rangle U_{Xe}^{*} + X_{Kr}\langle\sigma_{Kr}^{*}v_e\rangle U_{Kr}^{*}}{X_{Xe}\langle\sigma_+^{Xe}v_e\rangle + X_{Kr}\langle\sigma_+^{Kr}v_e\rangle} \tag{3-42}$$

- equivalent neutral atom velocity, v_0^{mix}

$$v_0^{mix} = X_{Xe}v_0^{Xe} + X_{Kr}v_0^{Kr} \tag{3-43}$$

- equivalent total inelastic collision cross section for primary electron-neutral atom collisions, σ_0^{mix}

$$\sigma_0^{mix} = X_{Xe}\sigma_0^{Xe} + X_{Kr}\sigma_0^{Kr} \tag{3-44}$$

Finally, the production of doubly charged ions is neglected in the model described above, but their presence is one of the principal effects leading to a loss of effective thrust and, consequently, to a reduction in thruster efficiency, but, above all, they are the primary driver limiting the discharge chamber lifetime. Reference [75] provides a formula for calculating the double ion density for a single gas and this formula is reported in Appendix B.2.4 together with its rederivation for a mixture of gases.

3.2.2 Simulation of Ion Thruster Operation without Beam Extraction: Discharge-only Mode

The design, development and life testing of a discharge chamber are essential but not trivial tasks within the overall development of a gridded ion engine. In particular, life testing requires vacuum facilities capable of achieving high pumping speeds to maintain sufficiently low background pressures during beam extraction, and these facilities are usually expensive to build and maintain. A partial solution to this problem that simplifies the initial development and optimisation of a new discharge chamber comes from the use of a technique which simulates the ion beam extraction operating conditions of the discharge chamber without actually extracting a beam, the so-called "discharge-only" mode. This mode consists of operating the discharge chamber at full operative conditions (i.e. complete discharge and plasma production), but the ions arriving at the grids are collected and not accelerated to form a beam. Therefore, a lower-than-normal mass flow rate of propellant needs to be injected into the chamber because a large part of the ions collected by the grids returns into the thruster as neutrals. Several models that allow the conversion of the thruster performance (beam current, mass utilisation efficiency, discharge loss, etc.) between operations with high voltage beam extraction and without beam extraction have been developed in the past [14], [75], [78], [79], but the method described by Brophy in his paper [80] is the actual state-of-the-art, and it was used as the basis for the experimental campaign.

The author suggests that, in order to simulate beam extraction, two fundamental similarity conditions are required to simultaneously match the respective values which would be obtained with beam extraction:

- the discharge chamber average neutral atom density $n_0 = \hat{n}_0$, and
- the product of the average ion density and the square root of the average electron temperature $n_i\sqrt{T_e} = \hat{n}_i\sqrt{\hat{T}_e}$.

Before describing the details of this technique, it is useful to examine the theory behind it and the necessary modifications to the discharge chamber's electrical setup. During normal

thruster operation with beam extraction, the ion density in the discharge chamber is much smaller than the neutral propellant density, but, at the same time, more than 90% of the propellant leaving the chamber is in the form of ions. This is due to the fact that ions move towards the ion optics at Bohm velocity, which depends on the electron temperature, and T_e is usually more than 500 times the neutral atom temperature, which dictates the neutral atoms' escape velocity. Moreover, the effective transparency of the ion optics to ions is much greater (usually in a proportion of 4 to 1) than the effective transparency to neutral atoms. During thruster operation without beam extraction, the removal of high voltage from the grids leads to a significant drop in the ion optics transparency to ions: in fact, a large fraction of the ions reaching the ion optics collides with the grids and recombine with the electrons at the grid surfaces. These recombined neutral atoms either re-enter the discharge chamber or leave the thruster completely, causing an increment in the fraction of propellant which leaves the discharge chamber as neutral atoms instead of as ions. A consequence of this diverse environment is that, if the propellant flow rate into the discharge chamber remains unchanged after the removal of the high voltage, the neutral atom density will increase significantly to satisfy the continuity principle. Therefore, in order to simulate the beam extraction operating conditions without beam extraction, the propellant flow rate must be reduced and, additionally, the average neutral atom density in the discharge chamber needs to be maintained constant with and without beam extraction as well as the product of the ion density and the square root of the average electron temperature. An observed consequence of the discharge-only mode is the significantly higher screen grid temperature, which is a result of the supplementary thermal load due to the increased ion flux to the grid surface.

The differences in the electrical schemes for the operation with and without beam extraction are shown in Figure 11. In the case of operation without beam extraction, the cathode common (negative of the anode supply) needs to be biased 20-25 V positive with respect to facility ground to prevent electrons from escaping the discharge chamber, while the grids are biased up to 30 V negative with respect to the cathode common to repel electrons. In addition, the neutraliser needs to be switched off to prevent electron backstreaming to the ion source and the flow rate through the main cathode is held constant. The measurement of the ion currents to the screen grid and the accel grid allows to estimate the expected performance with beam extraction applying the following procedure.

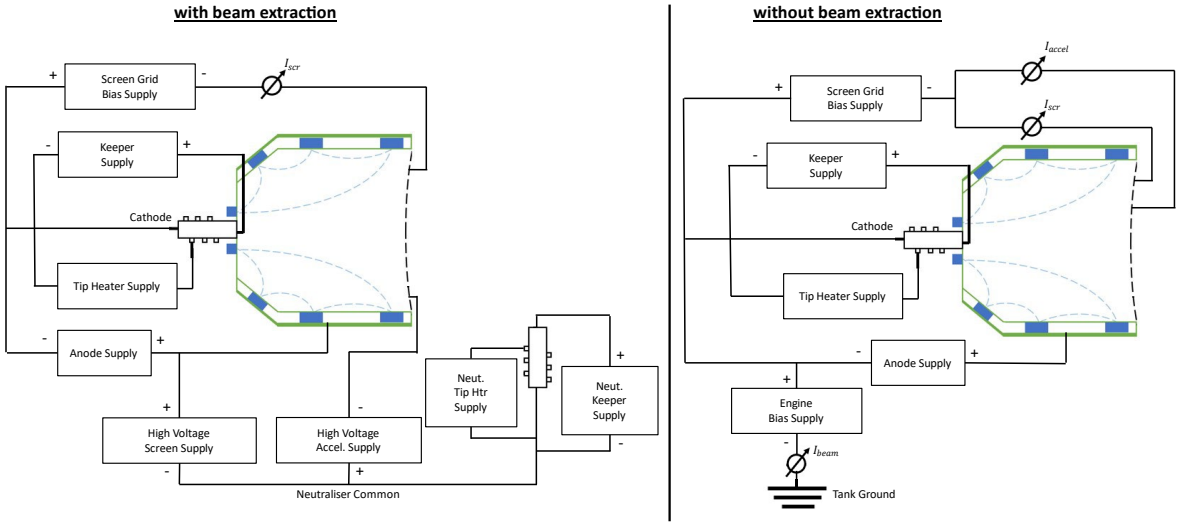

Figure 11 – Electrical diagram for operation with (left) and without (right) beam extraction [80]

In order to estimate the ion beam current I_b with beam extraction, the total ion current I_{tot} collected on the grids and leaving the discharge chamber is taken into account as follows [81]:

$$I_{tot} = \hat{I}_{screen} + \hat{I}_{accel} + \hat{I}_{beam\_dc} \tag{3-45}$$

where $\hat{I}_{screen}$ is the ion current collected by the screen grid, $\hat{I}_{accel}$ is the ion current collected by the accel grid, and $\hat{I}_{beam\_dc}$ is the ion beam produced by the ions escaping the thruster in discharge-only mode, which is negligible when compared with the other two terms. Using the total ion current collected, the simulated ion beam current I_b can be obtained from the ion optics transparency T_{beam} with beam extraction (usually calculated with an ion optics code) as:

$$I_b = I_{tot} T_{beam} \tag{3-46}$$

Then, the discharge current with beam extraction I_d is calculated from the conservation of the discharge current without beam extraction $\hat{I}_d$ as:

$$\hat{I}_d = I_e + \hat{I}_{screen} + \hat{I}_{accel} \tag{3-47}$$

where I_e is the electron current from the cathode. The collected currents on the grids $\hat{I}_{screen}$ and $\hat{I}_{accel}$ without beam extraction are equal to the current collected on the screen grid I_{screen} and the ion beam current I_b with beam extraction as:

$$\hat{I}_{screen} + \hat{I}_{accel} \approx \hat{I}_{screen} + \hat{I}_{accel} + \hat{I}_{beam\_dc} = I_{screen} + I_{accel} + I_b \approx I_{screen} + I_b \tag{3-48}$$

Consequently, the simulated discharge current I_d is given by:

$$I_d = I_e + I_{screen} \qquad \leftrightarrow \qquad I_d = \hat{I}_d - I_b \tag{3-49}$$

Finally, the equivalent discharge loss η_d with beam extraction is:

$$\eta_d = \frac{I_d V_d}{I_b} = \frac{(\hat{I}_d - I_b)\hat{V}_d}{I_b} \tag{3-50}$$

As described previously, operating a discharge chamber without beam extraction has an impact on the required total mass flow rate $\dot{m}_p$ that is injected into the chamber. In order to quantify this value, firstly, the mass utilisation efficiency η_m with beam extraction is defined as the ratio between the simulated ion beam I_b and the sum of used and unused flows leaving the discharge chamber:

$$\eta_m = \frac{I_b}{Q_{out}+I_b} = \frac{I_b}{e\frac{\dot{m}_{dc}}{M}+I_b\left(1-\frac{T_{dc}}{T_{beam}}\right)} \tag{3-51}$$

where $Q_{out} = e\frac{\dot{m}_{dc}}{M} - I_{tot}T_{dc}$ is the unused flow leaving the discharge chamber, T_{dc} is the grid transparency in discharge-only mode, and $\dot{m}_{dc}$ is the reduced total mass flow rate without beam extraction. This last term should take into account the ingested flow from the background pressure of the vacuum chamber, which is ideally below 10% of the total mass flow rate injected. By experimentally measuring the ion currents reaching the grid plane, the grid transparency T_{dc} without beam extraction can be calculated as:

$$T_{dc} = \frac{\hat{I}_{beam\_dc}+\gamma_{i-n}\,\hat{I}_{accel}}{\hat{I}_{beam\_dc}+\hat{I}_{screen}+\hat{I}_{accel}} \tag{3-52}$$

where γ_{i-n} is the ratio of ions impacting the accel grid that successively leaves the grids as neutrals (e.g. it was equal to 0.55 in Ref. [80]). Finally, the simulated total mass flow rate $\dot{m}_p$ can be expressed as:

$$\dot{m}_p = \frac{I_b M}{e\eta_m} = \frac{\dot{m}_{dc}}{1-\eta_m\left(1-\frac{T_{dc}}{T_{beam}}\right)} \tag{3-53}$$

By using these two conditions and by measuring the ion current collected at the grids, it is possible to operate a thruster without beam extraction and to estimate the expected performance with beam extraction. This model has been demonstrated to be a reliable tool with different configurations [81], [82] running with xenon as the propellant. However, its applicability when used to predict the performance of thrusters using alternative propellants has yet to be demonstrated. The following modifications are expected to be necessary:

- The second similarity condition, $n_i\sqrt{T_e} = \hat{n}_i\sqrt{\hat{T}_e}$: needs to be re-derived for the mixture.
- Ion optics transparency, T_{beam}: different values are expected due to the difference in the alternative propellants' ion masses and the value of the transparency needs to be as accurate as possible to obtain the correct value of the simulated ion beam. Such value can be calculated using ion optics models as described in the next subsection.
- The ratio of ions impacting the accel grid that leaves the grids as neutrals, γ_{i-n}: is dependent on the configuration of the discharge chamber/ion optics (e.g. active grid

area, transparency to neutral atoms, ion velocity to the grid) and it is expected to be different from the value of 0.55 obtained in [80].

- Bias values for the “engine bias supply” and the “screen grid bias supply”: the ion current to the grid is a function of the bias applied to the grid and measurements away from the “knee” of the curve, where the ion current saturates, are required as demonstrated in Ref. [80].

Since the experimental campaign was carried out without beam extraction, the applicability of this technique and the validation of these hypotheses for alternative propellants were of fundamental importance in the analysis of the experimental data, as described in Chapter 5.

3.2.3 Ion Optics Models

As seen in Section 2.2.1, the three different stages (i.e. ionisation, beam extraction, and neutralisation) are strongly coupled but distinct in a GIE, therefore it is possible to develop models for each stage. In particular, the ion optics models focus on the high-energy beam ions extracted from the discharge chamber and these ions are the primary species in this kind of simulation, in contrast to the discharge chamber performance models, discussed in the previous section. A brief review of ion optics models is provided in Appendix B.3.

As described in the Appendix, several models have been developed in the past, but the code used for the simulations during the experimental campaign is the FFX model from CSU [1], which was made available by Mars Space Ltd. This code takes as inputs the ion optics geometry, the plasma density and the electron temperature at the grids, the grid potentials, the propellant utilisation efficiency, and the double-to-single current ratio (obtained either experimentally or via simulation) to self-consistently calculate the beamlet current, the current to the grids, and the lifetime of the ion optics. The FFX code has been successfully used and validated with measurements done on HiPEP and NEXT thrusters [83], [84]. In particular, a very good agreement was observed for the HiPEP thruster between numerically estimated (via FFX [84]) and experimentally measured [85] sensitivities, which show that most of the essential physics has been correctly included in the model.

The plasma density and electron temperature profiles used for the ion optics simulations were obtained experimentally using a single Langmuir probe as a diagnostics tool, as described in the next section.

Finally, it is worth highlighting that the FFX code cannot model the ion optics for a mixture of propellants because of the inherent difficulty of modelling the sheath’s behaviour in multi-species plasmas [86]. Consequently, the approach of applying the superposition principle

treating the two propellants as independent at the screen grid with the plasma parameters' profiles obtained with the Langmuir probe was not successful: an effective temperature profile was used and the ion density profile for the single propellant was calculated using the plasma neutrality principle (i.e. $n_e \approx \sum_j n_{i,j}$).

3.3 Plasma Diagnostic Tools: Single Langmuir Probe

In the previous sections, different discharge chamber analytical and numerical models have been described, but these models must be validated by comparison with experimental data. Therefore, measurements of plasma parameters (ions, electrons, and neutrals properties) are needed not only for validation purposes but also to further improve the performance and lifetime of GIEs thanks to a better understanding of the involved physical processes.

3.3.1 Use of Electric Probes for Discharge Chamber Measurements in GIEs

As described in Appendix C, the single Langmuir probe is the simplest and most widely used electrostatic diagnostics tool, and it allows the highest spatial resolution compared to the multiple-electrode versions. It gives the possibility to calculate the fundamental local plasma parameters (e.g. plasma density, electron temperature, floating potential, plasma potential) and, in addition, it can extract the primary electron density and energy with a suitable analysis method.

Therefore, the position of the probe is of great importance depending on the purpose of the investigation. In an operative GIE, plasma can be split into three regions: the coupling plasma area (immediately downstream of the cathode), the discharge plasma region (between the coupling plasma and the extraction grids), and the beam plasma region (downstream of the extraction grids). Consequently, the probe can be positioned:

- Around the area between the coupling plasma and discharge plasma [43], to understand how the population of primary electrons affects the performance of the thruster.
- Inside the discharge plasma region [87], to determine the dependence of plasma confinement and uniformity on the magnetic field configuration (especially valid for ring-cusp GIEs).
- At the interface between the discharge plasma and the ion optics [81], to verify the performance of the discharge chamber with different working conditions (e.g. magnetic field, mass flow rate, operating parameters).
- In the plasma plume [88], to measure spacecraft interaction, plume divergence, and ion beam properties.

For the diagnostic campaign with the small GIE, the third option has been chosen, which allows the measurement of plasma properties as close as possible to the grid plane; in fact, the other options were excluded for different reasons: the first one is mainly focused on the performance of the cathode, the second one on the behaviour of the plasma following modifications of the magnetic field, and the fourth one on the performance in the plume which would be irrelevant for this study since no beam was extracted during the experimental campaign. This solution allowed the evaluation of the impact of different propellants on the plasma properties at the screen grid, and the calculation of the plasma density and electron temperature profiles used for the ion optics simulations as described in the following subsection.

3.3.2 Calculation of EEDF and Determination of Plasma Parameters

As described in Section C.3.2, one of the methods for the estimation of the plasma parameters is to use the electron energy distribution function, which can be obtained from Druyvesteyn's formula and the second derivative of the I-V characteristic as (Eq. (C-2)):

$$F(\varepsilon) = -\frac{4}{e^2 A_{Lp}} \sqrt{\frac{mV_{Lp}}{2e}} \frac{\mathrm{d}^2 I_e}{\mathrm{d}V_{Lp}^2} \tag{3-54}$$

This method is applicable regardless of the size of the sheath, but the process of calculating the second derivative amplifies any noise present in the signal, and numerical smoothing techniques are required to obtain usable results. An example of a Langmuir I-V trace obtained from the experimental campaign is shown in Figure 12. Attempting to numerically differentiate the raw data produces extremely noisy results, which would make the method inapplicable. Consequently, before differentiation, a smoothing technique was applied and the Savitzky-Golay method was found to produce the best results (Figure 12)[89].

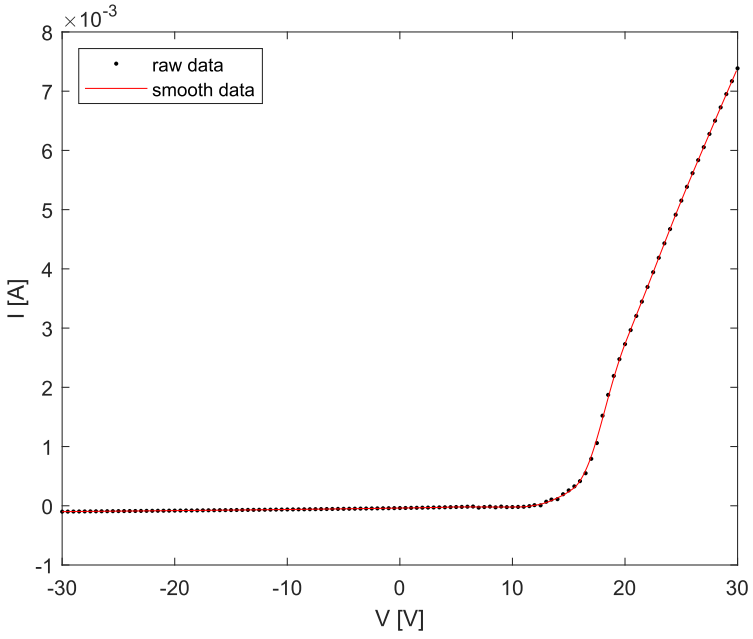

Figure 12 – I-V characteristic: raw data and smoothed trace

After the smoothing, the I-V trace was numerically differentiated using a second-order finite difference approximation. Since the differentiation amplifies the noise, the first derivative of the characteristic was smoothed again using the same technique as shown in Figure 13. The last step before calculating the EEDF is the calculation of the second derivative. Again, the first derivative was numerically differentiated and then smoothed in order to eliminate the noise that was amplified during the differentiation process as shown in Figure 13.

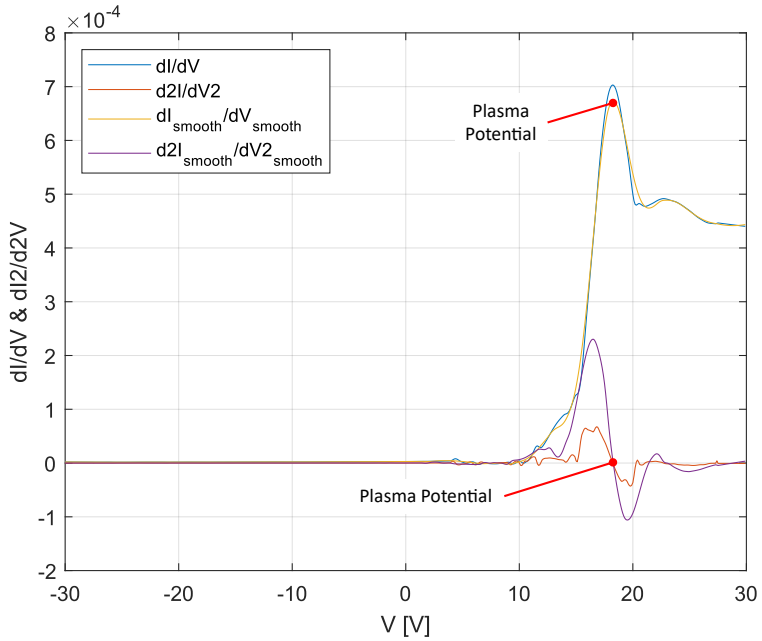

Figure 13 – 1st and 2nd derivative of the I-V characteristic and respective smoothed traces.

Finally, the plasma potential must be known to apply Druyvesteyn's formula because this method assumes that the applied probe bias potential is measured with respect to the plasma potential. Several methods can be used to determine the plasma potential, such as:

- In many cases, it is possible to locate the plasma potential directly from the I-V trace by locating the knee which indicates the transition from the exponential region to the electron saturation region. However, in some cases, such as the one under consideration, a knee is not easily distinguishable, and additional processing techniques are needed to evaluate the plasma potential.
- Plotting the natural logarithm of the measured current against the probe bias voltage makes it easier to analyse the exponential region, and the intersection of the lines drawn to fit the exponential and the electron saturation regions can be used to estimate the plasma potential.
- Finding the maximum of the computed first derivative of the I-V characteristic also allows for finding the value of the plasma potential (Figure 13). Due to the presence of noise in the data, this method can sometimes produce less reliable results, but

restricting the search area to a small window around the value obtained with the previous method can help improve the accuracy.

- Using the computed second derivative of the trace also allows the determination of the plasma potential (Figure 13), but the reliability of this method is inferior to the above ones because of the heavily processed dataset.

In this analysis, the first and second derivative methods have been used for all the datasets, but, in some cases of particularly noisy data, the curve fit method has been used to improve the reliability.

Once the plasma potential is extracted, the EEDF can be calculated using Eq. (C-2) and it is shown in Figure 14 for the I-V characteristics shown above. As described in Section C.3.2, the integration of the EEDF allows obtaining the plasma density (in m^{-3}) and the electron temperature (in eV) as follows:

$$n_e = \int_0^{-\infty} F(\varepsilon)\mathrm{d}\varepsilon \tag{3-55}$$

and

$$T_e = \frac{2}{3n_e}\int_0^{-\infty} \varepsilon F(\varepsilon)\mathrm{d}\varepsilon \tag{3-56}$$

In Figure 14, it is possible to notice that a part of the curve has negative values and, since negative probabilities are certainly nonphysical, this element represents a source of uncertainty for the results calculated using the EEDF.

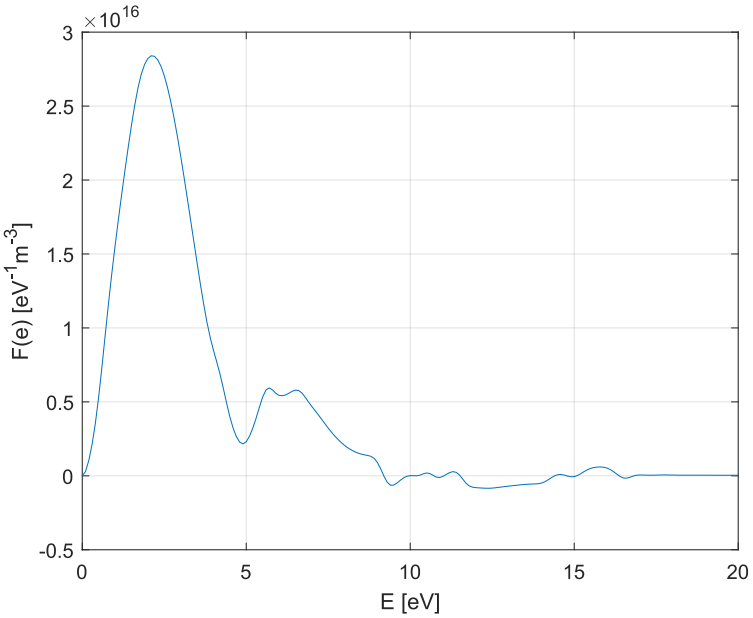

Figure 14 – Example of Electron Energy Distribution Function

Finally, during the analysis of the collected data, the electron temperatures calculated with the method described above showed evident incongruencies, especially in the case of particularly

noisy datasets. Therefore, the analysis was repeated using the "tangent" method, as described in Section C.3.2: in fact, the electron current within the transition region can be considered linear if plotted on a semi-log plot against probe bias and the electron temperature T_e is defined by the linear segment of the $[\ln I_e(V)]$-curve as follows:

$$T_e = \frac{k}{e}\left[\frac{\mathrm{d}(\ln I_e)}{\mathrm{d}V_{Lp}}\right]^{-1} \tag{3-57}$$

3.3.3 Langmuir Probe in Multi-Species Plasmas

In the previous subsection and Appendix C.3, the methods used for the calculation of the plasma parameters with a single Langmuir probe in single-species plasmas were described. This subsection focuses on the techniques used for the calculation of the same parameters in multi-species plasmas, such as the mixture of xenon/krypton considered in this work.

Similarly to the case when a single species is present, multi-species plasmas are nonequilibrium plasmas since the electrons are not in energy equilibrium with ions and neutrals having an electron temperature T_e which is usually much (orders of magnitude) greater than the neutral and ion temperatures, T_g and T_i respectively [90]. The procedure to extrapolate the plasma parameters (i.e. plasma and floating potential, plasma density and electron temperature) in a multi-component plasma is equal to that widely used for single species plasmas [91], [92] by calculating the EEDF with the Druyvesteyn's technique. However, the electron energy distribution in the case of multi-species plasmas is generally non-Maxwellian and the electron temperature can be thought of as an effective electron temperature T_{eff} corresponding to a mean energy determined from the EEDF [90], [91]. This electron temperature is inversely proportional to the ionisation cross-section of the propellant: since the ionisation cross-section of xenon is bigger than that of krypton, the addition of xenon in the Xe/Kr mixture increases the probability of inelastic collisions of electrons and, therefore, a decrease in the effective electron temperature is expected compared to the case with pure krypton.

3.4 Summary

Gridded ion engines have a long-flight heritage, and their working principles are well-known and understood, allowing reliable prediction of their performance and lifetime via numerical simulation. This chapter presents the formulas for the evaluation of the performance parameters of GIEs with a particular focus on the impact of the propellant atomic mass on these parameters at a first-order approximation. Subsequently, a brief description of the performance models (for discharge chamber, discharge-only operations, and ion optics) used

within this work is given showing that, since they were developed to be used with xenon, they might be adapted and modified to be used with alternative propellants.

Furthermore, it is essential that the outputs of these models can be compared with experimental data. Therefore, measurements of plasma parameters (i.e. ions, electrons, and neutrals properties) are required not only for validation purposes, but also to further improve the models thanks to a better understanding of the involved processes. Even though a comprehensive method for the determination of all the plasma parameters does not exist, Langmuir probes were used during the experimental campaign, since they are the simplest and most versatile tool for the investigation of different plasma parameters, such as electron energy distribution function, plasma density, plasma potential, and electron temperature.

Finally, all the concepts presented throughout the chapter were reevaluated to account for the use of alternative propellants and of the mixture, and the required modifications were highlighted.

The next chapter will focus on the experimental setups used during the testing campaign by describing the facilities, systems, and diagnostics.

Chapter 4 Experimental Setup

This chapter provides an overview of the two experimental configurations, including the description of the vacuum facilities, experimental arrangements, and diagnostic setups utilised for the operational characterisation of a ring-cusp discharge chamber and a hollow cathode with different propellants. Finally, the testing procedures followed during the testing phase are outlined.

4.1 Experimental Setups

The experimental campaign, which allowed the evaluation and quantification of the impact of propellants alternative to xenon (i.e. krypton and Xe/Kr mixture), was performed using two different setups:

- a prototype model of a small GIE
- a hollow cathode.

A description of the two setups, facilities, and experimental arrangements is provided in the following subsections.

4.1.1 Ring-Cusp Discharge Chamber Testing

Typically, GIEs are categorised as, based on the diameter of the discharge chamber [72]:

- miniature (<5 cm),
- small (5-10 cm),
- conventional (10-30 cm),
- large (>30 cm).

Based on their experience with the development of a large ring-cusp discharge chamber (RCDC) [81], [93], Mars Space Ltd (MSL) has designed and manufactured a small RCDC with an extraction grid diameter of 10 cm, which was made available for testing with alternative propellants at MSL's facilities.

The choice of testing the 10-cm RCDC is based on the following reasons:

- Limited data exist in the literature on alternative propellants in combination with this type and size of thrusters.
- This was the only available thruster within the scope and timeframe of this research.

- This size of thrusters should benefit the most from the switch to alternative propellants within the growing development of 'mega-constellations' of satellites within the 'New Space' approach, as also described in a recent publication by the author on mission cost analysis [19].
- In Europe, two of the thrusters with space-flown heritage are the ArianeGroup's RIT10EVO (RF-type) and QinetiQ's T5 (Kaufman-type), and both have an active beam diameter of 10 cm.

The discharge chamber's shape, and the number and position of the magnet rings are similar to other thrusters of this size present in the literature [72]. A schematic of the discharge chamber with the position of the magnets is shown in Figure 15: two magnet rings are positioned along the straight part of the discharge chamber and one along the conical section.

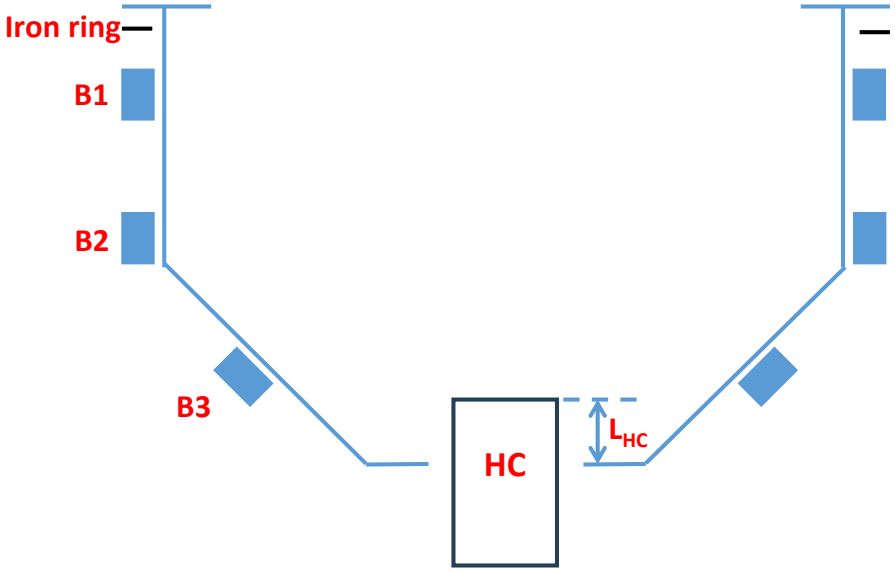

Figure 15 – Schematic of the discharge chamber (reference only)

Because of limitations on the pumping speed of the available vacuum chamber, the discharge chamber run in discharge-only mode without beam extraction using Brophy's method as described in Ref. [80] and in Section 3.2.2, so no neutralisation of the beam was required, and the injected mass flow rate is lower than that necessary for operation with beam extraction. In addition, the ingested gas from background pressure was calculated to be lower than 10% of the total mass flow rate injected through the discharge chamber during the experiment, which is a more than acceptable value.

The discharge cathode used for this experimental characterisation is a scaled-down version of MSL's existing hollow cathodes, such as the one used for the tests in diode mode and described in more detail in the following section. The hollow cathode used for the characterisation features a barium oxide (BaO) impregnated tungsten emitter, and the orifice diameter of the cathode was kept constant for the tests with xenon and the alternative propellants.

4.1.1.1 Vacuum Chamber

The small RCDC was tested inside the MSL-VC1 vacuum chamber, shown in Figure 16. It consists of a stainless-steel L-shaped chamber, 0.52 m in diameter and 1.2 m long, which is equipped with the following pumping system:

- an Edwards xDS35i dry scroll pump for low vacuum with a pumping speed of 35 m^3/h was used to bring the chamber pressure down to $5x10^{-2}$ mbar and as a backing pump for the turbopump;
- an Edwards STP-iXA4506C turbo-molecular pump for high vacuum, which gives an effective xenon pumping speed of 3000 L/s and achieves a base pressure below $1x10^{-7}$ mbar.

The pressure inside the chamber was measured by a calibrated Kurt J. Lesker KJLC 354 Series Ion Gauge, with pre-configured correction factors for the gases used, which covers the high vacuum pressure range.

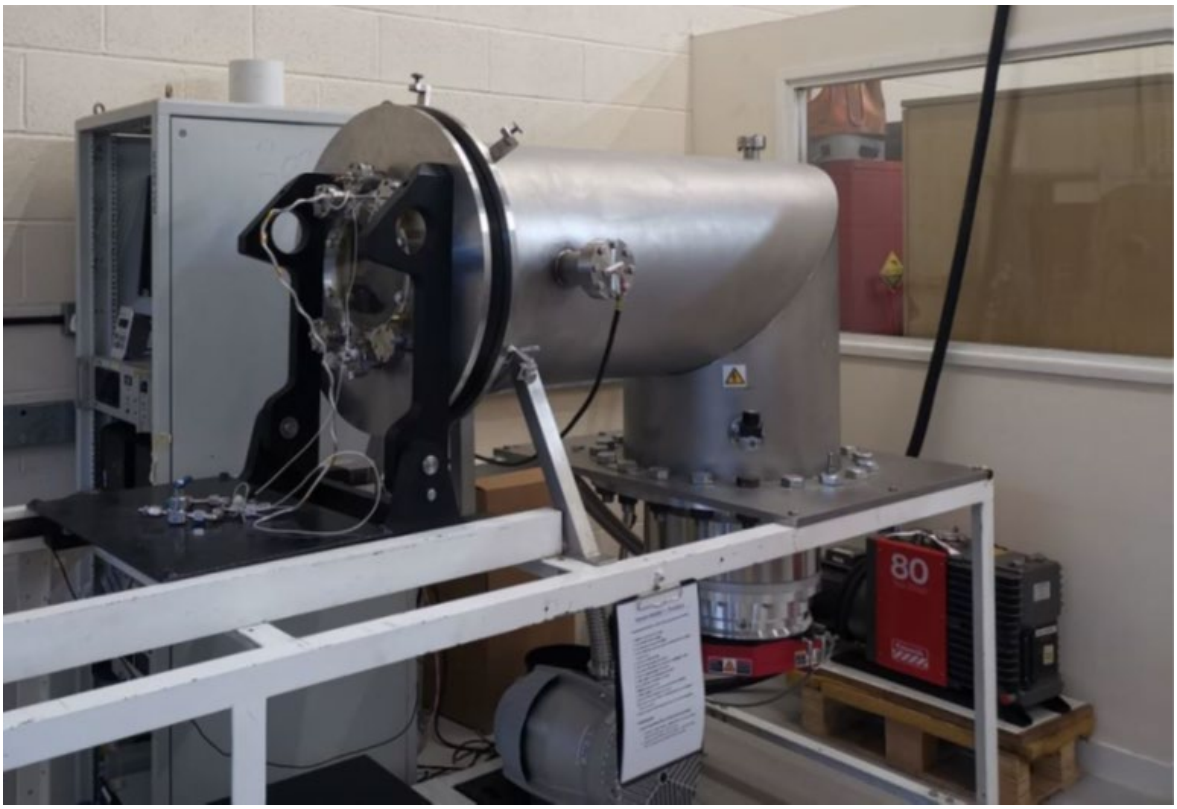

Figure 16 – VC1 vacuum chamber in MSL propulsion laboratory

4.1.1.2 Fluidic Setup

A Fluid Ground Support Equipment (FGSE) was designed and assembled by the author to be used during the test campaign to supply the gas inlets (i.e. main and the hollow cathode) of the discharge chamber with xenon and krypton at the desired flow rate, as shown in Figure 17.

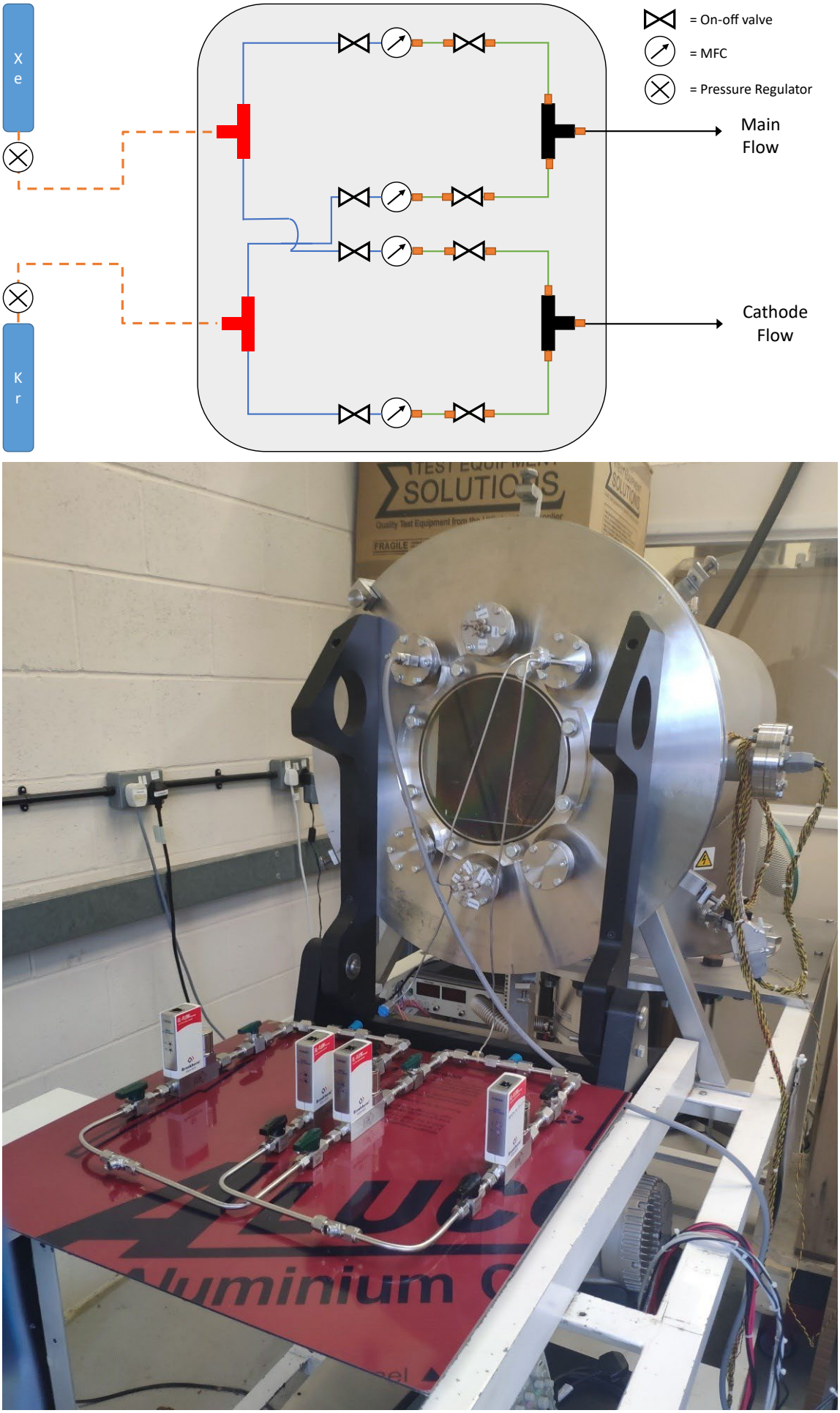

Figure 17 – Test fluidic setup

Xenon and krypton were supplied from two independent cylinders equipped with their pressure regulators, which maintain a constant upstream (i.e. up to the mass flow controllers, MFCs) pressure of 2.5 bar during the test. Two pairs of Bronkhorst factory-calibrated MFCs were used to regulate the flow rate to the cathode and discharge chamber independently within the following flow rate ranges:

- for the cathode line: two MFCs with a range of 0-10 sccm and calibrated for Xe and Kr
- for the main line: two MFCs with a range of 0-5 sccm and calibrated for Xe and Kr.

Furthermore, this setup was designed to allow the testing of a mixture of xenon and krypton at the desired mixture ratio.

Moreover, all air-side FGSE piping is 1/4" stainless steel with Swagelok connectors used on the high-pressure joints and with Swagelok VCR seals used on the low-pressure joints to minimise the risk of air leaks. Finally, a series of on-off manual valves are in place to enable the isolation of various parts of the FGSE.

4.1.1.3 Electrical Setup

MSL's Electrical Ground Support Equipment (EGSE) was used for the test campaign, and it consists of a dedicated rack comprising of:

- Several power supplies rated and interconnected to supply the GIE with the power it needs to operate;
- A digital multiplexer monitoring currents, voltages and temperatures (via thermocouples) used to measure the status of the GIE;
- A dedicated hardware protection system operating independently to disable the power supplies with a hard shutdown to protect both the hardware and the personnel.

The schematic of the electrical setup is presented in Figure 18 and it is similar to the one used by MSL in previous experiments [81], which is based on the one used by Brophy [80] (see Figure 11 in Section 3.2.2). This setup allows the operation of the discharge chamber without beam extraction and estimates the expected performance with beam extraction by measuring the ion current collected at the grids.

The main characteristics of this setup are:

- The discharge chamber body is electrically isolated from the vacuum chamber, which is connected to the facility ground.
- The cathode heater is operated when required using the keeper supply, which will be switched to the heater line via a dedicated relay.

- The screen and accel grids can be biased at various potentials using a dedicated grid supply to repel electrons while allowing the measurement of the collected ion current.
- The cathode (i.e. negative of the anode supply) is connected to an "engine bias" supply which allows biasing of the engine up to 20 V positive with respect to the ground in accordance with Brophy's method to avoid the escape of electrons from the discharge chamber volume. The residual ion beam leaving the discharge chamber is expected to be in the order of tens of mA.

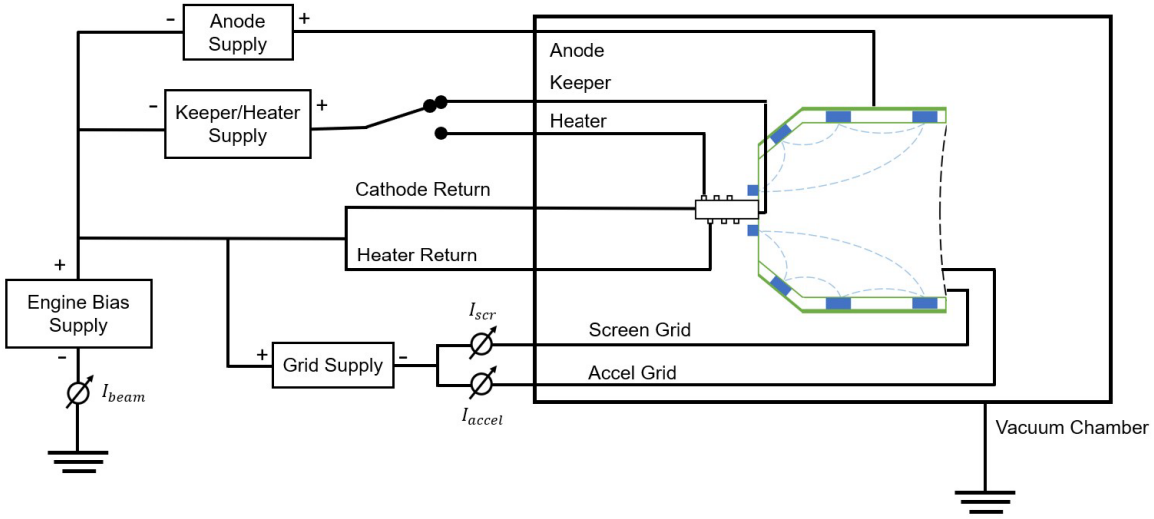

Figure 18 – EGSE setup (without beam extraction)[81]

In Figure 18, all voltages and currents are recorded directly and independently from the relative power supplies via the multiplexer. In addition, two differential probes whose signal is acquired by an oscilloscope are used to monitor the voltage and the associated peak-to-peak noise of the cathode keeper and the anode relative to the cathode.

Finally, all the discharge chamber control commands and data acquisition are done using a LabView program which communicates with the instrumentation (i.e. multiplexer, oscilloscope, power supplies, and MFCs) using USB/RS232 connections. In addition, optocouplers are used to isolate the control system from electrical discharges caused by the test apparatus. The original program was written by MSL, but it was modified by the author to account for the particular FGSE setup.

4.1.2 Hollow Cathode Testing

The hollow cathode experimental campaign was carried out at the University of Southampton's TDHVL facilities. The hollow cathode (model name MSL_HC40), which was previously purchased from Mars Space Ltd, is optimised for a discharge current of 40 A at 20 sccm of xenon, but its flexible design allows operations at different operational points in terms of discharge current (from 40 A to 5 A) and mass flow rates in order to minimise the discharge

power [94]. A schematic diagram and an actual picture of the device are shown in Figure 19. The cathode uses a LaB_6 insert instead of the conventional tungsten-impregnated emitter because it has little to no susceptibility to oxygen poisoning which is a great advantage when several configurations need to be tested by removing the requirement for long outgassing procedures and allowing the use of lower-purity gases. LaB_6 inserts are also cheaper, but they cannot be in direct contact with many refractory metals because of chemical reactions at high temperature (i.e. boron diffusion) that can cause embrittlement in the metals. In addition, the LaB_6 work function is higher resulting in a higher working temperature for the same emitted current density.

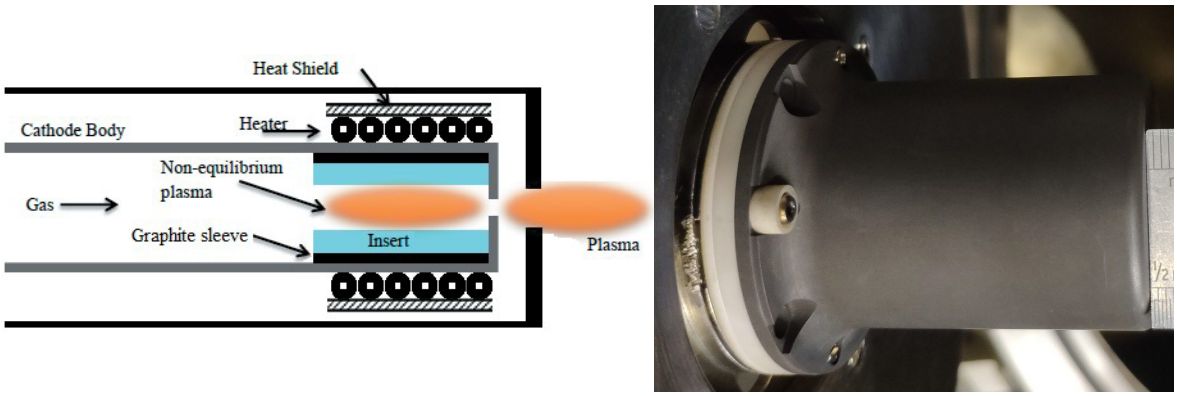

Figure 19 – General schematics of a hollow cathode [94] and picture of MSL_HC40

The hollow cathode consists of a stainless-steel mounting flange which is attached to the chamber mounting system using bolts which are electrically isolated with ceramic bushes. A 1/8” pipe is electron beam welded to the rear of the mounting flange and this pipe is connected to a ceramic isolator upstream, which is then connected to the main propellant line of the chamber. The cathode body (i.e. the tube containing the insert) is made of tantalum and is bolted to the mounting flange. The LaB_6 emitter is pushed to the end of the cathode body and its dimensions are 15 mm in length, 3.8 mm inner diameter, and 7 mm outer diameter. A thin graphite sleeve is used to mechanically separate the emitter from the tantalum tube to avoid the above-mentioned boron diffusion issues while maintaining the electrical connection. A graphite orifice disc is positioned between the end of the cathode body and the emitter, and its dimensions are 1 mm thickness and 1 mm nominal orifice diameter. The advantage of using this disc is that it can be substituted with similar discs having smaller or bigger orifice diameters, so that different configurations can be tested. The cathode body is surrounded by the heater and a multi-layered tantalum thermal shield is wrapped around it to decrease radiative thermal losses and improve thermal efficiency. A graphite casing is then used to support the thermal shield in place. The keeper electrode which encloses the entire assembly is made of graphite for its low sputter yield, and it is bolted to the stainless-steel base of the cathode with an insulating ceramic disc and with ceramic alumina washers to prevent short-circuiting of the electrodes. Ceramic discs with different thickness are present and stacking and/or removing them allow

changes in the distance between the cathode tube and the keeper for further flexibility during testing.

4.1.2.1 Vacuum Facility

The hollow cathode was tested in diode mode utilising TDHVL-VC1, shown in Figure 20. This is an ultra-high throughput bi-turbo cylindrical chamber, constructed from 404 stainless steel, and it is 1.2 m long and 0.6 m in diameter. The chamber has a 10 cm port on one end and a hinged door for quick access on the other end. The door has an ISO mounting point on the inside for experimental apparatus mounting, several ports for electrical/gas feedthroughs through the door, and more ports around the cylindrical surface. The pumping system consists of:

- an Edwards E2M40 oil-based mechanical pump for low vacuum used to bring the chamber pressure down to $5x10^{-2}$ mbar and as a backing pump for the turbopumps;
- two ultra-high throughput Edwards STP-iXA4506C turbomolecular maglev pumps giving a combined pumping speed of 8600 L/s of N_2 and reaching a base pressure below $1x10^{-8}$ mbar (unbaked).

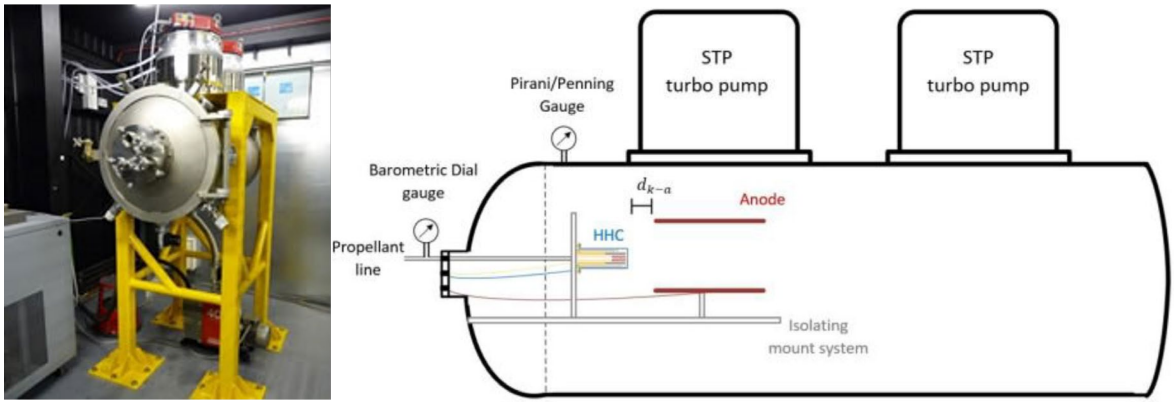

Figure 20 – Photo and drawing of the TDHVL-VC1 (pre-modifications)[95]

The pressure inside the chamber is measured by two gauges:

- a calibrated Edwards APG-M Active Pirani Gauge, with an Edwards active gauge controller, for low vacuum pressure range,
- a calibrated Kurt J. Lesker KJLC 354 Series Ion Gauge, with pre-configured correction factors for the gases used, for high vacuum pressure range.

The original setup with the hinged door was redesigned and modified to accommodate a sliding door, as shown in Figure 21.

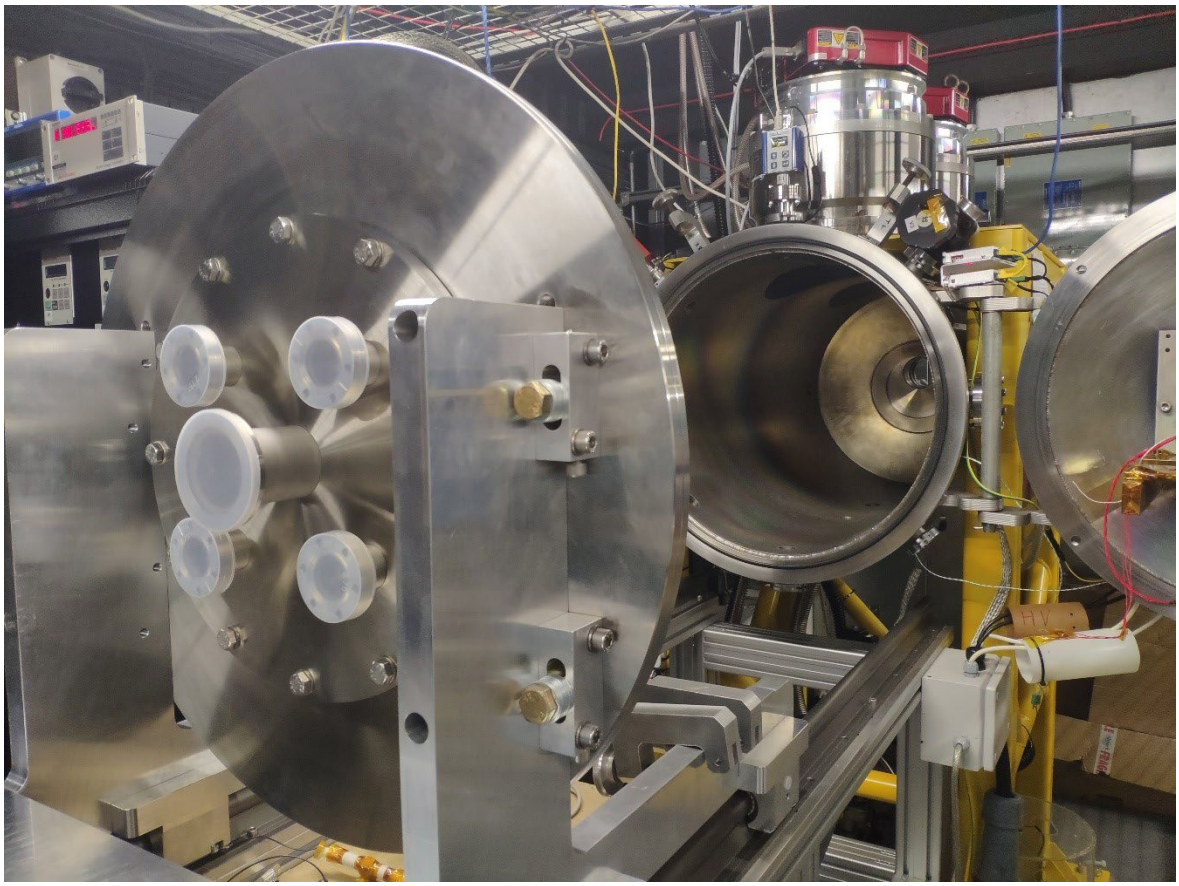

Figure 21 – VC1 setup with a sliding door

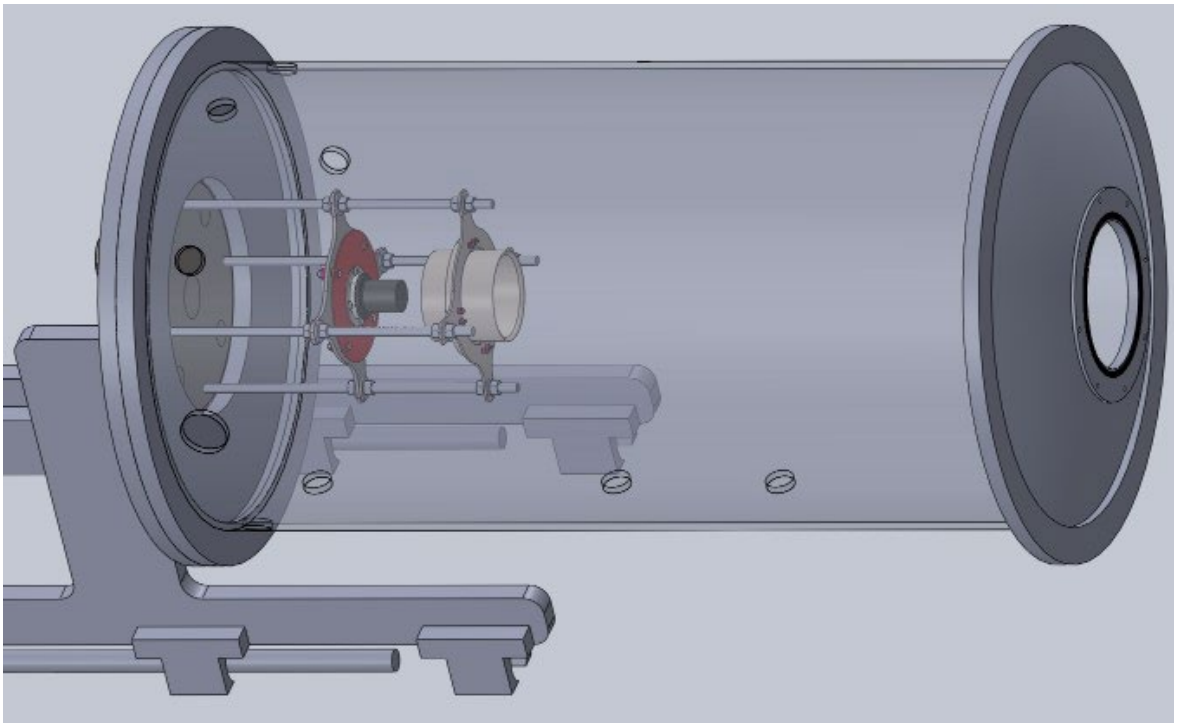

Figure 22 – New door mounting system

In fact, the use of the sliding door allowed changing the way the setup is supported: the cathode-anode setup is connected to the sliding door flange via four stainless steel threaded bars as illustrated in Figure 22. This modification allows easier access to the various parts of the

setup and gives more flexibility (e.g. changing the relative distance between cathode and anode) compared to the configuration with the platform which was used with the hinged door.

This setup was further developed and improved with the addition of a frame made out of aluminium profiles (Figure 23) allowing the installation of various motion mechanisms (i.e. stepper motors, linear translation stages) and diagnostic tools (e.g. webcam, Langmuir probe, E×B probe, pyrometer (not visible in the figure), etc.). A significant advantage of this setup is that it decouples the hollow cathode from the diagnostic equipment allowing modifications to either of them independently. Therefore, this final setup represents a comprehensive and flexible platform for the test of various cathode configurations.

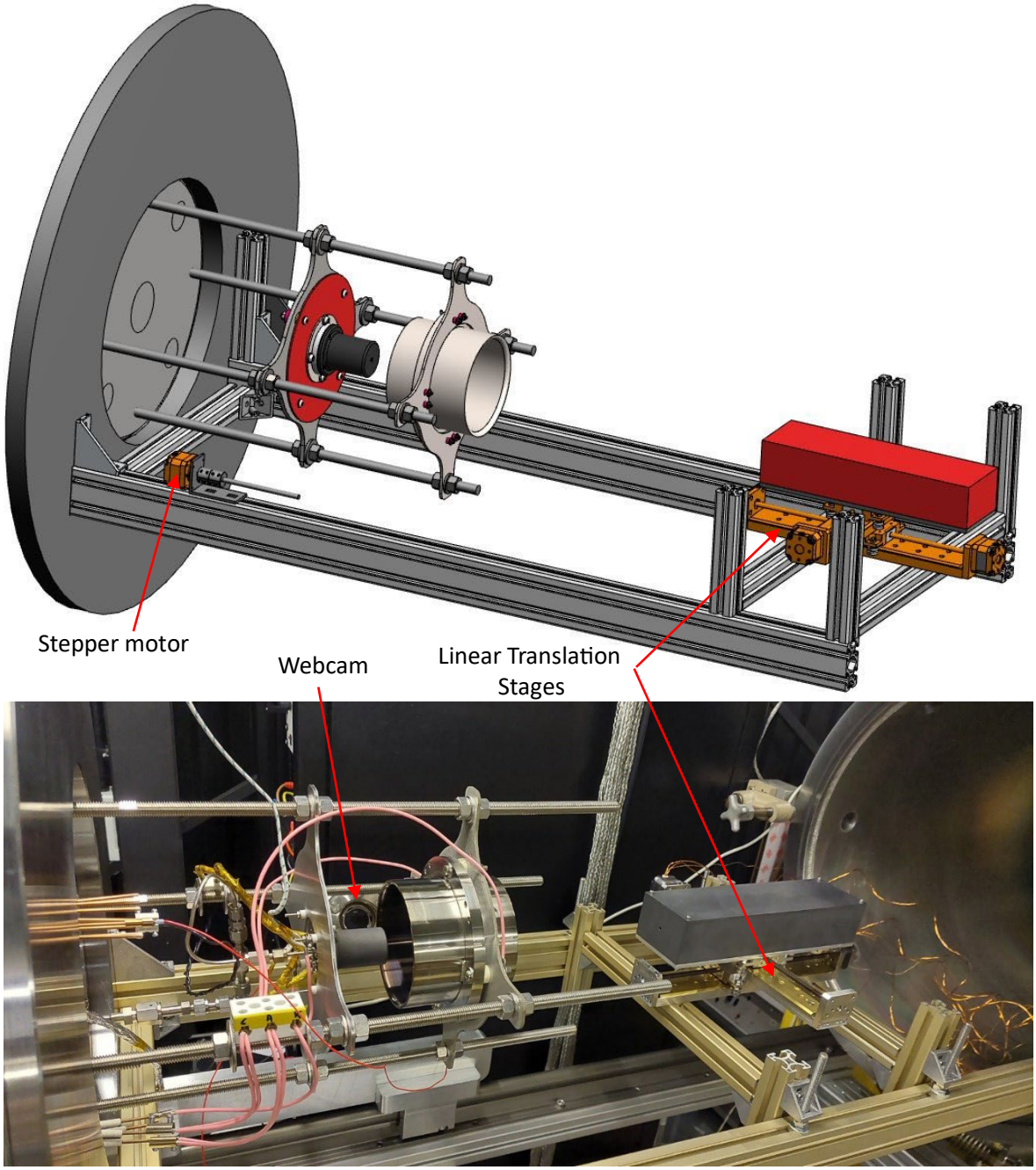

Figure 23 – Final setup with the addition of aluminium structure

4.1.2.2 Fluidic and Electrical Setup

A Fluidic Ground Support Equipment (FGSE), shown in Figure 24 and similar to the one assembled for the thruster setup described in Section 4.1.1.2, was designed and set up to supply the hollow cathode with the required gas at the desired flow rate. Two pressure regulators (one for each bottle) maintain a constant upstream pressure of 1.5 bar during the test. The flow rate to the cathode is controlled with two Bronkhorst mass flow controllers (MFCs) which are factory calibrated with an accuracy of ±0.5% read value plus ±0.1% full-scale value:

- a MFC for xenon with a full-scale value of 20 sccm, and
- a MFC for krypton with a full-scale value of 100 sccm.

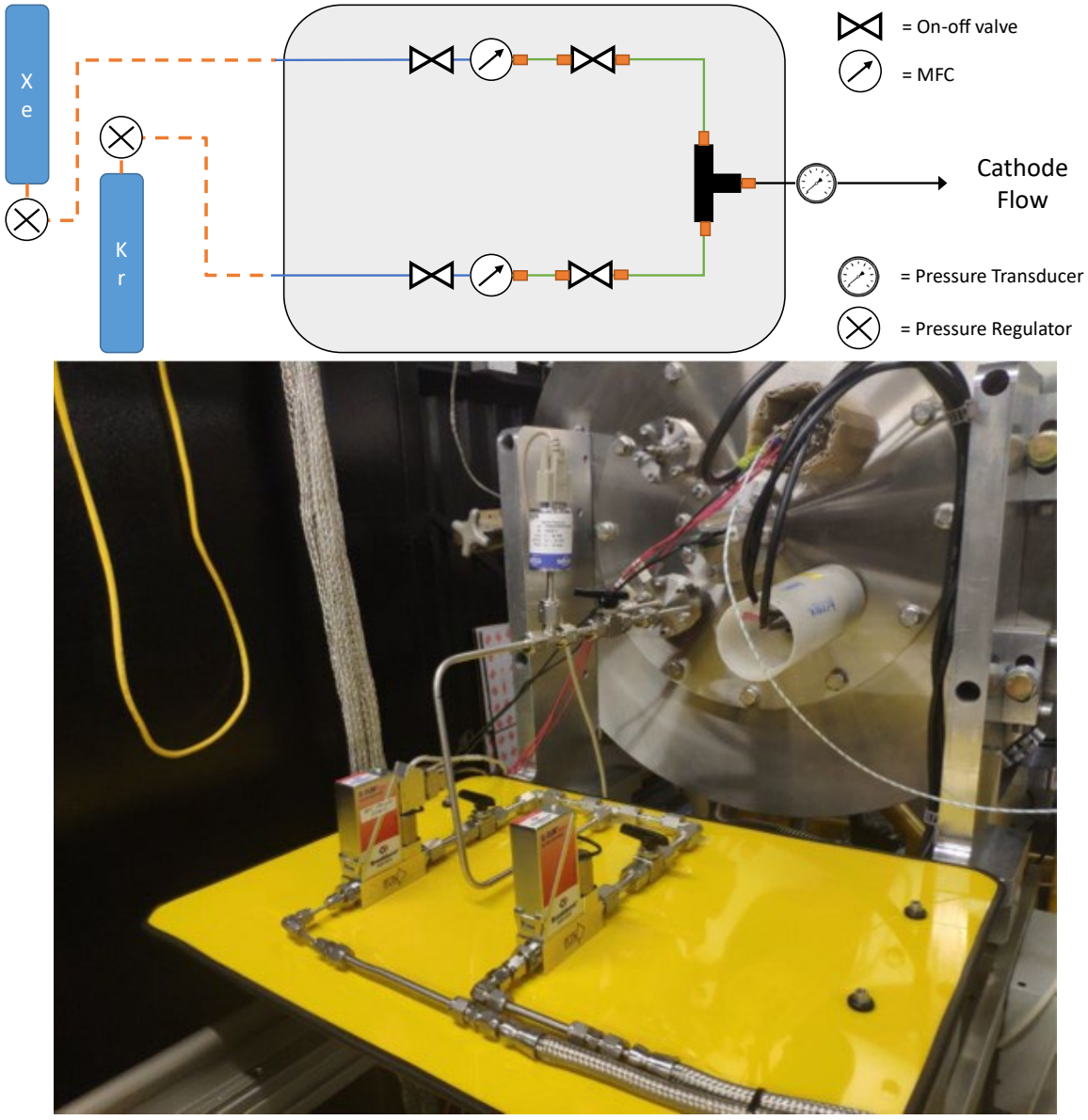

Figure 24 – Fluidic setup for testing with mixtures

Downstream of the MFC, 1/4” stainless steel piping with VCR seals is utilised to minimise the risk of air leak contamination. A series of on/off manual valves are in place to enable the

isolation of various parts of the FGSE. Furthermore, a Setra Model 730 pressure transducer was placed between the T-junction and the feedthrough for the measurement of the inline pressure, but, due to the limited range (0-20 absolute mbar) and the high flow rates, the device was out-of-scale most of the time during the tests and the logged data were of little use for the analysis. For the testing conducted in the study, xenon and krypton of 99.999% minimum purity (N5.0) were utilised.

When the cathode is operated in diode mode, electrical connections to the cathode body, to the heater, and to the anode are required. An overview of the Electrical Ground Support Equipment (EGSE) utilised for the tests is shown in Figure 25 and it consists of a dedicated rack comprising of:

- an EA PSI-5200-10 (output 200 V, 10 A) for the heater,
- an EA PS-9750-12 (output 750 V, 12 A) for the keeper,
- an EA PS-9200-70 (output 200 V, 70 A) for the anode,
- two sense DMMs to measure anode and keeper's voltages with higher accuracy.

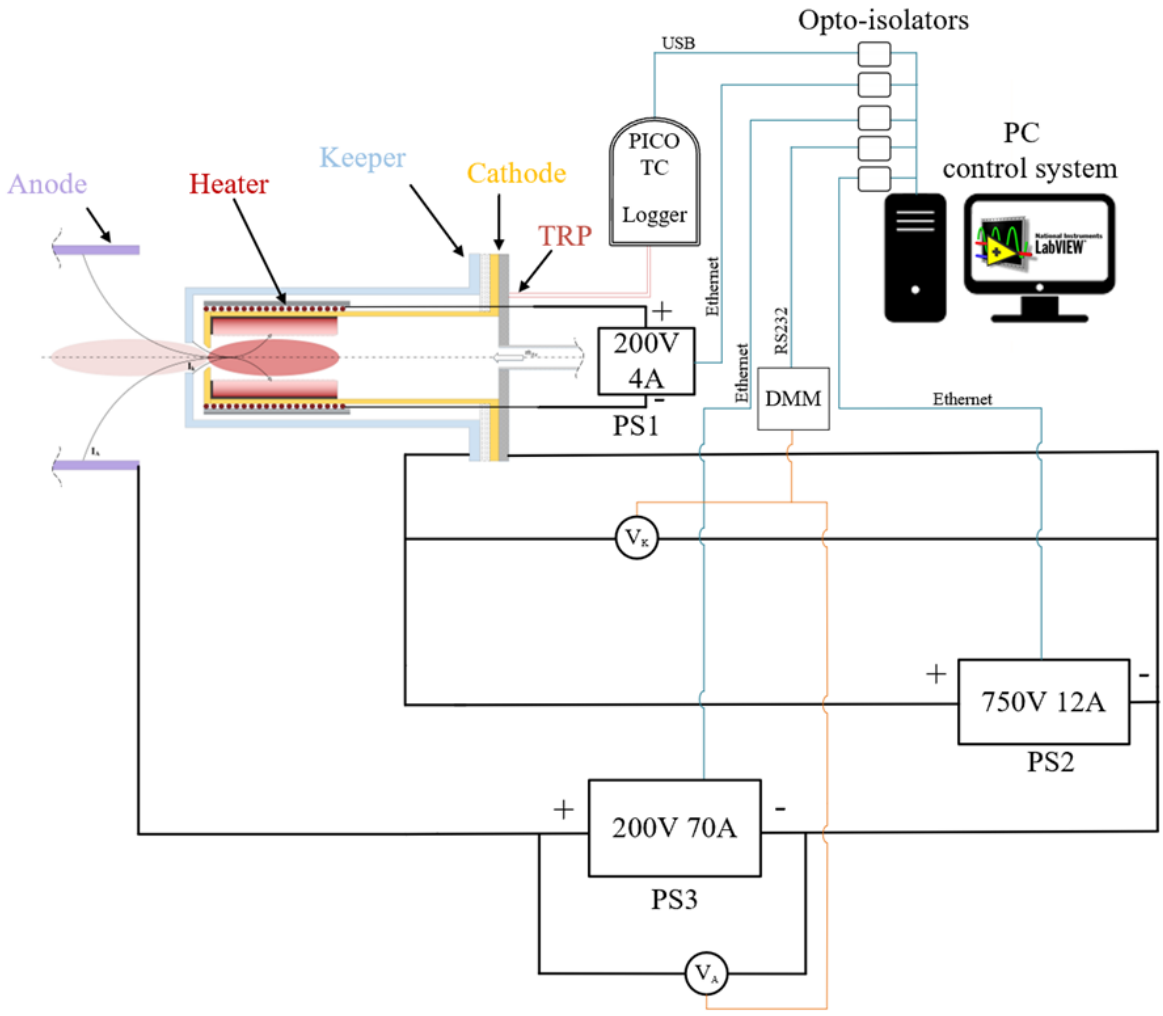

Figure 25 – Electrical schematic of the diode-mode setup

Furthermore, a Temperature Reference Point (TRP) is measured with Type-K thermocouples, which are located at the cathode base, to evaluate the thermal stability of the cathode before collecting the data points.

All the instrumentation (i.e. power supplies, MFCs, and pressure gauges) is connected to a PC and is controlled and logged using a LabView program at a sampling rate of 1 Hz. In addition, since electrical discharges can cause interference to the PC control system, all the interfaces between the control system and the test apparatus are isolated using inline USB/RS232 optocouplers.

4.2 Diagnostic Setup

A key objective of this study is to map the plasma parameters (i.e. electron temperature, plasma potential, and plasma density) and their spatial distribution inside the discharge chamber and in the hollow cathode's plume in order to evaluate the impact of using different propellants. The plasma diagnostics is performed via a single Langmuir probe, whose review and theory of operation are described in Appendix C.3. In the following subsections, a detailed description of the probe design and setup is provided for the two different configurations.

4.2.1 Langmuir Probe Design

A list of some of the possible effects (e.g. magnetic field effects, end effects, EEDF anisotropy), which can affect the analysis of the probe characteristic and should be considered in sizing the probe, is given in Appendix C.3. However, in practice, it is not possible to take into account all the possible effects, especially since most of them depend on the plasma parameters being investigated. On the other hand, some of these effects can be mitigated during the design phase and with an opportune positioning during the experiments.

In the RCDC configuration, the Langmuir probe was provided by MSL, since it is integrated within the design of the discharge chamber and a brief description is provided in the following subsection.

For the testing of the hollow cathode in diode mode at the TDHVL facilities, a Langmuir probe was designed and built, and the schematic of the probe construction and a photograph of the completed probe are shown in Figure 26. The probe was constructed from 0.1 mm diameter tungsten (99.95% purity) wire inserted through a series of single-bore tubes. The first two tubes are made of 99.8% alumina (Aluminium Oxide, Al_2O_3) measuring 30 mm in length with an outer diameter of 0.5 mm and an inner diameter of 0.2 mm, and 100 mm in length with an outer diameter of 1 mm and an inner diameter of 0.5 mm, respectively. The smaller tube is inserted

into the bigger one by 5 mm in length and it is kept in place by friction. The third tube is made of quartz with an outer diameter of 3 mm, an inner diameter of 1.5 mm and a length of 60 mm. The second alumina tube is inserted into the quartz tube 10 mm in length, and it is fixed in place using Kapton tape. All the materials (i.e. tungsten wire, alumina and quartz tubes) were chosen because of their high melting point and low secondary electron emission. To connect the tungsten wire (which is very small and cannot be soldered) to the external circuit, two bare terminal blocks were used: the first one has a structural function, which is to avoid movements of the wire inside the quartz tube, with one screw tightened onto the quartz tube and the other screw tightened onto tungsten wire; the second terminal is used for the electrical connection, with one screw tightened onto the tungsten wire and the other screw onto a single core copper wire. The exposed wire at the tip of the probe was cut to a length of 1.5 mm using a scalpel blade and checked using an optical microscope.

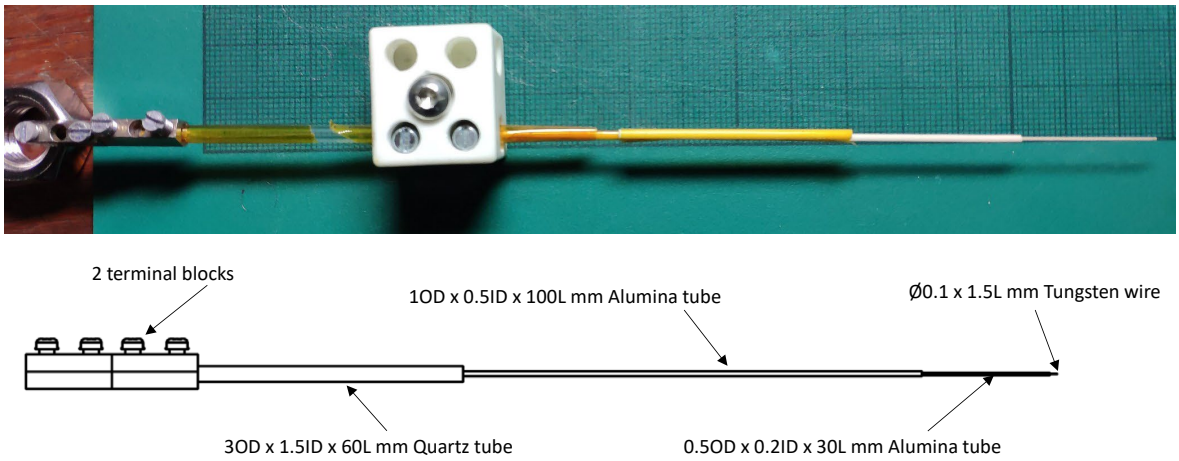

Figure 26 – Schematic and picture of the Langmuir probe for HC testing

The probe dimensioning was dictated by the design and operational considerations previously cited: the diameter of the probe allows the application of the collisionless theory and its length to minimise the end effects, which will be further reduced by positioning the probe perpendicularly to the plasma plume. In addition, no magnetic fields are present during the hollow cathode testing removing any related effects.

4.2.2 Langmuir Probe Operation: Probe Positioning and Acquisition Systems

As introduced in Section 4.1, two different experimental setups were used for the testing of alternative propellants and, as a result, two different diagnostic configurations were adopted as described below.

4.2.2.1 Ring-Cusp Discharge Chamber Configuration

In the case of the test with the small ring-cusp discharge chamber at MSL's facilities, the Langmuir probe was positioned as close as possible (i.e. 5 mm inside the discharge chamber) to

the grid plane to allow the measurement of the plasma parameters to verify the performance of the discharge chamber as described previously in Section 3.3.1. The LP consisted of a 0.125 mm diameter tungsten wire inserted through a thin L-shaped alumina tube with a small tip of 1.25 mm length exposed to the plasma. Additionally, the probe's axis of rotation will be positioned offset with the discharge chamber axis allowing the collection of data from one periphery of the discharge chamber to the other passing through the central axis, as shown in Figure 27. To obtain this change of the probe's angular position inside the discharge chamber, the LP was connected to a rotating stepper motor suitable for vacuum operations positioned behind the discharge chamber; the spatial positions of the Langmuir probe have been selected to have a resolution of 2 mm along the discharge chamber radius: from the initial position which is the outer position of the probe, the probe is moving clockwise crossing the centre of the discharge (front of the cathode) and at the end coming back to its original position by rotating counter clockwise. It is important to note that the probe position needs to be fixed when performing the measurements (i.e. the voltage scan). Furthermore, the alumina tube containing the LP needed to be inserted in the discharge chamber minimising any possible gas leak, for example using another short alumina tube fixed to the upstream wall of the discharge chamber (Figure 27).

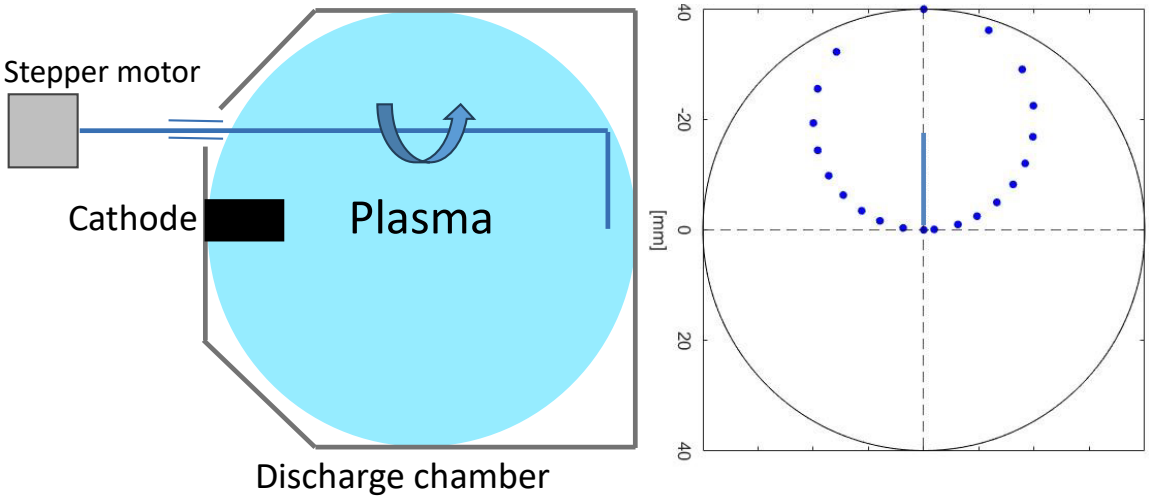

Figure 27 – Single Langmuir probe setup for the small RCDC configuration

Since strong magnets surround the discharge chamber, the presence of magnetic fields could have a relevant effect on the probe current collection, but, in this case, their impact is reduced because of the position of the probe in the proximity of the extraction grids, where the magnetic field strength is in the order of few tens of Gauss at most. In fact, the electron gyroradius is much bigger than the probe radius, therefore the curvature of the electron trajectory can be neglected, and unmagnetised probe theory can be applied. In addition, the EEDF can be considered isotropic since the ratio between the magnetic field and the pressure inside the discharge chamber is below the critical threshold, as described in Section C.3.3.

During a measurement, the LP is biased with respect to anode potential using a Keithley 2400 SourceMeter (SMU) power supply, and the current collected by the probe is measured by the same SMU. The bias voltage is swept from a suitable low voltage (i.e. -50 V) to capture adequately the ion saturation region to a few volts above the discharge voltage (i.e. 6 V) to capture the electron saturation region; the electron density and electron temperature are extracted from the I-V characteristics using the Druyvesteyn technique [96]. One spatial sweep takes approximately 30 minutes to complete. Furthermore, a ballast resistor of 100 Ω was included in the LP circuit for stabilisation and noise reduction. The entire setup (i.e. rotation stage motor, probe bias voltage supply, and SMU) is controlled by a LabView routine to produce an automated measurement system. The stored data can be saved as a CSV file and then imported into MATLAB for analysis using one or more methods described in Section 3.3.2.

4.2.2.2 Hollow Cathode Configuration

For the testing of the hollow cathode in diode mode at the TDHVL facilities, an initial Langmuir probe positioning system, which was used as part of a commercial testing activity, was built and it consisted of a ceramic terminal block (Figure 26) screwed onto a custom-made “slider” and with the probe screwed in place in one of the connectors (Figure 28). This “slider” was then screwed onto one of the threaded bars (Figure 22) allowing for modification of the distance and the angular position of the probe tip with respect to the cathode orifice.

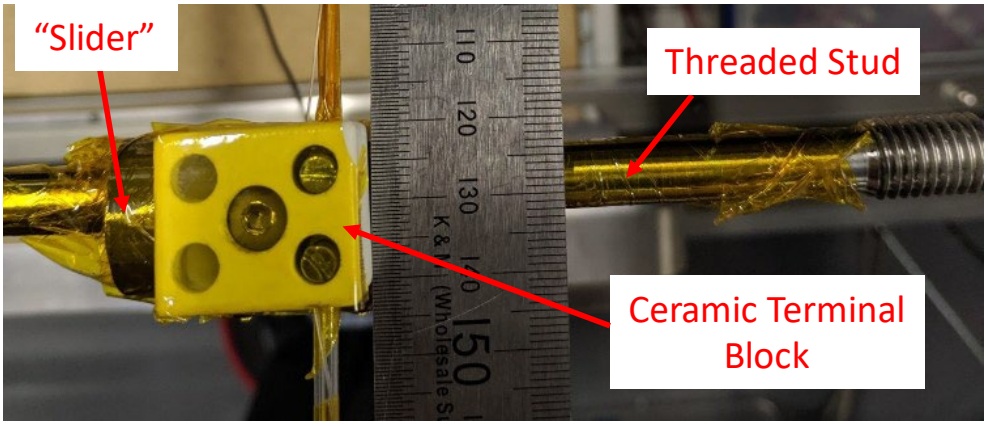

Figure 28 – Initial LP positioning system

After the conclusion of the commercial testing campaign, a new positioning system for the Langmuir probe has been designed (Figure 29) to take advantage of the new aluminium frame described in Section 4.1.2.1. The new system includes a rotating stepper motor which allows changing the position of the probe during the experiment without opening the vacuum chamber door. Furthermore, this system allows moving the probe away from the plasma plume when data are not collected and, consequently, preserving the integrity of the probe from particle bombardment and, hence, extending its lifetime. The probe is connected perpendicularly to the extension rod which is connected to the stepper motor via a fixed beam coupling.

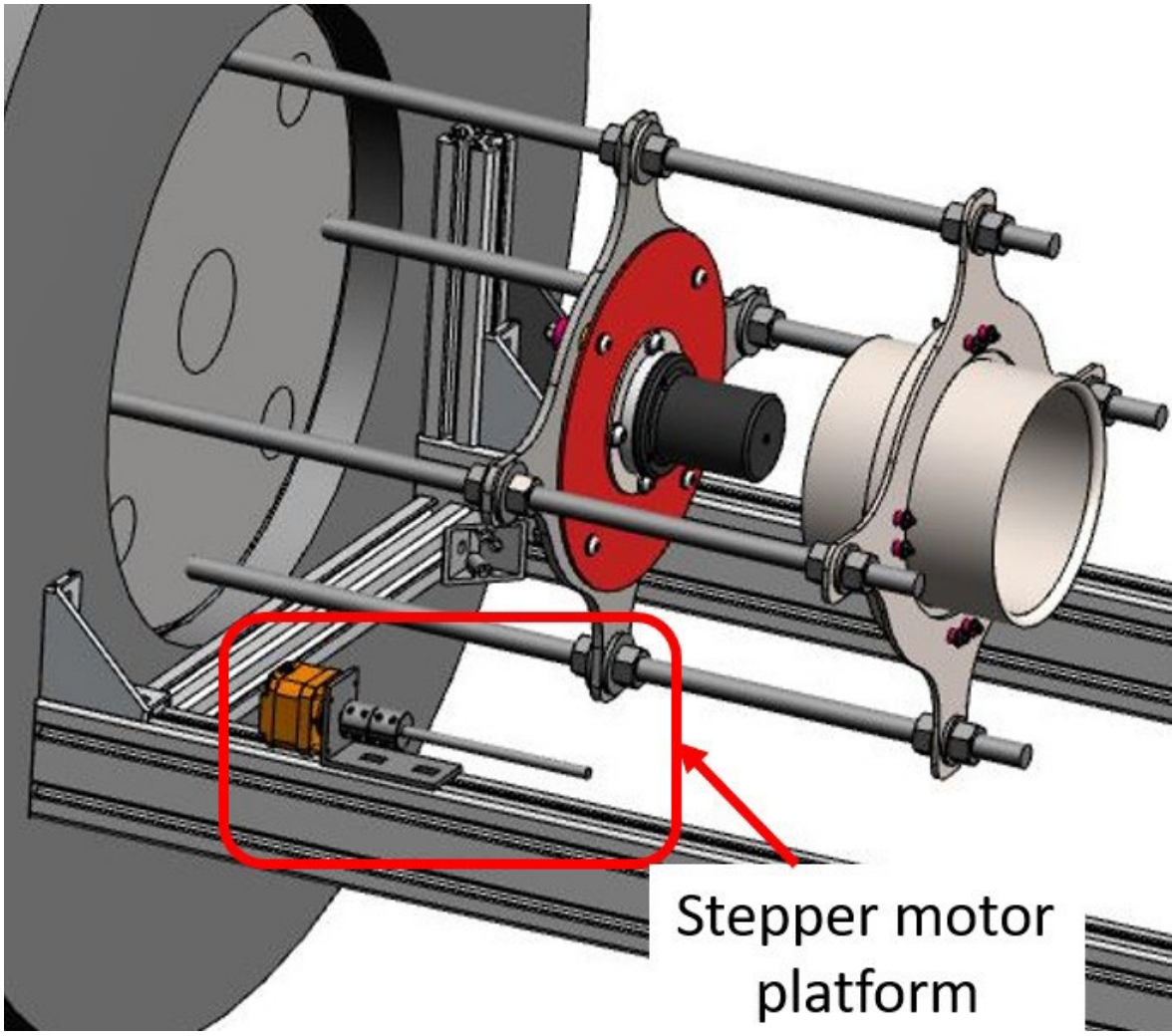

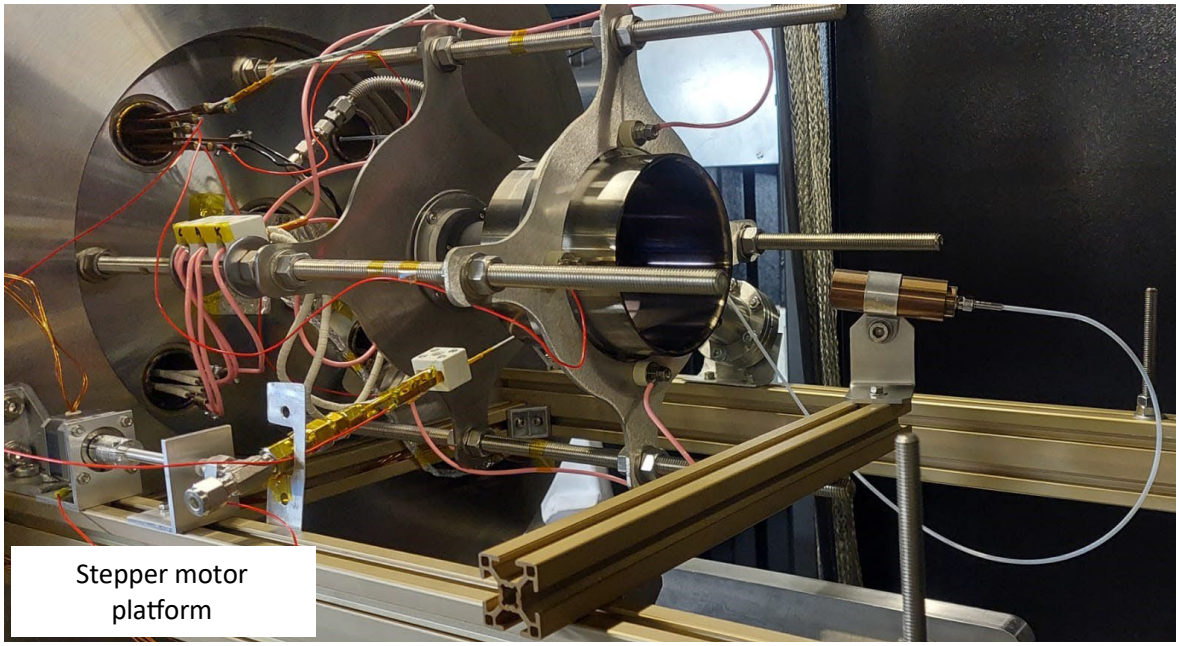

Figure 29 – New LP positioning system

A schematic of the probe biasing and acquisition circuit is shown in Figure 30. A calibrated Keithley 2450 SMU is used in voltage source mode to apply the DC voltage to the probe and simultaneously measure the current collected by the Langmuir probe. The device offers a broad range of sourced voltages (20 mV – 200 V, with a resolution of 500 nV – 5 mV depending on the

voltage range) and measured currents (10 nA – 1 A, with a resolution of 500 fA – 50 μA depending on the current range) with a high degree of stability and accuracy. The entire setup (i.e. rotation stage motor, probe bias voltage supply, and SMU) is controlled by a LabView routine to produce an automated measurement system. The stored data can be saved as a CSV file and then imported into MATLAB for analysis using one or more methods described in Section 3.3.2.

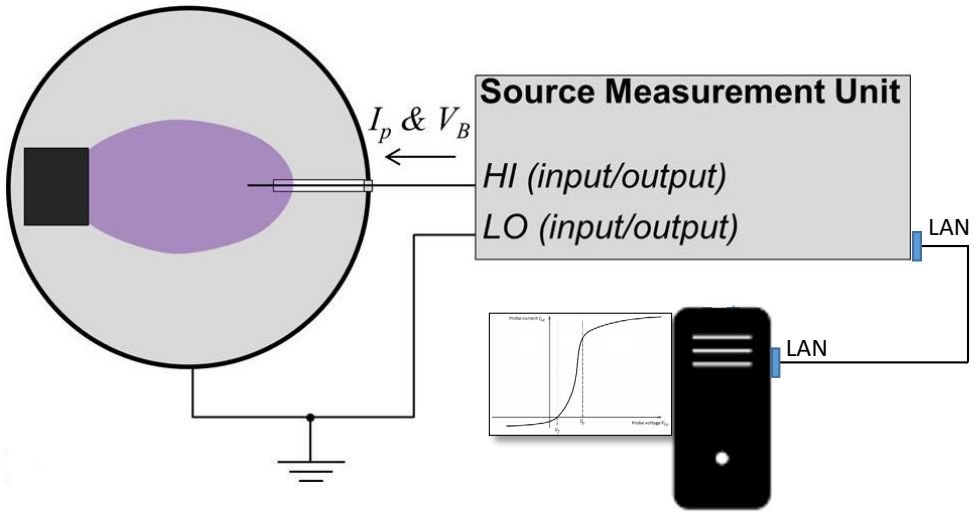

Figure 30 – Schematic of the probe biasing and data acquisition circuit

4.3 Tests Overview

As described in the previous sections, two different tests were carried out at two different testing facilities and the test objectives, campaign flow charts, and main test sequences are provided in the following subsections.

4.3.1 Ring-Cusp Discharge Chamber: Test Objectives and Campaign Overview

The main objective of the test campaign was to conduct a performance characterisation of the small ring-cusp discharge chamber with xenon and the selected alternative propellants (i.e. krypton and the 1:4 Xe/Kr mixture) by running the thruster in discharge-only mode and using Brophy's technique (described in detail in Section 3.2.2) to simulate the performance with beam extraction. The initial plan was to test the engine with the three propellants over a wide range of operating conditions while varying some design parameters (e.g. the cathode orifice's size), and also mapping the plasma parameters (i.e. electron temperature, plasma potential, and plasma density) and their spatial distribution inside the discharge chamber with a Langmuir probe. Unfortunately, due to various unforeseen events, the allocated time for the testing was limited to three weeks, comprising the preparation of the setup (hardware and software) and the actual test, and, because of this, the test plan had to be simplified to ensure that the main objectives could be completed. The deviation from the original test plan can be summarised as:

- only a limited number of operating conditions were tested
- the LP data collection was limited to one dataset per propellant at a selected operating condition
- only a cathode configuration was tested.

The overall top-level sequence of the campaign is outlined in Figure 31.

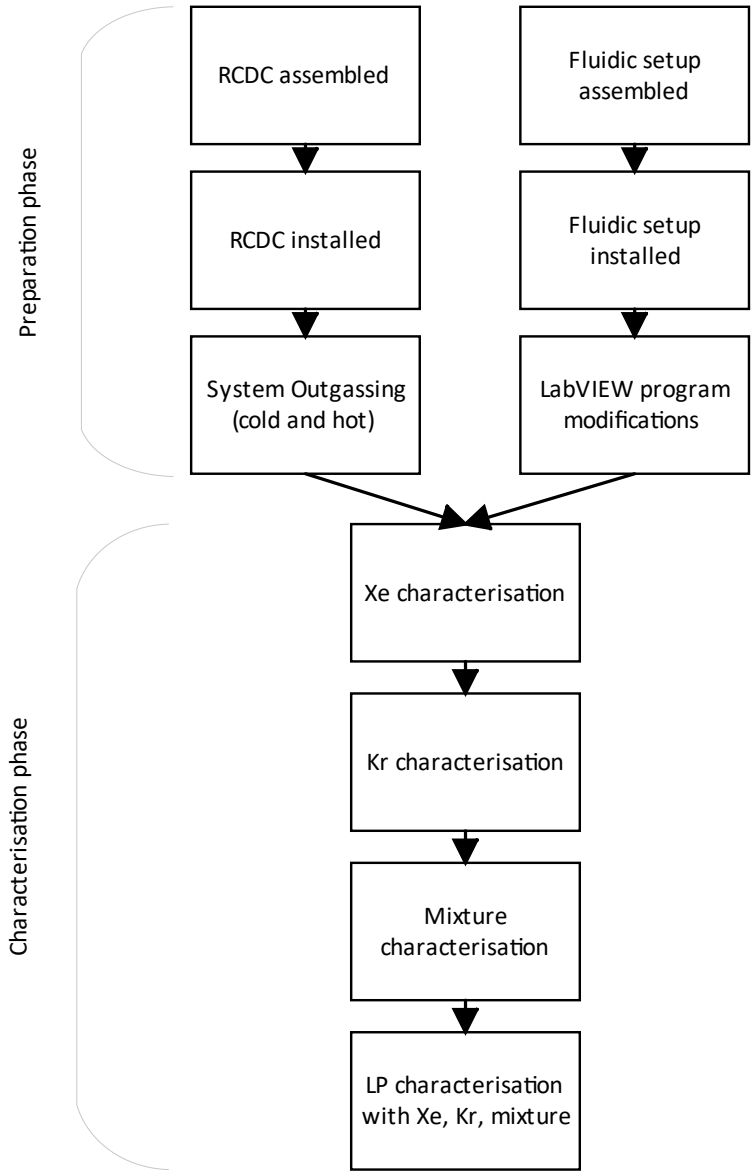

Figure 31 – Test campaign flow chart

The test campaign was divided into two main phases: a preparation phase and a characterisation phase. Furthermore, the preparation phase was split into two sets of tasks being carried out side-by-side by MSL's personnel (RCDC assembly and installation) and by the author (fluidic setup assembly and installation, and LabVIEW program modifications). Following a previous test activity, the small ring-cusp thruster had to be disassembled for inspection, and then reassembled for this campaign. An important part of the preparation phase included the mandatory electrical checks, leak detection test of the fluidic lines, and cold and hot outgassing according to MSL's standard procedures. Finally, before starting the characterisation phase, a

shakedown test was performed on the experimental setup to debug possible issues related to the modifications made (both hardware and software) to the overall system.

After several discussions with MSL's personnel about the thruster's operational procedures and the way the system is operated using the LabVIEW program, but mainly due to the limited time available for the test, the thruster performance characterisation phase was carried out as follows:

- firstly, a baseline performance characterisation was obtained by running the discharge chamber with xenon at known (from previous tests) stable operating conditions;
- secondly, keeping the anode and keeper current fixed (equal to 4.5 A and 0 A, respectively), various operational points for the cathode flow rate were tested in order to identify a few points with stable operating conditions (e.g. stable voltage discharge) for the other two propellants (three for Kr, and two for the 1:4 Xe/Kr mixture);
- thirdly, for the selected cathode flow rates, the main flow rate was tuned in order to obtain the selected propellant utilisation efficiencies (between 0.6 and 0.85, where possible, with increments of 0.05);
- finally, the characterisation of the plasma properties inside the discharge chamber was carried out at a selected propellant utilisation efficiency (i.e. 0.6) for the three propellants;
- ultimately, two scans were performed for each set point, defined by the propellant used.

The resulting configuration set points were:

- Discharge current = 4.5 A;
- Cathode flow rates:
    - Xenon = 1.2 sccm
    - Krypton = 1.5, 1.6 & 1.9 sccm
    - 1:4 Xe/Kr mixture = 1.5 & 1.625 total sccm
- Propellant utilisation efficiency = from 0.6 to 0.85 (when possible, because of limitations on the minimum main flow rate).

During the characterisation phase, sensors and probes recorded the operating conditions, such as anode, keeper, grids and bias voltages, currents collected to the grids and by the bias supply, and the vacuum chamber's pressure. The discharge chamber's temperatures were also monitored throughout the test campaign.

4.3.2 Hollow Cathode: Test Objectives and Campaign Overview

The main objective of the hollow cathode testing was to carry out a performance characterisation of the LaB_6 cathode available at the TDHVL with xenon and the selected alternative propellants (i.e. krypton and the 1:4 Xe/Kr mixture) in diode mode. The initial plan was to test the cathode with the three propellants over a wide range of operating conditions using different cathode configurations (e.g. orifice shape, size, and the relative position between cathode tube and keeper, etc.) and with the addition of a comprehensive diagnostics setup (including Langmuir and emissive probes, E×B probe). Unfortunately, due to various unforeseen events, only a basic performance mapping was completed, and the overall flow chart is shown in Figure 32 for each propellant.

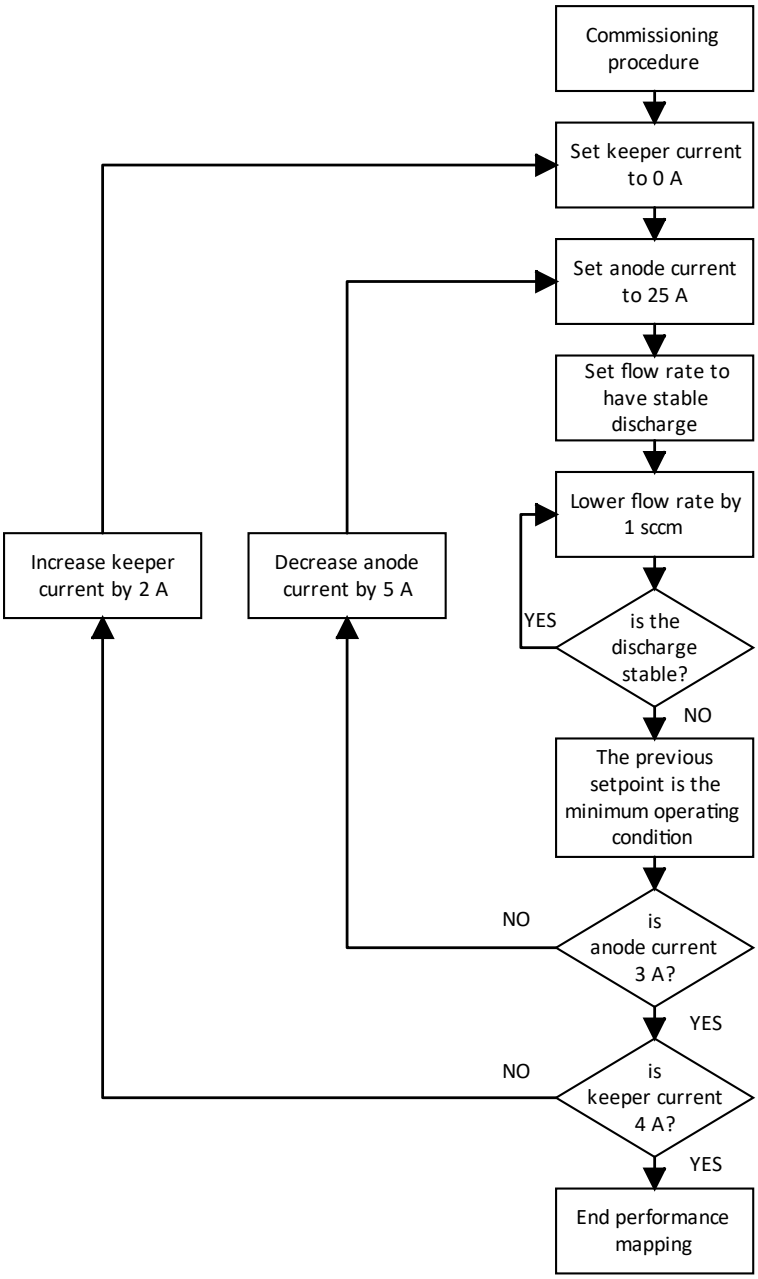

Figure 32 – Performance mapping flow chart

The test started with the commissioning procedure, which included the following tasks: cathode inspection and installation in the vacuum chamber, electrical checks, leak detection test of the fluidic line, pumping down, and cold and hot outgassing of the cathode. After the successful completion of the commissioning procedure, the testing was carried out at a range of control parameters (i.e. keeper current, anode current, and cathode flow rate) and their possible permutations while measuring the operating conditions with the sensors and probes described in Section 4.1.2.

The configuration set points were:

- Keeper current = 0 (floating), 2 and 4 A;
- Anode current = 3, 5, 10, 15, 20 and 25 A.

4.4 Summary

This chapter focuses on the two setups used during the test campaign with a small ring-cusp thruster and a hollow cathode carried out at Mars Space Ltd facilities and at the University of Southampton's TDHVL, respectively: both experimental configurations are described in detail including the vacuum facility, fluidic and electrical setup. Afterwards, the diagnostic tools and their positioning are summarised since they are an important feature of the two systems: for example, an essential parameter for analysis of the performance of a discharge chamber is the uniformity of the plasma at the grids and, using the Langmuir probe setup described above, the plasma parameters were calculated. Finally, the final part of this chapter is dedicated to the description of the test plans, including testing objectives and procedures used during the campaign.

The results of this experimental effort are presented in the following chapter.

Chapter 5 Experimental Results: Performance Study and Analysis

This chapter presents the operational characterisation of a gridded ion engine and a hollow cathode with alternative propellants (i.e. krypton and the Xe/Kr mixture) with emphasis on the performance results and measurements from internal diagnostics tools.

5.1 Performance Results of the Small RCDC

The small RCDC was tested in discharge-only mode to characterise the impact of using krypton and a 1:4 Xe/Kr mixture instead of xenon by applying the Brophy simulated technique, as described in Section 3.2.2. This technique of operating the discharge chamber without beam extraction was proposed by Brophy [80] in the 1990s and has been used in the last three decades to characterise and optimise discharge chambers in laboratories [97]–[99]. The main advantage of this technique is found in the simplicity of the experimental setup which does not need high voltage to bias the grids and gives more flexibility during the testing campaign. However, the main implication of operating the thruster without beam extraction is that the ion optics transparency to ions is reduced drastically and, therefore, changes the discharge equilibrium. The ions striking the grids recombine as neutral atoms, which either re-enter the discharge chamber or leave the thruster completely, causing an increase in the neutral density that changes the overall equilibrium between species compared to the case with beam extraction. Consequently, the propellant flow rate into the discharge chamber must be reduced without beam extraction, and the average ion density needs to be maintained constant with and without beam extraction.

Following the theory just described, the two criteria of similarity that need to be satisfied when operating with and without beam extraction are:

- the discharge chamber average neutral atom density $n_0 = \hat{n}_0$, and
- the product of the average ion density and the square root of the average electron temperature $n_i\sqrt{T_e} = \hat{n}_i\sqrt{\hat{T}_e}$.

As described in detail in Section 3.2.2, in order to estimate the equivalent performance and operating conditions of a discharge chamber tested without beam extraction if the high voltage was applied to the grids, the following identities are used:

- Ion beam current: $I_b = \sum_j I_{tot,j} T_{beam,j}$ (5-1)

- Mass utilisation efficiency: $$\eta_m = \sum_j \frac{I_{b,j}}{e\frac{\dot{m}_{dc,j}}{M,j} + I_{b,j}\left(1-\frac{T_{dc}}{T_{beam,j}}\right)}$$ (5-2)

- Total mass flow rate: $$\dot{m}_p = \sum_j \frac{\dot{m}_{dc,j}}{1-\eta_{m,j}\left(1-\frac{T_{dc}}{T_{beam,j}}\right)}$$ (5-3)

- Discharge loss: $$\eta_d = \frac{I_d V_d}{I_b} = \frac{(\hat{I}_d - I_b)\hat{V}_d}{I_b}$$ (5-4)

where the symbol $\widehat{\ }$ and the subscript dc designate the case without beam extraction. Equations (5-1)–(5-3) are expanded to include the case when a mixture of gases is used and the subscript j represents the j-th ion species.

In Section 3.2.2, the following hypotheses were presented for using this technique with different propellants:

- The second similarity condition, $n_i\sqrt{T_e} = \hat{n}_i\sqrt{\hat{T}_e}$: it was re-derived for the Xe/Kr mixture and the resulting criterion is:

$$\sqrt{T_{eff}}\sum_j \frac{n_{i,j}}{\sqrt{M_{i,j}}} = \sqrt{\hat{T}_{eff}}\sum_j \frac{\hat{n}_{i,j}}{\sqrt{M_{i,j}}}$$

  with T_{eff} representing the effective electron temperature of the mixture, as described in Section 3.3.3.

- Ion optics transparency, T_{beam}: for this experiment, it was calculated using an ion optics code (i.e. FFX) and the results are shown in Figure 33 as a function of the total current reaching the grids' plane.

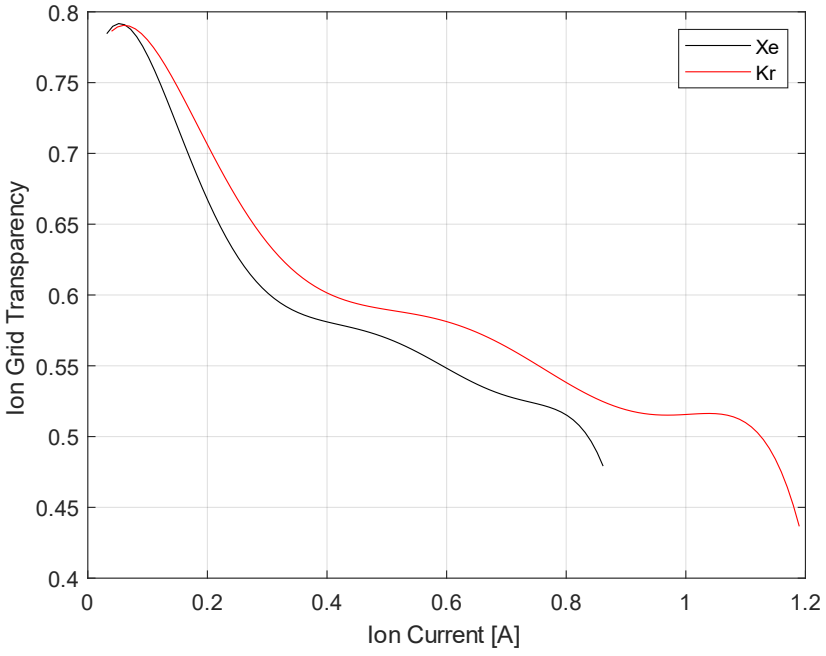

Figure 33 – Ion Grid Transparency, T_{beam}, from FFX code

- The ratio of ions impacting the accel grid that leave the grids as neutrals, γ_{i-n}: it was calculated with a Monte-Carlo model and the value 51% was used for the three propellants in the following calculations. A sensitivity analysis of impact of this parameter on the mass utilisation efficiency η_m as given in Equation (5-2) is shown in Figure 34: even a relevant variation of about 16% in the value of the ratio (from the reference value of 51%) has a limited impact (i.e. between 1% and 2%) on the value of η_m.

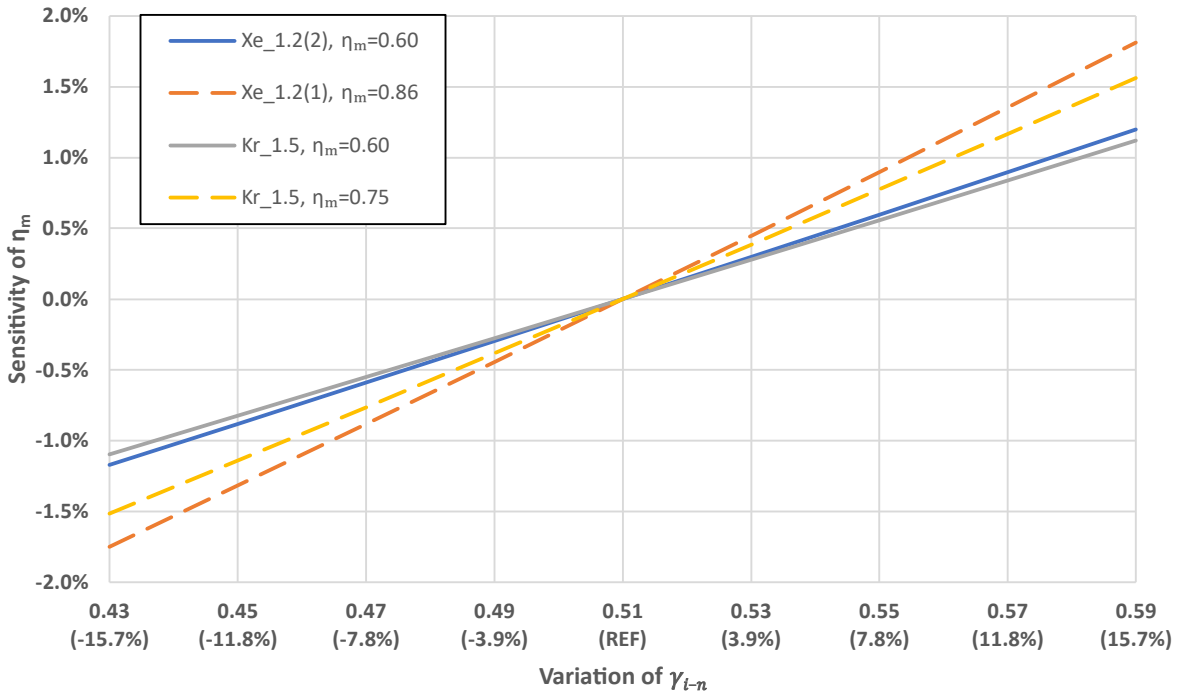

Figure 34 – Sensitivity of η_m as function of the variation of γ_{i-n}

- Bias values for the "engine bias supply" and the "screen grid bias supply": they were kept constant for the three propellants.

As described in the test plan in Section 4.3.1, all of the data presented below were taken as follows: firstly, the baseline performance was obtained by running the discharge chamber with xenon; secondly, the tests were repeated with krypton at different flow rates in order to match xenon propellant utilisation efficiencies; finally, the same procedure was applied for the mixture.

Table 2 reports the discharge parameters of the set points used to characterise the discharge with xenon, krypton and the 1:4 Xe/Kr mixture (in curly brackets is the nomenclature used for the particular combination propellant-volumetric flow rate in the figures in this chapter).

Table 2 – Discharge parameters for the test without extraction (discharge current = 4.5 A)

Propellant	*Utilisation efficiency*	*Discharge voltage* [V]	*Flow (HC)* [sccm]	*Flow (main)* [sccm]	*Total grids current* [A]
Xenon {Xe_1.2(1)}	0.70	20.60	1.2	0.95	0.489
	0.75	21.25	1.2	0.65	0.504
	0.80	22.01	1.2	0.35	0.516
	0.85	23.01	1.2	0.05	0.524
	0.86	23.17	1.2	0	0.521
Xenon {Xe_1.2(2)}	0.60	19.13	1.2	1.58	0.449
	0.65	19.73	1.2	1.24	0.466
	0.70	20.34	1.2	0.90	0.481
	0.75	20.95	1.2	0.58	0.492
	0.80	21.64	1.2	0.28	0.497
Krypton {Kr_1.5}	0.60	24.29	1.5	1.97	0.545
	0.65	24.42	1.5	1.28	0.518
	0.70	24.62	1.5	0.70	0.486
	0.75	24.86	1.5	0.25	0.448
Krypton {Kr_1.6}	0.60	23.75	1.6	1.70	0.515
	0.65	23.82	1.6	1.03	0.486
	0.70	23.95	1.6	0.46	0.449
	0.75	24.19	1.6	0	0.408
Krypton {Kr_1.9}	0.60	22.86	1.9	1.08	0.457
	0.65	23.06	1.9	0.48	0.431
	0.70	23.28	1.9	0	0.400
Mixture Xe/Kr {Mix_1.5}	0.60	22.98	1.5 (0.3/1.2)	1.9375 (0.3875+1.55)	0.538
	0.65	23.17	1.5 (0.3/1.2)	1.3125 (0.2625+1.05)	0.523
	0.70	23.35	1.5 (0.3/1.2)	0.7625 (0.1525+0.61)	0.501
	0.75	23.52	1.5 (0.3/1.2)	0.275 (0.055+0.22)	0.468
Mixture Xe/Kr {Mix_1.625}	0.60	22.54	1.625 (0.325+1.3)	1.625 (0.325+1.3)	0.506
	0.65	22.75	1.625 (0.325+1.3)	1.0375 (0.2075+0.83)	0.491
	0.70	22.94	1.625 (0.325+1.3)	0.5375 (0.1075+0.43)	0.473
	0.75	23.25	1.625 (0.325+1.3)	0.075 (0.015+0.06)	0.437

Furthermore, it is worth highlighting that the small RCDC and the relative hollow cathode used for the testing are in development to run mainly with xenon, and that the tests with alternative propellants were carried out using the same thruster configuration (e.g. hollow cathode orifice, ion optics, magnetic fields).

5.1.1 Discharge Loss Trends

A typical way to characterise the discharge chamber performance of an ion thruster is by plotting the discharge loss as a function of the propellant utilisation efficiency, the so-called performance curve, as already described in Section 3.1.4. However, it is worth highlighting that, as described in Section 3.1.4, performance curves are normally taken at constant beam current and discharge voltage so that the efficiency of producing and delivering ions to the beam is not masked by changes in the discharge voltage or average plasma density at the grids. Figure 35

compares the simulated discharge losses (calculated using Eq. (5-4)) for xenon, krypton and the mixture for a given propellant efficiency (calculated using Eq. (5-2)). Since the characterisation has been carried out at a constant discharge current, the dotted lines in Figure 35 represent the trend curves in the discharge loss and not the performance curves.

As predicted from the literature review in Section 2.3.2, the discharge losses operating on krypton are higher than those obtained with xenon, and the gap, small at lower efficiencies, increases substantially moving towards higher efficiencies. The difference in discharge losses can be mainly linked to the difference in discharge voltages (on average 4 V higher for krypton as shown in Table 2) and a possible lack of optimisation for krypton (e.g. related to the ion optics and the cathode geometries).

The performance with the mixture is expected to be between that of pure xenon and that of pure krypton: at lower efficiencies, the discharge losses for the mixture tend to converge with those of xenon and krypton, but the presence of xenon seems to mitigate the losses obtained with pure krypton at higher utilisation efficiencies. This result is very promising, and it requires further investigation to confirm it.

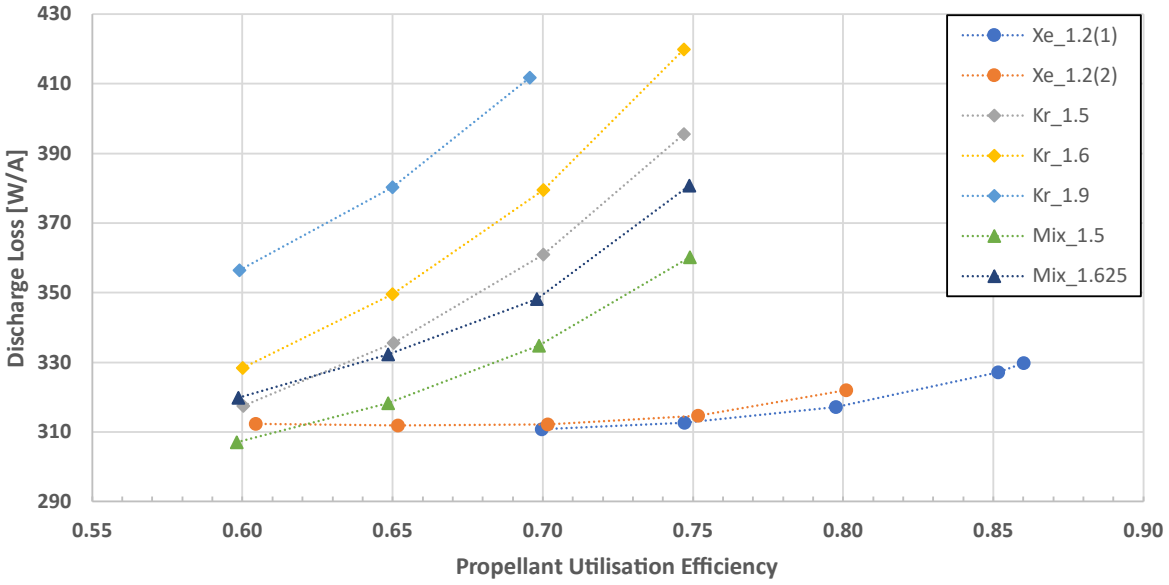

Figure 35 – Simulated discharge losses and their trends

Finally, Figure 36 shows the discharge loss as a function of the total volumetric flow rate into the thruster in sccm (calculated using Eq. (5-3)). It can be observed that there is a trend with the discharge loss decreasing when increasing the propellant mass flow rate as expected, where the use of alternative propellants introduces a clear penalty in terms of W/A for equivalent flow rates, and the difference is in the range of 20-40 W/A for the mixture and 40-80 W/A for krypton.

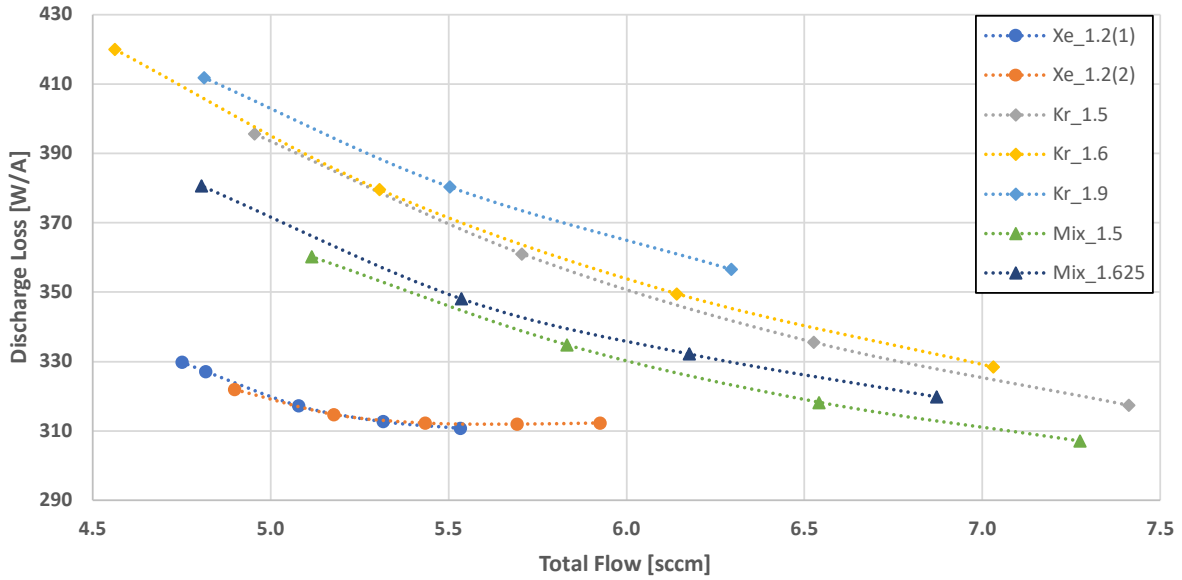

Figure 36 – Discharge loss as a function of total flow rate in sccm

5.1.2 Specific Impulse Trends

Although a performance gap exists between xenon and the alternative propellants under investigation, Figure 37 shows one of the benefits of using krypton and the mixture: at similar thruster efficiencies, the specific impulse is higher than with xenon, as expected from the definition of specific impulse and its dependence on the square root of the propellant atomic mass (see Sections 3.1.2 and 3.1.5). The values for the specific impulse and total thruster efficiency were calculated using Eq. (3-30), which includes the case for mixtures, and Eq. (3-22) from Section 3.1, respectively, and reported below:

$$I_{sp} = \sum_j \frac{T_j}{\dot{m}_{p,j} g_0} = 1.417x10^3 \gamma \sqrt{V_b} \sum_j \eta_{m,j} \frac{1}{\sqrt{M_{a,j}}} \tag{5-5}$$

$$\eta_T = \gamma^2 \eta_e \eta_m \tag{5-6}$$

However, the overall thruster efficiency is approximately 10% lower with alternative propellants than that with xenon at a given specific impulse. Interestingly, the results with the mixture are much closer to those obtained with pure krypton compared for example to the trends seen in Figure 35, where the mixture was almost halfway between pure xenon and pure krypton.

Furthermore, it has been demonstrated that it is possible to increase the maximum obtainable specific impulse with krypton even further by using optimised ion optics (e.g. with lower neutral transparency) and higher beam voltages [11].

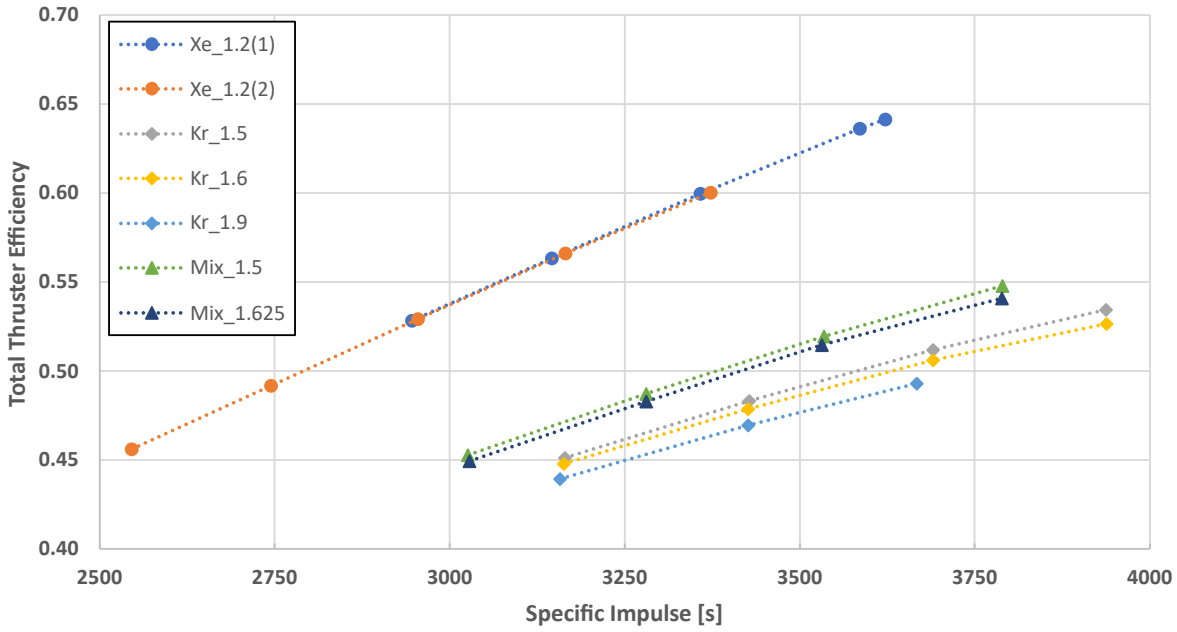

Figure 37 – Total thruster efficiency as a function of specific impulse

5.1.3 Voltage Trends

The plot of discharge voltage as a function of propellant utilisation efficiency is shown in Figure 38. As expected, higher discharge voltages are required for krypton compared to those for xenon, and this behaviour can be associated mainly with krypton's higher ionisation energy compared to xenon (14 eV vs 12.1 eV). However, the discharge voltage with krypton has a smaller gradient when increasing the efficiency compared to the values with xenon, which show a slightly steeper increment. This difference in discharge voltages between krypton and xenon partially explains the difference in discharge losses, as seen in Section 5.1.1, which are directly proportional to the discharge voltage. The figure also shows that the values of the discharge voltage for the mixture are between that of pure xenon and that of pure krypton, showing a similar behaviour to that of pure krypton.

The higher discharge voltages obtained for the alternative propellants are likely to have an impact on the lifetime of both the internal walls of the discharge chamber at anode potential and of the ion optics (i.e. the screen grid, in particular), due to the higher energy of the ions and electrons impacting these surfaces. In fact, krypton has higher sputter yields compared to xenon at the same impact energy with materials typically used for ion optics (e.g. it is roughly double with graphite grids [100]).

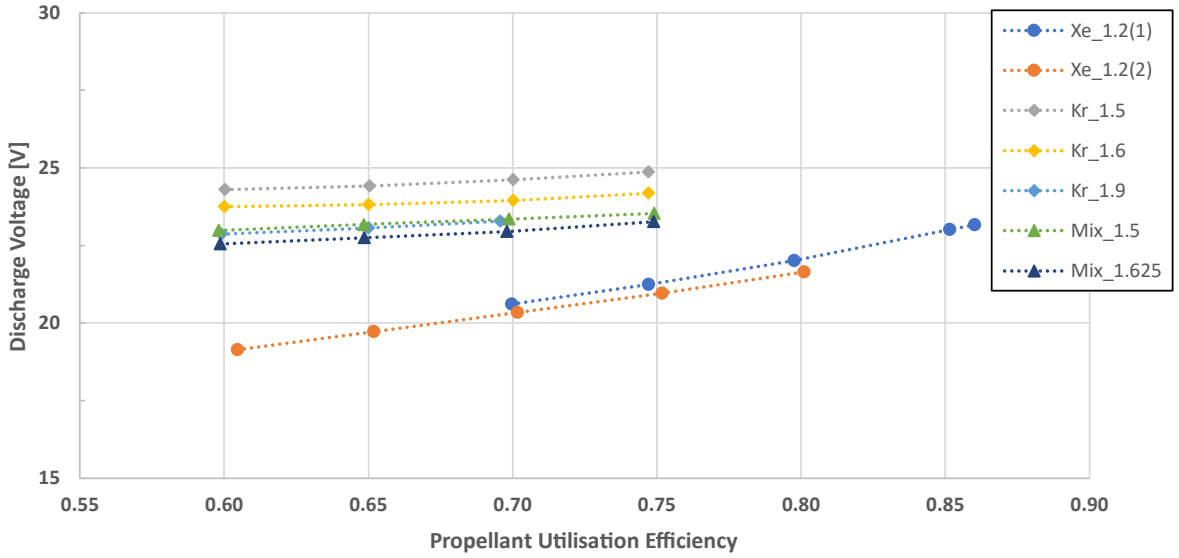

Figure 38 – Discharge voltage as a function of propellant utilisation efficiency

5.1.4 Power Trends

The total thruster efficiency as a function of the total input power is shown in Figure 39. The total input power was calculated (from Section 3.1.4) as follows:

$$P_{tot} = I_b V_b + I_d V_d + P_{other} \tag{5-7}$$

where $P_b = I_b V_b$ is the beam power, $P_d = I_d V_d$ is the discharge power and P_{other} represents the other power input to the thruster required to create the thrust beam (e.g. cathode heater and keeper power, neutraliser power, etc.). In this case, the total power can be considered to be almost directly proportional to the beam current I_b, since the beam voltage and the discharge current are kept constant, the discharge voltage does not change much for the different propellants (as seen in the previous subsection), and P_{other} has been assumed to be zero for these calculations (in fact, the cathode heater was turned off during the operations, the cathode keeper was floating, and the neutraliser was not present since there was no extracted beam to be neutralised). This dependency of the total power from the beam current can be seen comparing Figure 39 and Figure 40. Also, the beam currents are directly dependent on the total current collected on the grids I_{tot}, as obtained using Eq. (5-1) and reported in Table 2.

The results obtained for the various propellants are conflicting: the thruster efficiency increases for xenon when the total current I_{tot} increases, but the opposite is true for the alternative propellants under consideration. The reasons for this behaviour are not clear, and the assumption is that it is related to the balance of the energy loss mechanisms within the discharge chamber, such as excitation, ionisation, and ion and electron losses. Furthermore, the inconsistent nature of this phenomenon has been identified in a similar test run at MSL's facilities with a bigger RCDC [101] using xenon as propellant: in that specific case, the total

thruster efficiency increases or decreases with the total input power depending on the discharge power levels, and, in particular, they both increase at the highest power level (i.e. discharge current of 28 A) but not at the lower power levels (i.e. medium and low power levels with a discharge current of 20 A and 15 A, respectively).

This behaviour was highlighted during the data analysis phase, and it was not possible to verify it with further tests, but it will need to be taken into account during any future testing campaign.

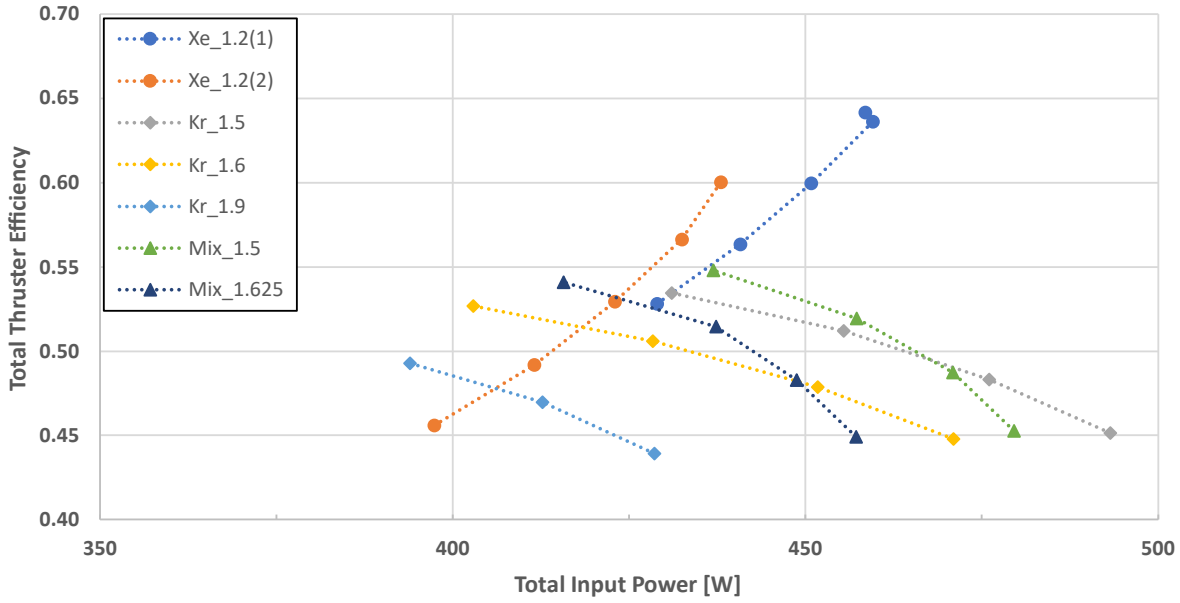

Figure 39 – Total thruster efficiency as a function of total input power

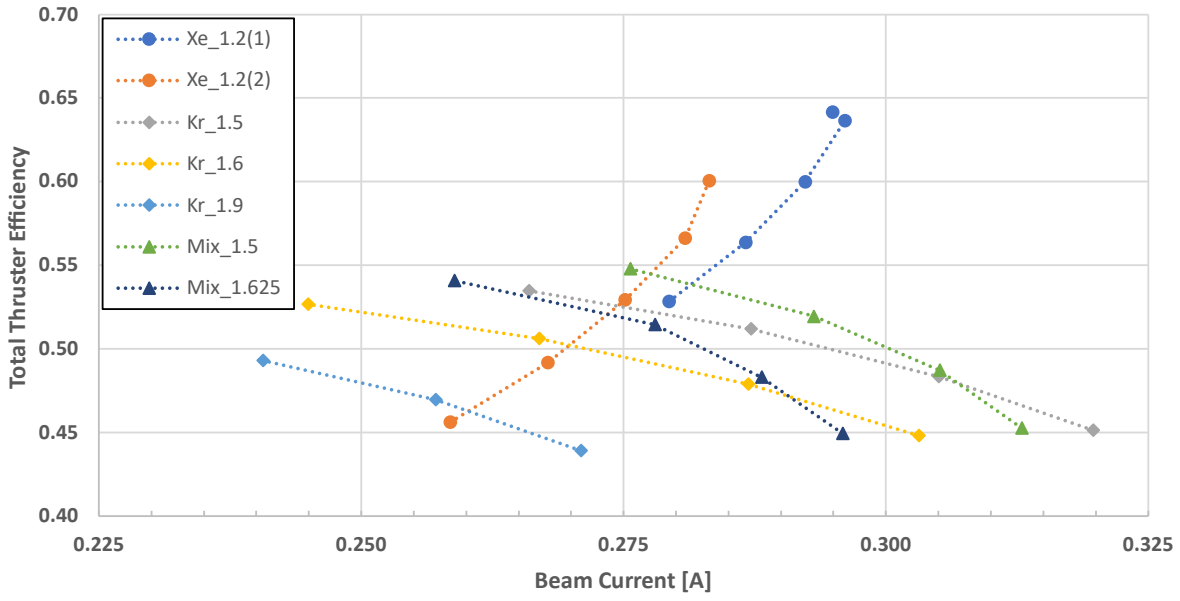

Figure 40 – Total thruster efficiency as a function of the beam current

Figure 41 shows the thrust-to-power ratio (TTPR) as a function of the specific impulse for the three propellants. The separation between xenon and the considered alternative propellants is quite evident: xenon is the best choice when the thrust is the most important parameter for the mission (i.e. time-critical missions), but, if specific impulse is more important during the mission design phase, krypton and the mixture have an advantage if a penalty of about 10% in

TTPR is acceptable (i.e. longer missions depending on high mass efficiency with higher specific impulse). The curves for constant values of the total thruster efficiency (see Equation (3-23) in Section 3.1.4) are also shown in Figure 41 and compared with the experimental data: it is visible that the experimental trends are almost linear (i.e. similar TTPR) for each propellant due to the changing thruster efficiency across each data set, and that the main reason for the difference between each propellant is related to the thruster efficiency. Finally, this figure shows that increasing the I_{sp} reduces the thrust available for a given input power and total thruster efficiency and, consequently, this trade-off can only be improved by achieving higher efficiencies.

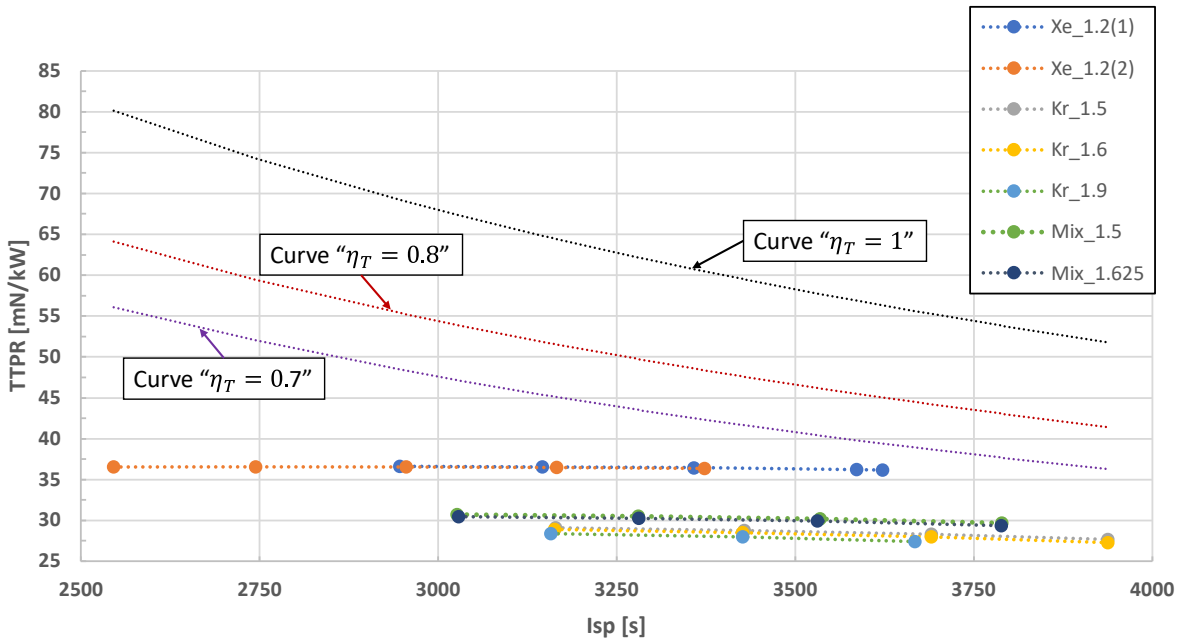

Figure 41 – Thrust-to-Power ratio as a function of specific impulse

5.2 Langmuir Probe Data Analysis: Results

An important design parameter for the optimisation of ion optics and, hence, the performance of ion thrusters is the uniformity and characteristics of the plasma at the grids. During the experimental campaign, the Langmuir probe setup described in Section 4.2.2.1 was used to measure the plasma parameters (e.g. density and electron temperature) of the discharge at a distance of 5 mm away from the grid extraction plane.

The results of the post-processed data for all the Langmuir probe scans collected during the test campaign for the different propellants are presented in the following subsections. The configuration set points were as follows, and they were selected because of their discharge stability compared to the other set points listed in Section 5.1:

- Discharge current = 4.5 A;
- Flow rates (cathode/total (i.e. main + cathode)):
  - Xenon = 1.2/5.93 sccm
  - Krypton = 1.9/6.29 sccm
  - 1:4 Xe/Kr mixture = 1.625/7.27 sccm
- Propellant utilisation efficiency = 0.6
- LP position = 5 mm upstream from the screen grid's plane
- Two scans were performed at each setpoint.

5.2.1 Plasma Density, Electron Temperature, and Relative Error

In Section 3.3.2, the procedure for the calculation of the electron energy distribution function using Druyvesteyn's formula was described and the equation for the calculations of the plasma density (in m^{-3}) was given as follows via integration of the EEDF, $F(\varepsilon)$:

$$n_e = \int_0^{-\infty} F(\varepsilon)\mathrm{d}\varepsilon \tag{5-8}$$

and for the calculation of the electron temperature (in eV) via the "tangent" method as follows:

$$T_e = \frac{k}{e}\left[\frac{\mathrm{d}(\ln I_e)}{\mathrm{d}V_{Lp}}\right]^{-1} \tag{5-9}$$

The results of the data analysis are shown in Figure 42 and Figure 43, which illustrate the plasma density and electron temperature profiles, respectively, as a function of the radius, where each point represents the average value of two scans that were performed for each radial position and the error bars represent the standard deviation of the data sets.

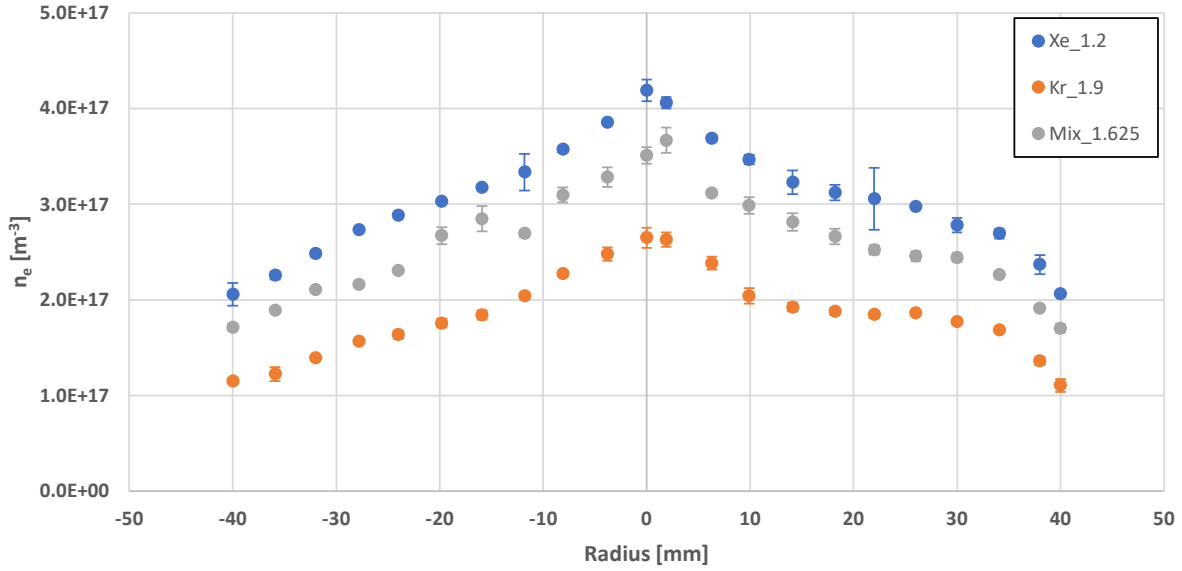

Figure 42 – Plasma density profiles near the grid extraction plane

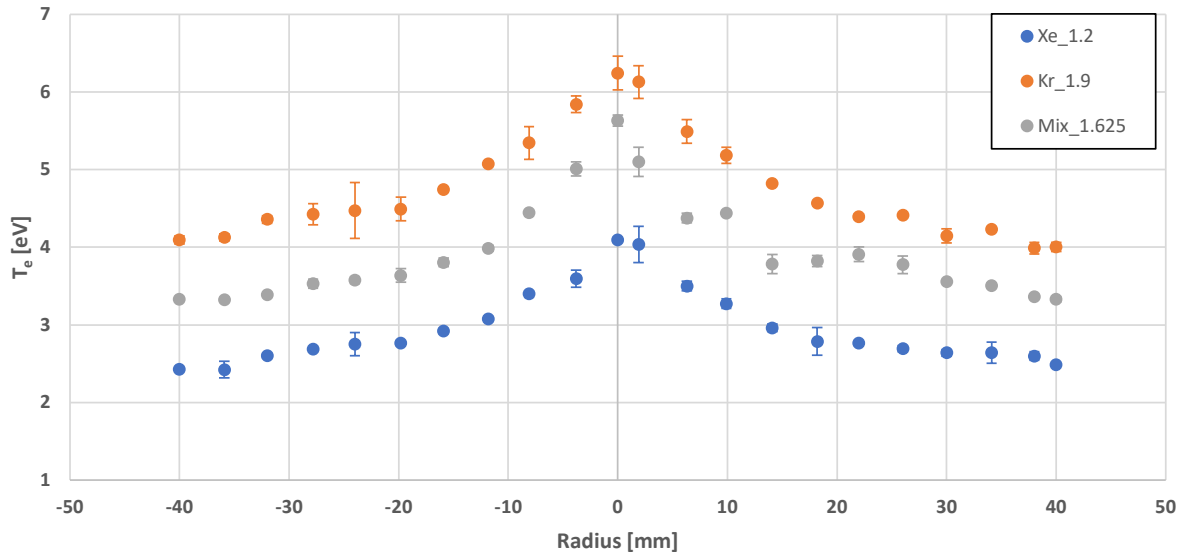

Figure 43 – Electron temperature profiles near the grid extraction plane

The figure of the plasma density profiles (Figure 42) shows values for krypton lower than xenon with the values for the mixture between those of the pure gases as expected due to the values of the mass flow rate. The general trend observed in Figure 43 is that the krypton case has the higher electron temperature profile and xenon has the lower one with the mixture results in between. This outcome is as expected since the electron temperature is inversely proportional to the ionisation cross-section of the propellant, and the higher discharge voltages (Section 5.1.3) required to sustain the plasma with alternative propellants have the direct consequence of more energetic electrons in the discharge chamber. The values obtained for the mixture case should be considered as an effective electron temperature T_{eff}, as described in 3.3.3: as predicted by the theory, the presence of xenon in the mixture Xe/Kr produces a decrease in T_{eff} compared to the case with pure krypton.

In addition, Figure 42 and Figure 43 show a symmetry of the two halves of the same profile for all the plasma density and electron temperature profiles that indicate excellent plasma stability, an adequate collection of the LP trace and its analysis, and a desirable positional accuracy in the stepper motor-driven assembly (i.e. absence of drift).

Furthermore, the least squared polynomial fitted data normalised to the centre peak for the plasma density and electron temperature are presented in Figure 44. Two trends are visible in the figure: first, the profiles for both density and temperature are essentially insensitive to the propellant used, except for the krypton's temperature profile which remains flatter compared to the peak value; secondly, the temperature profiles are more uniform along the radius of the grid, while the density profiles dip towards the edge of the grid.

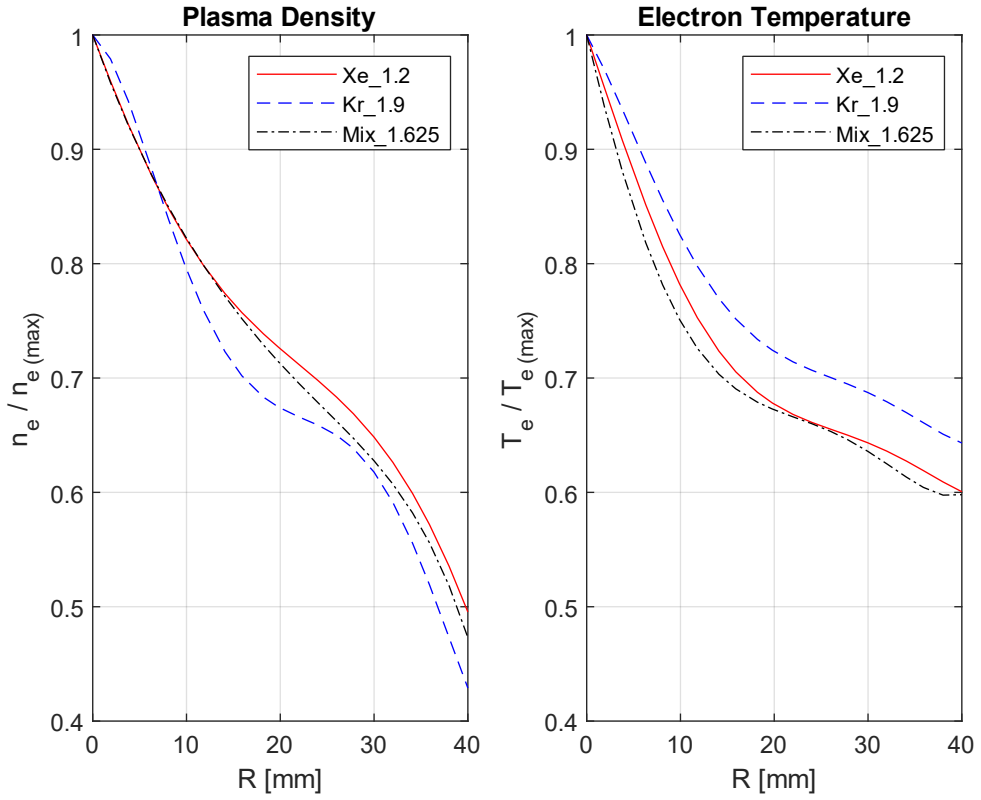

Figure 44 – Plasma density (left) and electron temperature (right) fit profiles normalised to the centre peak

As described at the beginning of this subsection, the plasma density has been calculated using Druyvesteyn's method, while the "tangent" method has been used to evaluate the electron temperature. From the literature [102], an estimated relative error of up to ±30% for the electron temperature and of up to ±50% for the plasma density is expected in line with these types of diagnostics and data analysis methods, but the obtained results can still be considered representative of the plasma parameters since the error is consistent across the entire dataset. However, in order to have an estimate of the accuracy of the data in this particular case, the radial integration of the Bohm current to the grids, which can be obtained from the measured plasma density and electron temperature, can be compared with the current measured with the EGSE described in Section 4.1.1.3. Therefore, the relative error can be calculated as follows:

$$\epsilon_r = 1 - \frac{2\pi e \int_0^R n_e(r) \cdot v_B(r) \cdot r \mathrm{d}r}{I_{tot}} \tag{5-10}$$

The result of this calculation gives an error of 28.5% for xenon, 33.8% for krypton, and 26.0% for the mixture. It is worth noting that this error represents an overestimation, since the current measured on the EGSE circuit accounts also for the masked area of the grids, while the integration of the Bohm current to the grids does not.

5.2.2 Current Density and Beam Flatness

As mentioned at the beginning of this section, an important parameter for ion optics design and, consequently, ion thruster performance is the uniformity of the plasma at the grids. Using the values of the electron temperature and plasma density obtained with the Langmuir probe's measurements and presented in the previous subsection, it is possible to calculate the screen current density, assuming a Bohm flux at the grids, and then plotted against radial distance for the various propellants (Figure 45) as (in this case, $X_{Xe} = 0.2$ and $X_{Kr} = 0.8$):

$$j(r) = en_e(r)v_B(r) = en_e(r)\sqrt{\frac{eT_{eV}(r)}{m_i}} \qquad \text{(for pure gases)} \qquad (5\text{-}11)$$

$$j_{mix}(r) = en_{e_{mix}}(r)\sqrt{eT_{eV_{mix}}(r)}\left(\frac{X_{Xe}}{\sqrt{m_{Xe}}} + \frac{X_{Kr}}{\sqrt{m_{Kr}}}\right) \qquad \text{(for the mixture)} \qquad (5\text{-}12)$$

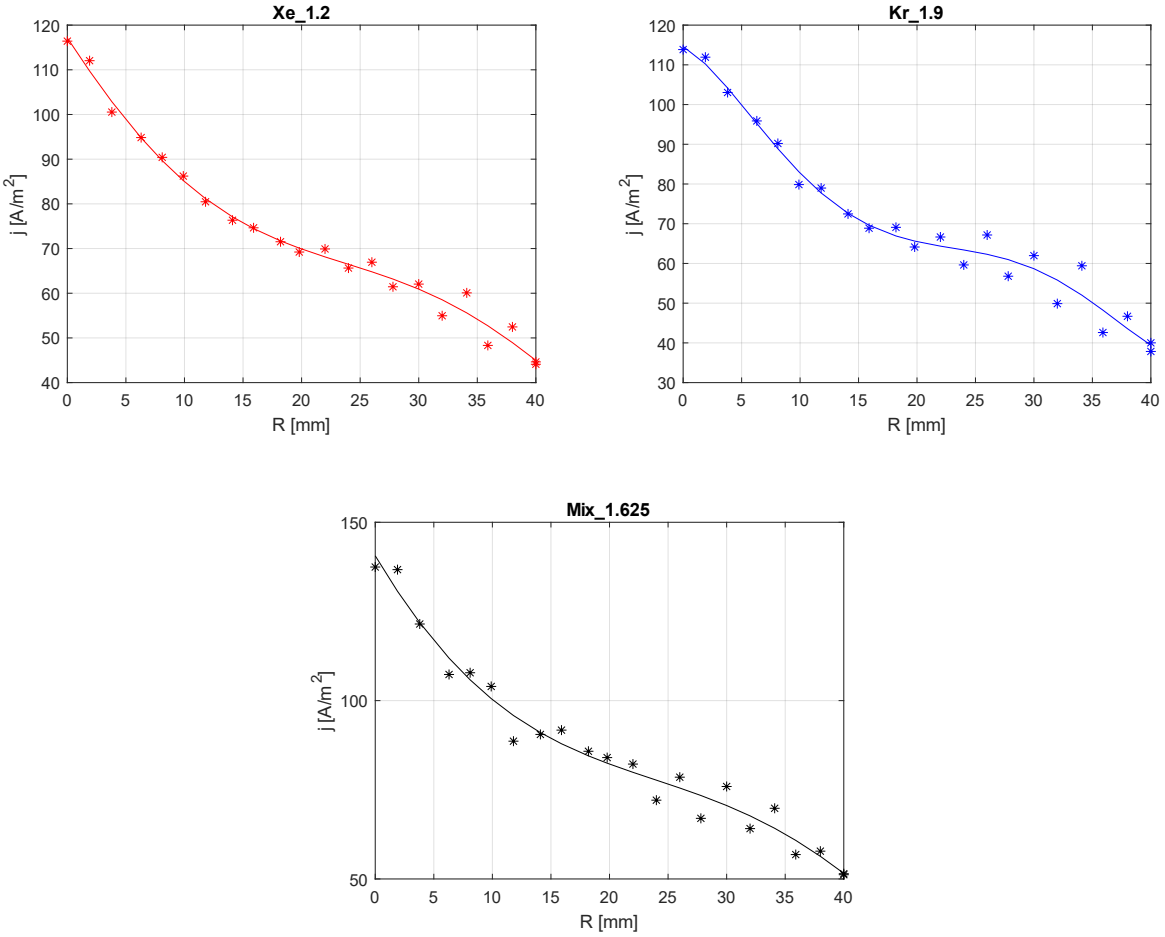

Figure 45 – Average of LP scans and polynomial fit for the screen current density

These results for the screen current densities allow the calculation of another important performance parameter of a discharge chamber, the beam flatness, which is usually evaluated as the ratio of the average current density divided by the peak value over the ion optics as [20]:

$$f_b \equiv \frac{\text{average current density}}{\text{peak current density}} = \frac{j_{avg}}{j_{max}} = \frac{2\pi \int_0^R r \cdot j(r)\, dr}{2\pi R^2 j(0)} \qquad (5\text{-}13)$$

A uniform profile has a flatness parameter of 1, and cosine profiles have a f_b close to 0.5. This indicates that the current density at the centre of the beam is more than twice the value that would exist with a uniform profile having the same integrated current. In addition, a high value of beam flatness for the grids translates into a flatter current density profile, which enables keeping the grid geometry unchanged across the total extraction system.

Computing the beam flatness with the fitted current densities of Figure 45, a value of 0.54 for xenon and a value of 0.53 for both krypton and the mixture was obtained, as shown in Figure 46.

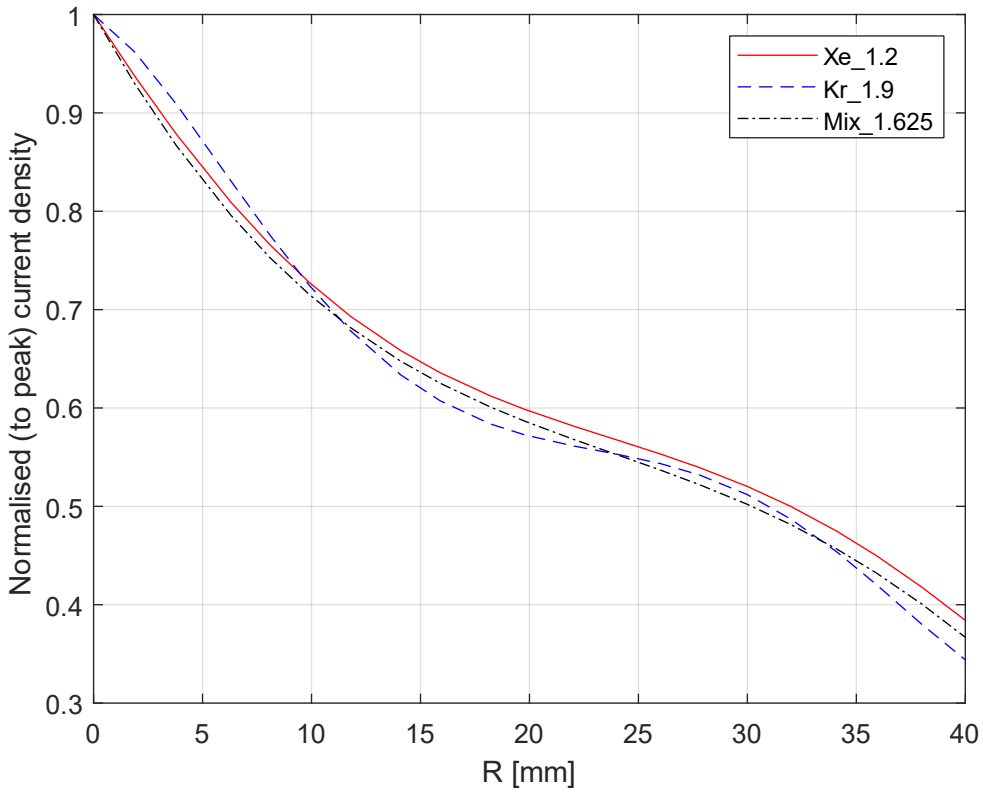

Figure 46 – Current density profiles normalised to peak density

Since a significant difference in beam flatness is usually associated with the topology and values of the magnetic field inside the discharge chamber [15], a very important outcome of this calculation is that the profile of the current density at the ion optics is almost independent of the choice of propellant.

5.2.3 Current Density Profiles and Impingement Limits

In Section 5.2.2, the screen current densities and their fitted profiles have been calculated for the various propellants. Normalising those current densities to the average integrated values allows to gauge the experimentally collected current for different operating conditions, and to get an estimate of peak and edge current density at the grids as shown in Figure 47:

$$\hat{j}(r) = \frac{I_{grid}}{A_{grid}} 2\pi \int_0^R r \cdot j(r) \mathrm{d}r \tag{5-14}$$

The polynomial fitting expressions for these profiles are (using a 5th degree polynomial):

$$\begin{aligned}\hat{j}_{Xe}(r) = \; & 2.4849 \cdot 10^7 * r^5 - 2.6229 \cdot 10^6 * r^4 + 6.6613 \cdot 10^4 * r^3 + \\ & +8.0267 \cdot 10^2 * r^2 - 62.728 * r + 1.8376 \\ \hat{j}_{Kr}(r) = \; & 1.3128 \cdot 10^8 * r^5 - 1.4425 \cdot 10^7 * r^4 + 5.2583 \cdot 10^5 * r^3 + \\ & -6.4341 \cdot 10^3 * r^2 - 28.053 * r + 1.9039 \\ \hat{j}_{Mix}(r) = \; & 9.7959 \cdot 10^6 * r^5 - 8.7231 \cdot 10^5 * r^4 - 7.4820 \cdot 10^3 * r^3 + \\ & +2.1826 \cdot 10^3 * r^2 - 74.527 * r + 1.8917\end{aligned} \tag{5-15}$$

and the radial current density can be written as:

$$j(r) = \frac{I_{grid}}{A_{grid}} \hat{j}(r) \tag{5-16}$$

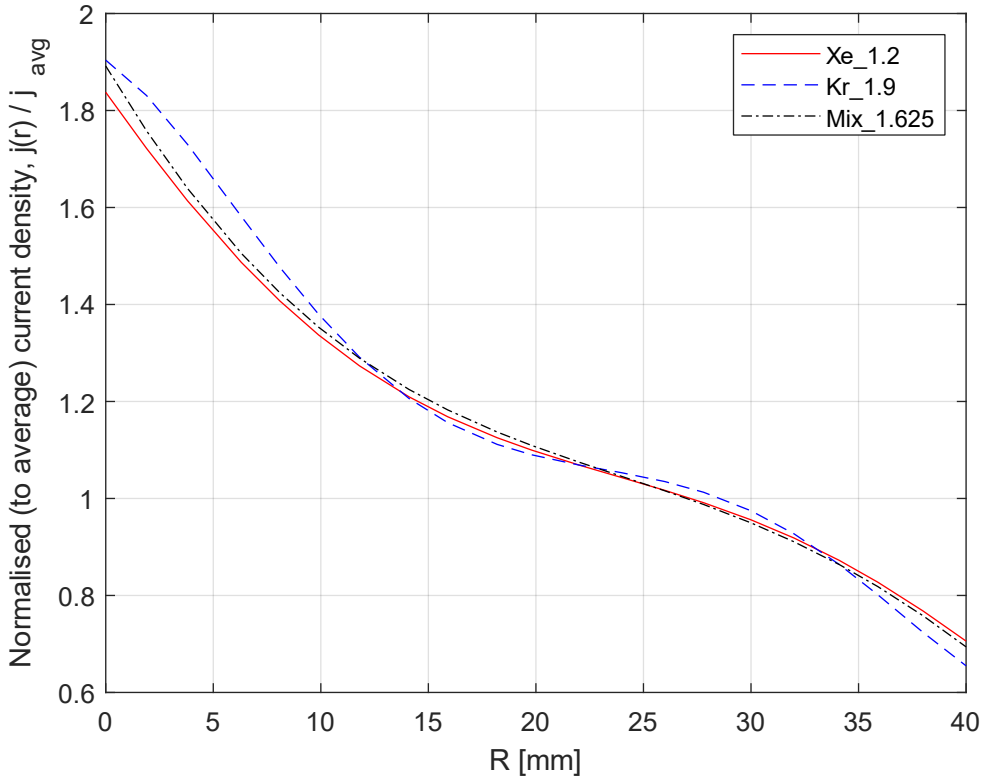

Figure 47 – Current density profiles normalised to average integrated value

If it is assumed that the shape of the normalised current densities is preserved at different values of discharge current, as it has been demonstrated to be the case for this particular thruster using xenon [103], it is possible to scale the current collected at the grids for different grid geometries to calculate the current distribution, and the central peak and edge current densities in order to evaluate if these values are within the perveance limits of specific ion optics configuration. The multiplication factors to be used with Eq. (5-16) to obtain the maximum and minimum current densities from the average $\frac{I_{grid}}{A_{grid}}$ are reported in Table 3.

Table 3 – Max and min current density multiplication factors

Propellant	*Max*	*Min*
Xenon	1.84	0.71
Krypton	1.90	0.65
Mixture	1.89	0.69

Comparing the max and min current densities with the perveance limit of a grid configuration, it is possible to assess whether these limits fall within the crossover and perveance limits calculated using an ion optics code.

Figure 48 and Figure 49 show the crossover/perveance curve for xenon and krypton, respectively, as a function of the current density $j(r)$ calculated using Eq. (5-16) and the grey area represents the current density between the maximum value at the centre of the grid and the minimum at the periphery of the grid. It is evident that the operating conditions the thruster has been operated at exceed in both cases the perveance limit and, as expected, krypton has a higher perveance limit (due to its lighter atomic mass) of about 22%, which is close to the theoretical value of about 25% (see Section 3.1.5), compared to xenon for the same ion optics. The operation of the thruster over the perveance limit does not have an immediate impact on the performance, however there could be consequences if the direct impingement is allowed to continue for a long time, such as structural failure of the accel grid due to the erosion caused by the impact of the high energy ions, and high rates of material sputtering from the accel grid that may re-deposit onto grid surfaces [1].

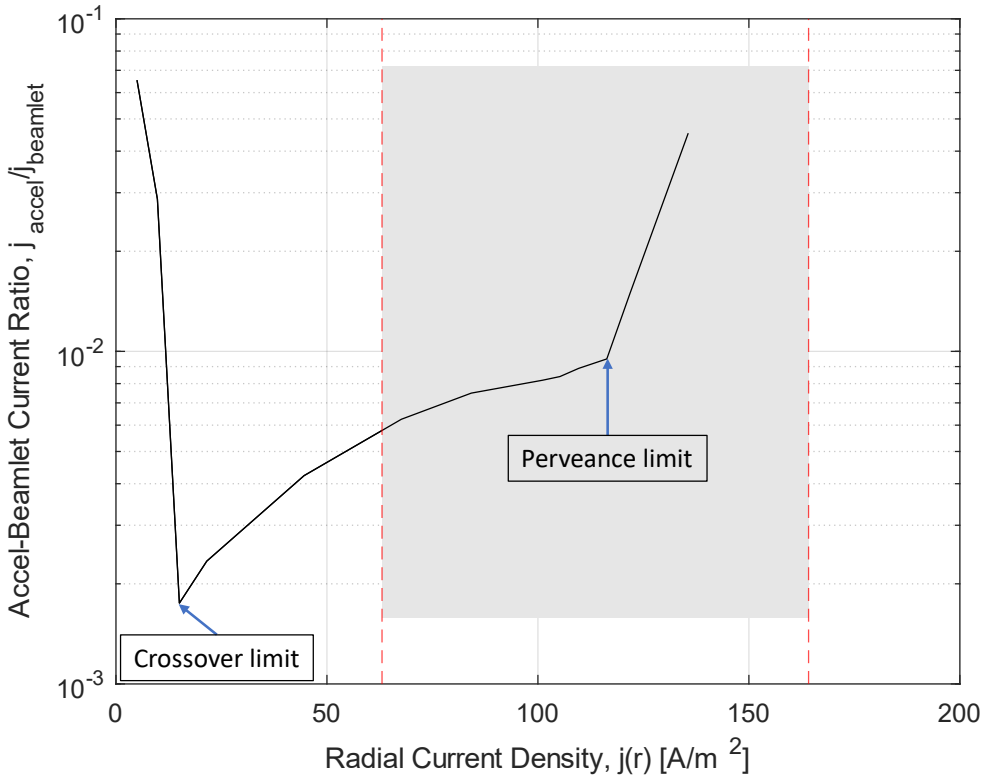

Figure 48 – Perveance limits as function of current density for xenon

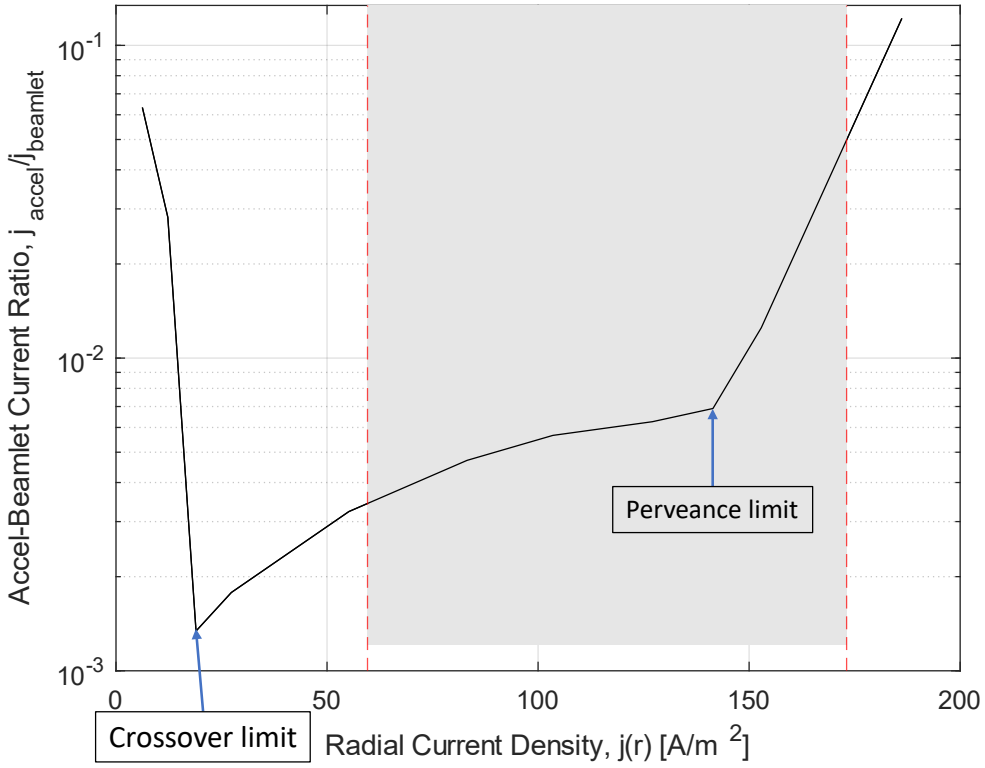

Figure 49 – Perveance limits as function of current density for krypton

As described at the beginning of Section 5.2, the plasma parameters (i.e. plasma density and electron temperature) that resulted in the calculation of the above crossover/perveance curves were measured only for a subset of operating conditions due to time constraints and, in particular, those points were selected because of their discharge stability compared to the other set points listed in Section 5.1.

As mentioned in Section 3.2.3, the perveance curve for the mixture could not be calculated because of limitations of the ion optics code, which does not allow the simulation of multiple-species plasmas, and, in addition, the approach of using the superposition principle did not produce acceptable results and, therefore, it was discarded. However, the current density of the1:4 Xe/Kr mixture, calculated using Eq. (5-16), is plotted in Figure 50 and compared with the crossover/perveance curve for pure xenon and pure krypton with the grey area representing the current density between the maximum value at the centre of the grid and the minimum at the periphery of the grid. The perveance limits for the pure gases represent the two extremes within which the perveance limit of the mixture should be. Even using this approach for the estimation of the perveance limit of the mixture, it is evident that the thruster has been operated at operating conditions that exceed the “perveance limit”.

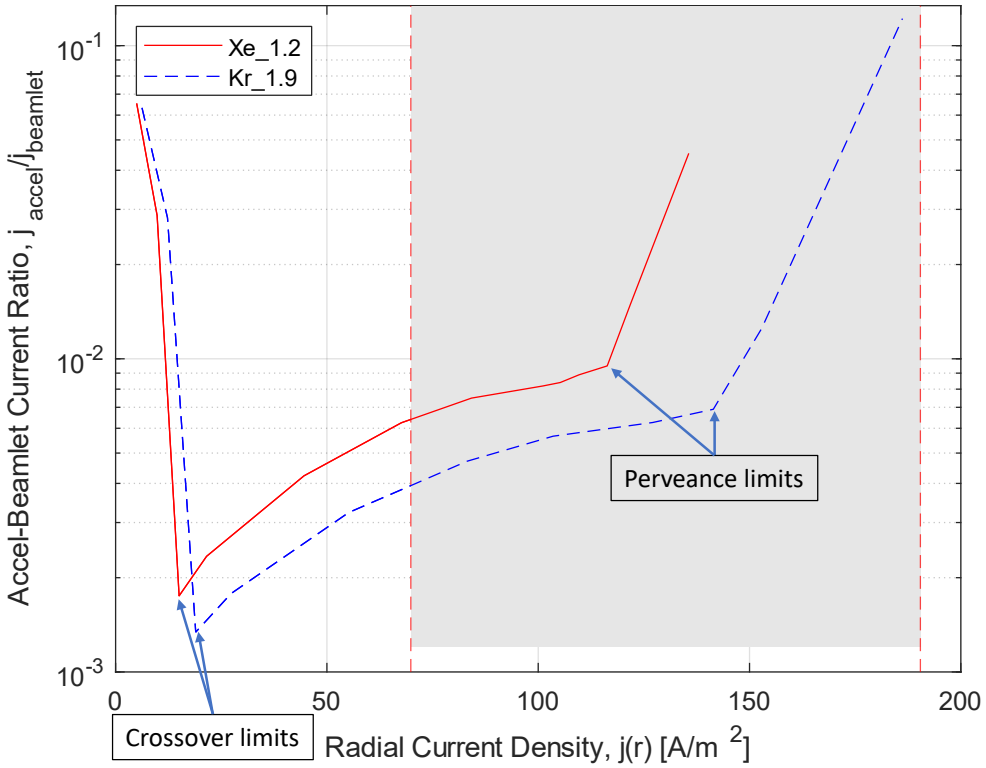

Figure 50 – Perveance limits for pure Xe and pure Kr as function of current density for the mixture

5.3 Simulated Results with a 0-D Model

In Section 5.1.1, the discharge loss trends obtained experimentally have been shown, and the plots were defined as trends instead of performance curves, since performance curves are normally taken at constant beam current and discharge voltage, so that the efficiency of producing and delivering ions to the beam is not masked by changes in the discharge voltage or average plasma density at the grids. In this section, the experimental data are compared to the theoretical results obtained using the 0-D model described in Section 3.2.1.

The performance curves shown in Figure 51 and Figure 52 for xenon and krypton (case Xe_1.2(2) and case Kr_1.5 from Table 2, respectively) are plotted at constant beam current and discharge voltage for each experimental point, instead that at constant discharge current as done in Section 5.1.1.

These figures allow the simulation of the behaviour of the thruster at higher propellant utilisation efficiencies compared to those obtained during the experimental campaign, limited by the main flow rates as shown in Table 2. The resulting curves confirm that the discharge losses are nearly the same for the two propellants at lower utilisation efficiencies, while a penalty in the propellant efficiency of about 8% was estimated for krypton at comparable values of the discharge loss (e.g. 400 W/A).

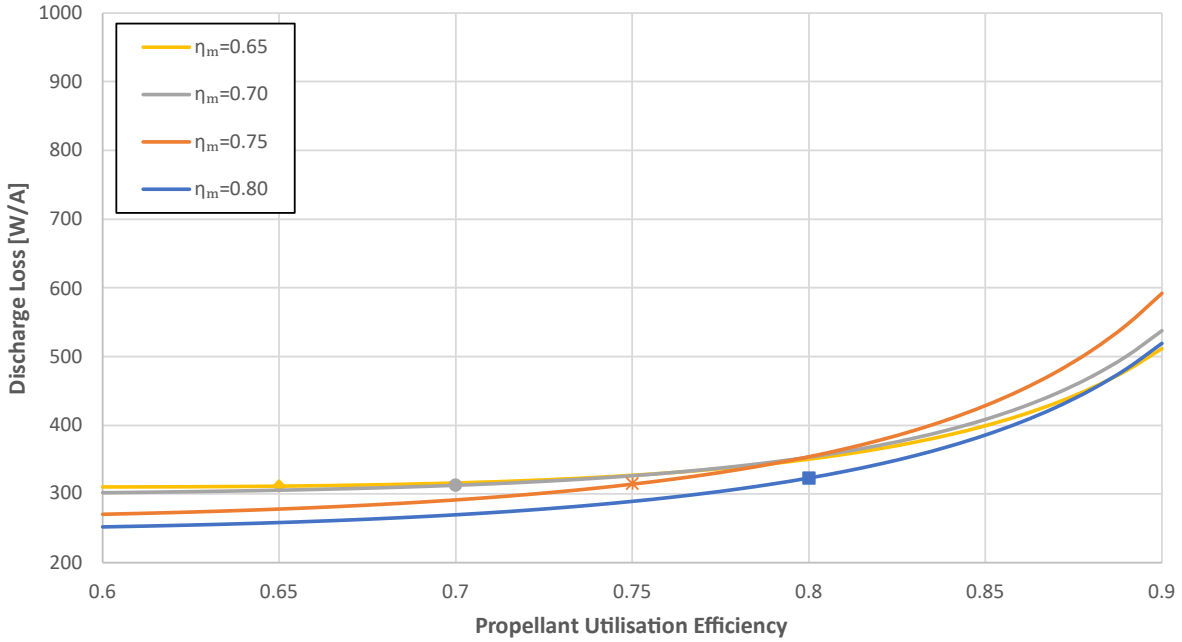

Figure 51 – 0-D Simulated discharge losses for xenon (case Xe_1.2(2))

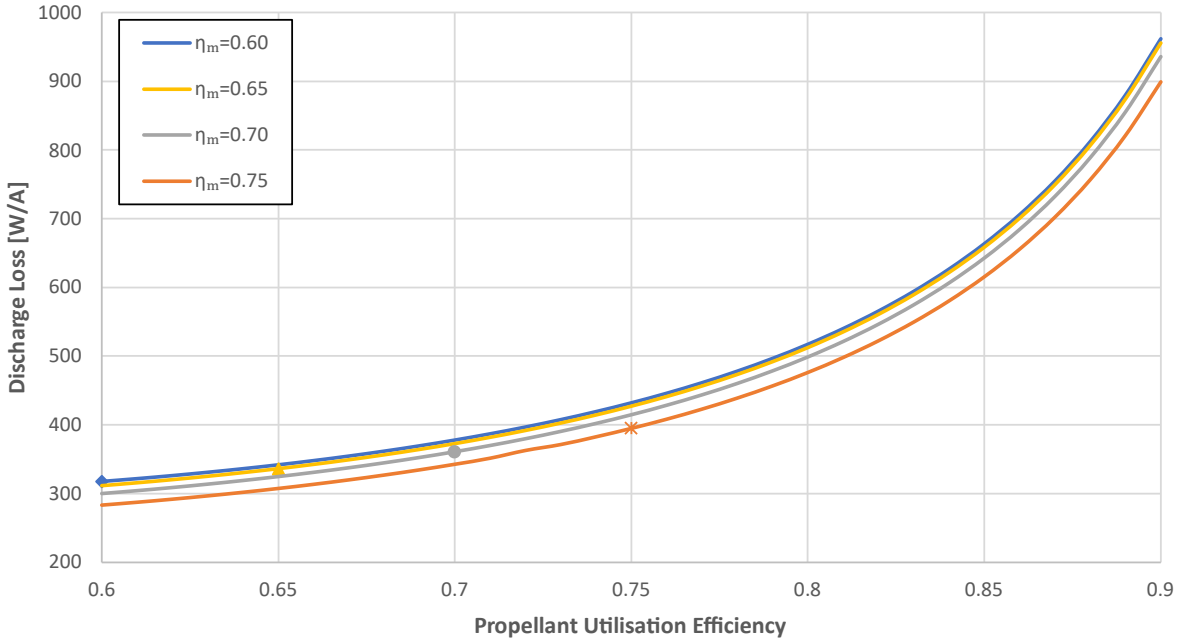

Figure 52 – 0-D Simulated discharge losses for krypton (case Kr_1.5)

Finally, the results obtained using the 0-D model allow the revisitation of the anomalous behaviour seen in the experimental results and reported in Section 5.1.4 in Figure 39 and Figure 40. However, Figure 53 shows similar results, and it is mostly expected since the 0-D model takes as an input the beam current, which is the main parameter that affects the outcome seen in the previous section.

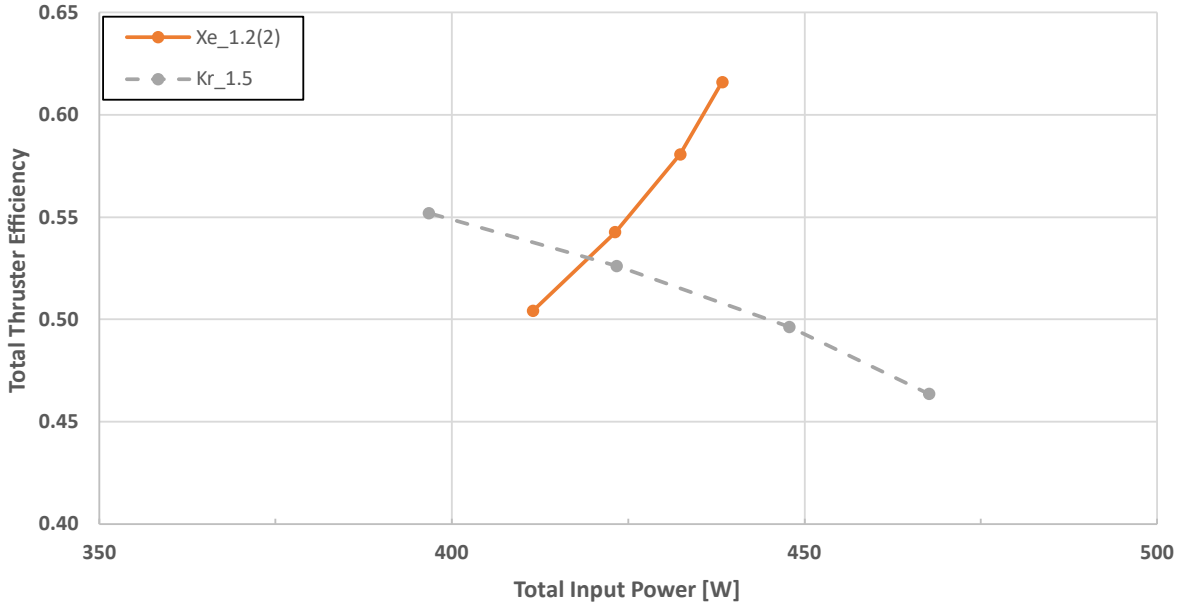

Figure 53 – Simulated total thruster efficiency as a function of total input power

5.4 Performance Results of the Hollow Cathode

The hollow cathode experimental campaign was carried out at the University of Southampton TDHVL facilities and the setup was described in detail in Section 4.1.2 following the test plan reported in Section 4.3.2. In addition, the anode ring (consisting of a stainless-steel tube 100 mm in length and 100 mm in diameter) was positioned 10 mm downstream of the keeper orifice. The hollow cathode was operated in both spot and plume mode, allowing the measurement of the operating parameters at different operating conditions with xenon, krypton, and the 1:4 Xe/Kr mixture. As mentioned in Section 2.2.4, a hollow cathode in diode configuration has two distinct modes of operation, called spot mode and plume mode, with the former one being more desirable due to more stable and less noisy plasma. An example of the visual difference between the two modes is shown in Figure 54.

The preliminary results for operations of the HC40 cathode with xenon, krypton and the 1:4 Xe/Kr mixture are presented here, with a particular focus on the transition from spot to plume mode and the relative operating conditions (i.e. mass flow rate, and anode/keeper voltages and currents). The configuration set points were:

- Keeper current = 0 (floating), 2 and 4 A;
- Anode current = 3, 5, 10, 15, 20 and 25 A.

The minimum flow rates needed for spot mode for each gas at different operating conditions are shown in Table 4, Table 5 and Table 6. The missing data points are due to limitations in the maximum flow rate allowed by the MFCs used in the testing (and to corrupted data for the mixture with floating keeper at $I_a = 20$ A).

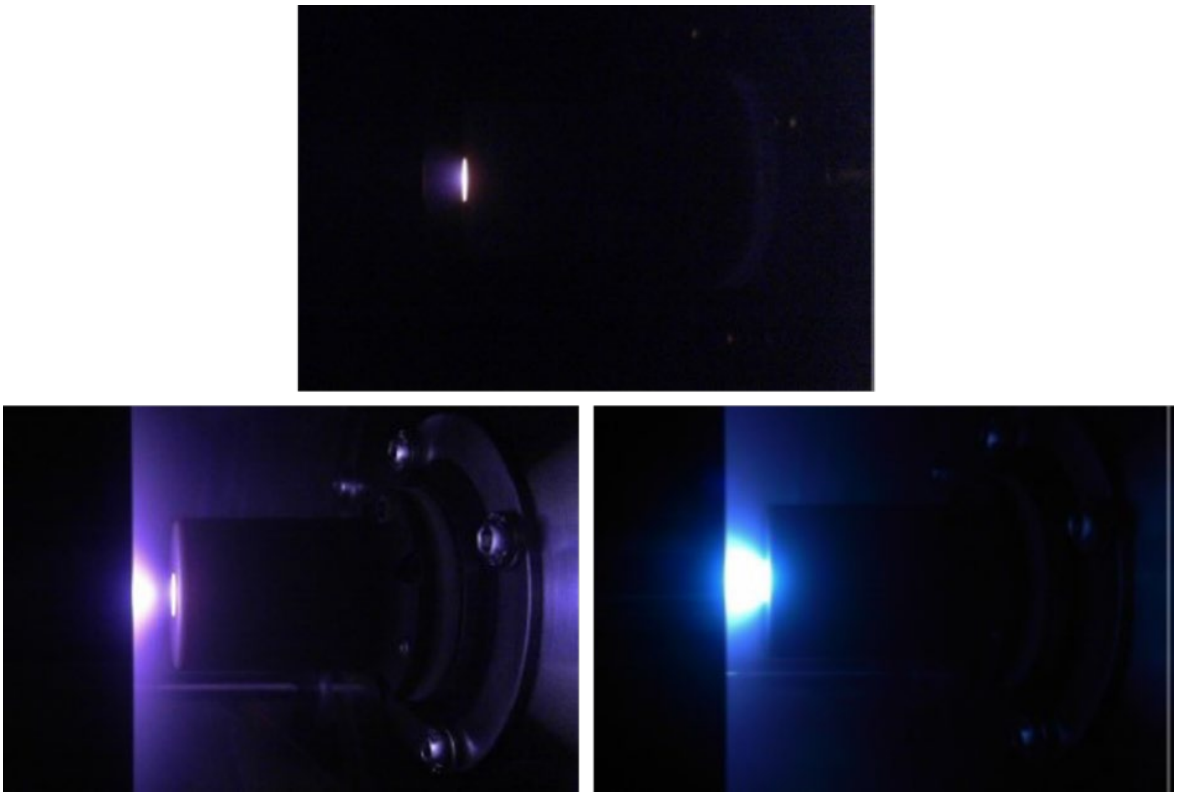

Figure 54 – Example of operation in spot mode (top, Xe)
and plume mode (Xe bottom right, Kr bottom left)

Table 4 – Results of HC40 testing with different gases for spot-to-plume transition
(Keeper Current I_k=0 A, floating keeper)

GAS	Anode Current	3 A	5 A	10 A	15 A	20 A	25 A
Xenon	Flow Rate [sccm]	–	–	20	15	13	11
	Anode Voltage [V]	–	–	12.7	12.8	14.0	15.8
	Keeper Voltage [V]	–	–	7.4	6.0	5.3	9.0
Krypton	Flow Rate [sccm]	–	–	55	42	35	30
	Anode Voltage [V]	–	–	12.9	12.1	12.1	13.3
	Keeper Voltage [V]	–	–	7.8	6.2	5.3	4.7
1:4 Xe/Kr	Flow Rate [sccm]	–	85 (17+68)	55 (11+44)	45 (9+36)	–	30 (6+24)
	Anode Voltage [V]	–	15.7	13.0	12.1	–	13.5
	Keeper Voltage [V]	–	11.2	7.8	6.6	–	5.1

Table 5 – Results of HC40 testing with different gases for spot-to-plume transition (Keeper Current I_k=2 A)

GAS	Anode Current	3 A	5 A	10 A	15 A	20 A	25 A
Xenon	Flow Rate [sccm]	–	–	15	12	10	9
	Anode Voltage [V]	–	–	12.7	13.6	16.5	16.4
	Keeper Voltage [V]	–	–	12.4	11.5	11.2	11.3
Krypton	Flow Rate [sccm]	57	52	42	36	30	27
	Anode Voltage [V]	15.7	14.1	12.8	12.0	12.8	13.8
	Keeper Voltage [V]	17.4	14.9	12.8	11.7	11.3	11.1
1:4 Xe/Kr	Flow Rate [sccm]	–	55 (11+44)	45 (9+36)	35 (7+28)	30 (6+24)	25 (5+20)
	Anode Voltage [V]	–	14.0	12.4	12.4	12.9	14.4
	Keeper Voltage [V]	–	14.6	12.3	11.6	11.0	10.9

Table 6 – Results of HC40 testing with different gases for spot-to-plume transition (Keeper Current I_k=4 A)

GAS	Anode Current	3 A	5 A	10 A	15 A	20 A	25 A
Xenon	Flow Rate [sccm]	–	14	12	10	9	7
	Anode Voltage [V]	–	12.1	12.3	15.0	15.3	19.1
	Keeper Voltage [V]	–	13.0	13.1	12.3	12.2	12.5
Krypton	Flow Rate [sccm]	37	36	33	30	27	24
	Anode Voltage [V]	13.1	12.6	12.2	12.2	12.8	14.3
	Keeper Voltage [V]	30.5	15.8	13.4	12.4	12.0	12.0
1:4 Xe/Kr	Flow Rate [sccm]	45 (9+36)	40 (8+32)	35 (7+28)	30 (6+24)	25 (5+20)	20 (4+16)
	Anode Voltage [V]	13.1	12.7	12.1	12.2	13.7	15.9
	Keeper Voltage [V]	19.2	15.6	13.0	12.3	12.1	12.1

5.4.1 Discharge Voltage Dependence on Flow Rate

As mentioned in Section 4.3.2, the spot-to-plume transition was achieved by variation of the flow rate at constant discharge current, while voltage measurements were taken in order to identify noise in the anode voltage from the power supply reading. This transition with decreasing flow rate is visible in Figure 55 for different discharge and keeper currents. From this figure, it is possible to note that the spot-to-plume transition is dependent on the propellant, with higher values of flow rate required to maintain the spot mode as the propellant atomic weight is reduced. In addition, the anode potential of the various propellants when in spot mode are arranged according to their ionisation potentials, with the mixture showing a behaviour similar to pure krypton, both for the transition flow rates and for the discharge voltages in spot mode.

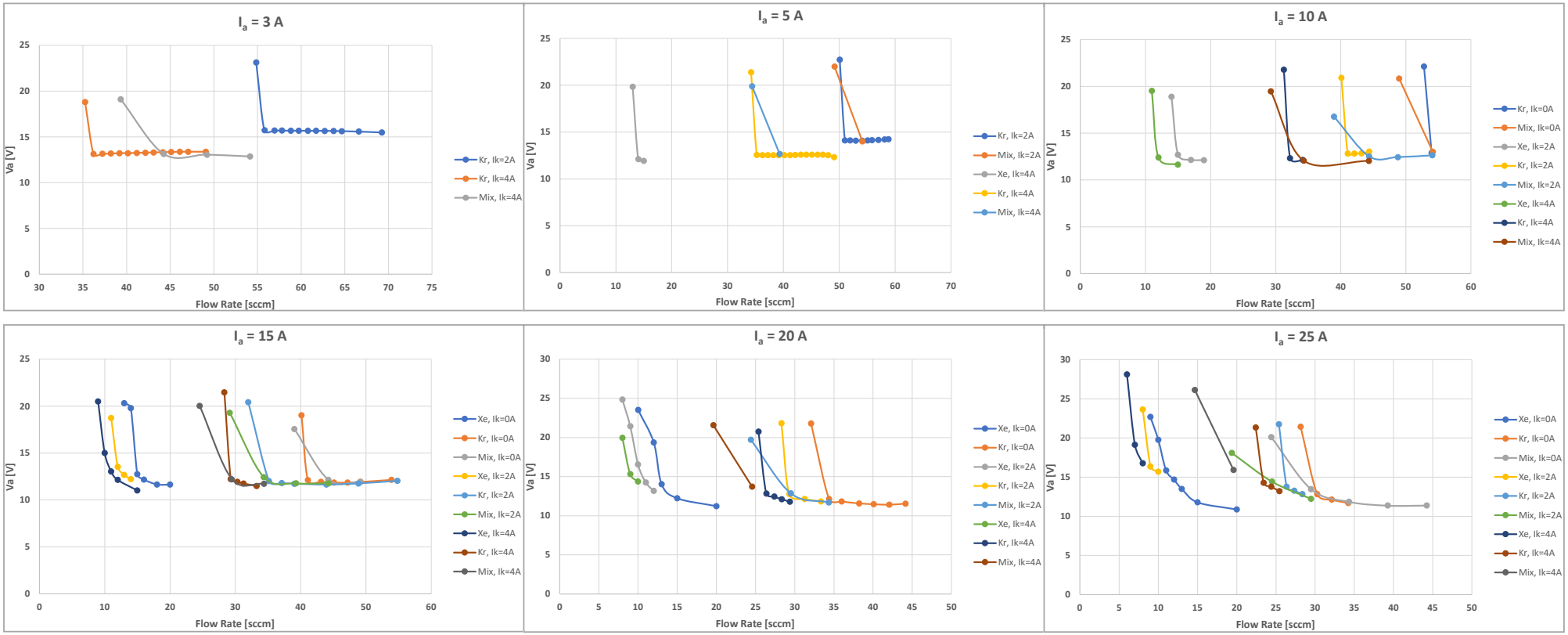

Figure 55 – Discharge voltage as a function of flow rate in sccm

Figure 56 shows the minimum flow rate before the spot-to-plume transition for different set points, and it is evident that higher mass flow rates were necessary to maintain the cathode in spot mode when operating with krypton and the mixture compared to xenon. Overall, two general trends can be identified:

- Xe vs Kr: Kr flow rate is around 2 times higher than Xe flow rate, and the ratio is almost constant across the different anode and keeper currents.
- Kr vs mixture: have a very similar behaviour and, specifically at lower anode currents, the total mixture flow rate slightly exceeds the Kr flow rate, but the values converge at higher anode currents.

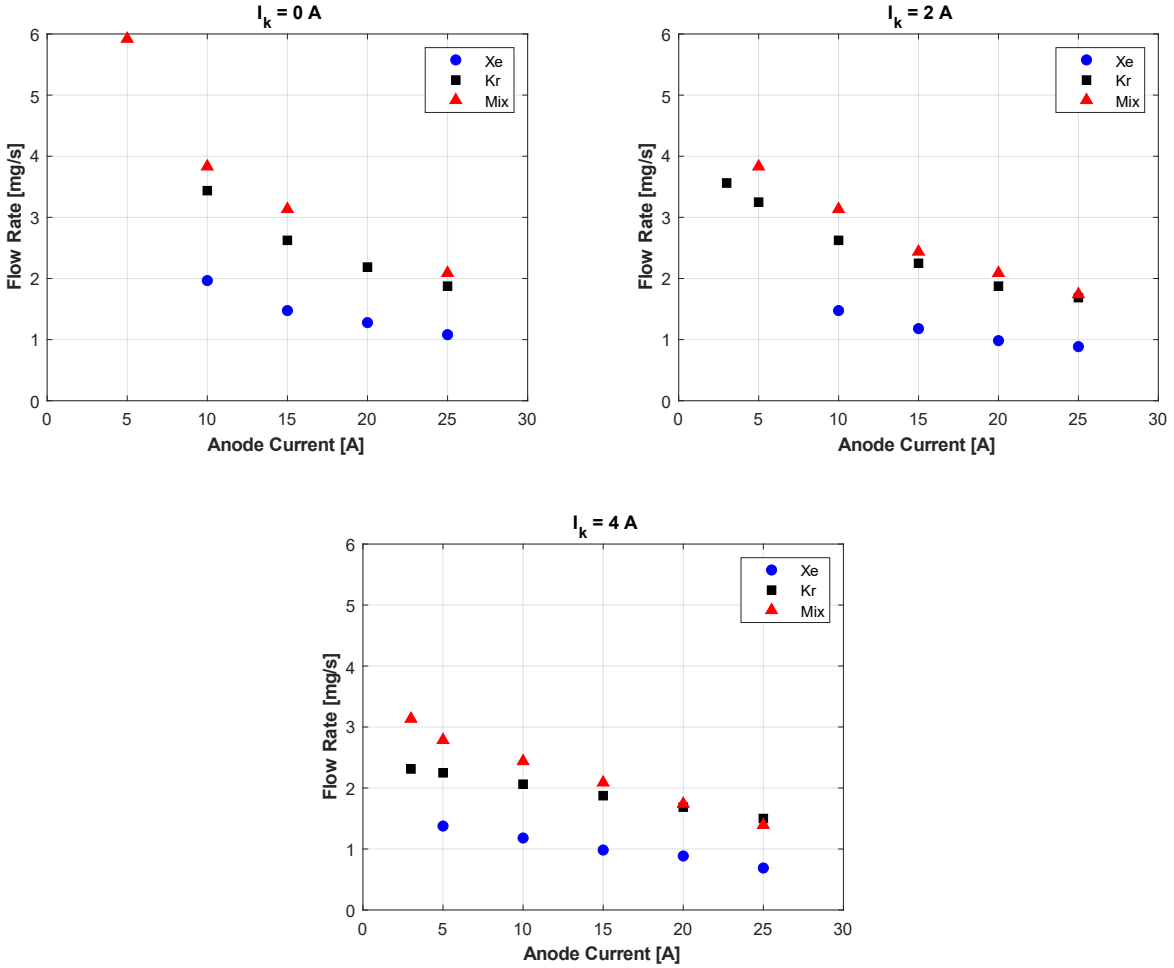

Figure 56 – Minimum flow rate before spot-plume transition for different set points

By analysing these results, it is evident that the flow rates with alternative propellants are much closer to those with xenon in the full thruster configuration as shown in Section 5.1, as expected from the literature.

5.4.2 Discharge Voltage Dependence on Anode and Keeper Current

Similarly to Figure 56, Figure 57 summarises the discharge voltage before the spot-to-plume transition for the considered range of anode and keeper currents. This figure shows that the anode voltages for the three propellants are generally comparable at lower anode currents and for the various keeper setpoints, but they are slightly higher (2-4 V) for xenon compared to krypton at higher anode currents, with the mixture results between the other two gases. This counter-intuitive behaviour with xenon can be explained by the fact that the anode voltages for the alternative propellants were obtained at much higher flow rates compared to those with xenon and, therefore, a slightly higher voltage was required to maintain the stability of the plume mode.

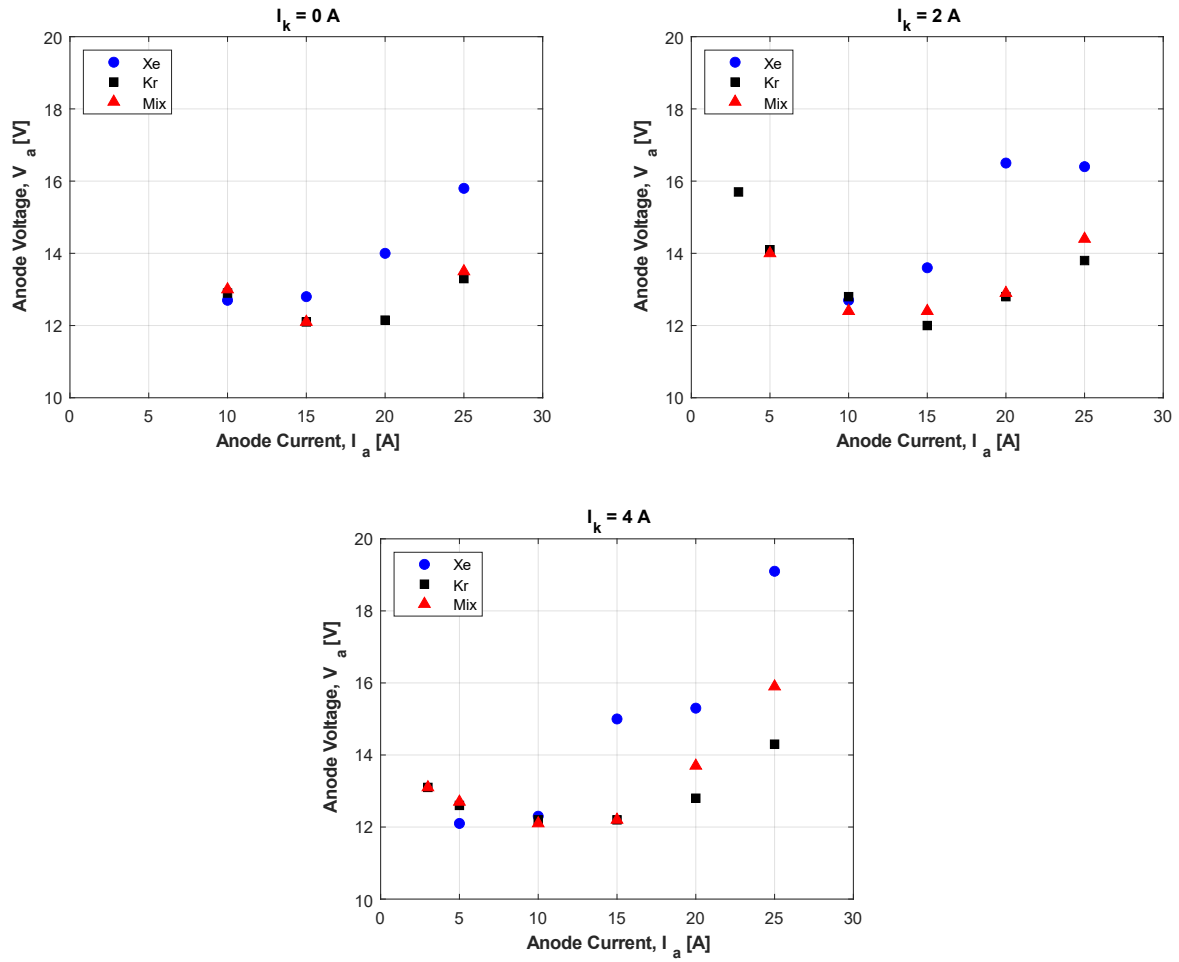

Figure 57 – Discharge voltage before the spot-to-plume transition for different set points

5.4.3 Keeper Voltage Dependence on Anode and Keeper Current

Finally, Figure 58 shows the keeper voltages before the spot-to-plume transition for the considered operating points: except for a few data points, the keeper voltage does not seem to be strongly influenced by the change of propellant or by the transition from spot mode to plume mode (not shown here), confirming the very scarce results available in the literature [42].

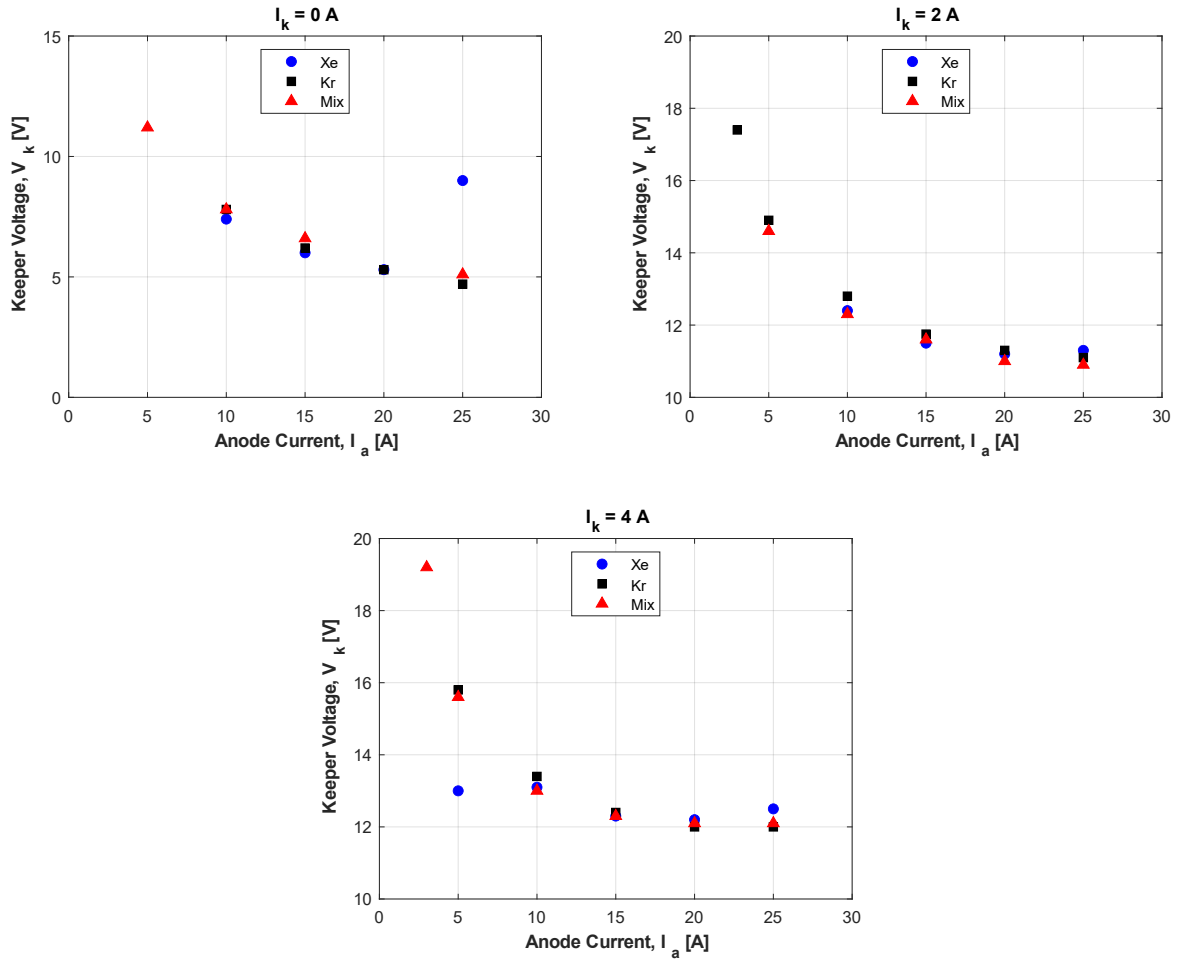

Figure 58 – Keeper voltage before spot-plume transition for different set points

It is evident that these tests and their respective results do not provide a definitive analysis of the operating conditions of a hollow cathode running with different gases, but, as reported in Section 4.3.2, they were only supposed to provide an initial benchmark and validation for these operating conditions. Unfortunately, further tests that were planned to be conducted using various cathode configurations (e.g. changing orifice size, the distance between orifice and keeper, etc.) and with the support of additional diagnostics tools (e.g. Langmuir probe, emissive probe, E×B probe) to verify these initial results and to measure the plasma parameters could not be carried out due to unforeseen events.

5.5 Summary

In this chapter, the experimental characterisation of a small ring-cusp gridded ion engine and a hollow cathode using xenon (as baseline) and the two selected alternative propellants (i.e. krypton and a 1:4 Xe/Kr mixture) has been presented with a particular emphasis on the performance results and measurements from internal diagnostics tools. The results of the test campaign have shown that:

- the performance reduction when using krypton compared to xenon are comparable with the data available in the literature for thrusters of different sizes and discharge chamber configuration (e.g. Kaufman as shown in Section 2.3.2, RF in Ref. [104] and ECR in Ref. [105])
- some of the initial results for the mixture are encouraging for its viability and suitability to be used as propellant in GIEs.

These results represent the worst-case scenario for alternative propellants, but they allow the identification of possible modifications (e.g. cathode geometry and ion optics geometry) that could reduce the gap between xenon and the selected alternative propellants.

A very relevant outcome of the measurements of the plasma parameters inside the discharge chamber is that the profile of the current density at the ion optics seems to be independent of the choice of propellant, and this result can be used to design ion optics at different operating conditions and with different propellants than the ones being investigated.

Chapter 6 Conclusions and Future Work

The main objective of this thesis is to assess the feasibility of replacing xenon as the main propellant, and to investigate the impact of alternative propellants on a gridded ion engine propulsion system designed for xenon. In fact, this gas is the rarest of Earth's stable elements, and its limited availability and high cost can be a severe constraint for the expected future growth of the sector. This aspect has been boosted by the "New Space" revolution, which demands cheaper and simpler systems even at the cost of lower performance. This chapter summarises the main conclusions drawn from the present work.

6.1 Summary of Research Findings

A comprehensive review of the published data on the usage of alternative propellants, such as other noble gases, iodine, and other more exotic propellants (i.e. Buckminsterfullerene and Adamantane), was carried out as an initial assessment. This was followed by a qualitative and quantitative analysis of the impact of the alternative propellants on the different parts of a GIE's systems and on performance. Based on these preliminary results, krypton appears to be an effective alternative if all of the selected impacts are taken into consideration, since only minimal variations to the existing propulsion systems are expected.

Krypton as propellant has attracted the interest of the EP community for a long time (between the early 1980s and the mid-1990s) as a possible propellant for use in GIEs and as an alternative to xenon, due to its higher specific impulse, relative abundance, and lower price compared to xenon. However, its use has been limited due to its relatively poor performance with respect to xenon. In particular, no publications are available on either the use of krypton or the difference in performance between xenon and krypton in a small ring-cusp gridded ion engine. Furthermore, another unexplored (with GIEs) alternative propellant is the mixture of Xe/Kr in their production ratio of 1:4, which is very attractive from an economic point of view (e.g. could offer a 15-fold cost saving when compared to pure xenon, and 2-3 times cheaper when compared to pure krypton [19]).

Following the selection of the alternative propellants, the main parameters used to evaluate the performance of a GIE have been revised to outline the impact of the propellant atomic mass for the single gas case, and their formulation has been completely rederived to estimate such parameters for the mixture of gases and multi-species plasmas to complement the existing literature.

Similarly, the performance models (i.e. 0-D model for discharge chamber, technique for discharge-only operation, and ion optics model) available in the literature for xenon have been expanded to allow their use with krypton and, more importantly, with the mixture.

A small ring-cusp gridded ion engine and a hollow cathode (in discharge-only mode and diode configuration, respectively) have been experimentally characterised with xenon (as baseline), krypton and a 1:4 Xe/Kr mixture. The performance reduction when using krypton compared to xenon reflects the data available in the literature for thrusters of different sizes and types, while some of the initial results for the 1:4 Xe/Kr mixture are encouraging for its viability and suitability to be used as propellant in GIEs, even if the main difficulty of matching the ion optics to two atomic species could complicate its adoption. However, it is worth noting that these results represent the worst-case scenario for alternative propellants, but they allow the identification of possible modifications (e.g. cathode geometry and ion optics geometry) that could reduce the gap between xenon and the selected alternative propellants, making them a more attractive proposal for future use.

Finally, the measurements of the plasma parameters inside the discharge chamber provide an interesting overview of the behaviour of the propellants in the proximity of the ion optics, and a very relevant and noteworthy outcome is that the profile of the current density at the ion optics seems to be independent of the choice of propellant.

The novel contributions are summarised below:

Ring-Cusp Gridded Ion Engine

- No prior performance characterisation of a GIE with a mixture of Xe/Kr was carried out, and it represents a novelty and a relevant starting point for future investigations.
- The baseline performance gap existing between xenon and alternative propellants (i.e. krypton and the 1:4 Xe/Kr mixture) with a small ring-cusp GIE designed for xenon has been assessed. This gap represents the worst-case scenario for alternative propellants, but also the starting point for the identification of possible modifications (e.g. ion optics and cathode geometry) that could mitigate the difference in performance.
- The performance reduction when using krypton compared to xenon reflects the data available in the literature for thrusters of different sizes and types as described in Section 2.3.2 for Kaufman and ring-cusp thrusters, in Ref. [104] for RF thrusters, and in Ref. [105] for microwave thrusters. This similarity in the performance gap across various systems optimised for xenon and run with krypton without any modifications is also described in Ref. [106] for Hall Effect thrusters and it could be associated with the

inherent penalty when using the lighter gas compared to xenon due to their physical properties.

- The mixture Xe/Kr offers significant cost savings [19] and some of the initial results (e.g. discharge losses' behaviour, where the presence of xenon mitigates the gap compared to pure krypton) are encouraging for its viability and suitability to be used as propellant in GIEs, even if the main difficulty of matching the ion optics to two atomic species could complicate its adoption.
- The measurements of the plasma parameters inside the discharge chamber provided an interesting overview of the behaviour of the propellants in the proximity of the ion optics, such as:
    - The plasma density and electron temperature profiles normalised to the centre peak look to be essentially insensitive to the propellant used, except for the krypton's temperature profile that remains flatter towards the edge of the grid compared to the peak value.
    - The beam flatness for xenon and krypton is very similar and it confirms that significant differences in this parameter can be usually associated with the topology and values of the magnetic field inside the discharge chamber.
    - A relevant and noteworthy outcome is that the profile of the current density at the ion optics seems to be independent of the choice of propellant.

Hollow Cathode

- This is the first time that the characterisation of the discharge behaviour of a hollow cathode in diode configuration with a Xe/Kr mixture in their production ratio of 1:4 was carried out.
- Although the discharge efficiency is expected to decrease, the diode tests with the alternative propellants have demonstrated that operation with these gases is feasible at the cost of a significant increase (around 2 times higher) in flow rates, but very little increase in the operating potentials.
- Similarly to the case in full thruster configuration, this performance gap represents the worst-case scenario for krypton and the mixture since the tests were carried out with a hollow cathode optimised for xenon.

6.2 Recommendations for Future Work

The investigations presented in this thesis delineate the motivation for krypton and the viability of the 1:4 Xe/Kr mixture as propellant in gridded ion engines. Additionally, there are remaining areas in which the understanding of the underlying physics of the operation can be enhanced to

support performance and lifetime optimisation. The following list of future work seems the next logical step following these present results:

1. In Section 4.3, the original plan for the testing of the small ring-cusp GIE and of the hollow cathode in diode mode was presented. Such a plan relied on:
   a. testing the engine with the three propellants over a wide range of operating conditions while varying some design parameters (e.g. the cathode orifice's size) and mapping the plasma parameters (i.e. electron temperature, plasma potential, and plasma density) and their spatial distribution inside the discharge chamber with a Langmuir probe;
   b. testing the cathode with the three propellants over a wide range of operating conditions using different cathode configurations (e.g. orifice shape, size, and the relative position between cathode tube and keeper, etc.) and with the addition of a comprehensive diagnostics setup (including Langmuir and emissive probes, E×B probe).

   Unfortunately, due to various unforeseen events, only a basic performance mapping was completed for both setups and the results were presented in Chapter 5. Therefore, a natural recommendation would be to carry out and complete the initial plan in order to have a detailed picture of the performance with the selected alternative propellants and of the internal thruster physics.
2. Some of the results obtained with alternative propellants (e.g. discharge loss performance and independence of the current density profiles to the choice of the propellant) are relevant and worth investigating further, possibly in full beam extraction configuration.
3. The conflicting and not very clear behaviour identified in Section 5.1.4 about the calculated power and beam current trends should be investigated further to identify the reasons and patterns behind such an outcome.
4. The results for the mixture presented in Chapter 5 are promising and further investigations on its behaviour inside an electric propulsion system could help to extend the understanding of the plasma physics of mixtures and, possibly, answer some of the unknowns described in Section 2.3.3 about the impact on the various components of these thrusters, such as the plasma sheath at the grids, the cathode, etc.
5. Following the point above, the identification of a pattern that would allow the extension of the results to various mixing ratios would be beneficial from both a purely physical and performance point of view.
6. Although the functionality and viability of using these alternative propellants have been shown, the assessment of the impact on the lifetime of the various components (mainly cathode and ion optics) together with the demonstration of a long lifetime is critical for the use in space missions.

This is particularly complicated in the case of the mixture by the difficulty of matching the ion optics to two atomic species and a compromise will be required on either performance or lifetime optimisation.

The recommended future work can be divided into two different development paths:

- Improvement of the performance of the thruster with krypton to make it a suitable alternative to xenon for specific missions
- Further investigation of the feasibility of using mixtures (in different mixing ratios) to identify the possible advantages compared to the pure gases.

The first point has a much higher readiness level compared to the second point. In fact, the effort required to progress the use of krypton so that it would be able to compete with xenon in selected scenarios can be summarised as follows: initially, the modifications (i.e. ion optics and cathode geometry) that have been identified as the most probable in achieving a reduction in the performance gap between krypton and xenon should be pursued with an extended experimental campaign in order to establish the configurations and operating conditions that are more favourable for krypton. Following this, a substantial lifetime demonstration is required because, as highlighted in previous chapters, the operating conditions required to run the thruster with krypton (e.g. higher discharge currents, more energetic ions impacting the ion optics, etc.) indicate that a shorter lifetime is expected and, therefore, mitigating the life limiting mechanisms would be beneficial to further extend operational lifetime of the thruster, and to boost the attractiveness of krypton. Finally, the development of the electric propulsion system towards mission configuration would require an optimisation of all the involved subsystems (e.g. storage, PPU, FCU, etc.) to support the operations with krypton.

On the other hand, the use of mixtures with a gridded ion engine is still at a much more immature stage. In fact, even if an initial feasibility study was carried out in this work, there is still plenty of work to be done regarding this subject to make the Xe/Kr mixture competitive with the pure gases. The initial focus would be on the understanding of the plasma physics of mixtures and, in particular, on their interaction with the various components of the GIEs, such as the plasma sheath at the grids, the cathode, etc. Afterwards, the focus could be moved towards the identification of the operating conditions which would make the use of the mixture advantageous compared to the pure gases. Finally, the steps described above for the development of a thruster with krypton can be replicated for the mixtures.

Appendix A Propellants' Properties

A.1 Availability, Production Process, and Trends in Production and Prices of Xenon

Xenon has been the selected propellant for EP since the 1980s and its properties satisfy several criteria listed in Table 1 in Section 2.3: high atomic mass and low first ionisation potential allow for higher thrust efficiency compared to the other noble gases, good storability due to its high density and low tank mass-to-propellant mass ratio when stored in a supercritical state, and high compatibility with spacecraft materials since it is an inert gas. However, xenon presents some disadvantages: higher atomic mass compared to other gases means lower specific impulse, lower density compared to liquid and solid propellants, and, most importantly, scarce availability (and, consequently, high cost). In particular, its scarcity is predicted to become more and more relevant in the future due to the increasing demand not only in the space propulsion sector, but in many other industries: in 2017, the space industry accounted only for 23% of the global demand compared to 34% for the lighting industry (in decline due to the increased use of LED technology), 20% for the research industry, 14% for the electronics industry, and 8% for medical use [2].

Xenon is naturally found in the atmosphere at a concentration of only 0.087 ppmv (parts per million by volume) or 0.39 ppm (parts per million by mass). Despite the low concentration, there is a large amount of this gas in the air: based on a total estimated mass of air of $5x10^{18}$ kg, the Earth's atmosphere contains $2x10^{12}$ kg of xenon. Therefore, the amount of available xenon is limited only by how much is collected. Typically, xenon is obtained as a by-product of cryogenic air separation inside plants called air separation units (ASUs), but, because of its low concentration, only the larger ASUs (producing at least 2000 tonne/day of oxygen) are suitable for xenon collection. It should also be noted that krypton is collected during the same process because the last stream out of the plant is a mixture of these two gases. Consequently, krypton is available at a ratio of 11:1 in volume because of its greater abundance in the atmosphere (1.14 ppmv or 3.3 ppm). Alternative production approaches were described by Welle [45] in the 1990s, but they are still not as cost-effective as the method outlined above.

The price of xenon (Figure 59) depends on the balance between supply and demand and it has been highly volatile over the years due to the uncertainty of its demand and usage by the various industries and markets (Figure 60). On the other hand, because of the extraction process, the global availability of xenon is generally driven by the demand for oxygen, but it is worth noting

that the demand and supply of xenon have increased ten-fold over the last 40 years. According to the German Federal Institute for Geosciences and Natural Resources [2], the annual production of xenon in 2017 was about 72 tons (12200 m^3). In addition, as previously stated, xenon and krypton are collected together, and the price and availability of the latter are affected by the price and demand of the former: if the demand for one gas is not mirrored by the other, the production cost will need to shift towards the gas with the higher demand (usually, xenon)(Figure 60-Figure 61). It is worth noticing that the supply of krypton is roughly 10 times more than the supply of xenon because of their natural ratio of 11:1 in volume.

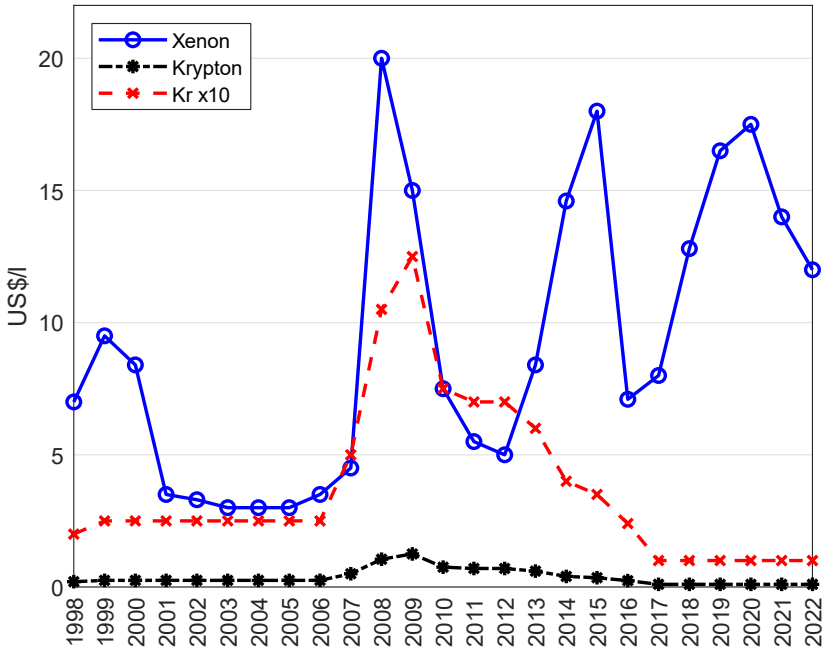

Figure 59 – Wholesale price (trend since 1998 and forecast from 2018) for Xe and Kr (in US$/l)[2]

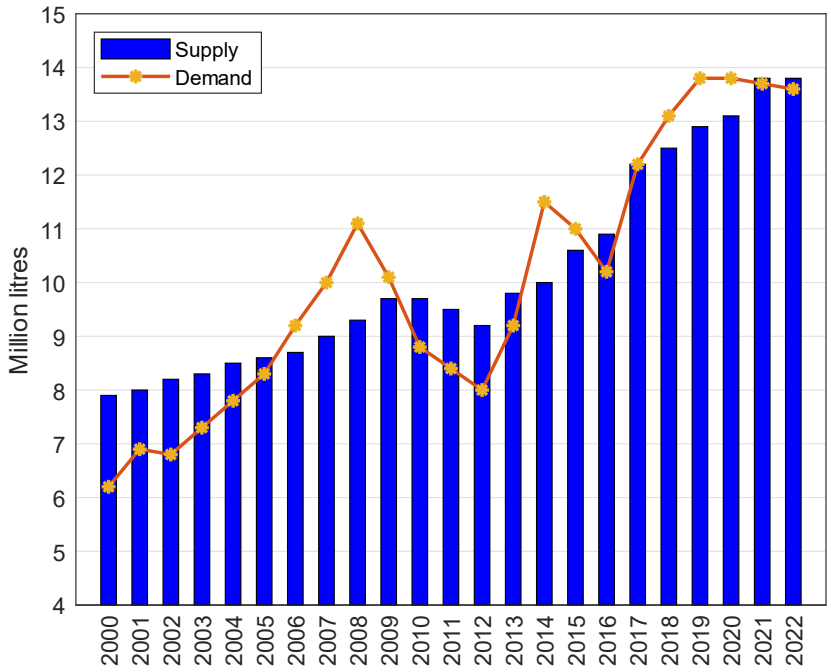

Figure 60 – Xenon supply and demand since 2000, including forecast from 2018 [2]

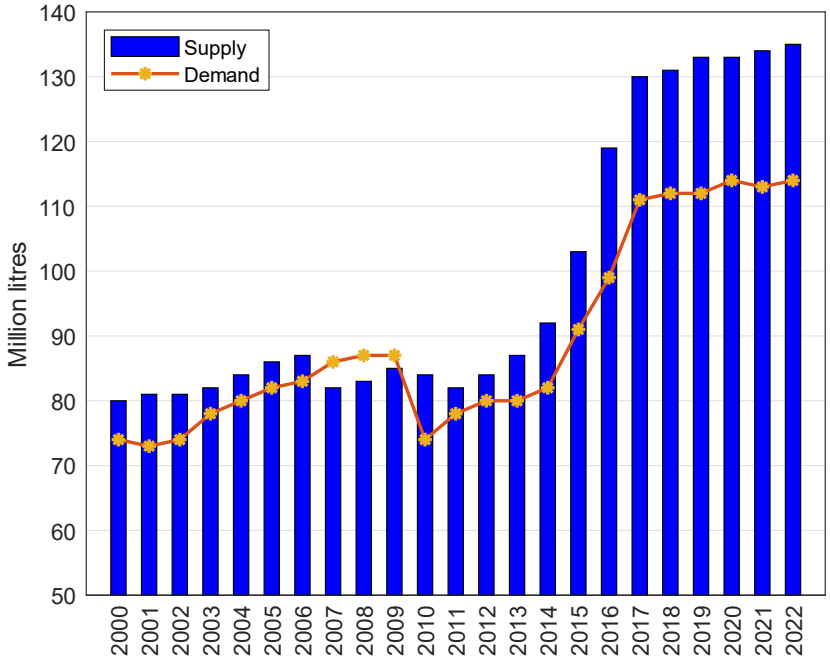

Figure 61 – Krypton supply and demand since 2000, including forecast from 2018 [2]

Because of xenon availability and cost problems, the search for viable alternative propellants has gained momentum in the last decade thanks to the revival of EP technologies targeting a growing diversity of spacecrafts, missions, and manoeuvres. Furthermore, the “New Space” era with the related development of LEO mega-constellations has exacerbated these issues and it has had a positive effect on this search for alternative propellants.

A.2 Physical Properties of the Alternative Propellants

In Section 2.3, an overview of the propellants used with GIEs has been provided and their properties are reported in Table 7 (STP stands for Standard Temperature and Pressure, 273.15 K and 101325 Pa). It is worth highlighting that the listed relative cost compared to xenon is given as a reference, since the price of each propellant is highly dependent on the balance between supply and demand, and it is highly volatile over the years due to the uncertainty of demand and usage by the various industries and markets.

Table 7 – Alternative propellants' physical properties [107] and relative cost [108]

Propellant	*Mass* [AMU]	*State @ STP*	*1st / 2nd Ionisation energy* [eV]	*Melting / boiling point* [K]	*Critical temperature* [K] / *pressure* [MPa]	*Density* [g/cm³] *@ STP*	*Relative Cost (vs Xe)*
Xe	131.3	Gas	12.13 / 20.97	161.4 / 165.1	289.7 / 5.8	0.0059	1
Kr	83.8	Gas	14 / 24.36	115.8 / 119.7	209.5 / 5.5	0.0037	0.16
Ar	39.9	Gas	15.76 / 27.63	83.8 / 87.3	150.7 / 4.9	0.0018	0.0005
I_2 (I)	253.8 (126.9)	Solid	9.3 / - (10.45 / 19.13)	386.9 / 457.6	819 / 11.7	4.933	0.02
C_{60}	720.6	Solid	7.5 / 12	sublimate @ 823	-	1.65	55.6
$C_{10}H_{16}$	136.2	Solid	9.23 / -	sublimate @ 543	-	1.07	0.56
Hg	200.6	Liquid	10.44 / 18.76	234.3 / 629.8	1764 / 167	13.534	0.02

A.3 Propellants' Density and Tankage Mass Fraction

The propellants considered in this report are naturally in the gaseous state and they need to be stored as high-pressure supercritical fluids in a volume-limited spacecraft. In this state, a substance is at temperature and pressure above its critical point, where distinct liquid and gas phases do not exist. In Figure 62, density as a function of storage pressure (above P_c) at a temperature of 325 K is plotted using the data tabulated on the NIST website [109]. The values for the mixture are calculated using the formula for the density of a mixture. It is evident that replacing xenon with krypton or the Xe/Kr mixture causes substantial penalties, even increasing the pressure considerably.

The highlighted points are those typically adopted on spacecraft to store gaseous propellants: 186 bar for xenon and 310 bar for krypton and the mixture (assuming that the tanks typically adopted for helium would be used).

The tankage fractions (given by tank mass over propellant mass) for the three propellants were calculated using Figure 62 for the densities and the following values for the tank mass-to-volume ratios: ~150 g/litre for xenon at 186 bar and ~220 g/litre for krypton and the mixture at 310 bar, which are within the common values found in the literature ([110]–[114]). The resulting tankage fractions are the following:

- The density for xenon at 325 K and 186 bar is 1808.82 kg/m^3 resulting in a tankage fraction of 0.083,
- The density for krypton at 325 K and 310 bar is 1119.35 kg/m^3 resulting in a tankage fraction of 0.197,
- The density for the mixture Xe/Kr at 325 K and 310 bar is 1314.44 kg/m^3 resulting in a tankage fraction of 0.167.

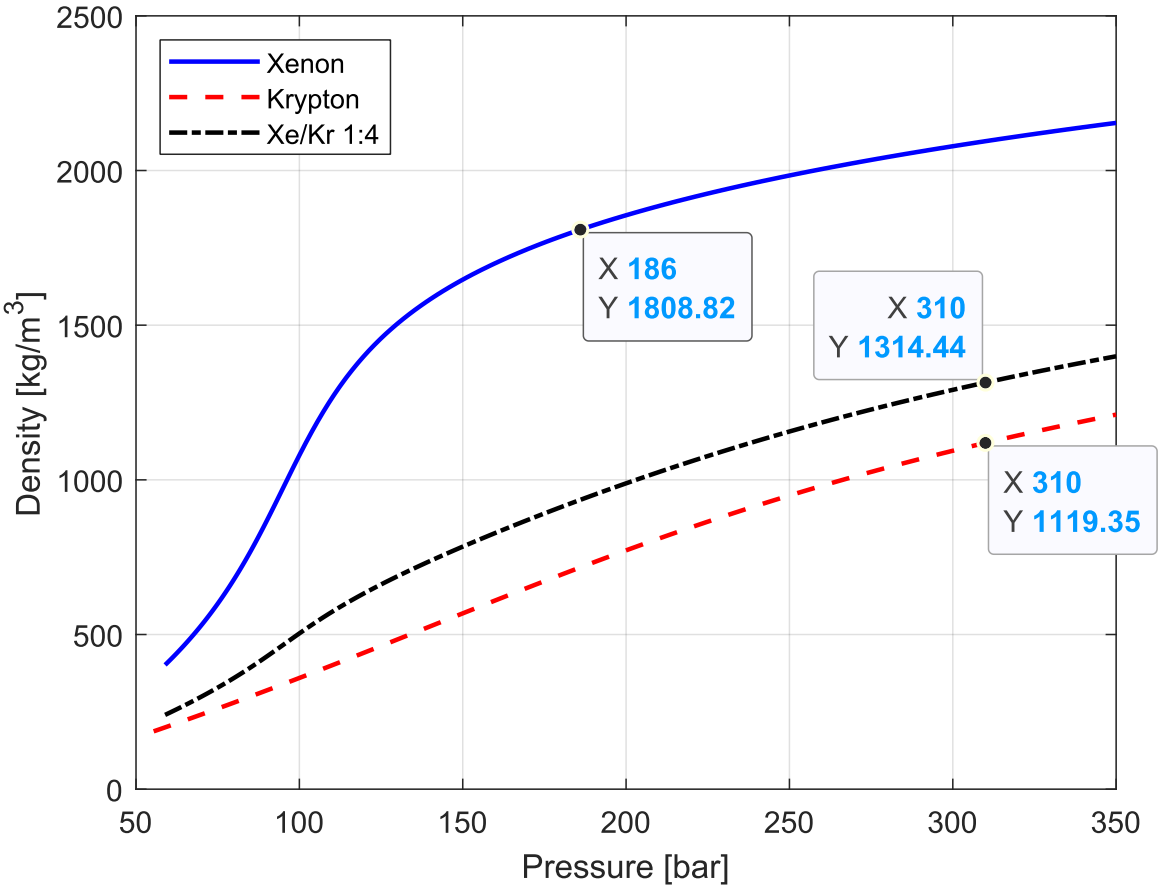

Figure 62 – Density as a function of storage pressure for different propellants at 325 K

A.4 Gas Flow Unit Conversions

Conversion between the different systems of flow units is necessary to calculate various parameters used in evaluating thruster performance, and converting flow from standard cubic centimetres per minute (sccm) to other flow units for an ideal gas at STP (Standard Temperature and Pressure, 273.15 K and 101325 Pa) conditions is achieved as follows:

for xenon: 1 sccm = 0.09830 mg/s = 4.50893×10^{17} particles/s = 7.22410×10^{-2} A eq.

for krypton: 1 sccm = 0.06248 mg/s = 4.49043×10^{17} particles/s = 7.19447×10^{-2} A eq.

A.5 Cross Sections and Reaction Rates for Xenon and Krypton

As described in Section 3.2.1 and in the following Appendix B, the collision frequencies, the cross sections and the reaction rates for the various propellants are of interest for use in modelling the thruster discharge and performance. In the following subsections, the cross section and reaction rates for xenon and krypton are reported and calculated.

A.5.1 Ionisation, Excitation, and Elastic Cross Sections

The following references were used for the cross sections for xenon and krypton:

- Ref. [115] for first ionisation, excitation, and elastic cross section for xenon and krypton,
- Ref. [116] for the second ionisation cross section for xenon
- Ref. [117] for the second ionisation cross section for krypton.

The cross sections for xenon and krypton from threshold to 100 eV from the above references are shown in Figure 63 and Figure 64, respectively.

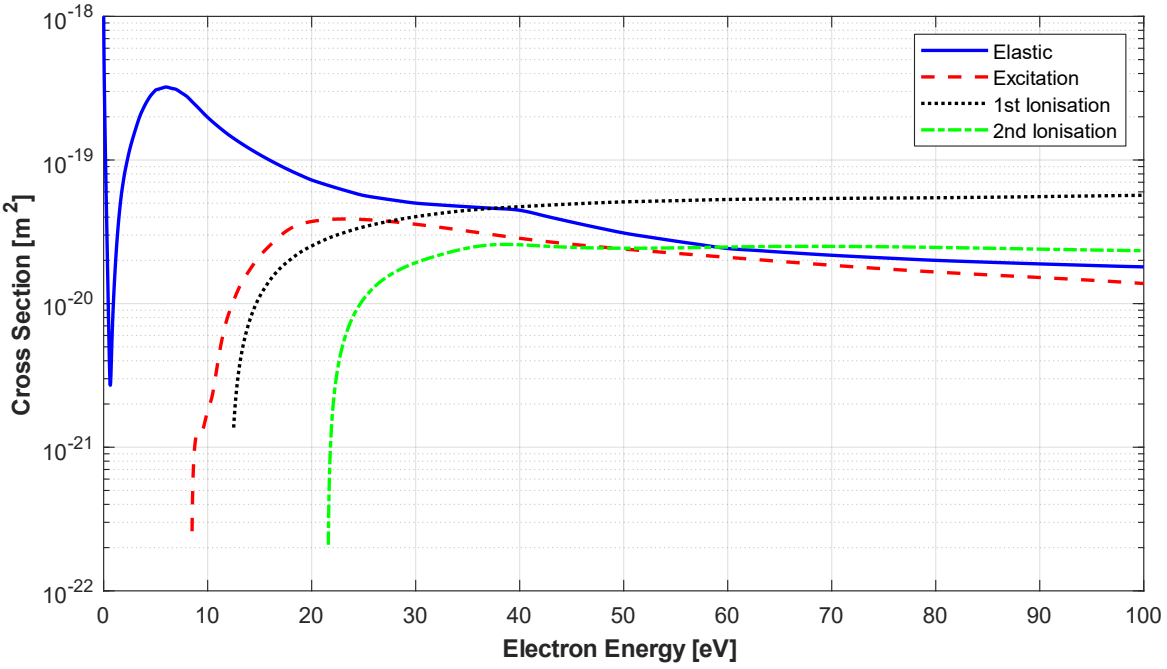

Figure 63 – Cross sections for xenon

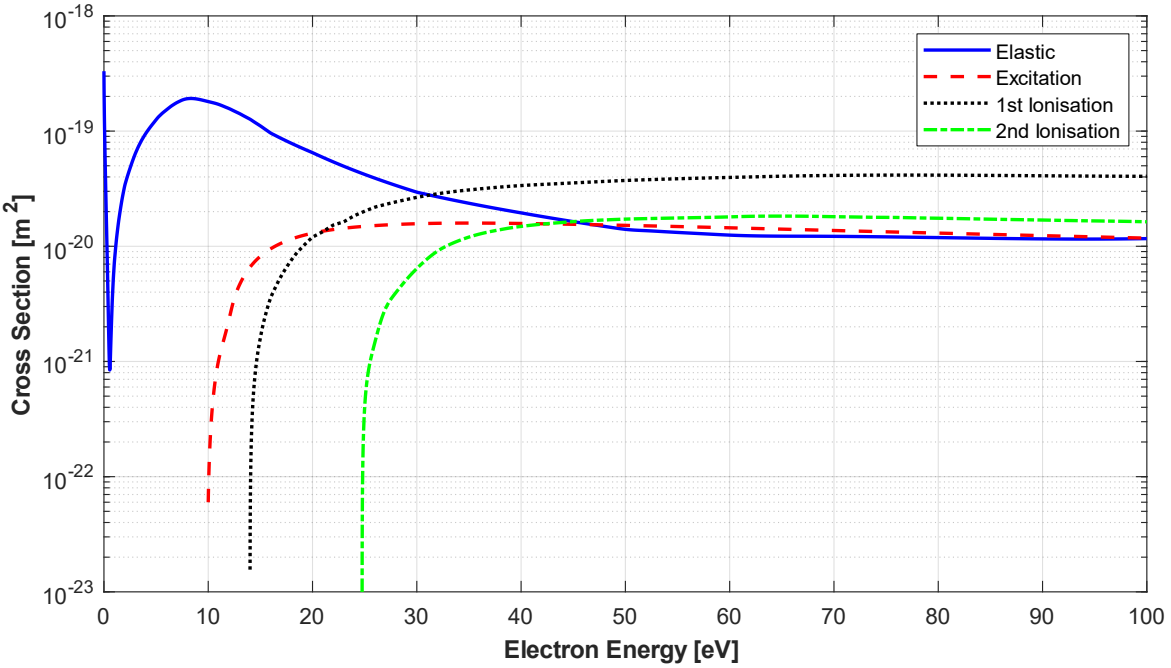

Figure 64 – Cross sections for krypton

A.5.2 Ionisation, Excitation, and Elastic Reaction Rates in Maxwellian Plasmas

In Section 3.2.1, the secondary electrons are called Maxwellian electrons since their energy distribution can be approximated by a Maxwellian distribution, which is the most probable distribution of velocities for a group of particles in thermal equilibrium. Such a distribution can be generalised in three dimensions as follows [20]:

$$f(\vec{v})\mathrm{d}^3v = \left(\frac{m}{2\pi kT}\right)^{\frac{3}{2}} \exp\left(-\frac{mv^2}{2kT}\right) \mathrm{d}^3v \tag{A-1}$$

where $f(\vec{v})$ is a probability distribution function. The average speed of a particle in the Maxwellian distribution is [20]:

$$\bar{v} = \int_0^\infty v \left(\frac{m}{2\pi kT}\right)^{\frac{3}{2}} \exp\left(-\frac{v^2}{v_{th}^2}\right) 4\pi v^2 \mathrm{d}v = \left(\frac{8kT}{\pi m}\right)^{\frac{1}{2}} \tag{A-2}$$

where v is the particle speed and $v_{th} = \left(\frac{2kT}{m}\right)^{\frac{1}{2}}$ is the thermal velocity.

The reaction rates coefficients $\langle \sigma v \rangle$ for xenon and krypton required for the model described in Section 3.2.1 can be calculated from the data in the previous subsection averaged over a Maxwellian electron distribution. For the range 0.5-15 eV, the fits to the calculated values are as follows (where T_{eV} is the temperature in eV) and they are shown in Figure 65 and Figure 66:

- **Xenon**:
    - First ionisation

$$\langle \sigma_i^+ v_e \rangle = \langle \sigma_i^+ \rangle \bar{v_e} = 10^{-20} \left[(7.713 - 0.06355T_{eV} + 0.0005159T_{eV}^2) \cdot exp\left(-\frac{12.94}{T_{eV}}\right) \right] \left(\frac{8eT_{eV}}{\pi m}\right)^{1/2}$$

    - Second ionisation

$$\langle \sigma_i^{++} v_e \rangle = \langle \sigma_i^{++} \rangle \bar{v_e} = 10^{-20} \left[(7.099 - 0.1803T_{eV} + 0.001591T_{eV}^2) \cdot exp\left(-\frac{21.2}{T_{eV}}\right) \right] \left(\frac{8eT_{eV}}{\pi m}\right)^{1/2}$$

    - Excitation

$$\langle \sigma^* v_e \rangle = \langle \sigma^* \rangle \bar{v_e} = 10^{-19}(-0.02599T_{eV}^2 + 1.508T_{eV}) \cdot \frac{exp\left(-\frac{11.41}{T_{eV}}\right)}{T_{eV}^{1.297}} \left(\frac{8eT_{eV}}{\pi m}\right)^{1/2}$$

    - Electron-neutral scattering

$$\langle \sigma_{en} v_e \rangle = \langle \sigma_{en} \rangle \bar{v_e} = 10^{-19} \cdot \frac{15.81T_{eV}^2 - 10.65T_{eV} + 3.17}{T_{eV}^3 + 1.276T_{eV}^2 + 6.161T_{eV} + 0.6767}$$

- **Krypton:**
  - First ionisation

$$\langle \sigma_i^+ v_e \rangle = \langle \sigma_i^+ \rangle \bar{v_e} = 10^{-20} \left[-0.0005434 * T_{eV}^2 + 5.522 \cdot exp\left(-\frac{15.18}{T_{eV}} \right) \right] \left(\frac{8eT_{eV}}{\pi m} \right)^{1/2}$$

  - Second ionisation

$$\langle \sigma_i^{++} v_e \rangle = \langle \sigma_i^{++} \rangle \bar{v_e} =$$

$$= 10^{-20} \left[(3.664 - 0.008825 T_{eV} + 0.002746 T_{eV}^2) \cdot exp\left(-\frac{24.5}{T_{eV}} \right) \right] \left(\frac{8eT_{eV}}{\pi m} \right)^{1/2}$$

  - Excitation

$$\langle \sigma^* v_e \rangle = \langle \sigma^* \rangle \bar{v_e} = 10^{-19} \left[-0.0001141 * T_{eV}^2 + 0.2629 \cdot exp\left(-\frac{10.14}{T_{eV}} \right) \right] \left(\frac{8eT_{eV}}{\pi m} \right)^{1/2}$$

  - Electron-neutral scattering

$$\langle \sigma_{en} v_e \rangle = \langle \sigma_{en} \rangle \bar{v_e} = 10^{-19} \cdot \frac{-0.1396 T_{eV}^3 + 14.47 T_{eV}^2 - 7.246 T_{eV} + 2.571}{T_{eV}^3 + 2.378 T_{eV}^2 + 13.63 T_{eV} + 8.498}$$

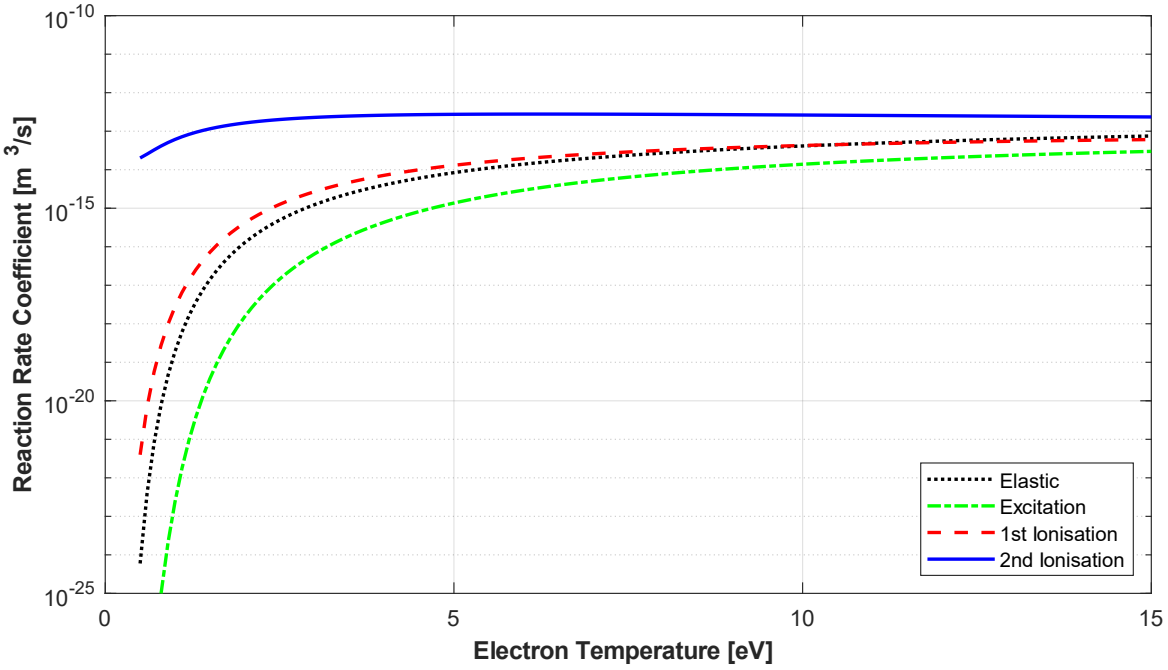

Figure 65 – Reaction rate coefficients for xenon

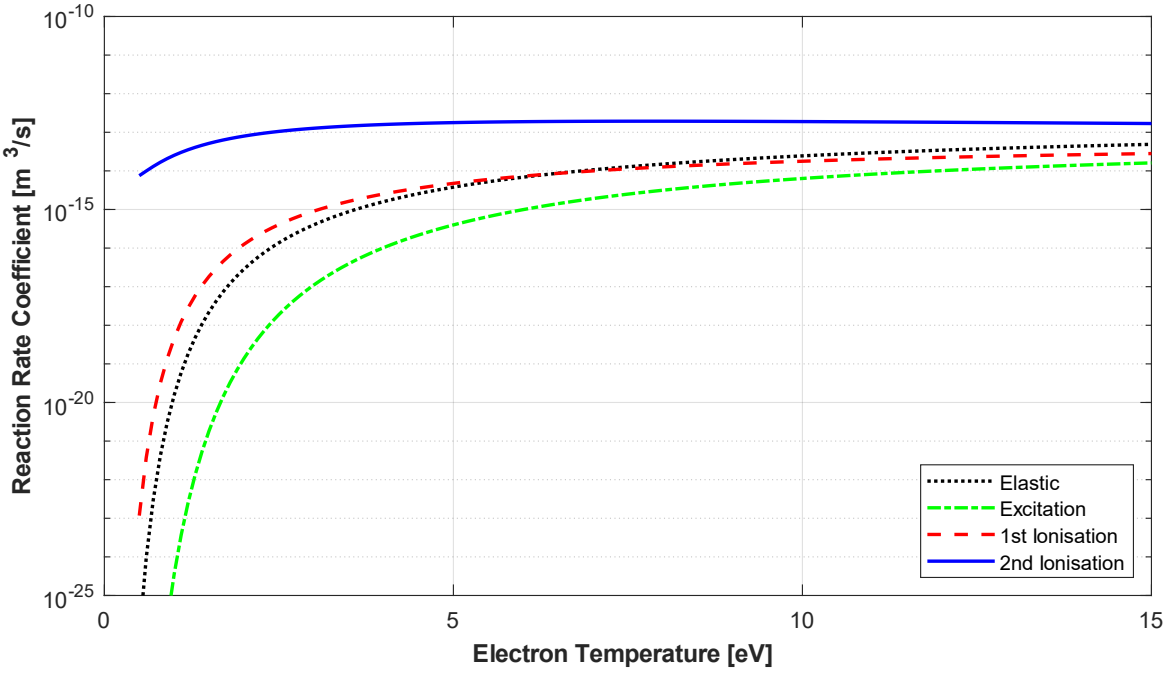

Figure 66 – Reaction rate coefficients for krypton

Appendix B Performance Models for GIEs

In Section 3.2, Brophy's 0-D model used for the analysis of the performance with xenon and alternative propellants was described and, in the following sections, a background on 0-D models is provided followed by the impact of various parameters on the output of Brophy's model. Furthermore, a brief review of ion optics models is offered.

B.1 Background on 0-dimensional (0-D) Models for Ring-Cusp Thrusters

Several discharge chamber models for Kaufman and ring-cusp thrusters have been developed in the past [118], [119], but Brophy and Wilbur's model [75], [120] was the first comprehensive analytical discharge chamber model based on particle, charge and energy balance in the chamber. A uniform plasma (e.g. uniform species densities) and volume-averaged ionisation and excitation rates (i.e. the average of the ion production and loss) were used in this model and, therefore, it can be considered a 0-dimensional (0-D) model. It was initially developed to describe the performance of a ring-cusped magnetic field, high flux density electron bombardment thruster, but, as suggested by Brophy [75], it can be expanded to other typologies of discharge chamber, but its validity with Kaufman-type thrusters was never validated.

In their model, Brophy and Wilbur compute the engine performance as a function of 4 configuration/propellant parameters (the primary electron utilisation factor function of the primary electron confinement length, the baseline ion energy cost, the extracted ion fraction, and the cathode potential surface ion fraction) and 2 operating parameters (the propellant flow rate and the discharge voltage). Their model concludes that the primary factor affecting the efficiency is the direct loss of primary electrons to the anode wall, and it suggests that improved performances are characterised by large extracted ion fractions, long primary electron confinement lengths, small effective grid transparencies to neutral atoms, and operation at high propellant flow rates. It also shows that, when using the same propellant and grid transparencies, the engine performance depends only on the primary electron confinement length and on the baseline plasma ion energy cost. However, since this model does not track the path of primary electrons and, consequently, it cannot predict the primary electron confinement length, this value needs to be obtained experimentally (or computationally) as well as the extracted-ion fraction. Because of this prerequisite, this model cannot be considered a self-consistent predictive tool.

Several 2-D computational models have been developed based on Brophy and Wilbur's model to calculate the two required inputs and, in particular, Arakawa and Ishihara [121] developed a computation model of the plasma in a ring-cusped discharge chamber that combined the models refined by Arakawa and Wilbur [122] for the plasma density distribution, Arakawa and Yamada [123] for the electron trajectories, and Brophy [75] for the discharge chamber performance. Combining these models, Arakawa and Ishihara included the magnetic field effect, the primary and secondary electrons, and the first ions to calculate the primary electron confinement length and the extracted ion fraction. This code was considered state-of-the-art during the 1990s and following years.

Recently, Goebel and Wirz [20], [124] further expanded Brophy's analytical 0-D model by including ambipolar ion diffusion, sheath, and cathode effects to close the set of equations and provide a self-consistent tool to calculate the discharge loss as a function of the mass utilisation efficiency to characterise and optimise the discharge chamber performance. This model allows the determination of the neutral gas density, the electron temperature, the plasma density and potential, the discharge current, the primary electron density, and the ion fluxes to the boundaries of the discharge chamber starting from the following inputs: the desired beam current, the discharge voltage, the discharge chamber surface area and volume, the magnetic field design (from a separate magnetic code), the grid area and transparency (from an ion optics code), the beam flatness parameter, the gas temperature, and the cathode voltage drop (from either a cathode plasma model or direct measurements).

In general, 0-D models can provide very good information on the design parameters of thrusters and can predict their performance reasonably well, but the assumption of uniformity throughout the discharge chamber can lead to some inaccuracies, especially in areas where the plasma is known to be non-uniform, such as around the hollow cathode's orifice, the gas injection aperture, and near the walls. Both Brophy's model [75] and Goebel's model [124], [125] have proven to be in good agreement with experimental results for a different range of thrusters, and they are very useful in understanding ion thruster performance and behaviour as operational parameters are modified. In particular, Brophy's model has shown some flexibility when used to predict the performance of thrusters run with alternative propellants (such as noble gases (xenon, krypton, and argon) in Ref. [75], and Buckminsterfullerene in Ref. [76]) and the impact of changing the propellant on the model is described in the next subsection.

B.2 Impact of Performance Parameters in Brophy's 0-D Models

In the previous section, Brophy's model is described as a function of 4 configuration/propellant parameters (the primary electron utilisation factor function of the primary electron confinement

length, the baseline ion energy cost, the extracted ion fraction, and the cathode potential surface ion fraction) and 2 operating parameters (the propellant flow rate and the discharge voltage). The effect of these parameters on the performance of an electron bombardment thruster is given by Eq. (3-36)(reported here for convenience):

$$\eta_d = \frac{\epsilon_P^*}{f_B\{1-\exp[-C_0\dot{m}_p(1-\eta_m)]\}} + \frac{f_C}{f_B}V_d \tag{B-1}$$

The impact of each parameter can be easily investigated analytically by specifying a value for each of the parameters in the equation, and then varying each parameter individually to determine its effect on performance, as shown in the following subsections.

B.2.1 Primary Electron Utilisation Factor C_0 and Primary Electron Containment Length l_c

As seen in Section 3.2.1, the primary electron utilisation factor C_0 gives a qualitative measurement of the utilisation of the primary electrons inside the discharge chamber and, therefore, it should be as high as possible to have a lower plasma ion energy cost. The effect of changing C_0 is shown in Figure 67, where the other parameters (V_d, V_C, f_B, f_C, $\dot{m}_p$, and ϵ_P^*) are kept constant and their values are reported in the figure. This factor has a strong effect on performance and, especially, on the shape of the performance curve, where improved performance and curves with more sharply defined "knees" are the result of larger values of C_0. However, at high values, the differences between the performance curves become less evident as the function tends to a lower limit which also depends on the other parameters of the equation.

A number of ways in which the value of C_0 may be increased are suggested in the definition itself given in Eq. (3-37) and reported here:

$$C_0 = \frac{4\sigma_0 l_c}{e v_0 A_g \phi_0} \tag{B-2}$$

For example, a propellant with a larger total inelastic collision cross section (σ_0) will have a larger C_0 as well as heavier gas particles which have lower neutral velocities (v_0). It can also be increased by decreasing the grid transparency to neutral atoms, ϕ_0, using, for example, a three-grid system instead of a two-grid system. Another option for increasing the value of C_0 is by reducing the area of the grids, A_g, through which the beam is extracted; however, decreasing A_g will involve a significant reduction in the extracted ion fraction, f_B, and, consequently, an overall decrease in performance.

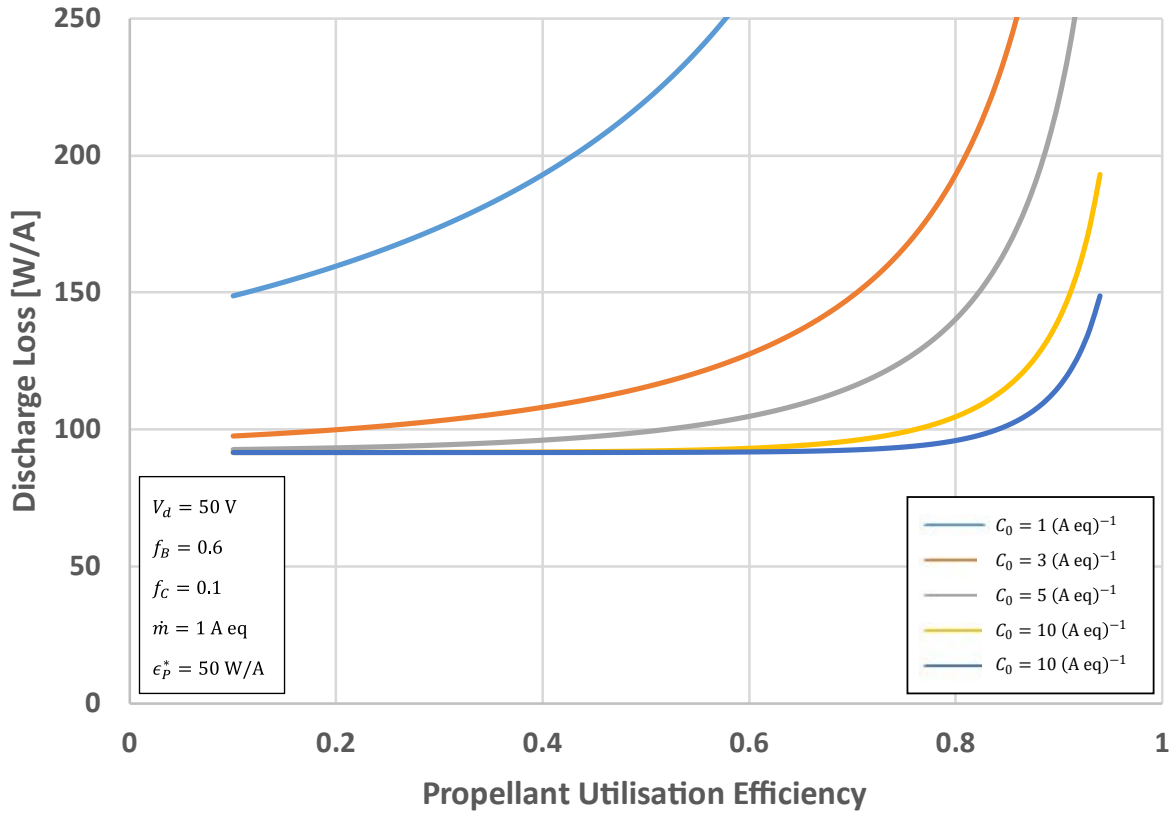

Figure 67 – Effect of C_0 on performance [120]

Finally, one of the most important ways of increasing C_0 is by increasing the primary electron containment length, l_c. This length can be defined as the average length of the helical path that a primary electron would travel in the discharge chamber before being collected by an anode, assuming it had no elastic collisions. Therefore, l_c is a function primarily of the thruster geometry, magnetic field configuration, and cathode position. In cusped magnetic field thrusters, primary electrons are lost to the anode through the cusps, and it follows that this length can be increased by decreasing the number of cusps at the anode potential or increasing the flux density at the cusp. However, the effective anode cusp area cannot be reduced below a certain limit, where the discharge becomes unstable [77].

As reported in Section B.1, the value of l_c cannot be determined using this model and the author also suggests that this length should increase in roughly direct proportion to the thruster diameter, so thrusters with a smaller diameter should be less efficient than larger ones if, at the same time, f_B remains constant [120]. To calculate this parameter, several numerical models have been developed and used in the past [121]–[123] and typical calculated values for ring-cusp thrusters are $l_c = 0.7$ m for a 7 cm-grid thruster [121] and $l_c = 4.1$ m for a 13 cm-grid thruster [76].

B.2.2 Extracted Ion Fraction f_B

One of the most important parameters in the evaluation of a thruster performance is the extracted ion fraction f_B, already defined in Section 3.2.1 as the ratio of the beam current, I_b, to the total ion current produced, I_P. It is fundamental not only to produce ions efficiently, but also to extract as many of them as possible into the beam.

Brophy's theory [120] does not allow the calculation of the value of f_B from design data, but it needs to be determined experimentally by measuring it for different configurations (Figure 68).

The obtained data suggest that:

- f_B is relatively independent of the neutral density parameter, $\dot{m}_p\ (1-\eta_m)$, for a given thruster configuration
- f_B is slightly greater at lower discharge voltages
- the values of f_B for argon are higher than those for krypton, while those for xenon (not shown) are between these two.

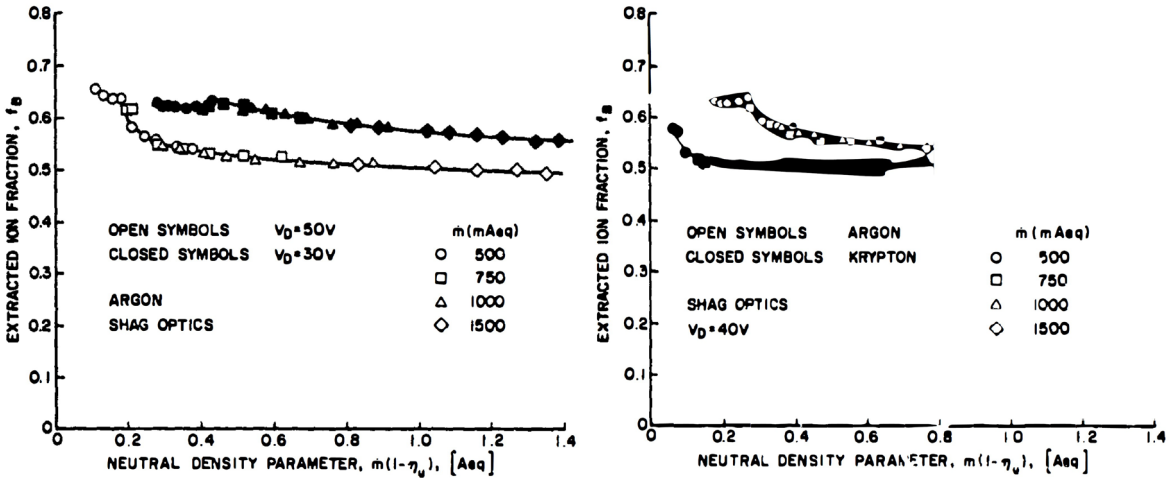

Figure 68 – Effect of discharge voltage (left) and propellant (right) on the extracted ion beam [75]

As a result, Brophy [75] suggests that the extracted ion fraction is a strong function of the magnetic field configuration and thruster geometry, weakly dependent on the discharge voltage and propellant, and not dependent on the neutral density parameter. Consequently, for simplicity, f_B can be taken to be constant for a given thruster geometry, magnetic field configuration, propellant, and discharge voltage.

Keeping this in mind, the effect of changing f_B is shown in Figure 69, where the other parameters (V_d, V_C, C_0, f_C, $\dot{m}_p$, and ϵ_P^*) are kept constant and their values are reported in the figure. It is evident that this parameter has a strong effect on performance, shifting its curve up or down, but without noticeably changing the shape. It is also worth noting the difference between consecutive values is larger for low f_B.

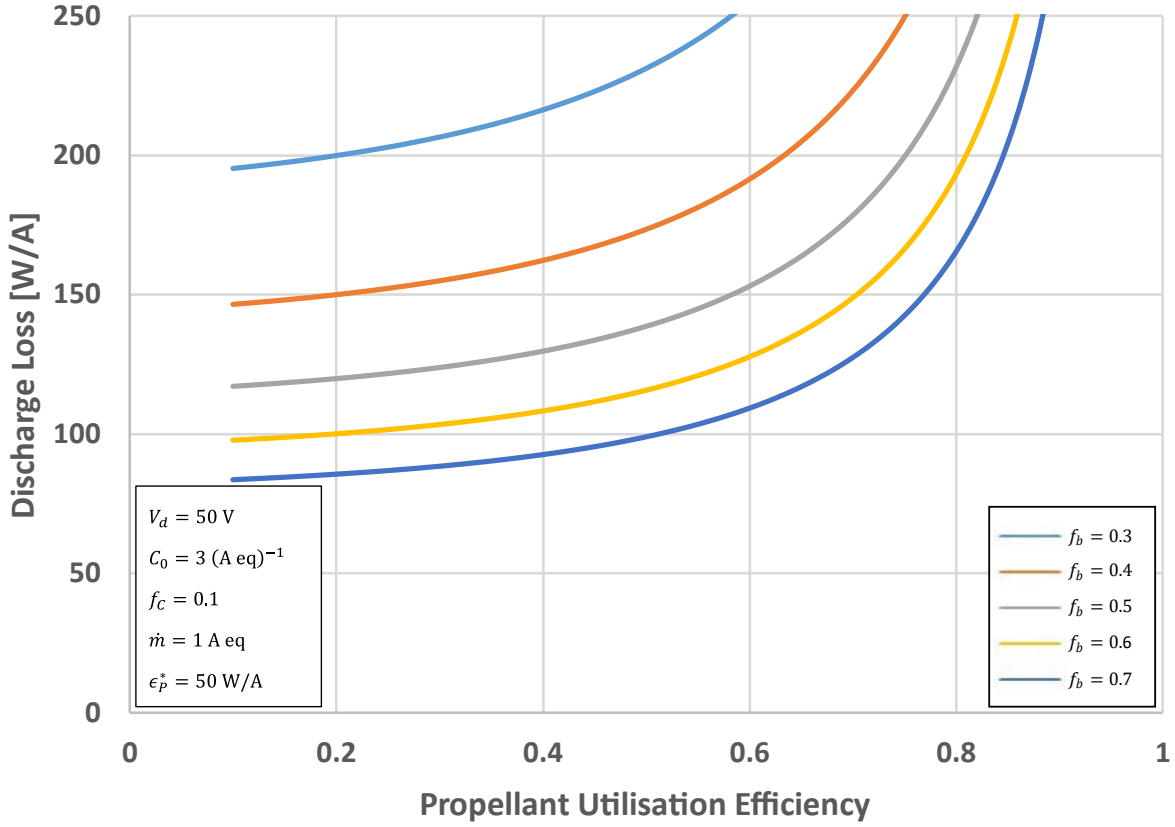

Figure 69 – Effect of f_B on performance [120]

B.2.3 Fraction of Ion Current to Cathode Surfaces f_C

Another important parameter when calculating the performance of a thruster is the fraction of ion current lost to the cathode potential surfaces f_C, already defined in Section 3.2.1 as the ratio of the current to cathode potential surfaces, I_C, to the total ion current produced, I_P. Changes in this parameter also tend to shift the performance curves up or down, and low values are preferable. To reduce the value of f_C and, subsequently, improve the performance, ring cusp ion thrusters typically operate the discharge chamber body at anode rather than cathode potential. Additionally, this reduction of the cathode discharge regions helps to decrease both f_C and V_C, contributing to improved performance.

The value of f_C, as well as that of f_B described above, cannot be calculated from design data using Brophy's model [120], but it must be determined experimentally. Similarly to f_B, f_C is strongly dependent on the design of the thruster, but it is not a function of the neutral density parameter or the operating point. Accordingly, it can be taken as constant for a given configuration and typical values for ring-cusped thrusters are around 0.1 [120].

B.2.4 Double Ion Production

As mentioned in Section 3.2.1, Brophy's model does not include the production of doubly charged ions, which represent both a performance loss factor and, mainly, the primary driver limiting the discharge chamber lifetime. However, a simple formulation for the ratio of doubly-to-singly charged ion current in the beam is developed in the same reference [75] where the 0-D model is described, starting from the production rate of singly (I_P^+) and doubly (I_P^{++}) charged ions as currents given by:

$$I_P^+ = \left(n_0 n_p P_0^+ + n_0 n_M Q_0^+\right) e V_P \tag{B-3}$$

$$I_P^{++} = \left(n_0 n_p P_0^{++} + n_0 n_M Q_0^{++} + n_+ n_p P_+^{++} + n_+ n_M Q_+^{++}\right) 2 e V_P \tag{B-4}$$

where $P_0^+ = \langle \sigma_i v_p \rangle$ is the primary electron rate factor for the production of single ions from ground state neutrals, $Q_0^+ = \langle \sigma_i v_e \rangle$ is the Maxwellian rate factor for the production of single ions from ground state neutral atoms, n_+ is the singly charged ion density, P_0^{++} and Q_0^{++} are the primary and the Maxwellian electron rate factors for double ion production from ground state neutrals, and P_+^{++} and Q_+^{++} are the rate factors for double ion production from ground state ions. By dividing Eq. (B-4) by Eq. (B-3), and combining and simplifying the ratio, the average ratio of doubly-to-singly charged ion current in the beam for a single gas can be written as follows:

$$\frac{I_b^{++}}{I_b^+} = \frac{2\left(Q_0^{++} + \frac{n_p}{n_M} P_0^{++}\right)}{Q_0^+ + \frac{n_p}{n_M} P_0^+} + 0.83 \left(\frac{v_0}{v_B}\right) \left(\frac{\phi_0}{\phi_i}\right) \left(\frac{Q_+^{++} + \frac{n_p}{n_M} P_+^{++}}{Q_0^+ + \frac{n_p}{n_M} P_0^+}\right) \left(\frac{\eta_m}{1-\eta_m}\right) \tag{B-5}$$

The first term on the right-hand side of Equation (B-5) represents the production of double ions from ground state neutral atoms (where $\frac{n_p}{n_M}$ is the primary-to-Maxwellian electron density ratio), while the second term represents the double ion production from singly charged ions.

Likewise, a formulation for a mixture of gases can be rederived as (X_j is the mole fraction of the j-th species):

$$I_P^+ = \left[n_0 n_p \left(X_{Xe} P_{0_{Xe}}^+ + X_{Kr} P_{0_{Kr}}^+\right) + n_0 n_M \left(X_{Xe} Q_{0_{Xe}}^+ + X_{Kr} Q_{0_{Kr}}^+\right)\right] e V_P \tag{B-6}$$

$$\begin{aligned} I_P^{++} = &\left[n_0 n_p \left(X_{Xe} P_{0_{Xe}}^{++} + X_{Kr} P_{0_{Kr}}^{++}\right) + n_0 n_M \left(X_{Xe} Q_{0_{Xe}}^{++} + X_{Kr} Q_{0_{Kr}}^{++}\right)\right] 2 e V_P + \\ &+\left[n_p \left(n_{+_{Xe}} P_{+_{Xe}}^{++} + n_{+_{Kr}} P_{+_{Kr}}^{++}\right) + n_M \left(n_{+_{Xe}} Q_{+_{Xe}}^{++} + n_{+_{Kr}} Q_{+_{Kr}}^{++}\right)\right] 2 e V_P \end{aligned} \tag{B-7}$$

Using a similar approach to the one used above, the average ratio of doubly-to-singly charged ion current in the beam for a mixture Xe/Kr can be approximated as follows:

$$\frac{I_b^{++}}{I_b^{+}} = \frac{2\left[\left(X_{Xe}Q_{0_{Xe}}^{++}+X_{Kr}Q_{0_{Kr}}^{++}\right)+\frac{n_p}{n_M}\left(X_{Xe}P_{0_{Xe}}^{++}+X_{Kr}P_{0_{Kr}}^{++}\right)\right]}{\left(X_{Xe}Q_{0_{Xe}}^{+}+X_{Kr}Q_{0_{Kr}}^{+}\right)+\frac{n_p}{n_M}\left(X_{Xe}P_{0_{Xe}}^{+}+X_{Kr}P_{0_{Kr}}^{+}\right)} + \\ +0.83\left(\frac{v_0^{mix}}{v_b^{Xe}}\right)\left(\frac{\phi_0}{\phi_i^{Xe}}\right)\left(\frac{\dot{m}_{Xe}}{\dot{m}_{mix}}\right)\left[\frac{\left(Q_{+Xe}^{++}+\frac{n_{+Kr}}{n_{+Xe}}Q_{+Kr}^{++}\right)+\frac{n_p}{n_M}\left(P_{+Xe}^{++}+\frac{n_{+Kr}}{n_{+Xe}}P_{+Kr}^{++}\right)}{\left(X_{Xe}Q_{0_{Xe}}^{+}+X_{Kr}Q_{0_{Kr}}^{+}\right)+\frac{n_p}{n_M}\left(X_{Xe}P_{0_{Xe}}^{+}+X_{Kr}P_{0_{Kr}}^{+}\right)}\right]\left(\frac{\eta_m^{Xe}}{1-\eta_m^{mix}}\right) \quad \text{(B-8)}$$

The terms on the right-hand side represent the same productions as in the case with a single gas.

B.3 Background on Ion Optics Models

As seen in Section 2.2.1, the three different stages (i.e. ionisation, beam extraction, and neutralisation) are strongly coupled but distinct in a GIE, therefore it is possible to develop models for each stage. In particular, the ion optics models focus on the high-energy beam ions extracted from the discharge chamber and these ions are the primary species considered in this kind of simulation, in contrast to the discharge chamber performance models, discussed in the previous section, that focus on the electrons in the discharge chamber. The electrons are confined within the discharge chamber by the grids' plasma sheath. The extracted ions are subject to different types of collisions with the neutrals leaving the chamber: specifically, the ions created from charge exchange (CEX) interactions are the main cause of grid erosion and any model that predicts the lifetime of a GIE needs to include them. The ion optics models can be divided into two macro modelling techniques and, eventually, hybrid versions of the two:

- Monte Carlo (MC) models, also called gun or "flux-tube" models.
- Particle-In-Cell (PIC) models.

These two methods present a lot of similarities and a few major differences. Both methods use a similar simulation approach for particle tracking, field solver, and charge/field interactions: they track the trajectories of the ions in the beam, which are treated as particles, within the space-charge-defined fields by decoupling the particle motion from the calculation of the electric field, whose transient or dynamic processes are ignored and only the steady-state solutions are considered. The simulation starts at an inflow boundary, where the particles are traced inside the computational domain from each time step to the next until they completely leave the domain, while the electric potential is frozen. At that point, the charges related to the trajectories of all particles are included in the considered mesh domain and, consequently, the electric field and trajectories are updated for the next time-step of the simulation. This process is repeated until a converged steady-state solution is obtained for the trajectories and/or the electric field at a given time.

Starting from this common basis, the two methods present the following differences. In the MC approach, the neutral density is calculated independently from the beam ions, using analytical equations or the Monte Carlo technique, and it is assumed that the CEX interactions do not considerably affect the neutral density. In the PIC approach, the Boltzmann distribution is used for the electron density, and the movement of all the species is considered simultaneously within the simulation time-step; consequently, the species interactions are incorporated more directly. Specifically, the particle trajectories change at each time step as a result of the computation of the collisions between similar or differently charged particles. Furthermore, PIC simulations typically require very small time-steps and, therefore, a very large number of iterations is needed to reach the converged solution. The main consequence of these differences is that PIC models are considered to be more accurate compared to MC models, which include several simplifications to achieve the result. However, the higher fidelity of PIC codes requires higher computational cost due to the higher amount of simulation particles, compared to a simplified MC code: e.g. a complete simulation may take up to a few days for the former as opposed to minutes or, at most, hours for the latter.

Comprehensive reviews of several ion optics codes for GIEs that have been developed in Europe, the USA, Japan, and China since the early 1990s were published in [126], [127]. Among the MC codes worth mentioning are CEX2D and CEX3D developed at NASA JPL in the USA [128], [129], IGX and FFX developed at Colorado State University (CSU) in the USA [1], [130], OPT developed at University of Tokyo [121] and extended by other Japanese institutions as OPT-J [131], and IGUN developed in Germany [132]. In addition, NASA's codes and their Japanese counterparts have recently been modified into a PIC and a hybrid model, respectively [131], [133]. These methods share a common structure, and the main difference is in the calculation of the neutral density. CEX2D/3D and IGX/FFX use analytical formulas to approximate the neutral atom density with the difference that the required transmission factor for the grid system is computed using the MC approach in CEX2D/3D and using an analytical formula in IGX/FFX. Instead, IGUN and early versions of OPT/OPT-J use a free molecular flow model (FMF) to calculate the distribution of neutrals.

Compared to MC models, fewer PIC codes are available in the literature, such as IBEX-T developed in Japan [134], ERODE developed at the University of Michigan in the USA [135], [136], PICLas developed at the University of Stuttgart in Germany [127], and IFE-PIC developed at Virginia Tech Institute (VT) in the USA [137], which started as a hybrid code and evolved into a full PIC version with the collaboration of the Harbin Institute of Technology in China [138]. Nonetheless, the industry is leaning toward the development of 3-D PIC models, which are more complete and accurate compared to MC models, and this is due principally to the increased availability of computational power.

Comparative results were published by Farnell [1] and Emhoff [139] taking into consideration the accel grid-to-beamlet current ratio and the minimum centreline potential as a function of the beamlet current calculated using different ion optics models available in the USA (i.e. IGX, FFX, CEX2D/3D, and ERODE). The models generally showed a good agreement, apart from a few acceptable discrepancies: CEX2D slightly overpredicted the direct impingement current, and IGX/FFX underpredicted the saddle point potential.

Appendix C Plasma Diagnostic Tools

In Section 3.3, plasma diagnostics tools and single Langmuir probes were described with a focus on their relevance to this work. In the following sections, a background on plasma diagnostic techniques, on the use of electrostatic probes for the measurement of the plasma properties in GIE's systems, and, finally, on the theory of operation of single Langmuir probes is provided.

C.1 Overview of Plasma Diagnostic Techniques

The field of plasma diagnostics is extensive and many different diagnostic tools, which have been developed over the past decades, can be used depending on the type of plasma under investigation and on the specific information that is required. However, despite the numerous plasma diagnostic techniques available, a comprehensive method that allows the determination of all the plasma parameters of interest still does not exist. Usually, different methods are applied, and their results are then compared to validate them and improve accuracy. Two of the techniques most frequently used in both academia [67], [140], [141] and industrial environments [81] are:

- Electrostatic probes (e.g. Langmuir probes, Faraday probes, Retarding Potential Analyser, E×B probes) are, by their nature, intrusive, since their presence affects the plasma under investigation, and, more importantly, their use is confined to low-pressure and low-temperature conditions in which their integrity is not at risk.
- Optical emission spectroscopy is a non-perturbing technique, but the analysis of the spectra is not trivial in low-pressure plasmas where the species are not in local thermodynamic equilibrium. It is the most widely applicable tool for plasma diagnostics, especially for hot and high-density plasmas where other probes cannot be inserted into the plasma.

Electrostatic probes are the simplest and most versatile diagnostic tools for the experimental investigation of different plasma parameters, such as electron energy distribution function, plasma density, plasma potential, electron temperature, ion energy and ion charge state. In particular, they are the ideal choice when information about the local parameters in cold plasma is required. Among those probes, the most widely used in electric propulsion are [88]:

- Faraday probes (FP) are usually negatively polarised devices, which repel electrons and collect only ions to measure the ion beam current density distribution of the plasma

plume. There are different versions of this kind of probe, such as nude, collimated, cupped, or gridded probes. A Faraday probe can also be positively polarised to attract electrons, but this version is not employed in electric propulsion.

- A Retarding Potential Analyser (RPA) uses a series of grids to filter ions and determine their energy distribution and it is used to analyse the plume and the backflow of electric propulsion devices.
- An E×B probe, known also as Wien filter, uses perpendicular applied electric and magnetic fields to determine ion charge states and it achieves this by acting as a velocity filter that separates ion species according to their velocities.
- Langmuir collecting probes, or simply Langmuir probes (LP), consist of one or more conducting elements inserted into the plasma and connected to an external electrical circuit to obtain the current-voltage characteristic which can be used to determine plasma density, electron temperature, and electron distribution function. There are single, double, or triple LPs depending on the number of probe tips.
- Langmuir emissive probes, or simply emissive probes, comprise a filament heated by applying a current to it to reach thermionic electron emission, which substantially neutralises the sheath surrounding the probe that floats at the local plasma potential, allowing its direct measurement.

The first three electrostatic probes listed above, i.e. FP, RPA and E×B probe, are only used for measurement of plasma parameters in the plume of electric propulsion devices and they can be included in the subcategory of the ion beam diagnostics, while the two Langmuir probes can also be used inside the discharge chamber [88]. In particular, because of this flexibility, the Langmuir collecting probes (LP) were used within this research for the measurement of the plasma parameters, and their working principle are described in more detail in Section 3.3 and in the following subsections.

A second technique of great utility in electric propulsion and, probably, the most powerful technique available to plasma physicists is optical emission spectroscopy, which is a passive spectroscopic method that allows the observation and study of the electromagnetic radiation emitted by the plasma. In particular, the method of the spectral line ratios is a very important tool to obtain the temperature and density of plasma by taking and comparing the emission intensities of various atomic spectral lines, since the measurement of an absolute intensity can be challenging. While in conventional spectroscopy the interest is on the atomic structure of an isolated atom, the radiation in plasma depends both on the properties of the isolated radiating species and on the plasma properties near the radiator, as a consequence of the fact that ions and electrons interact with the radiator through processes of ionisation, recombination,

excitation and de-excitation. Therefore, the main disadvantage of this method is that local measurements are not possible since the radiation is collected along the whole line of sight.

C.2 Background on the Use of Electric Probes in GIEs

As described in the previous section, electrostatic probes are an intrusive technique that involves their insertion into a plasma for the measurement of the current to/from it. Such interaction allows the extraction of information from the local plasma, but the presence of the probe causes perturbations which should be kept to a minimum.

In the past, several techniques and configurations involving electrostatic probes have been used with success in EP plasmas [32], [87], [140], [142] and each one presents its benefits and downsides, as shown in Table 8, when measuring the plasma parameters, such as electron temperature T_e, electron/ion density $n_{e/i}$, plasma potential V_p, floating potential V_f, ion flow velocity v_i, and Electron Energy Distribution Function (EEDF).

Table 8 – Summary of electrostatic probe techniques

Probe technique	***Accessible plasma parameters***	***Advantages***
Single LP	$T_e, n_{e/i}, V_p, V_f$, EEDF	Access to many parameters
Double LP	$T_e, n_{e/i}, V_f$	Reduced perturbation, RF plasmas
Triple LP	$T_e, n_{e/i}, V_f$	No bias sweep
Quadruple LP	$T_e, n_{e/i}, V_f, u_i$	Flowing plasma measurements
Emissive Probe	$V_p, V_f, (T_e, n_{e/i})$	Improved accuracy on V_p
Capacitive Probe	$T_e, n_{e/i}$, EEDF	Robust to probe contamination

The single Langmuir probe is the simplest and most widely used configuration and it allows the highest spatial resolution compared to the multiple-electrode versions. It gives the possibility to calculate the fundamental local plasma parameters (e.g. plasma density, electron temperature, floating potential, plasma potential) and, in addition, it can extract the primary electron density and energy with a suitable analytical method. This configuration is mainly used in combination with DC discharge chambers, but it starts to show its limits when used in RF plasmas. In fact, RF discharges introduce perturbations and oscillation of the plasma potential that require the use of compensation techniques to obtain reliable data on plasma properties.

The double Langmuir probe configuration [140] utilises two equally sized and near electrodes, which float as a whole and draw no net current from the plasma, and it is typically used if: there is no well-defined ground (e.g. RF plasmas), or large plasma fluctuations are present making difficult to obtain a clear I-V curve, or it is necessary to minimise plasma perturbations. The inferior spatial resolution, the lack of distinction between primary and Maxwellian electrons, and the lack of plasma potential information are the main drawbacks of this setup.

The triple Langmuir probe technique [32] uses three Langmuir probes of the same dimension and close to one another, such that the sheaths surrounding each probe should not interact with the others. In this case, the fixed bias is applied between two of the probes and the third one is left floating. Properly configured, this method allows instantaneous and simultaneous measurements of plasma parameters since the probe remains near the floating potential and it does not need to be swept in voltage, providing three points on the I-V characteristic. This solution is very attractive when collecting data in time-dependent plasmas and time resolution is fundamental. However, the spatial resolution is severely affected when using this probe.

C.3 Single Langmuir Probe

After almost a century, Langmuir probes, introduced by Langmuir and analysed in detail by Mott-Smith and Langmuir [143] in the mid-1920s, represent one of the most widely used diagnostic tools to measure plasma parameters in low-temperature plasmas (approximately a few electron volts). A single Langmuir probe consists of a single electrode (usually a bare wire or a metal disk) inserted into a plasma and connected to an external electric circuit allowing bias of the probe voltage with respect to a reference electrode to collect electron and/or ion currents. As the applied bias voltage is swept from a negative to a positive potential, the collected current is measured and plotted to give the current voltage characteristic (I-V curve). The simplicity of the Langmuir probe concept is offset by the difficulty in interpreting the curve to obtain the required plasma parameters. This complexity is linked to the conditions of the plasma (i.e. multiple regimes of operation, flowing effect, and magnetic field) as well as the local plasma perturbations that need to be accounted for; in fact, a probe immersed in plasma causes local perturbation creating a sheath and presheath area around the probe itself that should be made small enough to reduce disturbances in the plasma ionisation, electron energy balances, and discharge current distribution. Extensive literature on Langmuir probes and associated issues exists [144]–[147], and, in the following subsections, an overview will be provided of a typical I-V characteristic, of various methods used to accurately estimate the plasma parameters in single and multi-species plasmas, and of the different effects that make the analysis of the trace more challenging.

C.3.1 Current-Voltage Characteristic

A typical Langmuir probe I-V characteristic (Figure 70) is divided into three parts by the floating potential V_f, at which the insulated probe cannot draw current and it will float, and by the plasma potential V_p, at which the probe is at the same potential as the plasma and the drawn current is only due to the random thermal flux of ions and electrons. A universally used

convention is to plot the current from the probe, i.e. to display the ion current collected by the probe as negative and the electron current as positive.

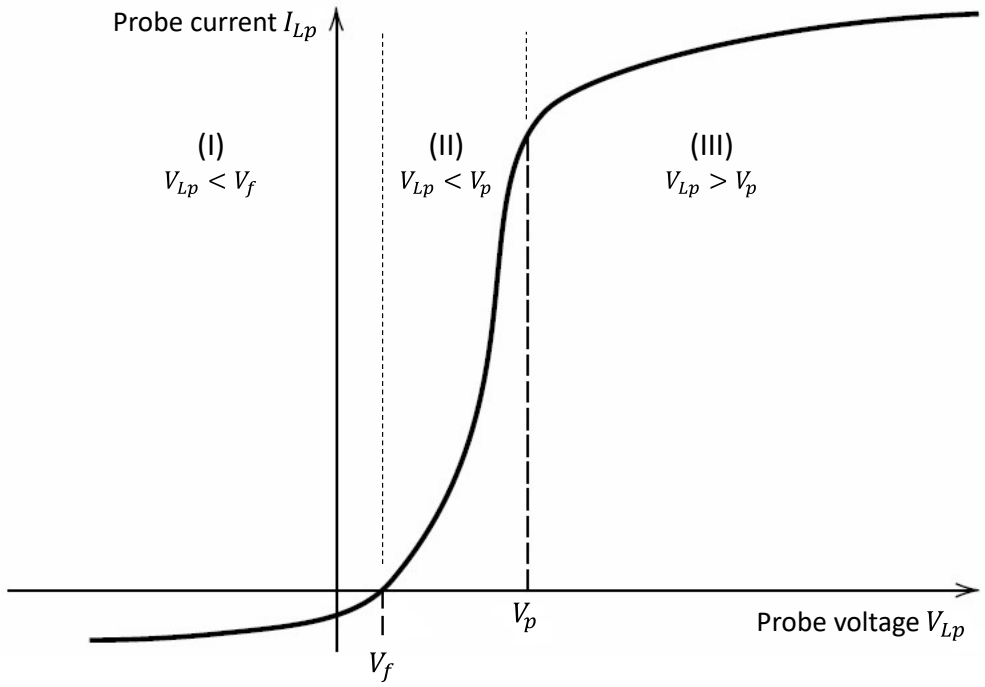

Figure 70 – Typical I-V characteristic for a single Langmuir probe [73]

The three regions are:

I. The ion attracting part at $V_{Lp} < V_f$ called the ion saturation region

When the probe bias becomes increasingly negative with respect to the plasma, the ion current increases since only ions are collected with a formation of a positive space charge around the probe that screens the bulk plasma from the effect of this potential. The ion saturation current is not constant, but the magnitude may vary with the voltage as a result of sheath effects: an increase in the potential across the sheath leads to a bigger sheath thickness and, therefore, to a larger effective collection area for ions.

II. The electron repelling part at $V_f < V_{Lp} < V_p$ called the transition region

In this range of potentials, both ion and electron currents are collected by the probe and the probe current displays an exponential behaviour; in fact, high-energy electrons are collected by the probe overcoming the Coulomb barrier due to the increasingly positive bias and, at the same time, low-energy ions are repelled.

III. The electron attracting part at $V_{Lp} > V_p$ called the electron saturation region

For increasing values of the probe voltage, the current tends to saturate at the electron saturation current, since the low-energy ions are repelled and only electrons are collected. This saturation current shows a positive gradient due to sheath effects. The magnitude of the electron saturation current is much greater than the ion saturation current due to the greater ion mass.

Information about the plasma parameters can be obtained from each of these regions of the curve, but the accuracy and readiness of these parameters vary substantially for the different parts, as described in the following subsection.

C.3.2 Theory of Operation

As previously said, the challenging part of using Langmuir probes consists of the analysis of the I-V curve to obtain the plasma parameters of interest (usually, electron temperature, plasma potential, and plasma density). There are three main methods used to carry out this diagnosis [148]:

- The classic Langmuir procedure, where the electron part of the probe characteristic (EPPC) is used to obtain the plasma density and the electron temperature.
- The procedure that uses the ion part of the probe characteristic (IPPC) is based on theories of orbital and radial ion motion around the probe.
- The measurement of the electron energy distribution function (EEDF) is based on Druyvesteyn's theory.

In the classic Langmuir procedure, it is assumed that the electron energy distribution is Maxwellian and there are no electron collisions in the vicinity of the probe. Using these assumptions and the fact that the electron current within the transition region appears to be linear if plotted on a semi-log plot against probe bias, the electron temperature T_e is defined by the linear segment of the $[\ln I_e(V)]$-curve, while the plasma potential V_p and the electron saturation current I_{e0} are defined by the asymptotic crossing point, according to the following formulas:

$$\frac{\mathrm{d}(\ln I_e)}{\mathrm{d}V_{Lp}} = \frac{e}{kT_e} \qquad \text{and} \qquad n_e = \frac{I_{e0}}{eA_{Lp}}\left(\frac{2\pi m_e}{kT_e}\right)^{1/2} \tag{C-1}$$

where A_{Lp} is the probe surface area. The plasma potential can be found from the maximum of the first derivative of the electron current (I_e') or the zero of the second derivative of the electron current (I_e''). Ideally, an ideal Langmuir probe characteristic displays a noticeable 'knee' at the plasma potential, however, in practice, the transition is relatively smooth since visible saturation and sharp bends are obtained only when the probe is large e/o the plasma density is high. Because of this and of the assumptions stated above, the plasma parameters obtained using this method can have associated uncertainties, especially in the case of the plasma density where the IPPC technique gives more accurate estimates.

The IPPC method is often used to estimate plasma density and temperature because of its simplicity. The electron temperature is found from the first formula in Eq. (C-1) in the vicinity or

at the floating potential V_f using $I_e = I_{Lp} - I_i$. The estimation of the ion density (and, assuming quasi-neutrality, electron density) is obtained from the ion saturation current at high negative potential using two main theories:

- the radial motion theory (RMT, known also as Allen-Boyd-Reynolds-Chen, ABRC, theory) that accounts only for the radial motion to the probe, and
- the orbital motion limited theory (OML, later refined by Bernstein-Rabinowitz-Laframboise, BRL) that accounts only for the orbital motion.

Both assume Maxwellian ion and electron energy distributions and collisionless sheath, however, even if a clear limit in the applicability does not exist, the OML-BRL theory is applied when $\frac{r_{Lp}}{\lambda_D} \ll 1$, while RMT is usually applied when $\frac{r_{Lp}}{\lambda_D} > 1$, where r_{Lp} is the probe radius and $\lambda_D = \left(\frac{\epsilon_0 kT_e}{e^2 n_e}\right)^{1/2}$ is the electron Debye length. In a typical discharge chamber of a GIE, a properly designed single Langmuir probe crosses two different sheath regimes for typical ranges of electron temperature (2-11 eV) and plasma density (10^{16}-10^{18} m^{-3}). The density is expected to have a maximum on the cathode centreline and decrease up to two orders of magnitude moving away from the centre with the effect of an increasing Debye length, which determines the probe operating regime. As a result, the plasma density near the anode is low enough for a complete OML analysis to be used, whereas, in the bulk of the discharge plasma, the conditions are in the transition range between the two theories.

The third method of analysis of the I-V characteristic to obtain the plasma parameters is based on Druyvesteyn's technique [96], which is generally used for measurements in weakly ionised, low pressure and isotropic plasmas, with increasing use in other cases. The main advantages of this method are:

- It is valid for any isotropic electron velocity distribution and any geometry of the probe (convex, planar, cylindrical, or spherical)
- It allows measurements in non-Maxwellian distributions, and it is the only option in case of non-equilibrium plasmas with non-Maxwellian electron energy distributions
- It does not depend on the ratio $\frac{r_{Lp}}{\lambda_D}$.

Its main limitations come from the noise generated in the gas discharge plasma and from the noise amplification intrinsic with the differentiation procedure. In his work, Druyvesteyn [96] demonstrated that $\frac{d^2 I_{Lp}}{dV_{Lp}^2}$ is proportional to the electron energy distribution function (EEDF) in the plasma, according to the following formula [149]:

$$\frac{\mathrm{d}^2 I_e}{\mathrm{d}V_{Lp}^2} = I_e'' = -\frac{e^2 A_{Lp}}{4}\sqrt{\frac{2e}{mV_{Lp}}}F(\varepsilon) \tag{C-2}$$

where $F(\varepsilon)$ is the EEDF as a function of the electron kinetic energy ε. Hence, using measurements of I_e'', it is possible to obtain the plasma density and electron temperature as [149]:

$$n_e = \frac{2\sqrt{2m}}{|e|A_{Lp}}\int_0^{-\infty} I_e''(V)\sqrt{\frac{V_{Lp}}{e}}\,\mathrm{d}V_{Lp} \tag{C-3}$$

and

$$T_e = \frac{4\sqrt{\frac{2}{|e|}}}{3n_e A_{Lp}}\int_0^{-\infty} I_e''(V)|V|^{3/2}\mathrm{d}V_{Lp} \tag{C-4}$$

This last method proved to be the most reliable when compared to the EPPC and IPPC methods [148] and, because of this, it was used in the analysis of the data collected with the single Langmuir probes during the experimental campaign. However, this method requires a very good signal-to-noise ratio that might not be available in every condition. In these situations, conventional fitting of the I–V trace for T_e and n_e is a much more practical method as noise amplifications through the associated differential operations are avoided. On the other hand, for experiments that have a very large amount of data, fitting I–V traces manually is unrealistic and the Druyvesteyn's method is easier to automatise using software codes.

C.3.3 Summary of Magnetic Fields and Other Effects

As was already said, the use of Langmuir probes is conceptually easy, but the interpretation of the I-V characteristics is markedly complicated by a multitude of effects, such as plasma collisionality, presence of magnetic fields, plasma flow velocity and the so-called "end effects", material interactions of the probe with the plasma, presence of multiple ion species, etc.

In addition to the ratio of the Debye length to probe radius described in the previous subsection, another important parameter used to determine the sheath analysis and the plasma collisionality is the Knudsen number Kn, which relates the ion or electron mean free path λ_{MFP} to the probe radius r_{Lp}. This number gives a relative measure of the number of ion or electron collisions with respect to the size of the probe, and it also determines if the probe is in the collisionless or continuum plasma regime. Since the mean free path of both ions and electrons in a typical GIE's discharge chamber is much larger than the probe radius, Kn is much greater than one and the probe operates in the collisionless regime.

The presence of magnetic fields can impact the Langmuir probe results by modifying the motion of the charged particle and, consequently, distorting the I-V characteristic and the sheath

structure around the probe. In the case of GIEs, ions are generally not affected by magnetic fields and their presence can be assumed to have a negligible impact on the ion collection part of the curve. On the contrary, the electron part of the trace can be disturbed by magnetic fields and an important parameter that allows the evaluation of this impact is the relative size of the probe radius r_{Lp} compared to the electron gyroradius $r_e = \frac{mv_e}{eB}$ as follows (Figure 71):

- If $r_e \ll r_{Lp}$, particle trajectories are helical or cycloidal, and the probe collected current is suppressed compared to the unmagnetised case
- If $r_e \gg r_{Lp}$, the curvature of the electron trajectory can be neglected, and unmagnetised probe theory can be applied.

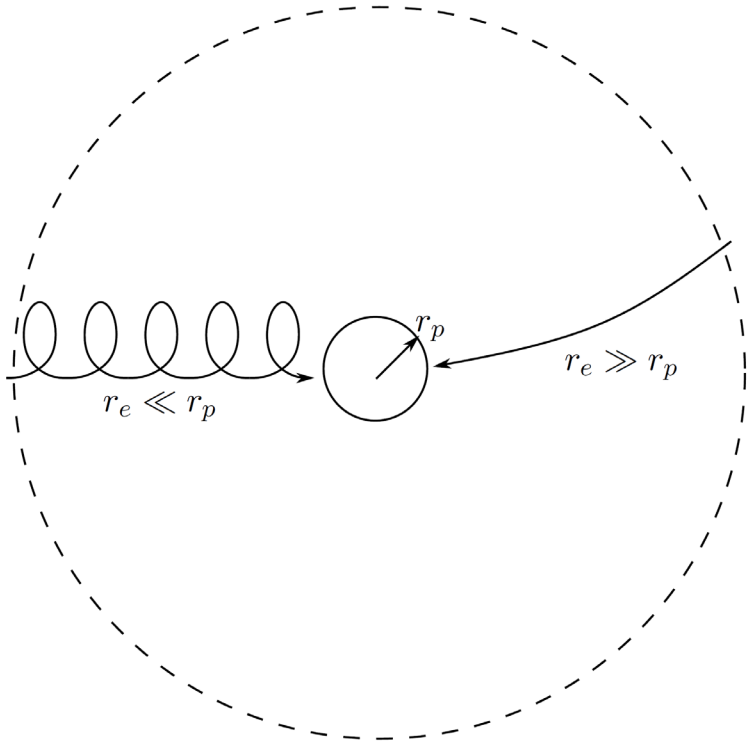

Figure 71 – Effect of magnetic field parallel to the probe's sheath on electron trajectories [150]

When the effect of magnetic fields is important, it can suppress the electron saturation current and the electron retarding region making it difficult to measure the electron density and the plasma potential, and overpredicting the electron temperature, respectively. In the case of a GIE's discharge chamber, the effect of magnetic fields can be neglected as the probe radius is from a few times to several times smaller than the gyroradius depending on the position of the probe.

A second element to consider when evaluating the impact of magnetic fields is the relative position of the probe within the field. The effect of the magnetic field is minimised when its lines are perpendicular to the probe axis, but it can be relevant when its lines are parallel to the probe as described above.

Finally, magnetised plasma can cause anisotropy of the electron energy distribution function (EEDF), which can affect the electron temperature measurement. This effect can be considered small if the ratio $\frac{B}{P}$ is small, where P is the pressure inside the discharge chamber. Aikawa [151] demonstrated experimentally that the EEDF is isotropic if $\frac{B}{P} < 2.5x10^6 G/torr$. Using typical numbers for a GIE [20], such as a neutral temperature of 290 K, and a neutral density of 10^{18} m^{-3}, the pressure in the discharge chamber is $3x10^{-5}$ and, with a magnetic field on the order of a few tens of G at most in the proximity of the ion optics, the ratio $\frac{B}{P}$ is well below the threshold value proposed by Aikawa.

When a cylindrical Langmuir probe is used in a flowing plasma (e.g. inside the discharge chamber at the interface with the ion optics and in the plume) and it is aligned with the flow direction, ions moving with a flow velocity v_i in addition to random thermal velocity v_B can distort the sheath and contribute to an unexpected current collected by the probe (Figure 72). In this situation, the so-called "end effect" becomes relevant and an additional parameter is introduced: the probe length to Debye length ratio, $\frac{l_{Lp}}{\lambda_D}$. This parameter can be considered as arising from the introduction of the aspect or "fineness" ratio $\frac{l_{Lp}}{r_{Lp}}$, in the form of the product $\left(\frac{l_{Lp}}{r_{Lp}}\right)\left(\frac{r_{Lp}}{\lambda_D}\right)$. Chung, Talbot, and Touryan [152] introduced the parameter τ_l to evaluate the relative importance of end effects in collisionless plasmas and it is defined as:

$$\tau_l = \frac{l_{Lp}}{\lambda_D}\frac{v_B}{v_i} \tag{C-5}$$

When $\tau_l \gg 1$, end effects can be considered negligible.

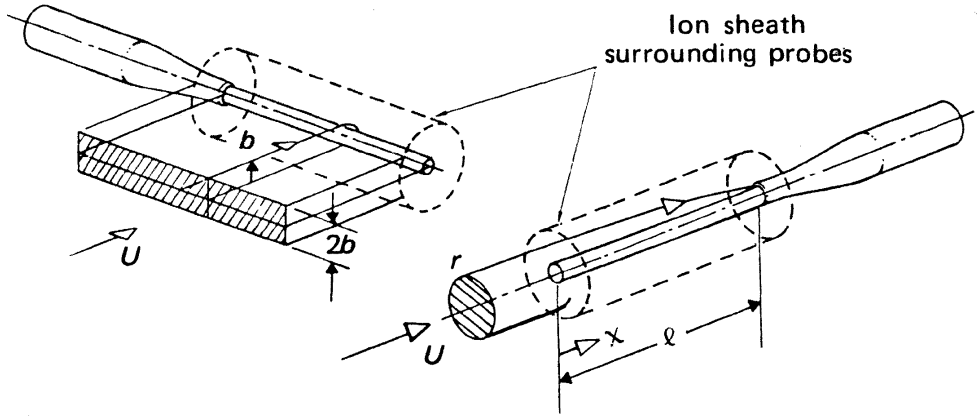

Figure 72 – Schematic of ion sheath around probes showing the origin of the end effect [152]

Another possible cause of distortion of the I-V trace is related to the material interactions of the probe with the plasma (e.g. probe heating, surface contamination, and secondary electron emission from the probe and/or probe holder). To reduce this effect, the probe should be

cleaned in ion/electron saturation regime between measurements, and bias sweeps should be performed multiple times in both ways so that any hysteresis can be identified.

It is clear that it is not possible to include all the above effects in the analysis of the I-V characteristic, because most of them depend on the plasma parameters that are being investigated. Because of these uncertainties, density measurements using a Langmuir probe are generally accurate to within an order of magnitude, while measurements of plasma potential and electron temperature are considered to be accurate with 20% or less, assuming a Maxwellian and isotropic EEDF, and mitigated magnetic fields and end effects. Even though the magnitude of the error is rather large, the relative error should be coherent from point to point resulting in accurate relative trends.

Bibliography

[1] C. C. Farnell and J. D. Williams, “Performance and Lifetime Simulation of Ion Thruster Optics,” Colorado State University, Fort Collins, Colorado, USA, 2007. [Online]. Available: https://search.proquest.com/docview/304861129

[2] H. Elsner, “Noble Gases: Supply Really Critical?,” Berlin, GER, 2018. [Online]. Available: https://www.deutsche-rohstoffagentur.de/DE/Gemeinsames/Produkte/Downloads/DERA_Rohstoffinformationen/rohstoffinformationen-39_en.pdf?__blob=publicationFile&v=2

[3] V. K. Rawlin, “Operation of the J-Series Thruster Using Inert Gas,” in *16th AIAA/JSASS/DGLR International Electric Propulsion Conference*, 1982. doi: 10.2514/6.1982-1929.

[4] N. L. Milder, “A Survey and Evaluation of Research on the Discharge Chamber Plasma of Kaufman Thrusters,” *J. Spacecr. Rockets*, vol. 7, no. 6, pp. 641–649, Jun. 1970, doi: 10.2514/3.30014.

[5] O. S. Tverdokhlebov and A. V Semenkin, “Iodine Propellant for Electric Propulsion - to Be or not to Be,” in *37th AIAA/ASME/SAE/ASEE Joint Propulsion Conference and Exhibit*, 2001. doi: doi:10.2514/6.2001-3350 10.2514/6.2001-3350.

[6] S. D. Leifer, D. Rapp, and W. A. Saunders, “Electrostatic Propulsion Using C60 Molecules,” *J. Propuls. Power*, vol. 8, no. 6, pp. 1297–1300, 1992, doi: 10.2514/3.11476.

[7] K. Holste *et al.*, “In Search of Alternative Propellants for Ion Thrusters,” in *Joint Conference of 30th International Symposium on Space Technology and Science, 34th International Electric Propulsion Conference, and 6th Nano-satellite Symposium*, 2015.

[8] D. R. Lev, G. D. Emsellem, and A. K. Hallock, “The Rise of the Electric Age for Satellite Propulsion,” *New Sp.*, vol. 5, no. 1, pp. 4–14, Mar. 2017, doi: 10.1089/space.2016.0020.

[9] A. Golkar and A. Salado, “Definition of New Space—Expert Survey Results and Key Technology Trends,” *IEEE J. Miniaturization Air Sp. Syst.*, vol. 2, no. 1, pp. 2–9, Mar. 2021, doi: 10.1109/JMASS.2020.3045851.

[10] Wikipedia contributors, “Starlink,” 2023. https://en.wikipedia.org/wiki/Starlink (accessed Sep. 13, 2023).

[11] M. J. Patterson and J. G. J. Williams, “Krypton Ion Thruster Performance,” in *28th*

AIAA/SAE/ASME/ASEE Joint Propulsion Conference and Exhibit, 1992. doi: 10.2514/6.1992-3144.

[12] D. C. Byers and P. D. Reader, "Operation of an Electron-Bombardment Ion Source using Various Gases," Cleveland, Ohio, USA, NASA #TN D-6620, 1971.

[13] W. L. Owens Jr, "A Noble Gas Ion Propulsion System," in *10th AIAA Electric Propulsion Conference*, 1973. doi: 10.2514/6.1973-1114.

[14] J. S. Sovey, "Improved Ion Containment using a Ring-Cusp Ion Thruster," *J. Spacecr. Rockets*, vol. 21, no. 5, pp. 488–495, Sep. 1984, doi: 10.2514/3.25684.

[15] V. K. Rawlin, "Characterization of Ion Accelerating Systems on NASA LeRC's Ion Thrusters," in *28th AIAA/SAE/ASME/ASEE Joint Propulsion Conference and Exhibit*, 1992. doi: 10.2514/6.1992-3827.

[16] B. A. Arkhipov *et al.*, "The Results of Testing and Effectiveness of the Kr-Xe Mixture Application in SPT," in *27th International Electric Propulsion Conference*, 2001.

[17] C. Ducci *et al.*, "Investigation of a 5 kW Class Hall-Effect Thruster Operating with Different Xenon-Krypton Mixtures," in *Joint Conference of 30th International Symposium on Space Technology and Science, 34th International Electric Propulsion Conference, and 6th Nano-satellite Symposium*, 2015.

[18] I. F. M. Ahmed Rudwan and S. B. Gabriel, "Investigation of the Discharge Characteristics of the T6 Hollow Cathode Operating on Several Inert Gases and a Kr/Xe Mixture," *AIP Conf. Proc.*, pp. 294–297, 2003, doi: 10.1063/1.1593923.

[19] N. Fazio, S. B. Gabriel, I. O. Golosnoy, and B. Wollenhaupt, "Mission Cost for Gridded Ion Engines using Alternative Propellants," in *36th International Electric Propulsion Conference*, 2019, pp. 1–21. [Online]. Available: https://eprints.soton.ac.uk/434549/

[20] D. M. Goebel and I. Katz, *Fundamentals of Electric Propulsion: Ion and Hall Thrusters*, 1st ed. Hoboken, New Jersey, USA: John Wiley & Sons, 2008.

[21] R. G. Jahn, *Physics of Electric Propulsion*, 1st ed. New York, USA: McGraw-Hill, 1968.

[22] R. G. Jahn and E. Y. Choueiri, "Electric Propulsion," *Acad. Press*, vol. 3, pp. 125–141, 2002.

[23] R. E. Wirz and D. M. Goebel, "Effects of Magnetic Field Topography on Ion Thruster Discharge Performance," *Plasma Sources Sci. Technol.*, vol. 17, no. 3, p. 035010, Aug. 2008, doi: 10.1088/0963-0252/17/3/035010.

[24] H. W. Loeb, “Plasma-based ion beam sources,” *Plasma Phys. Control. Fusion*, vol. 47, no. 12B, pp. B565–B576, 2005, doi: 10.1088/0741-3335/47/12b/s41.

[25] M. S. Hutchins, H. B. Simpson, and J. J. Palencia, “QinetiQ’s T6 and T5 Ion Thruster Electric Propulsion System Architectures and Performances,” in *Joint Conference of 30th International Symposium on Space Technology and Science, 34th International Electric Propulsion Conference, and 6th Nano-satellite Symposium*, 2015.

[26] D. A. Herman and A. D. Gallimore, “Discharge Chamber Plasma Structure of a 40-cm NEXT-type Ion Engine,” in *41st AIAA/ASME/SAE/ASEE Joint Propulsion Conference & Exhibit*, 2005, p. 4250.

[27] M. Coletti, N. C. Wallace, S. B. Gabriel, D. Frollani, and H. B. Simpson, “Ring Cusp Ion Engine Development in the UK,” in *Joint Conference of 30th International Symposium on Space Technology and Science, 34th International Electric Propulsion Conference, and 6th Nano-satellite Symposium*, 2015.

[28] M. Y. Selivanov and A. S. Lovtsov, “IT-200PM Ring-Cusp Ion Thruster,” in *36th International Electric Propulsion Conference*, 2019, pp. 1–10.

[29] M. M.-T. Tsay, J. Frongillo, J. Model, J. Zwahlen, and L. Paritsky, “Maturation of Iodine Fueled BIT-3 RF Ion Thruster and RF Neutralizer,” in *52nd AIAA/SAE/ASEE Joint Propulsion Conference*, 2016. doi: 10.2514/6.2016-4544.

[30] H. J. Leiter, C. Altmann, J.-P. Porst, D. Lauer, M. Berger, and M. Rath, “Six Decades of Thrust - The Ariane Group Radiofrequency Ion Thrusters and Systems Family,” in *35th International Electric Propulsion Conference*, 2017.

[31] Busek Co. Inc., “RF Ion Thrusters — Busek,” 2023. https://www.busek.com/rf-ion-thrusters (accessed Sep. 13, 2023).

[32] C. Collingwood and S. B. Gabriel, “Investigation of a Miniature Differential Ion Thruster,” University of Southampton, Southampton, UK, 2011. [Online]. Available: https://eprints.soton.ac.uk/334166/

[33] M. Dobkevicius and D. Feili, “Modelling and Design of Inductively Coupled Radio Frequency Gridded Ion Thrusters with an Application to Ion Beam Shepherd Type Space Missions,” University of Southampton, Southampton, UK, 2017. [Online]. Available: https://eprints.soton.ac.uk/413768/

[34] F. Guarducci *et al.*, “Development and Industrialization of the RIT 3.5,” in *37th International Electric Propulsion Conference*, 2022, pp. 1–17.

[35] H. J. Leiter *et al.*, “Evolution of the AIRBUS DS GmbH Radio Frequency Ion Thruster Family,” in *Joint Conference of 30th International Symposium on Space Technology and Science, 34th International Electric Propulsion Conference, and 6th Nano-satellite Symposium*, 2015.

[36] Y. Takao, H. Kataharada, T. Miyamoto, H. Masui, N. Yamamoto, and H. Nakashima, “Performance test of micro ion thruster using microwave discharge,” *Vacuum*, vol. 80, no. 11–12, pp. 1239–1243, 2006, doi: 10.1016/j.vacuum.2006.01.071.

[37] C. Bramanti *et al.*, “The Innovative Dual-Stage 4-Grid Ion Thruster Concept – Theory and Experimental Results,” in *57th International Astronautical Congress*, 2006.

[38] S. Mazouffre, “Electric propulsion for satellites and spacecraft: established technologies and novel approaches,” *Plasma Sources Sci. Technol.*, vol. 25, no. 3, 2016, doi: 10.1088/0963-0252/25/3/033002.

[39] J. E. Polk *et al.*, “An Overview of NASA’s Electric Propulsion Programs, 2010-11,” in *32nd International Electric Propulsion Conference*, 2011, no. 2011–330.

[40] D. R. Lev, I. G. Mikellides, D. Pedrini, D. M. Goebel, B. A. Jorns, and M. S. McDonald, “Recent Progress in Research and Development of Hollow Cathodes for Electric Propulsion,” *Rev. Mod. Plasma Phys.*, vol. 3, no. 1, p. 6, Dec. 2019, doi: 10.1007/s41614-019-0026-0.

[41] C. H. Edwards, “Discharge Characteristics and Instabilities in the UK-25 Ion Thruster Operating on Inert Gas Propellants,” University of Southampton, 1997. [Online]. Available: http://eprints.soton.ac.uk/id/eprint/463034

[42] I. F. M. Ahmed Rudwan and S. B. Gabriel, “Physics of Hollow Cathode Breakdown and Steady-State Operation with Several Inert Gas Propellants,” University of Southampton, 2003.

[43] D. J. Milligan and S. B. Gabriel, “Investigation of the Baffle Annulus region of the UK-25 ion thruster,” in *35th AIAA/ASME/SAE/ASEE Joint Propulsion Conference and Exhibit*, 1999.

[44] N. C. Wallace, D. G. Fearn, and R. E. Copleston, “The Design and Performance of the T6 Ion Thruster,” in *34th AIAA/ASME/SAE/ASEE Joint Propulsion Conference and Exhibit*, 1998. doi: doi:10.2514/6.1998-3342 10.2514/6.1998-3342.

[45] R. P. Welle, “Availability Considerations in the Select ion of Inert Prop ellant s for Ion Engines,” in *21st AIAA/DGLR/JSASS International Electric Propulsion Conference*, 1990. doi: 10.2514/6.1990-2589.

[46] R. P. Welle, “Xenon and Krypton Availability for Electric Propulsion: An Updated Assessment,” in *29th AIAA/ASME/SAE/ASEE Joint Propulsion Conference and Exhibit*, 1993. doi: doi:10.2514/6.1993-2401 10.2514/6.1993-2401.

[47] J. R. Anderson and D. Fitzgerald, “Fullerene Propellant Research for Electric Propulsion,” in *32nd AIAA/ASME/SAE/ASEE Joint Propulsion Conference and Exhibit*, 1996. doi: doi:10.2514/6.1996-3211 10.2514/6.1996-3211.

[48] C. A. Scharlemann, “Theoretical and Experimental Investigation of C60-Propellant for Ion Propulsion,” *Acta Astronaut.*, vol. 51, no. 12, pp. 865–872, 2002, doi: https://doi.org/10.1016/S0094-5765(02)00115-7.

[49] R. A. Dressler, D. J. Levandier, and Y.-H. Chiu, “Iodine Electric Propulsion Thrusters,” US 6,609,363 B1, 2003

[50] A. Kieckhafer and L. B. King, “Energetics of Propellant Options for High-Power Hall Thrusters,” *J. Propuls. Power*, vol. 23, no. 1, pp. 21–26, 2007, doi: 10.2514/1.16376.

[51] J. J. Szabo, M. Robin, S. Paintal, B. Pote, V. Hruby, and C. Freeman, “Iodine Propellant Space Propulsion,” in *33rd International Electric Propulsion Conference*, 2013, no. 2013–311.

[52] M. M.-T. Tsay, J. Frongillo, and K. Hohman, “Iodine-Fueled Mini RF Ion Thruster for CubeSat Applications,” in *Joint Conference of 30th International Symposium on Space Technology and Science, 34th International Electric Propulsion Conference, and 6th Nano-satellite Symposium*, 2015.

[53] D. Rafalskyi *et al.*, “In-orbit Demonstration of an Iodine Electric Propulsion System,” *Nature*, vol. 599, no. 7885, pp. 411–415, 2021, doi: 10.1038/s41586-021-04015-y.

[54] P. Dietz, K. Holste, W. Gartner, P. E. Kohler, P. J. Klar, and P. R. Schreiner, “Status Report of Diamondoids as Alternative Propellants for Ion-Thrusters,” in *35th International Electric Propulsion Conference*, 2017.

[55] J. S. Sovey, “Improved Ion Containment Using a Ring-Cusp Ion Thruster,” in *16th AIAA/JSASS/DGLR International Electric Propulsion Conference*, 1982.

[56] Y. Nakamura, K. Miyazaki, and E. Suzuki, “Operations and Performances of a 5 cm Diameter Ion Thruster by using Inert Gases,” in *16th International Electric Propulsion Conference*, Nov. 1982. doi: 10.2514/6.1982-1924.

[57] M. J. Patterson, R. F. Roman, and J. E. Foster, “Ion Engine Development for Interstellar

Precursor Missions," in *36th AIAA/ASME/SAE/ASEE Joint Propulsion Conference and Exhibit*, Jul. 2000, no. January. doi: 10.2514/6.2000-3811.

[58] V. K. Rawlin, J. G. J. Williams, L. R. Pinero, and R. F. Roman, "Status of Ion Engine Development for High Power, High Specific Impulse Missions," in *27th International Electric Propulsion Conference*, 2001.

[59] V. K. Rawlin, G. C. Soulas, J. G. J. Williams, and R. F. Roman, "High Specific Impulse, High Power Ion Engine Operation," in *38th AIAA/ASME/SAE/ASEE Joint Propulsion Conference & Exhibit*, Jul. 2002, no. July, pp. 1–12. doi: 10.2514/6.2002-3838.

[60] C. M. Simon, R. Mercado, S. K. Schnell, B. Smit, and M. Haranczyk, "What Are the Best Materials To Separate a Xenon/Krypton Mixture?," *Chem. Mater.*, vol. 27, no. 12, pp. 4459–4475, Jun. 2015, doi: 10.1021/acs.chemmater.5b01475.

[61] F. G. Kerry, *Industrial Gas Handbook: Gas Separation and Purification*, 1st ed. Boca Raton, Florida, USA: CRC Press, 2007. doi: 10.1201/9781420008265.

[62] M. R. Nakles, J. W. A. Hargus, J. J. Delgado, and R. L. Corey, "A Performance Comparison of Xenon and Krypton Propellant on an SPT-100 Hall Thruster," in *32nd International Electric Propulsion Conference*, 2011.

[63] V. P. Kim, G. A. Popov, V. I. Kozlov, A. I. Skrylnikov, and D. P. Grdlichko, "Investigation of SPT Performance and Particularities of its Operation with Kr and Kr/Xe Mixtures," in *27th International Electric Propulsion Conference*, 2001.

[64] B. A. Arkhipov, I. A. Khoromsky, and V. M. Murashko, "Problems of Designing EPS's with SPT's Working on Krypton-Xenon Mixture," in *38th AIAA/ASME/SAE/ASEE Joint Propulsion Conference & Exhibit*, 2002. doi: 10.2514/6.2002-3682.

[65] T. Andreussi *et al.*, "Identification, Evaluation and Testing of Alternative Propellants for Hall Effect Thrusters," in *35th International Electric Propulsion Conference*, 2017.

[66] D. G. Fearn, A. Singfield, N. C. Wallace, S. A. Gair, and P. T. Harris, "The Operation of Ion Thruster Hollow Cathodes using Rare Gas Propellants," in *21st AIAA/DGLR/JSASS International Electric Propulsion Conference*, 1990. doi: 10.2514/6.1990-2584.

[67] S. Pottinger and S. B. Gabriel, "Investigation of Steady State Characteristics of Hollow Cathode Internal Plasmas using Optical Emission Spectroscopy," University of Southampton, Southampton, UK, 2005. [Online]. Available: https://eprints.soton.ac.uk/345074/

[68] A. N. Grubisic, “Microthrusters Based on the T5 and T6 Hollow Cathode,” University of Southampton, 2009. [Online]. Available: https://eprints.soton.ac.uk/181509/

[69] S. B. Gabriel, A. J. N. Daykin-Iliopoulos, M. Praeger, and M. Coletti, “Hollow Cathode Operation with Different Gases,” in *35th International Electric Propulsion Conference*, 2017.

[70] A. Neumann and M. Brchnelova, “Modelling of Cryopumps for Space Electric Propulsion Usage,” *Aerospace*, vol. 11, no. 3, p. 177, Feb. 2024, doi: 10.3390/aerospace11030177.

[71] Leybold, “A guide to preparing your vacuum system for Thruster Testing chambers,” 2024. https://www.leybold.com/en/knowledge/blog/vacuum-systems-for-thruster-testing (accessed Jul. 08, 2024).

[72] R. E. Wirz and F. E. C. Culick, “Discharge Plasma Processes of Ring-Cusp Ion Thrusters,” California Institute of Technology, Pasadena, California, USA, 2005. [Online]. Available: http://resolver.caltech.edu/CaltechETD:etd-05232005-162628

[73] M. A. Lieberman and A. J. Lichtenberg, *Principles of Plasma Discharges and Materials Processing*, 2nd ed. Hoboken, New Jersey, USA: John Wiley & Sons, 2005.

[74] C. Y. J. Wong and S. M. Lund, “Multi-Species Child-Langmuir Law with Application to ECR Ion Sources,” *Proc. ECRIS2020*, no. 8, pp. 106–109, 2021, doi: 10.18429/JACoW-ECRIS2020-TUZZO05.

[75] J. R. Brophy and P. J. Wilbur, “Ion Thruster Performance Model,” Colorado State University, Fort Collins, Colorado, USA, 1984.

[76] E. R. Torres and M. Martinez-Sanchez, “Prediction of the Performance of an Ion Thruster Using Buckminsterfullerene as Propellant,” Massachusetts Institute of Technology, Cambridge, Massachusetts, USA, 1993. [Online]. Available: http://hdl.handle.net/1721.1/31042

[77] D. M. Goebel, “Ion Source Discharge Performance and Stability,” *Phys. Fluids*, vol. 25, no. 6, p. 1093, 1982, doi: 10.1063/1.863842.

[78] R. T. Carpenter, S. A. Boardsen, and S. W. Daniels, “Plasma Characteristics of a 17 cm Diameter Line-Cusp Ion Thruster,” in *16th AIAA/JSASS/DGLR International Electric Propulsion Conference*, 1982.

[79] G. Aston and W. D. Deininger, “Test Bed Ion Engine Development,” Pasadena, California, USA, CR-174623, 1984.

[80] J. R. Brophy, “Simulated Ion Thruster Operation without Beam Extraction,” in *21st AIAA/DGLR/JSASS International Electric Propulsion Conference*, Jul. 1990. doi: 10.2514/6.1990-2655.

[81] F. Cannat, F. Guarducci, S. Ciaralli, M. Coletti, and S. B. Gabriel, “Design and Optimization of a Ring Cusp Thruster with Simulated Beam Extraction,” in *35th International Electric Propulsion Conference*, 2017.

[82] R. Shastry, M. J. Patterson, D. A. Herman, and J. E. Foster, “Current Density Measurements of an Annular-Geometry Ion Engine,” in *48th AIAA/ASME/SAE/ASEE Joint Propulsion Conference & Exhibit*, 2012. doi: 10.2514/6.2012-4186.

[83] C. C. Farnell, J. D. Williams, and P. J. Wilbur, “NEXT Ion Optics Simulation via ffx,” in *39th AIAA/ASME/SAE/ASEE Joint Propulsion Conference and Exhibit*, 2003.

[84] C. C. Farnell, “Numerical Simulation of HiPEP Ion Optics,” in *40th AIAA/ASME/SAE/ASEE Joint Propulsion Conference and Exhibit*, 2004. doi: doi:10.2514/6.2004-3818 10.2514/6.2004-3818.

[85] J. D. Williams, C. C. Farnell, D. M. Laufer, and R. A. Martinez, “HiPEP Ion Optics System Evaluation Using Gridlets,” in *40th AIAA/ASME/SAE/ASEE Joint Propulsion Conference and Exhibit*, 2004.

[86] E. M. Aguirre, E. E. Scime, and T. N. Good, “Ion Beams in Multi-Species Plasmas,” *Phys. Plasmas*, vol. 25, no. 4, 2018, doi: 10.1063/1.5021941.

[87] A. Sengupta, D. M. Goebel, and A. G. Owens, “Langmuir Probe Studies of Magnetic Confinement in an Ion Thruster Discharge Plasma,” *J. Propuls. Power*, vol. 25, no. 2, pp. 387–396, 2009, doi: 10.2514/1.36547.

[88] K. Dannenmayer, A. Bulit, and J. Gonzalez del Amo, “Measurements of Plasma Parameters in the Plume of Electric Propulsion Devices - Recent works performed at the ESA Propulsion Lab,” in *Joint Conference of 30th International Symposium on Space Technology and Science, 34th International Electric Propulsion Conference, and 6th Nano-satellite Symposium*, 2015.

[89] F. Magnus and J. T. Gudmundsson, “Digital Smoothing of the Langmuir Probe I-V Characteristic,” *Rev. Sci. Instrum.*, vol. 79, no. 7, p. 073503, Jul. 2008, doi: 10.1063/1.2956970.

[90] V. A. Godyak, R. B. Piejak, and B. M. Alexandrovich, “Probe Diagnostics of non-Maxwellian Plasmas,” *J. Appl. Phys.*, vol. 73, no. 8, pp. 3657–3663, 1993, doi:

10.1063/1.352924.

[91] M. A. Naveed, N. U. Rehman, S. Zeb, S. Hussain, and M. Zakaullah, “Langmuir Probe and Spectroscopic Studies of RF Generated Helium-Nitrogen Mixture Plasma,” *Eur. Phys. J. D*, vol. 47, no. 3, pp. 395–402, 2008, doi: 10.1140/epjd/e2008-00055-9.

[92] R. F. Fernsler, “Modeling Langmuir Probes in Multi-Component Plasmas,” *Plasma Sources Sci. Technol.*, vol. 18, no. 1, 2009, doi: 10.1088/0963-0252/18/1/014012.

[93] F. Cannat, F. Guarducci, S. Ciaralli, and S. B. Gabriel, “Development of a 30-cm Ring Cusp Discharge Chamber - Design and Performance Characterization with Simulated Ion Beam Extraction,” in *6th Space Propulsion Conference*, 2018.

[94] D. Frollani, M. Coletti, and S. B. Gabriel, “Flexible LaB6 Hollow Cathode for Lab Tests,” in *34th International Electric Propulsion Conference*, 2015.

[95] A. J. N. Daykin-Iliopoulos, I. O. Golosnoy, and S. B. Gabriel, “Development of a High Current Heaterless Hollow Cathode,” in *6th Space Propulsion Conference*, 2018.

[96] M. J. Druyvesteyn, “Der Niedervoltbogen,” *Zeitschrift für Phys.*, vol. 64, no. 11, pp. 781–798, 1930, doi: 10.1007/bf01773007.

[97] D. M. Goebel, J. E. Polk, and A. Sengupta, “Discharge Chamber Performance of the NEXIS Ion Thruster,” in *40th AIAA/ASME/SAE/ASEE Joint Propulsion Conference and Exhibit*, 2004. doi: doi:10.2514/6.2004-3813 10.2514/6.2004-3813.

[98] A. S. Sanghera and D. J. DeTurris, “Performance Characterization of a 15-cm Ion Thruster with Simulated Beam Extraction,” in *43rd AIAA/ASME/SAE/ASEE Joint Propulsion Conference & Exhibit*, Jul. 2007, vol. 3, no. July, pp. 2137–2151. doi: 10.2514/6.2007-5219.

[99] J. E. Foster *et al.*, “Simulated Beam Extraction Performance Characterization of a 50-cm Ion Thruster Discharge,” in *48th AIAA/ASME/SAE/ASEE Joint Propulsion Conference & Exhibit*, Jul. 2012, no. August, pp. 1–12. doi: 10.2514/6.2012-3795.

[100] E. Oyarzabal, R. P. Doerner, M. Shimada, and G. R. Tynan, “Carbon Atom and Cluster Sputtering under Low-Energy Noble Gas Plasma Bombardment,” *J. Appl. Phys.*, vol. 104, no. 4, Aug. 2008, doi: 10.1063/1.2968549.

[101] F. Bosi, F. Cannat, F. Guarducci, and S. B. Gabriel, “Experimental Characterization of a Ring-Cusp Discharge Chamber with Xenon and Krypton,” in *37th International Electric Propulsion Conference*, 2022, pp. 1–13.

[102] A. Sengupta, D. M. Goebel, D. Fitzgerald, A. G. Owens, G. Tynan, and R. Doerner, "Experimentally Determined Neutral Density and Plasma Parameters in a 30 cm Ion Engine," in *40th AIAA/ASME/SAE/ASEE Joint Propulsion Conference and Exhibit*, 2004.

[103] F. Bosi, "GIE150 Discharge-only LP Characterisation (internal report)," 2022.

[104] N. Fazio, I. O. Golosnoy, and S. B. Gabriel, "Discharge Performance Analysis of different types of Gridded Ion Engines using Alternative Propellants," in *37th International Electric Propulsion Conference*, 2022, pp. 1–14.

[105] S. Barquero, K. Tabata, R. Tsukizaki, M. Merino, J. Navarro-Cavallé, and K. Nishiyama, "Performance Characterization of the μ10 Electron-Cyclotron-Resonance Ion Thruster using Alternative Propellants: Krypton vs. Xenon," *Acta Astronaut.*, vol. 211, no. January, pp. 750–754, 2023, doi: 10.1016/j.actaastro.2023.06.036.

[106] J. A. Linnell and A. D. Gallimore, "An Evaluation of Krypton Propellant in Hall Thrusters," University of Michigan, Ann Arbor, Michigan, USA, 2007. [Online]. Available: http://hdl.handle.net/2027.42/126493

[107] J. R. Rumble, *CRC Handbook of Chemistry and Physics, 98th Edition*, 98th ed. Boca Raton, Florida, USA: CRC Press, 2017. [Online]. Available: https://books.google.co.uk/books?id=4i_vAQAACAAJ

[108] Wikipedia contributors, "Prices of Chemical Elements," 2023. https://en.wikipedia.org/wiki/Prices_of_chemical_elements (accessed Mar. 31, 2023).

[109] E. W. Lemmon, M. O. McLinden, and D. G. Friend, "Thermophysical Properties of Fluid Systems," in *NIST Chemistry WebBook, NIST Standard Reference Database 69*, National Institute of Standards and Technology, 1997. doi: 10.18434/T4D303.

[110] G. Kawahara and S. F. McCleskey, "Titanium Lined, Carbon Composite Overwrapped Pressure Vessel," in *32nd AIAA/ASME/SAE/ASEE Joint Propulsion Conference and Exhibit*, Jul. 1996. doi: 10.2514/6.1996-2751.

[111] W. H. Tam *et al.*, "Design and Manufacture of a Composite Overwrapped Xenon Conical Pressure Vessel," in *32nd AIAA/ASME/SAE/ASEE Joint Propulsion Conference and Exhibit*, Jul. 1996. doi: 10.2514/6.1996-2752.

[112] W. H. Tam, A. C. Jackson, E. Nishida, Y. Kasai, A. Tsujihata, and K. Kajiwara, "Design and Manufacture of the ETS VIII Xenon Tank," in *36th AIAA/ASME/SAE/ASEE Joint Propulsion Conference and Exhibit*, Jul. 2000. doi: 10.2514/6.2000-3677.

[113] J. F. Benton, I. A. Ballinger, A. Ferretti, and N. Ierardo, “Design & Manufacture of a High Performance High Mass Efficient Gas Tank for the Vega Avum,” in *43rd AIAA/ASME/SAE/ASEE Joint Propulsion Conference & Exhibit*, Jul. 2007, pp. 4767–4780. doi: 10.2514/6.2007-5500.

[114] M. Aerospace, “Tank Catalogue,” 2020. https://www.mt-aerospace.de/downloads.html (accessed Feb. 25, 2020).

[115] M. C. Bordage *et al.*, “Comparisons of Sets of Electron–Neutral Scattering Cross Sections and Swarm Parameters in Noble Gases: III. Krypton and Xenon,” *J. Phys. D. Appl. Phys.*, vol. 46, no. 33, 2013, doi: 10.1088/0022-3727/46/33/334003.

[116] E. W. Bell, N. Djurić, and G. H. Dunn, “Electron-Impact Ionization of In+ and Xe+,” *Phys. Rev. A*, vol. 48, no. 6, pp. 4286–4291, Dec. 1993, doi: 10.1103/PhysRevA.48.4286.

[117] K. F. Man, A. C. H. Smith, and M. F. A. Harrison, “A Measurement of the Cross Section for Electron Impact Ionisation of Ne+ , Ar+ , Kr+ and Xe+,” *J. Phys. B At. Mol. Phys.*, vol. 20, no. 21, pp. 5865–5880, Nov. 1987, doi: 10.1088/0022-3700/20/21/030.

[118] T. D. Masek, “Plasma Properties and Performance of Mercury Ion Thrusters,” *AIAA J.*, vol. 9, no. 2, pp. 205–212, Feb. 1971, doi: 10.2514/3.6152.

[119] J. W. Ward and T. D. Masek, “A Discharge Computer Model for an Electron Bombardment Thruster,” in *12th AIAA International Electric Propulsion Conference*, 1976. doi: 10.2514/6.1976-1009.

[120] J. R. Brophy and P. J. Wilbur, “Simple Performance Model for Ring and Line Cusp Ion Thrusters,” *AIAA J.*, vol. 23, no. 11, pp. 1731–1736, Nov. 1985, doi: 10.2514/3.9158.

[121] Y. Arakawa and K. Ishihara, “A Numerical Code for Cusped Ion Thrusters,” in *22nd AIDAA/AIAA/DGLR/JSASS International Electric Propulsion Conference*, 1991.

[122] Y. Arakawa and P. J. Wilbur, “Finite Element Analysis of Plasma Flows in Cusped Discharge Chambers,” *J. Propuls. Power*, vol. 7, no. 1, pp. 125–128, Jan. 1991, doi: 10.2514/3.23303.

[123] Y. Arakawa and T. Yamada, “Monte Carlo Simulation of Primary Electron Motions in Cusped Discharge Chambers,” in *21st AIAA/DGLR/JSASS International Electric Propulsion Conference*, 1990. doi: 10.2514/6.1990-2654.

[124] D. M. Goebel, “Analytical Discharge Performance Model for RF and Kaufman Ion Thrusters,” in *43rd AIAA/ASME/SAE/ASEE Joint Propulsion Conference & Exhibit*, Jul.

2007. doi: 10.2514/6.2007-5246.

[125] D. M. Goebel, R. E. Wirz, and I. Katz, “Analytical Ion Thruster Discharge Performance Model,” *J. Propuls. Power*, vol. 23, no. 5, pp. 1055–1067, Sep. 2007, doi: 10.2514/1.26404.

[126] S. J. Araki and R. E. Wirz, “Multi-Scale Multi-Species Modeling for Plasma Devices,” University of California, Los Angeles, Los Angeles, California, USA, 2014. [Online]. Available: https://escholarship.org/uc/item/38d4h99p

[127] T. Binder, “Development and Application of PICLas for Combined Optic-/Plume-Simulation of Ion-Propulsion Systems,” University of Stuttgart, 2019. doi: 10.18419/opus-10657.

[128] I. Katz, J. E. Polk, J. R. Brophy, and J. R. Anderson, “Numerical Simulations of Ion Thruster Accelerator Grid Erosion,” in *38th AIAA/ASME/SAE/ASEE Joint Propulsion Conference & Exhibit*, 2002. doi: 10.2514/6.2002-4261.

[129] J. R. Anderson, I. Katz, and D. M. Goebel, “Numerical Simulation of Two-Grid Ion Optics Using a 3D Code,” in *40th AIAA/ASME/SAE/ASEE Joint Propulsion Conference and Exhibit*, 2004. doi: 10.2514/6.2004-3782.

[130] Y. Nakayama and P. J. Wilbur, “Numerical Simulation of Ion Beam Optics for Multiple-Grid Systems,” *J. Propuls. Power*, vol. 19, no. 4, pp. 607–613, Jul. 2003, doi: 10.2514/2.6148.

[131] I. Funaki *et al.*, “Numerical Lifetime Evaluation of Ion Thruster’s Ion Optics Using the JIEDI Tool,” in *48th AIAA/ASME/SAE/ASEE Joint Propulsion Conference & Exhibit*, Jul. 2012. doi: 10.2514/6.2012-3797.

[132] R. Becker and W. B. Herrmannsfeldt, “IGUN − A Program for the Simulation of Positive Ion Extraction including Magnetic Fields,” *Rev. Sci. Instrum.*, vol. 63, no. 4, pp. 2756–2758, Apr. 1992, doi: 10.1063/1.1142795.

[133] V. H. Chaplin *et al.*, “3D Simulations of Ion Thruster Accelerator Grid Erosion Accounting for Charge Exchange Ion Space Charge,” in *2018 Joint Propulsion Conference*, Jul. 2018. doi: 10.2514/6.2018-4812.

[134] Y. Okawa and H. Takegahara, “Numerical Study of Beam Extraction Phenomena in an Ion Thruster,” *Jpn. J. Appl. Phys.*, vol. 40, no. Part 1, No. 1, pp. 314–321, Jan. 2001, doi: 10.1143/JJAP.40.314.

[135] M. W. Crofton and I. D. Boyd, “The Origins of Accelerator Grid Current: Analysis of T5-Grid Test Results,” in *35th AIAA/ASME/SAE/ASEE Joint Propulsion Conference and Exhibit*, 1999. doi: doi:10.2514/6.1999-2443 10.2514/6.1999-2443.

[136] J. W. Emhoff and I. D. Boyd, “Simulation of Ion Optics Using Particle-In-Cell and Treecode Methods,” University of Michigan, Ann Arbor, Michigan, USA, 2005. [Online]. Available: http://hdl.handle.net/2027.42/125071

[137] R. Kafafy and J. Wang, “A HG-IFE-PIC Simulation Model for Ion Thruster Optics Plasma Flow,” in *36th AIAA Plasmadynamics and Lasers Conference*, Jun. 2005. doi: 10.2514/6.2005-4789.

[138] H. Cao, Y. Chu, E. Wang, Y. Cao, G. Xia, and Z. Zhang, “Numerical Simulation Study on Barrel Erosion of Ion Thruster Accelerator Grid,” *J. Propuls. Power*, vol. 31, no. 6, pp. 1785–1792, Nov. 2015, doi: 10.2514/1.B35717.

[139] J. W. Emhoff, I. D. Boyd, C. C. Farnell, and J. D. Williams, “Perveance and Beamlet Expansion Modeling of the NEXT Ion Engine,” in *29th International Electric Propulsion Conference*, 2005, pp. 1–12.

[140] D. A. Herman and A. D. Gallimore, “The Use of Electrostatic Probes to Characterize the Discharge Plasma Structure and Identify Discharge Cathode Erosion Mechanisms in Ring-Cusp Ion Thrusters,” University of Michigan, Ann Arbor, Michigan, USA, 2005. [Online]. Available: http://hdl.handle.net/2027.42/125382

[141] S. Mazouffre, G. Largeau, L. Garrigues, C. Boniface, and K. Dannenmayer, “Evaluation of Various Probe Designs for Measuring the Ion Current Density in a Hall Thruster Plume,” in *35th International Electric Propulsion Conference*, 2017, pp. 1–17.

[142] M. P. Monterde, M. G. Haines, A. E. Dangor, A. K. Malik, and D. G. Fearn, “Kaufman-type Xenon Ion Thruster Coupling Plasma: Langmuir Probe Measurements,” *J. Phys. D. Appl. Phys.*, vol. 30, no. 5, pp. 842–855, Mar. 1997, doi: 10.1088/0022-3727/30/5/017.

[143] H. M. Mott-Smith and I. Langmuir, “The Theory of Collectors in Gaseous Discharges,” *Phys. Rev.*, vol. 28, no. 4, p. 727, 1926.

[144] F. F. Chen, “Langmuir Probe Diagnostics,” Jeju, KP, 2003.

[145] F. F. Chen, “Electric Probes,” in *Plasma Diagnostic Techniques, edited by Huddlestone, RH and Leornard, SL*, New York, USA: Academic Press, 1965, pp. 113–200.

[146] I. H. Hutchinson, *Principles of Plasma Diagnostics*, 2nd ed. New York, USA: Cambridge

University Press, 2002.

[147] R. L. Merlino, “Understanding Langmuir Probe Current-Voltage Characteristics,” *Am. J. Phys.*, vol. 75, no. 12, pp. 1078–1085, 2007, doi: 10.1119/1.2772282.

[148] V. A. Godyak and B. M. Alexandrovich, “Comparative Analyses of Plasma Probe Diagnostics Techniques,” *J. Appl. Phys.*, vol. 118, no. 23, 2015.

[149] V. A. Godyak and V. I. Demidov, “Probe Measurements of Electron-Energy Distributions in Plasmas: what can we measure and how can we achieve reliable results?,” *J. Phys. D. Appl. Phys.*, vol. 44, no. 26, 2011, doi: 10.1088/0022-3727/44/26/269501.

[150] T. G. Wantock, “Thrust Balance Performance Characterisation and Internal Langmuir Probe Plasma Diagnostics for a Halo Thruster,” University of Surrey, 2017.

[151] H. Aikawa, “The Measurement of the Anisotropy of Electron Distribution Function of a Magnetized Plasma,” *J. Phys. Soc. Japan*, vol. 40, no. 6, pp. 1741–1749, Jun. 1976, doi: 10.1143/JPSJ.40.1741.

[152] P. M. Chung, L. Talbot, and K. J. Touryan, “Electric Probes in Stationary and Flowing Plasmas: Part 1. Collisionless and Transitional Probes,” *AIAA J.*, vol. 12, no. 2, pp. 133–144, 1974, doi: 10.2514/3.49184.